UNIVERSITY OF PADOVA
Department of Industrial Engineering
Doctoral Program in Industrial Engineering
Curriculum: Materials Engineering
Cohort XXXVIII

ENGINEERED COMPOSITES FOR WATER DECONTAMINATION FROM HEAVY METALS AND EMERGING POLLUTANTS

Thesis for the degree of Doctor of Philosophy

Prof. Andrea Ghiotti, Course Coordinator
Prof. Paolo Sgarbossa, Candidate's Supervisor
Prof. Roberta Bertani, Candidate's Co-supervisor

Ph.D. Candidate: ELEONORA RUSSO

Padua
November 10, 2025

Per aspera ad astra.

— Virgilio

ABSTRACT

The scarcity of clean water is a growing global concern, and proper wastewater management is essential to prevent environmental contamination. Conventional treatment methods, such as ultrafiltration, flocculation, coagulation, adsorption, and biological processes, are often limited by high costs and energy demand, incomplete removal of pollutants, and the generation of secondary wastes. This work focuses on the development of innovative, sustainable, and efficient materials for wastewater treatment.

Biocompatible and biodegradable sodium alginate-based hydrogels were prepared and added with nanomaterials, including magnetic nanoparticles and graphene oxide-based magnetic nanosheets, to enhance the adsorption capacity for heavy metals. The influence of crosslinker concentration and nanofiller loading on mechanical stability and adsorption efficiency was systematically studied.

In parallel, graphitic carbon nitride (g-C_3N_4) and its heteroatom-doped derivatives (Br, P, and B) were synthesized via co-pyrolysis and post-pyrolysis approaches. Doped g-C_3N_4 materials were obtained from different brominated precursors, enabling investigation of the effects of chemical structure on photocatalytic activity. The photocatalysts were tested for the degradation of organic dyes (Rhodamine B) and emerging pharmaceutical pollutants (sulfamethoxazole and atenolol), using UV-Vis spectrophotometry and HPLC, showing significant improvement compared to pristine g-C_3N_4.

Overall, the combination of modified alginate hydrogels and heteroatom-doped g-C_3N_4 provides a versatile, cost-effective, and environmentally friendly approach for the removal of inorganic and organic pollutants from water, demonstrating potential for large-scale water purification and environmental remediation applications.

CONTENTS

1 Introduction

Access to clean water is a fundamental requirement for human health and environmental sustainability. Even if the lack of potable water has not yet been experienced in the most developed areas, this could change in the next few decades, making the protection of water resources of paramount importance. According to the World Water Council, approximately 3.2 billion people are currently affected by water shortages, a figure projected to rise to 3.9 billion by 2030. Growing industrialization, fast population expansion, and unregulated freshwater usage have all contributed to the deterioration in groundwater quality and quantity. According to the World Health Organization (WHO), about 663 million people globally suffer from polluted water, and 1.2 billion people do not have access to drinkable water [1]. Clean water scarcity is consistently indicated as one of the most pressing environmental challenges.

Wastewater plays a central role in this scenario. Approximately 80% of the world's wastewater flows back into ecosystems without being treated or reused. It may contain a wide range of hazardous substances, including organic and inorganic chemicals, dust, solids, and biological agents [2]. In recent decades, the unregulated discharge of contaminants has posed significant threats to both natural ecosystems and public health [3]. Heavy metals, such as lead, cadmium, mercury, and arsenic, are particularly concerning due to their high stability, persistence, and tendency to bioaccumulate. Once deposited in sediments, these metals can enter the food chain, causing long-term toxic effects on living organisms. Industrial dyes generate wastewater streams laden with complex organic compounds resistant to natural biodegradation. Emerging pollutants, including pharmaceutical residues and other synthetic compounds, present additional challenges, as even minimal concentrations can disrupt biological processes and ecological balance. Collectively, heavy metals, dyes, and emerging pollutants represent particularly complex challenges that underscore the urgent need for effective wastewater treatment strategies.

Traditional wastewater treatment methods, including ultrafiltration, flocculation, coagulation, and biological processes, are widely applied but present notable limitations [4]. They often involve high capital and operational costs, substantial energy consumption, incomplete removal of pollutants, and secondary waste disposal. Chemical methods for the removal of heavy metals are generally expensive and exhibit low yields when applied at industrial scale [5]. These limitations highlight the need to design and develop advanced materials that leverage specific structural and functional properties to optimize the removal of waterborne contaminants.

Among available strategies, adsorption has emerged as a particularly promising technique. It is simple to operate, cost-effective, and efficient for both organic and inorganic substances in aqueous media [1]. Its efficiency strongly depends on the physicochemical properties of the adsorbent, making the exploration of textural, morphological, and chemical features crucial for selecting suitable materials. Adsorption can remove heavy metals, dyes, and other pollutants effectively, and its reversible and customizable nature allows for regeneration of the adsorbent. Nanomaterials provide additional advantages due to their high surface-to-volume ratio, which enhances interaction with contaminants. Composite nanomaterials, including porous materials such as zeolites [6], activated alumina, activated carbon (AC) [7], polymers [8, 9], magnetic nanoparticles [10, 11], polymer-coated nanoparticles [12], multiwalled carbon nanotubes (CNTs) [13], covalent

organic frameworks (COFs) [14], graphene oxide, and metal–organic frameworks (MOFs) [15], are considered effective and sustainable solutions for adsorption-based wastewater treatment [16, 1]. Photocatalysis represents another complementary approach for the removal of organic contaminants. During photocatalytic processes, the photocatalyst absorbs light energy, generating electron–hole pairs that trigger chemical reactions capable of degrading pollutants.

Given these challenges, the primary objective of this PhD thesis was to design, synthesize, and characterize new classes of advanced materials for the efficient purification of water contaminated with heavy metals, dyes, and emerging pollutants. As already mentioned, traditional treatment strategies often show limited efficiency, high costs, or environmental drawbacks; therefore, this research is directed toward developing sustainable alternatives that combine high performance with biocompatibility and environmental safety. To this end, two complementary research directions have been pursued:

- The design of biocompatible, non-toxic, and biodegradable composites based on sodium alginate, a polysaccharide biopolymer widely studied for environmental applications. By incorporating magnetic nanomaterials or introducing chemical modifications, the adsorption capacity of sodium alginate can be significantly improved, making it a promising candidate for the removal of heavy metals. Alginate provides natural biodegradability, easy functionalization, and the ability to form hydrogel beads, while the magnetic nanomaterials facilitate recovery and handling.

- The synthesis of photocatalytic materials derived from graphitic carbon nitride (g-C_3N_4), focusing on non-conventional derivatives doped with bromine, phosphorus, or boron. These engineered photocatalysts were tailored for the visible-light degradation of dyes and pharmaceutical pollutants, offering enhanced charge separation and extended light absorption in the visible region, compared to pristine g-C_3N_4.

As with any treatment technology, the use of these materials generates secondary waste. However, the amount and impact of this waste are considerably lower than in conventional systems. Alginate beads can be easily separated from water by simple filtration or, when magnetic nanoparticles are incorporated, by applying a magnetic field. Adsorbed pollutants can be removed under controlled conditions, allowing partial regeneration and reuse of the beads. Exhausted alginate beads can also be safely incinerated, leaving minimal residue. Carbon nitride powders, being chemically stable, can be recovered and reused multiple times, or incorporated into composite systems to extend their lifetime. Its porous structure facilitates the diffusion of contaminants during adsorption and desorption, improving efficiency and further reducing unusable waste. Overall, these features make the secondary waste from alginate and carbon nitride-based adsorbents easier to manage and more environmentally friendly.

The specific objectives of the research include:

- Development of advanced materials: designing and synthesizing nanocomposites and hybrid materials with functionalized surfaces for the removal of contaminants from the wastewater matrix.

- Optimization of synthesis processes: establishing reproducible protocols that ensure the stability and the durability of the materials.

- Analysis of interaction mechanisms: conducting detailed studies on the adsorption and degradation kinetics.
- Validation under laboratory conditions: evaluating the performance of the new materials in simulated operational settings to assess their potential for industrial and environmental applications.

The thesis is organized into two main chapters, addressing respectively the production, characterization, and testing of new adsorbent materials and the production, characterization, and testing of non-conventional g-C_3N_4 derivatives doped with different heteroatoms. Each chapter follows the same structure: a literature review providing the scientific and technological context, a detailed description of synthesis and functionalization strategies, physicochemical characterization of the materials using state-of-the-art techniques, and laboratory-scale water purification tests. The conclusions summarize the results, outline future research directions, and discuss potential improvements for scalable industrial applications.

The scientific and practical significance of this project lies in its integrated approach to one of the most pressing environmental challenges. Water purification is not solely an environmental management issue: it is also crucial for public health and socio-economic development. This research contributes to the field of materials engineering applied to water treatment by offering new insights and practical solutions for contaminant management, representing a step toward sustainable technologies for environment preservation.

1.1 Wastewater as an issue or as a resource

Traditionally viewed as an undesirable by-product that requires disposal, wastewater is increasingly recognized as a potential source of valuable resources such as water, energy, and nutrients. Its dual nature as both an issue and an opportunity has placed wastewater at the center of discussions on sustainability and circular economy. The complexity of wastewater streams depends strongly on their origin, ranging from domestic to highly specialized industrial effluents. Understanding these different pathways is essential for selecting the appropriate treatment strategy and for identifying opportunities for resource recovery.

In this context, Figure 1.1 presents a simplified overview of water uptake and subsequent wastewater pathways back to the environment. The effluents from certain industries may require treatment that is not commonly available in urban wastewater treatment plants and may therefore be treated on-site before direct release to water (scenario A). Some industrial units, such as cooling systems, generate wastewater streams with low pollutant content that can be directly released into receiving waters without treatments (scenario B). Some industrial installations generate effluents that cannot be directly released into surface water (and not treated on site) and thus are transferred off site for treatment at an urban or an independently operated wastewater treatment plant (scenario C), the so-called indirect releases.

The release of industrial wastewater in Europe is regulated both directly under environmental law on industrial activities and indirectly through EU policies on water protection. The cornerstone remains the Water Framework Directive (WFD, 2000/60/EC) [18], which is complemented by more specific legal instruments such as the Urban Waste Water Treatment Directive (UWWTD,

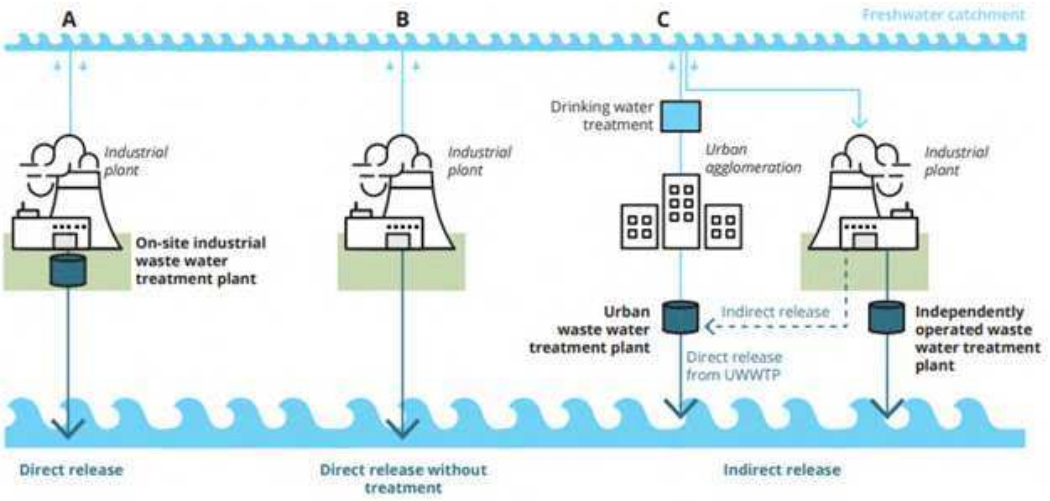

Figure 1.1: Simplified wastewater treatment cycle [17]

91/271/EEC) [19], the Groundwater Directive (2006/118/EC) [20], and the Environmental Quality Standards Directive (2008/105/EC) [21]. Industrial discharges to water and air are further controlled under the Industrial Emissions Directive (IED, 2010/75/EU) [22]. Since 2022, several major updates have been introduced to strengthen this framework. The UWWTD was recast as Directive (EU) 2024/3019 [23], in force since January 2025, introducing stricter requirements for nutrient and micropollutant removal (including PFAS and microplastics), energy-neutral wastewater treatment plants, integrated stormwater management, and a "producer pays" principle obliging pharmaceutical and cosmetic industries to cover at least 80% of the costs for advanced treatment. Similarly, the IED was revised in August 2024 to enforce more stringent emission limits, digitalized permitting, stronger penalties, and to extend its scope to new sectors such as mining, battery manufacturing and intensive livestock farming [24]. It also establishes the Industrial Emissions Portal (IEPR), which from 2028 will replace the E-PRTR by providing harmonized data on emissions and resource use. In parallel, the WFD and related directives are under revision to update pollutant lists, water quality standards, and to better address combination effects, in line with the objectives of the European Green Deal. Altogether, these instruments form the main regulatory framework for preventing and controlling industrial wastewater pollution in the EU.

Beyond its characterization as a potential pollutant, wastewater can also be regarded as a valuable resource when properly treated. One promising, though still relatively uncommon, approach is the reuse of treated effluents within the same industrial activity, often referred to as internal or closed-loop water recycling. When applied, recovered water may serve auxiliary operations such as cooling, washing, or rinsing, thereby reducing the need for continuous extraction and conditioning of freshwater supplies. Although its practical implementation remains limited to certain realities, such practices have the potential to minimize discharge volumes and generate energy savings, since the reuse of water streams already at process temperature or partially conditioned reduces the energy otherwise required for heating, cooling, or chemical adjustment. Moreover, lowering the demand for raw water intake can reduce the energy footprint associated with pumping and treatment, particularly in energy-intensive industries. In parallel, advances in treatment technolo-

gies open the possibility of recovering valuable by-products from wastewater, including nutrients, metals, and organic compounds, which can be reintegrated into production cycles or used as secondary raw materials. From a resource efficiency perspective, internal water recycling and resource recovery therefore represent emerging strategies that could offer synergies between reduced water consumption, lower energy requirements, and improved operational stability. When framed within the principles of the circular economy, these practices have the capacity to transform wastewater from an environmental burden into a managed resource, supporting long-term sustainability goals and reducing dependency on primary resources, even though widespread adoption is still at an early stage.

1.2 Wastewater pollution

As summarized in Figure 1.2, hazardous pollutants can be broadly grouped into different classes and are associated with a wide spectrum of detrimental effects. The scheme highlights three representative groups of contaminants—heavy metals, industrial dyes, and pharmaceuticals/personal care products—that are particularly relevant in the context of wastewater pollution and that will be addressed in detail in this work. Their impacts extend across multiple levels of the environment: plants, animals, humans, and entire ecosystems are simultaneously affected, although the severity and mechanisms differ. For instance, pollutants can interfere with fundamental processes such as photosynthesis and soil fertility, threaten aquatic life and biodiversity, or induce carcinogenic, neurotoxic, and developmental effects in humans. At the ecosystem scale, they contribute to increased chemical oxygen demand (COD) and biological oxygen demand (BOD), as well as to the release of toxic effluents that accelerate the degradation of natural waters. An important aspect that have to be emphasized is the interconnection between environmental compartments. Pollutants released into water bodies can transfer to soils and sediments, be absorbed by plants, accumulate in the food chain, and eventually reach humans, amplifying their long-term consequences. Moreover, these contaminants often occur as mixtures rather than isolated species, displaying additive or even synergistic effects that complicate their removal. Such characteristics make them a particularly urgent challenge for wastewater treatment.

1.2.1 Heavy metals

Heavy metals (HMs) are commonly defined as those elements having an atomic number greater than 20 and atomic density above 5 $\mathrm{g\,cm^{-3}}$ and must exhibit the properties of metal [25]. It is important to note that the term itself is not formally defined or recommended by IUPAC, and therefore lacks a universally accepted scientific basis. Nevertheless, due to its widespread use in the scientific literature and its practicality in describing certain classes of elements, we will employ this terminology consistently throughout this thesis.

Heavy metals can be broadly classified into two categories: essential and nonessential heavy metals. Essential heavy metals are those required in trace amounts by living organisms for carrying out the fundamental processes like growth, metabolism, and development of different organs. There are numerous essential heavy metals like Cu, Fe, Mn, Co, Zn, and Ni required by plants as they form cofactors that are structurally and functionally vital for enzymes and other proteins.

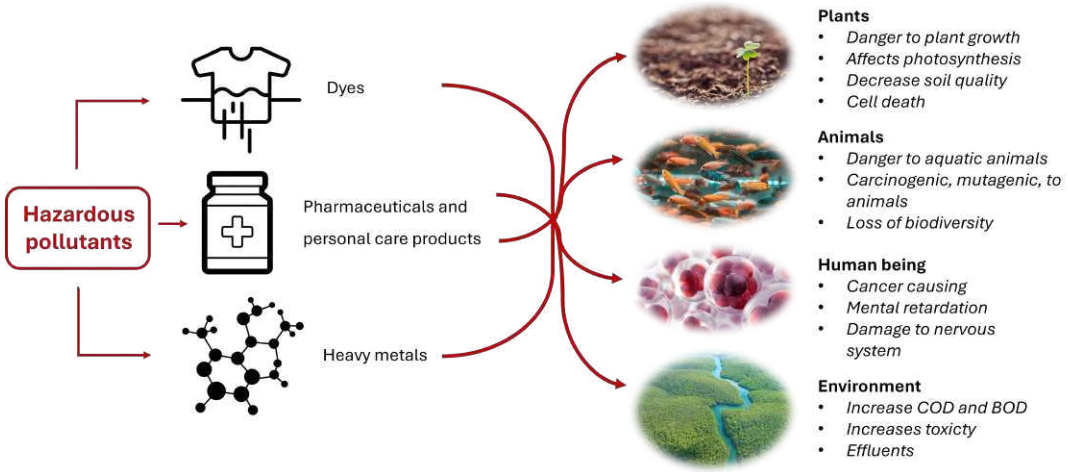

Figure 1.2: Broad classification and effects of hazardous pollutants

Essential elements are often required in the level of 10–15 ppm and are known as micronutrients. Nonessential heavy metals like Cd, Pb, Hg, Cr, and Al are not required by living organisms, even in trace amounts, for any of the metabolic processes [26].

Heavy metal pollution in water is a global environmental problem. This is mainly due to their excessive accumulation, biomagnification, toxicity, and persistency. In fact, they are not biodegradable and creates serious threats to human and nature. Heavy metals can derive from both natural and anthropogenic sources. Natural sources mainly comprise bedrock weathering, while anthropogenic sources include industrial production, fertilizer use, and sewage discharge. Heavy metals are not easily removed in a standard wastewater treatment plant configuration. In 2016, 68% of industrial emissions (1,402 tonnes) of heavy metals reported in the European Pollutant Release and Transfer Register (E-PRTR) were transferred to urban wastewater treatment plants. These, which also receive some input from municipal wastewater, released 1,276 tonnes of heavy metals directly to the environment. Fast growing activities have the potential to spread a substantial amount of harmful and undetected heavy metals into all segments of the ecosystem, particularly soil, water, air, and vegetation. Hazardous heavy metals discharged into the environment bioaccumulated into living beings via food intake, causing possibly health-threatening consequences. Chemical and physical remediation procedures are limited and confined, and are mostly addressed to sewage and soils rather than the plant [1].

Heavy metals such as nickel (Ni), chromium (Cr) and copper (Cu) are of particular regulatory concern in the European Union due to their toxicity, persistence and potential to bioaccumulate. These metals enter the aquatic systems mainly through industrial discharges (e.g., electroplating, metallurgy, mining, leather tanning), agricultural runoff, and municipal wastewater effluents. Chronic exposure, even at low concentrations, may cause adverse effects on aquatic organisms and human health. In particular, nickel and chromium are classified as carcinogenic in certain forms, while copper, although essential as a trace element, is toxic at elevated concentrations. The regulation of heavy metals in water has progressively evolved within EU legislation. The *Water Framework Directive (WFD) 2000/60/EC* established the basis for integrated water management,

introducing the concept of priority substances, including nickel and its compounds [18]. In 2008, the *Environmental Quality Standards Directive (EQSD) 2008/105/EC* set specific Environmental Quality Standards (EQS) for nickel in surface waters, subsequently amended by Directive 2013/39/EU, which maintained nickel on the priority substances list with defined annual average and maximum allowable concentrations [21, 27]. Copper and chromium, however, were not classified as priority substances at the EU level, though they remain regulated under national frameworks and through other instruments. At the drinking water level, heavy metals have long been included as parametric values. The *Drinking Water Directive (DWD) 98/83/EC* established initial parametric limits [28], later recast by Directive (EU) 2020/2184, which introduced stricter thresholds and a staged reduction for chromium. In particular, the parametric value for total chromium will be lowered from 50 µg/L to 25 µg/L as of 2036, reflecting updated toxicological evidence. Nickel retains a parametric limit of 20 µg/L, while copper is set at 2 mg/L, primarily due to organoleptic and infrastructure-related concerns (e.g., corrosion of copper pipes) [29].

Most recently, in June 2024 the Council of the European Union reached an agreement on a new water legislation (COM/2022/540 final), updating the list of priority substances under the WFD. The proposal confirmed nickel as a regulated substance, with stricter EQS values under discussion, while also introducing additional micropollutants of emerging concern [30, 31]. The revision of the *Urban Waste Water Treatment Directive*, adopted as Directive (EU) 2024/3019 and entering into force in January 2025, indirectly addresses heavy metals by requiring advanced treatment (the "fourth stage") in large wastewater treatment plants, aiming at improved removal of micropollutants, including metals [32]. Table 1.1 resumes the evolution during the years of the main legislation steps concerning heavy metals regulation, in aquatic environments.

Overall, while nickel remains the only one of these three metals with binding EU-wide EQS values for surface waters, all three are consistently regulated under the drinking water framework, and their control is reinforced by the progressive tightening of treatment and monitoring obligations. Table 1.2 indicates the current limits for the more widespread heavy metals, in aquatic environments.

1.2.2 Dyes

One of the most prevalent organic contaminants in water is represented by dyes, which often possess complex organic molecular structures. Among them, azo dyes account for more than 70% of all commercial dyes employed in the global textile industry [33]. Most of these compounds are hazardous, carcinogenic, and non-biodegradable, thus posing a severe threat to both the environment and human health [34, 35]. Approximately 50% of the synthetic dyes used in textile production fail to adhere to fabrics and are discharged into the environment together with other sources [36, 37]. Synthetic dyes in aquatic systems hinder light penetration, inhibit photosynthesis, and disrupt the entire biological balance. Furthermore, human exposure to dye pollution through the food chain is particularly harmful and can even be lethal. Dye residues in soil negatively affect both plant and animal health, in addition to reducing soil fertility. These colors are widely used in a variety of sectors, including textiles, tanneries, cosmetics, and foodstuffs, as well as human and animal pharmaceuticals. Because of their extensive usage and large-scale manufacture, artificial organic dyes have permeated into several sectors of the soil and water ecosystem. Dyes have

Table 1.1: Key EU policy milestones concerning Ni, Cr and Cu in the aquatic environment

Year	**Event / Regulatory milestone**	**Ref.**
2000	Adoption of the Water Framework Directive (WFD) 2000/60/EC, establishing the basis for priority substance regulation	[18]
2008	Environmental Quality Standards Directive (EQSD) 2008/105/EC sets EQS for nickel in surface waters	[21]
2013	Directive 2013/39/EU updates EQS values for nickel, maintaining its status as a priority substance	[27]
2020	Recast Drinking Water Directive (EU) 2020/2184 strengthens parametric values: Ni = 20 µg/L, Cu = 2 mg/L, Cr = 50 µg/L (to be reduced to 25 µg/L by 2036)	[29]
2022	Council agreement on revision of priority substances under the WFD (COM/2022/540 final), including stricter consideration of nickel	[30, 31]
2024	Adoption of Directive (EU) 2024/3019 on Urban Waste Water Treatment, requiring a fourth treatment stage from 2025 for improved removal of micropollutants including metals	[23]

Table 1.2: Current EU regulatory limit values for the more widespread heavy metals in water (surface EQS and drinking water standards).

Substance	**Surface water EQS (2008/105/EC, as amended)**	**Drinking water parametric value (2020/2184/EU)**
Nickel (Ni)	AA-EQS: 4 µg/L (inland); 8.6 µg/L (other) MAC-EQS: 34 µg/L	20 µg/L
Chromium (Cr)	Not listed as EU priority substance (no EQS)	50 µg/L (until 2036); 25 µg/L thereafter
Copper (Cu)	Not listed as EU priority substance (no EQS)	2.0 mg/L
Lead (Pb)	Not listed as EU priority substance (no EQS)	10 µg/L (until 2036); 5 µg/L thereafter
Cadmium (Cd)	Not listed as EU priority substance (no EQS)	5 µg/L
Mercury (Hg)	Not listed as EU priority substance (no EQS)	1 µg/L

previously been found in ecological specimens including water, suspended particulate matter, soil, and fish species. As a result, they are classified as aquatic ecosystem micro-pollutants. The majority of the dyes are a harmful class of water toxins that have had a significant impact on the ecosystem. Some dyes, such as methylene blue, rhodamine B, methyl violet, Congo red, and crystal violet, are toxic to humans. Acidic and azo dyes have detrimental effects on the gastrointestinal tract, eyes, respiratory system, and skin, and may also cause cancer and mutagenicity [38]. They can induce enzymatic abnormalities, with the amine group in azo dyes being primarily responsible for their toxicity. Basic dyes similarly affect human health, causing laryngitis, mutations, skin cancer, an increased incidence of shock, jaundice, neurotoxicity, cyanosis, and tissue necrosis, in addition to skin allergies, and reproductive and developmental complications [33]. Textile dye contamination has been handled using a variety of ways, mostly physical, chemical, biological, and acoustic. These methods primarily extract and/or remove the dye from water. Recently, advanced oxidation techniques were emphasized on dye removal from polluted water due to their benefits such as being environmentally friendly, economical, and effective of degrading various colors or organic pollutants soluble in wastewater. Chemical procedures, though very efficient, should be avoided in dye removal due to their hazardous side effects. Photocatalysis is a type of advanced oxidation technique that is primarily performed out underneath the influence of light and appropriate photocatalytic materials. The photocatalytic activity of photocatalytic materials is primarily determined by the band gap, surface area, and electron–hole pair production for degrading dyes present in the water. It was discovered that surface area performs a significant

part in photocatalytic degradation of dyes by increasing the surface area, which leads to greater adsorption of dye molecules on the surface of the photocatalyst and increases catalytic performance [39].

1.2.3 Emerging pollutants

Emerging pollutants (EPs) are a wide and heterogeneous group of chemical compounds that until recently were not commonly monitored in the environment and whose potential harmful effects were underestimated. The concept began to gain attention in the early 1990s, when improved analytical techniques allowed for the detection of trace organic contaminants previously overlooked. Since the 2000s, the topic has become increasingly central in environmental research, and in the last decade the number of studies reporting EPs in surface waters, groundwater, and even treated drinking water has grown exponentially [40, 41]. These pollutants are now recognized as a critical challenge for water quality management and public health. By definition, EPs include both synthetic and naturally occurring compounds that are not regulated or only partially regulated, but that can persist in the environment, accumulate in organisms, and exert biological activity even at low concentrations. They encompass pesticides, pharmaceuticals and personal care products (PPCPs), endocrine-disrupting chemicals (EDCs), disinfection byproducts (DBPs), flame retardants, surfactants, perfluorinated compounds (PFCs), antibiotic-resistant bacteria (ARB) and genes (ARGs), among others [40]. Their common feature is not their chemical nature but the fact that they have only recently been recognized as contaminants of concern, with toxicological and ecological risks that are still under active investigation. The widespread occurrence of EPs is linked to modern lifestyles and industrialization. PPCPs and pharmaceuticals, for example, are released into the environment through domestic sewage and hospital wastewaters; pesticides reach aquatic systems via agricultural runoff; industrial additives and solvents are discharged through manufacturing effluents. Conventional wastewater treatment plants, designed primarily for nutrients and suspended solids removal, are generally not equipped to completely eliminate such complex and persistent molecules. Once released, their chemical stability and partial resistance to natural degradation processes contribute to their persistence and mobility. Another critical aspect of EPs is their diversity. Unlike conventional pollutants, which often belong to a limited number of well-characterized classes, EPs include a constantly expanding list of compounds, reflecting new industrial practices, consumer habits, and chemical innovations. Each subgroup has specific pathways of release, persistence times, and toxicological profiles. This variability complicates monitoring, regulation, and remediation strategies, making EPs a dynamic and evolving environmental issue. The recognition of emerging pollutants has reshaped the research agenda on water treatment and environmental protection. Since the early 2000s, increasing efforts have been devoted to developing advanced analytical methods for their detection, assessing their toxicological profiles, and designing novel materials and technologies for their removal. Between 2010 and 2020, the number of scientific publications on EPs more than tripled, reflecting both the urgency and complexity of the problem [42].

The following sections will focus on one of the most relevant groups of EPs: pharmaceutical residues, which have become emblematic of the complexity and urgency associated with emerging contaminants.

Pharmaceutical pollutants

Among the emerging pollutants a relevant class is composed of pharmaceuticals, which are intentionally developed to treat diseases and improve human health. Nevertheless, the release of pharmaceuticals into the environment, especially antibiotics, can induce genetic exchange in microorganisms with long-lasting and irreversible consequences. This phenomenon significantly accelerates the development of pathogen resistance to a wide spectrum of antibiotics [43]. Pharmaceuticals are defined as prescription, over the counter and veterinary therapeutic drugs used to prevent or treat human and animal diseases, while personal care products (PCPs) are used mainly to improve the quality of daily life. Over the past few years, there has been increasing awareness of the unintentional presence of PPCPs in various compartments of the aquatic environment (e.g. water, sediments and biota) at concentrations capable of causing detrimental effects to the aquatic organisms. This has become a major concern because PPCPs are extensively and increasingly used in human and veterinary medicine, resulting in their continuous release to the environment. Priority pollutant lists have been developed both by the European Union (EU) and the United States Environmental Protection Agency (USEPA) identifying a wide variety of chemicals present in waste waters and storm water runoff that may pose a threat to receiving water bodies including surface water. In the year 2000, an initial list of 33 priority substances was also identified under the EU Water Framework Directive (WFD) 2000/60/EC to be used as a control measure for the next 20 years [18].

In 2006, Directive 2006/118/EC was adopted to protect groundwater against pollution and deterioration [20]. In 2007, certain pharmaceuticals and PPCPs such as diclofenac, iopamidol, and carbamazepine were identified as future emerging priority candidates. Ibuprofen, clofibric acid, triclosan, phthalates and bisphenol A are proposed additions to this list [40]. In 2008, Directive 2008/105/EC established environmental quality standards (EQS) in the field of water policy, and introduced Article 8c, which required the development of a strategic approach to pharmaceuticals [21]. In 2013, Directive 2013/39/EU amended the WFD and introduced an explicit obligation for the European Commission to develop a strategic approach to pharmaceuticals in the environment by 2015 and propose measures by 2017 [27]. Thus, a Watch List mechanism was also established in 2013 to improve the available information on identifying the substances of greatest concern. Member States have to monitor the substances on the list at least once per year for up to four years. The watch list was established in 2015 and updated in 2018, 2020, 2022 and again in 2025. In 2019, the European Commission published the *EU Strategic Approach to Pharmaceuticals in the Environment* (COM(2019)128 final), which set out actions across the life cycle of pharmaceuticals, from design and production to disposal, to reduce their environmental impact. The communication refears to the fact that the treatment of many diseases in humans and animals relies on access to effective pharmaceuticals. But, at the same time, pollution caused by some pharmaceuticals is an emerging problem, with well-documented evidence of risks to the environment and, particularly in relation to antimicrobial resistance, to human health. Residues of pharmaceutical products may thus enter the environment during their manufacture, use and disposal [44].

In 2022, the European Commission proposed an update of the priority substances lists, recommending the addition of approximately 25 new chemicals, including pharmaceuticals (notably several antibiotics and anti-inflammatory drugs), bisphenol A, silver, and selected per- and

polyfluoroalkyl substances (PFAS) [30, 31]. This proposal reflects increasing concerns about the ecotoxicological risks and potential human health implications of pharmaceutical residues in water. In June 2024, the Council of the European Union reached a negotiating mandate to strengthen the WFD by introducing more stringent environmental quality standards (EQS) for hazardous pharmaceuticals, alongside measures for PFAS and other micropollutants. In fact, The Council agreed that pharmaceutical active substances are of great concern for ecosystems. Groundwater quality standards for pharmaceuticals should therefore be aligned, for the substances most frequently encountered in groundwater bodies, with the values adopted or proposed as environmental quality standards to be achieved in surface waters. This should ensure the protection of associated aquatic ecosystems and dependent terrestrial ecosystems. Stricter standards are needed to protect sensitive groundwater ecosystems [24]. The mandate also emphasized the need for an expanded monitoring, not only in surface waters but also in groundwater, and recognized pharmaceuticals as a critical group of pollutants requiring long-term control.

In parallel, the Urban Waste Water Treatment Directive was revised and formally adopted as Directive (EU) 2024/3019, entering into force on 1 January 2025. The new legislation requires the implementation of a "fourth stage" of treatment in large wastewater treatment plants (serving more than 150,000 population equivalent), specifically designed to remove micro-pollutants such as pharmaceuticals and personal care products [23]. This marks a significant policy milestone, as it directly addresses the technical challenges of reducing PPCP concentrations in effluents before they reach receiving water bodies. Additionally, the EU "Watch List" mechanism under the WFD was updated in March 2025 to include twelve new contaminants for monitoring, among them the antidepressant fluoxetine, the beta-blocker propranolol, and several azole fungicides used both pharmaceutically and cosmetically. These substances will be monitored across Member States for at least two years to assess whether they should be upgraded to the list of priority substances with binding EQS values [32].

Overall, the trajectory of European water policy over the past two decades shows an increasing recognition of pharmaceuticals as pollutants of high regulatory concern. From their first consideration as emerging contaminants in the mid-2000s, through their inclusion in successive watch lists, to the binding obligations for advanced treatment technologies in 2025, pharmaceuticals are now firmly established within the EU environmental regulatory framework. This evolution underscores both the ubiquity of these substances in modern society and the growing awareness of their long-term ecological and health impacts. Table 1.3 resumes the evolution during the years of the main legislation steps concerning pharmaceuticals regulation in aquatic environments.

1.3 Wastewater treatment methods

In recent decades, numerous physical and chemical techniques have been developed and extensively studied for the removal of contaminants from wastewater, including heavy metals, dyes, pharmaceuticals, and other organic or inorganic pollutants. These methods can be broadly classified into two main categories: physical separation techniques and chemical transformation methods. Physical approaches are based on the transfer of contaminants from the aqueous phase to a solid surface or a separate phase, without altering the chemical nature of the pollutants. Examples of physical methods include membrane filtration, solvent extraction, and ion exchange.

Table 1.3: EU policy milestones concerning pharmaceuticals in the aquatic environment

Year	Event / Regulatory milestone	Ref.
2000	Adoption of the Water Framework Directive (WFD) 2000/60/EC, establishing an initial list of 33 priority substances for surface water monitoring and control	[18]
2006	Adoption of Directive 2006/118/EC on the protection of groundwater against pollution and deterioration	[20]
2008	Adoption of Directive 2008/105/EC on environmental quality standards (EQS) in water policy; Article 8c required the development of a strategic approach to pharmaceuticals	[21]
2013	Directive 2013/39/EU amending the WFD: explicit obligation for the Commission to develop a strategic approach to pharmaceuticals in the environment by 2015 and propose measures by 2017	[27]
2019	Publication of the *EU Strategic Approach to Pharmaceuticals in the Environment* (COM(2019)128 final)	[44]
2022	Commission proposal (COM(2022) 540 final) to update the priority substances list, including ∼25 new chemicals such as antibiotics, anti-inflammatory drugs, bisphenol A, silver, and PFAS	[30, 31]
2024	Council mandate to strengthen EQS for pharmaceuticals and expand monitoring to groundwater	[24]
2024	Adoption of Directive (EU) 2024/3019 on Urban Waste Water Treatment, requiring a fourth treatment stage in large wastewater treatment plants	[23]
2025	EU Watch List update: twelve substances added, including fluoxetine and propranolol	[32]

In contrast, chemical techniques involve the transformation of contaminants into less soluble or less harmful forms through chemical reactions. Common chemical methods include chemical precipitation, electrochemical treatment, and advanced oxidation processes. Each technique presents distinct advantages and limitations, and the choice of method often depends on the nature of the contaminant, the composition of the wastewater, and the desired treatment efficiency.

1.3.1 Physical Techniques

Among the physical techniques, membrane filtration has gained significant attention due to its versatility and effectiveness in removing a wide range of contaminants, from suspended solids to dissolved metal ions and organic molecules. Membrane filtration can be classified into ultrafiltration (UF), nanofiltration (NF), and reverse osmosis (RO), depending on the size of particles or molecules retained by the membrane. UF membranes are suitable for larger molecules and colloids, NF membranes can remove smaller organic and inorganic molecules, while RO membranes are capable of retaining ions and small dissolved compounds. Often, combinations of these filtration techniques are employed to create multi-barrier systems, enhancing the overall removal efficiency. Despite their effectiveness, membrane processes can suffer from fouling, which may reduce water flux and increase maintenance requirements, and they generally require relatively high initial capital investment.

Solvent extraction is another physical method used primarily for the recovery or removal of specific dissolved contaminants from concentrated streams. This approach exploits the preferential solubility of pollutants in an immiscible solvent, allowing selective separation from water. While highly effective for certain applications, solvent extraction is generally more suitable for high-concentration waste streams and may be less practical for dilute solutions due to economic and operational considerations.

Ion exchange represents a versatile physical-chemical approach in which ions present in solution are exchanged with ions immobilized on a solid matrix, typically a synthetic resin or a naturally occurring material such as zeolite. Cationic resins exchange positively charged ions in the water with hydrogen or sodium ions bound to the resin, while anionic resins perform analogous exchanges for negatively charged species. Ion exchange processes are highly selective, regenerable, and produce minimal sludge. However, their efficiency can be influenced by the pH of the solution, the presence of competing ions, and fouling of the resin by organic matter or suspended solids.

1.3.2 Chemical Techniques

Chemical transformation methods rely on reactions that convert pollutants into less soluble, less toxic, or more easily removable forms. Chemical precipitation is one of the most widely used techniques, in which reagents such as lime, sodium hydroxide, or other bases react with dissolved metal ions or other pollutants to form insoluble precipitates. These precipitates can then be separated from the water through sedimentation, filtration, or decantation. The effectiveness of chemical precipitation depends on key parameters such as pH, temperature, and the stoichiometry of the added reagents. While the method is simple, widely applicable, and cost-effective, it generates significant quantities of sludge that must be properly managed and disposed of.

Electrochemical treatment is another promising chemical approach that uses electric currents to remove or transform pollutants in aqueous solutions. Techniques such as electrocoagulation, electrodeposition, electroflotation, and electrodialysis can effectively treat complex wastewater streams containing multiple contaminants. In electrochemical processes, contaminants can be oxidized, reduced, or deposited on electrode surfaces, allowing their removal from the solution. Advantages of electrochemical treatment include high efficiency, adaptability to different types of pollutants, and potential recovery of valuable metals. Limitations include relatively high energy consumption, electrode wear, production of secondary sludge, and sensitivity to operating conditions such as pH, conductivity, and temperature.

Table 1.4 provides a comparative overview of the most common wastewater treatment techniques, outlining their applicability, main strengths, and associated limitations [45].

Table 1.4: Summary of conventional wastewater treatment methods

Method	**Applicability**	**Advantages**	**Limitations**
Membrane Filtration (UF, NF, RO)	Solids, metals, organics, pharmaceuticals	High efficiency, compact, multi-barrier	Fouling, high cost, brine disposal
Solvent Extraction	Valuable metals, hydrophobic organics, dyes	Selective, resource recovery	Viable for concentrated streams, solvent handling
Ion Exchange	Metals, nitrates, ammonium, water softening	Selective, regenerable, low sludge	pH sensitive, fouling, limited at high load
Chemical Precipitation	Metals, phosphates, anions	Simple, cheap, widely used	Sludge, non-selective, pH control
Electrochemical Methods	Metals, dyes, pharmaceuticals	Efficient, versatile, metal recovery	Energy demand, electrode wear, sludge

1.4 Adsorption Process

Among the different techniques available for wastewater remediation, this thesis will focus on two methods: adsorption and photocatalysis. In this section, adsorption will be described in detail as it represents one of the most widely applied and effective physicochemical processes for the removal of heavy metals from contaminated waters.

Adsorption is a physical separation process in which specific components of a fluid phase are transferred to the surface of a solid adsorbent. In the context of wastewater treatment, adsorption can be considered a physicochemical process that effectively removes heavy metals and other

pollutants from aqueous media. Despite the increasing cost of carbon-based adsorption materials, due to the depletion of coal-derived commercial carbons [46], adsorption remains one of the most preferred techniques owing to its efficiency, versatility, and reusability.

Compared to conventional methods, adsorption presents several advantages: (i) it minimizes the production of chemical and biological sludge, (ii) it is cost-effective, (iii) it achieves high removal efficiency at both high and low contaminant concentrations, (iv) adsorbents can often be regenerated, and (v) it enables the recovery of metals.

A wide variety of adsorbents have already been employed for heavy metal removal, including: activated carbon, zeolites, chitosan, carbon nanotubes, manganese oxides, agricultural by-products (e.g., water hyacinth, hazelnut shells, orange peel pith, sunflower residues, coconut coir pith), bacterial and fungal biosorbents, marine algae, and other plant- or microbially-derived biomass.

Adsorption is fundamentally a mass transfer process in which substances are bound to the surface of a solid material by means of physical and/or chemical interactions. It involves the transfer of a solute from the liquid (or gas) phase to the surface of a solid adsorbent. The binding forces can include:

- **Physical interactions**: electrostatic attraction, diffusion, van der Waals forces.
- **Chemical interactions**: coordination bonds, covalent bonding, acid–base interactions.

The adsorption process can be described in three main steps:

1. **Transport** of the pollutant from the bulk solution to the sorbent surface.
2. **Adsorption** of the pollutant onto the solid surface.
3. **Intraparticle transport** of the pollutant within the sorbent particle.

The study of adsorption involves several complementary aspects: evaluation of adsorption capacity, modeling the equilibrium behavior through isotherms, understanding the kinetics, and identifying the underlying mechanisms controlling the process [47].

The experimental adsorption capacity of a material can be calculated both at equilibrium and at any given time using the following relations:

$$\eta_{\mathrm{end}} = \frac{(C_0 - C_{\mathrm{end}})\, V_{\mathrm{sol}}}{m_{\mathrm{MNAs}}} \tag{1.1}$$

$$\eta_t = \frac{(C_0 - C_t)\, V_{\mathrm{sol}}}{m_{\mathrm{MNAs}}} \tag{1.2}$$

where:

- η_{end} (µmol/mg) = adsorption capacity at equilibrium,
- η_t (µmol/mg) = adsorption capacity at time t,
- C_0 (µmol/L) = initial concentration of pollutant,
- C_{end} (µmol/L) = equilibrium concentration,

- C_t (µmol/L) = concentration at time t,
- V_{sol} (L) = volume of solution,
- m_{MNAs} (mg) = mass of dry adsorbent.

These equations provide the fundamental quantitative description of adsorption and form the basis for modeling both equilibrium and kinetic processes.

1.4.1 Adsorption Isotherms

Adsorption isotherms describe the relationship between the amount of solute adsorbed and its equilibrium concentration in solution at constant temperature. They offer insights into the surface properties of the adsorbent and the potential adsorption mechanisms. The two most commonly applied models are the *Langmuir* and *Freundlich* isotherms.

Langmuir Isotherm The Langmuir model assumes monolayer adsorption of solute molecules on a homogeneous adsorbent surface with a finite number of identical sites. Once a site is occupied, no further adsorption can occur at that location. It is expressed as:

$$\eta_{\text{end}} = \frac{Q_{\max} K_L C_{\text{end}}}{1 + K_L C_{\text{end}}} \tag{1.3}$$

where:

- η_{end} (µmol/mg) = equilibrium adsorption capacity,
- $Q_{\max}$ (µmol/mg) = maximum adsorption capacity (monolayer),
- K_L (L/µmol) = Langmuir adsorption constant,
- C_{end} (µmol/L) = equilibrium solute concentration.

The Langmuir model is most suitable for describing adsorption on uniform surfaces but does not account for heterogeneity or multilayer adsorption.

Freundlich Isotherm The Freundlich isotherm is an empirical model that accounts for adsorption on heterogeneous surfaces and multilayer formation. It is given by:

$$\eta_{\text{end}} = K_f C_{\text{end}}^{1/n} \tag{1.4}$$

where:

- K_f (µmol/mg) = Freundlich adsorption constant related to adsorption capacity,
- $1/n$ = heterogeneity factor, with smaller values indicating stronger surface heterogeneity.

Unlike the Langmuir model, the Freundlich model allows for the possibility of continuous adsorption depending on concentration, reflecting non-uniform adsorption energies across the surface.

1.4.2 Adsorption Kinetics

The kinetics of adsorption describe the rate at which pollutants are removed from solution and provide insight into the mechanisms controlling the process. Several models are commonly applied:

Pseudo-first-order model Assumes that the rate of adsorption is proportional to the number of unoccupied sites:

$$\frac{d\eta_t}{dt} = k_1(\eta_{\text{end}} - \eta_t) \tag{1.5}$$

which by integration yields:

$$\ln(\eta_{\text{end}} - \eta_t) = \ln \eta_{\text{end}} - k_1 t \tag{1.6}$$

where k_1 (min^{-1}) is the pseudo-first-order rate constant. This model often describes physisorption-controlled processes but may be less accurate at later stages.

Pseudo-second-order model Assumes chemisorption is the rate-limiting step:

$$\frac{d\eta_t}{dt} = k_2(\eta_{\text{end}} - \eta_t)^2 \tag{1.7}$$

Integration gives:

$$\frac{t}{\eta_t} = \frac{1}{k_2 \eta_{\text{end}}^2} + \frac{t}{\eta_{\text{end}}} \tag{1.8}$$

where k_2 (mg µmol^{-1} min^{-1}) is the pseudo-second-order rate constant. This model typically fits heavy metal adsorption data more accurately, reflecting chemical interactions and surface heterogeneity.

Intraparticle Diffusion Model Diffusion within the pores may also control the overall adsorption rate:

$$\eta_t = k_{\text{id}}\, t^{1/2} + C \tag{1.9}$$

where k_{id} (µmol mg^{-1} min$^{-1/2}$) is the intraparticle diffusion rate constant, and C accounts for boundary layer effects. Non-linearity indicates multiple rate-limiting steps.

1.4.3 Adsorption Mechanisms

The removal of heavy metals involves multiple mechanisms, often acting simultaneously. Figure 1.3 illustrates the main types of adsorption for carbon-based adsorbents:

- **Physical adsorption:** diffusion and deposition of molecules and ions within the pores of the adsorbent without chemical bond formation. The extent depends on surface area and pore size distribution. Increased micro- and mesoporosity enhances diffusion and accelerates adsorption kinetics.

- **Electrostatic interactions:** attraction between charged adsorbent surfaces and opposite ions. This occurs in materials like activated carbon, carbon nanotubes, and graphene oxide, which have charged surface moieties.
- **Ion exchange:** replacement of protons or cations in functional groups (–COOH, –OH) with heavy metal ions (e.g., K^+, Na^+, Ca^{2+}, Mg^{2+}) from solution. This mechanism is common in exchange resins and functionalized biomass.
- **Surface complexation:** coordination of heavy metal ions with functional groups (–OH, –COOH, –O–, –CO-NH–) to form stable multi-atom complexes on the adsorbent surface.
- **Precipitation/coprecipitation:** formation of insoluble metal compounds or coprecipitation with other ions or functional groups. This is prevalent at high metal ions concentrations and can repeatedly occur on the surface.

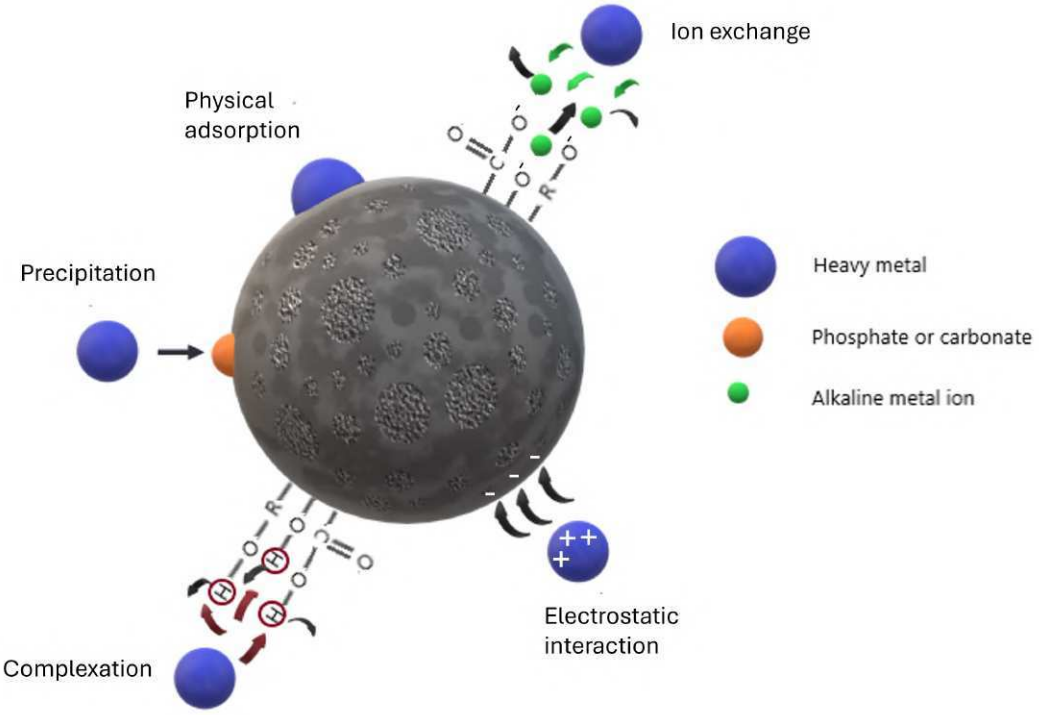

Figure 1.3: Main adsorption mechanisms of heavy metals by carbon-based materials

In some cases, reduction processes play a role: high-valent metals such as Cr(VI) may be reduced to lower-valent states (Cr(III)) by reducing groups on the adsorbent, followed by complexation or ion exchange.

These combined mechanisms allow carbon-based and functionalized adsorbents to achieve high versatility and efficiency in removing heavy metals from aqueous solutions [48, 49].

Common Adsorbents for Heavy Metal Removal

The selection of a suitable adsorbent is a fundamental aspect in the design of efficient wastewater treatment processes. An ideal adsorbent should possess high selectivity for target pollutants, large surface area, suitable pore size distribution, regenerability, ease of production, cost-effectiveness, and reusability. Based on their origin and composition, adsorbents can be classified into three main categories: inorganic, polymer-based, and composite materials (Figure 1.4).

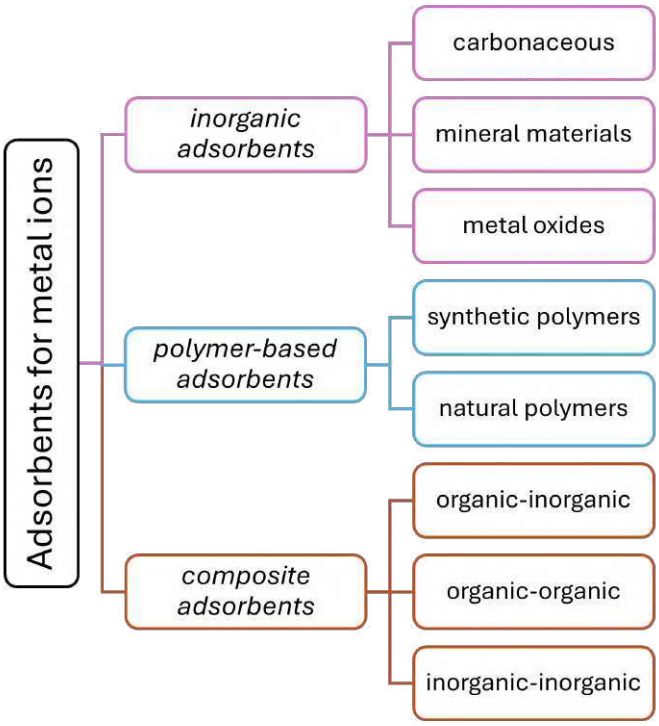

Figure 1.4: Classification of heavy metal adsorbents

Inorganic Adsorbents Inorganic adsorbents include carbonaceous materials, mineral materials, and metal oxides. Activated carbon (AC) is among the most widely used due to its large surface area, well-developed pore structure, and versatile surface chemistry. It can be prepared from a wide range of carbon-rich resources, including wood, coal, lignite, and agricultural wastes, through pyrolysis followed by thermal or chemical activation. The resulting porous structure and surface functional groups, such as hydroxyl, carboxyl, and carbonyl, make AC highly effective for heavy metal removal. Studies have demonstrated that AC produced from coconut shells, bamboo, grape industry wastes, and other biomass sources can efficiently remove Pb^{2+}, Cu^{2+}, Cd^{2+}, and Cr(VI), with adsorption capacities depending on the precursor material and activation method [50, 51]. Metal ion adsorption often occurs through multiple mechanisms including physical adsorption in pores, ion exchange with surface functional groups, and surface complexation [52]. Carbon nanotubes (CNTs) are another class of inorganic adsorbents, consisting of single-wall (SWCNTs) or multi-wall (MWCNTs) tubular carbon structures [53]. Their extremely high surface area, hollow structure, and tunable surface chemistry make them excellent adsorbents for both organic and

inorganic pollutants [54, 55]. Functional groups such as -COOH, -OH and -NH_2 can be introduced to enhance the binding of metal ions, and further modifications with catalysts such as Pd, Ni, or Pt can improve adsorption selectivity and efficiency [56, 57]. Biochar (BC) is a stable, porous carbon-rich solid obtained via pyrolysis of biomass under oxygen-limited conditions. BC can be produced from various agricultural residues, plant wastes, and other biomass sources, resulting in materials with diverse surface chemistry and porosity. Although BC generally has a lower specific surface area than activated carbon, it often contains a higher density of surface functional groups, which improves its interaction with heavy metal ions. Adsorption studies have shown that BC can effectively remove metals such as Pb^{2+}, Cd^{2+}, Zn^{2+}, Cu^{2+}, and As from aqueous solutions, with removal efficiency and selectivity strongly influenced by the feedstock, pyrolysis conditions, and the presence of competing ions [58, 59].

Polymer-Based Adsorbents Polymer-based adsorbents include synthetic resins and natural polymers. Synthetic resins are often used in ion exchange applications, where functional groups such as sulfonic acid or amine groups selectively bind heavy metal ions from aqueous solutions. Natural polymers, such as chitosan, alginate, and cellulose derivatives, contain abundant hydroxyl, carboxyl, or amino groups, which act as active sites for adsorption. These materials are generally biocompatible, biodegradable, and can be chemically modified to enhance their adsorption capacity and selectivity [60, 61, 62].

Composite Adsorbents Composite materials combine inorganic and polymeric components, or two different polymeric phases, to create adsorbents with synergistic properties. For example, carbon-based materials can be combined with polymers to enhance mechanical stability, porosity, or surface functionality. Composite adsorbents often show improved performance compared to their individual components due to the combination of high surface area, abundant functional groups, and structural robustness [63, 64, 65].

1.5 Photocatalysis

Photocatalysis is a process in which a chemical reaction is accelerated by the absorption of light by a semiconductor material. Known photocatalysts, which have been extensively studied also for water decontamination, are TiO_2 [66, 33, 67, 68, 69], CdS [70, 71, 72, 73], Fe_2O_3 [74, 75, 76], ZnO[77, 78], and ZnS [79]. The photocatalyst alters the reaction mechanism and enhances the degradation kinetics of pollutants when exposed to light. The concept is inspired by natural photosynthesis, where chlorophyll captures sunlight and generates reactive species capable of oxidizing organic molecules [80, 81].

The photocatalytic process relies on the energy conversion from photons to electronic excitations in the material. Semiconductors have a valence band (VB) and a conduction band (CB) separated by an energy gap (band gap, E_g). Excitation by photons with energy equal to or greater than the band gap promotes electrons from the VB to the CB, leaving behind positively charged holes (h^+) in the VB. The movement of these electrons and holes enables redox reactions on the photocatalyst surface, eventually leading to the degradation of pollutants [82].

As in the scheme illustrated in Figure 1.5, photocatalytic degradation of pollutants involves several key steps:

1. **Light Absorption and Charge Separation:** The photocatalyst absorbs photons, exciting electrons from the VB to the CB and generating electron-hole pairs:

$$\text{Photocatalyst} + h\nu \rightarrow e^- + h^+ \tag{1.10}$$

2. **Redox Reactions on the Catalyst Surface:** The photogenerated holes and electrons react with water, hydroxyl ions, and dissolved oxygen to generate reactive oxygen species (ROS) such as hydroxyl radicals (·OH) and superoxide radicals ($\cdot O_2^-$):

$$h^+ + H_2O \rightarrow H^+ + \cdot OH \tag{1.11}$$

$$h^+ + OH^- \rightarrow \cdot OH \tag{1.12}$$

$$e^- + O_2 \rightarrow \cdot O_2^- \tag{1.13}$$

3. **Recombination:** Some electron-hole pairs recombine, releasing energy as heat and lowering quantum efficiency:

$$h^+ + e^- \rightarrow \text{heat} \tag{1.14}$$

4. **Pollutant Degradation:** The generated ROS interact with pollutants, leading to their oxidation or reduction. These species are highly reactive and non-selective, enabling rapid degradation of a wide range of organic and inorganic contaminants [80, 82].

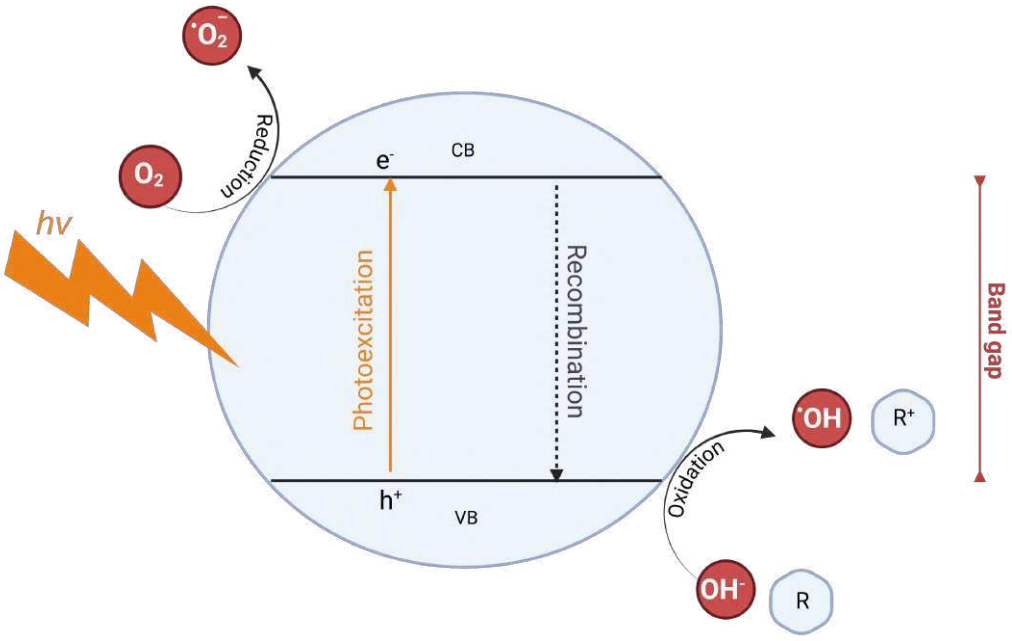

Figure 1.5: Schematic representation of the photocatalysis mechanism

Photocatalytic reactions can be classified into homogeneous and heterogeneous, depending on the phase of the photocatalyst relative to the reactants. Heterogeneous photocatalysis, where the

catalyst is solid and the pollutants are in aqueous solution, is the most widely used due to the ease of separation of the catalyst from the treated water and the scalability of the process [82].

The efficiency of photocatalysis depends on multiple factors, including:

- **Band Gap of the Photocatalyst:** Determines the wavelength of the light that can excite electrons and the overall energy efficiency.
- **Surface Area and Morphology:** High surface area enhances pollutant adsorption and availability of reactive sites.
- **Light Intensity and Wavelength:** Stronger light and suitable wavelengths improve electron excitation.
- **Pollutant Concentration:** High concentrations may saturate active sites and reduce efficiency.
- **Dissolved Oxygen and Water Matrix:** Oxygen acts as an electron acceptor forming ROS, while water composition can inhibit or enhance reactions.
- **pH:** Influences the charge of the photocatalyst surface and the speciation of pollutants.

Table 1.5 summarizes some of the most commonly investigated photocatalytic materials along with their main characteristics.

Photocatalysis has been successfully applied to degrade:

- Organic dyes such as methylene blue, methyl orange, and congo red [94, 35, 88].
- Pharmaceutical residues including antibiotics and endocrine disruptors [95, 96, 97].
- Heavy metals via reduction (e.g., Cr(VI) to Cr(III)) and complexation with photocatalyst surfaces [98, 99, 100].

The main advantages include high reaction rates, mineralization of pollutants, low secondary pollution, and potential use of sunlight as a renewable energy source. Challenges include recombination of electron-hole pairs, limited absorption of visible light for some semiconductors, and recovery of nanosized photocatalysts from treated water.

Photocatalysis represents a versatile and environmentally friendly approach for wastewater remediation. By selecting appropriate semiconductors, optimizing operational conditions, and potentially coupling with adsorption processes, photocatalysis can effectively degrade a broad spectrum of pollutants, offering a sustainable solution for water purification.

Table 1.5: Conventional semiconductor photocatalysts for wastewater remediation

Photocatalyst	**Advantages**	**Disadvantages**	**Ref.**
TiO_2	Durable, cheap, low toxicity, UV-active	High e^-–h^+ recombination, limited visible light response	[83, 33]
ZnO	Low cost, photosensitive, low toxicity	High e^-–h^+ recombination, poor visible light activity	[83]
CdS	Visible light active, narrow bandgap	Photocorrosion, toxic potential	[70, 73]
WO_3	Visible light responsive, acid-stable	High recombination, low activity	[83]
CeO_2	UV/visible active, strong redox	Limited efficiency, expensive	[84, 85]
CuO	Narrow bandgap, high conductivity	Photocorrosion, moderate activity	[86, 87]
NiO	Visible light active, stable	Low activity, complex synthesis	[88, 89]
SnO_2	Transparent, wide bandgap, stable	Inefficient under visible light, high recombination	[90, 91]
Cr_2O_3	Chemically stable	Low efficiency, toxicity concerns	[92]
ZrO_2	Thermally stable, nontoxic	High bandgap, moderate activity	[93]
Fe_2O_3	Solar-active, easy recovery, eco-friendly	High recombination	[74]

2 ALGINATE-BASED MATERIALS FOR HEAVY METALS ADSORPTION

The project ambition is to develop new wastewater treatment materials which are efficient, cost-effective, and not environmentally impacting. In this perspective, nontoxic, and biodegradable composites have been obtained working on the modification of sodium alginate (a polysaccharide biopolymer) with the incorporation of nanomaterials to improve their mechanical properties and adsorption capacities.

2.1 Introduction

2.1.1 Alginate

Adsorption is widely recognized as one of the most efficient and preferred techniques in wastewater treatment, with active carbon being still the most used adsorbent material, even though the cost of carbon-based adsorbents has been increasing due to the depletion of coal-derived commercial carbon [46]. Among the different materials investigated for adsorption, alginate, a natural anionic polysaccharide obtained from the cell walls of brown algae such as kelps, has received significant attention [2, 101]. The major component of alginate is alginic acid, while sodium alginate (SA), the sodium salt of alginic acid, is a polymer rich in hydroxyl and carboxyl functional groups distributed along its linear backbone, obtained from the condensation of β-D-mannuronopyranosyl and α-L-guluronopyranosyl acids (Figure 2.1). These groups confer hydrophilicity to the polymer and allow strong interactions with cationic species, including a wide range of heavy metal ions [49].

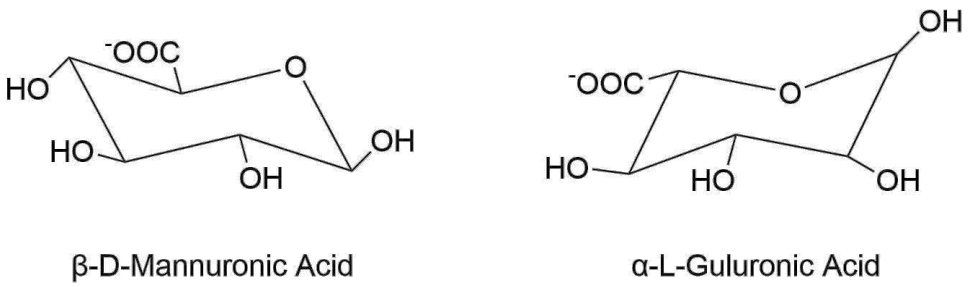

Figure 2.1: Structural units of alginate: β-D-mannuronopyranosyl (M) and α-L-guluronopyranosyl (G) residues

Structurally, alginate is composed of β-D-mannuronopyranosyl (M) and α-L-guluronopyranosyl (G) residues arranged in homopolymeric blocks of M (MM), homopolymeric blocks of G (GG), and heteropolymeric blocks of alternating M and G (MG) (Figure 2.2).

The distribution of carboxyl and hydroxyl groups along these blocks provides multiple coordination sites for divalent and trivalent cations such as Ca^{2+}, Ba^{2+}, Cu^{2+}, Pb^{2+}, Cd^{2+}, Fe^{3+}, and Al^{3+}, making alginate a particularly effective biosorbent for heavy metal removal from contaminated water. The interaction between alginate and metal ions is mainly electrostatic and

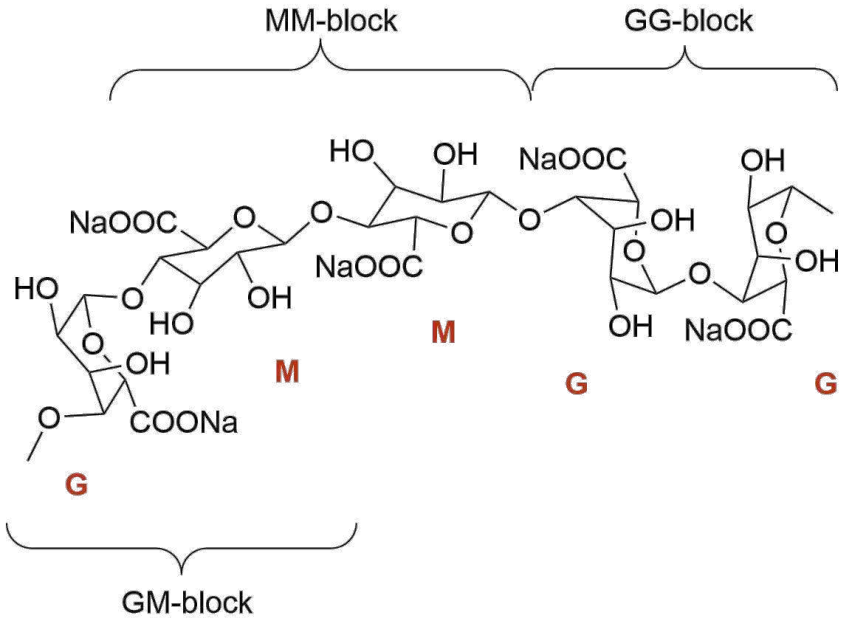

Figure 2.2: Alginate structure, composed of β-D-mannuronopyranosyl (M) and α-L-guluronopyranosyl (G) residues arranged in homopolymeric blocks of M units (MM), homopolymeric blocks of G units (GG), and heteropolymeric blocks with alternating M and G residues (MG)

coordinative, and it can also involve hydrogen bonding and chelation mechanisms depending on the nature of the metal and the polymer block composition.

Commercially, alginate is mainly extracted from brown seaweed and is marketed in the form of soluble sodium alginate. The estimated annual world production of brown algae in dry weight is approximately 85,000 tons, from which around 23,000 tons of sodium alginate are obtained [102]. Alginate is the principal structural constituent of the brown algae cell walls and intercellular matrix, providing the mechanical strength and the flexibility necessary for withstanding marine conditions. It is naturally found as an insoluble mixed salt of alginic acid bound to several cations, including Ca^{2+}, Na^{+}, Mg^{2+}, and K^{+}. From an industrial perspective, alginate extraction can be described as a mass transfer process, where solvents penetrate the algal matrix and dissolve the target polysaccharide. The most widely applied method is the conventional process, consisting of six main steps: pre-treatment of the algal biomass, acid treatment, alkaline extraction, precipitation, bleaching, and drying. Nevertheless, many variations of these steps exist, as process conditions strongly influence alginate yield, molecular weight, mannuronic-to-guluronic blocks (M/G) ratio, viscosity, and technological performance [103].

The main industrial steps are the following [104]:

- **Washing** of raw algae to remove salts, sand, impurities, and epiphytes.
- **Pre-treatment** of biomass:
  - Mechanical pre-treatment (drying, grinding, particle size reduction).

  - Solvent treatment with ethanol, acetone, chloroform, or formaldehyde, in order to remove impurities present in the cell matrix, which can be bound to the alginate.

- **Acid treatment** (low molarity HCl or organic acids) to convert alginate salts into alginic acid and remove unwanted compounds.
- **Alkaline extraction** (mainly with Na_2CO_3) to solubilize alginate as sodium alginate.
- **Solid/liquid separation** through filtration or centrifugation.
- **Precipitation** of alginate using alcohol (ethanol), $CaCl_2$, or HCl.
- **Purification and bleaching** to eliminate proteins, phenols, pigments, and endotoxins.
- **Drying and milling** of the fibrous alginate paste into powder form for commercialization.

A semplified flow chart of the process described is shown in Figure 2.3.

The industrial extraction process starts with **washing** of the raw algal biomass. Preferably performed with distilled water, effective washing is crucial to avoid contamination that could interfere with subsequent chemical treatments [105]. The next step is **pre-treatment**, which can be divided into two approaches. Mechanical pre-treatment consists of drying and milling the biomass. Drying can be performed using hot air, solar energy, or freeze-drying. While it prevents microbial growth and facilitates storage and transport, drying requires significant energy and can affect alginate quality [106]. Once dried, algae are milled to 0.5–6 mm particle size, which increases surface area and accelerates extraction. Solvent treatment aims to remove compounds such as phenols, proteins, pigments, and lipids. Ethanol, acetone, methanol, or chloroform solutions are typically used, although due to toxicity they remain mostly at laboratory scale. In industry, formaldehyde has been employed to prevent microbial degradation and pigment extraction; however, due to toxicity, allergenicity, and carcinogenicity, its use is increasingly discouraged. After pre-treatment, the biomass undergoes an **acid treatment**. Diluted HCl solutions (up to pH 4) are commonly used to convert alginate salts into alginic acid, eliminate polyphenols, mannitol, and co-extracted polysaccharides such as laminarins and fucoidans. Organic acids such as citric acid have also been tested, showing effects not only on yield but also on the M/G ratio of the extracted alginate [107]. The subsequent step is the **alkaline extraction**, the core of the process. The pre-treated biomass is treated with Na_2CO_3, NaOH, or $NaHCO_3$, adjusting the pH to 9–10. Under these conditions, alginic acid is converted in water-soluble sodium alginate, which is released into solution. Process variables such as temperature, extraction time, and alkali concentration significantly affect yield and viscosity of the final product. Following extraction, a **solid/liquid separation** (usually filtration or centrifugation) isolates the sodium alginate solution. To recover the polysaccharide, a **precipitation step** is required. Three major routes exist: (i) alcohol precipitation, predominantly with ethanol, which is simple, provides high yields, and preserves rheological properties; (ii) the $CaCl_2$ route, where sodium alginate is converted into calcium alginate, later treated with HCl to regenerate alginic acid; and (iii) direct HCl precipitation. The ethanol route is the most widely applied due to its simplicity and favorable product characteristics [108]. Once precipitated, alginate requires **purification and bleaching**. This step removes residual compounds, which affect quality and biocompatibility. Different strategies are reported, including

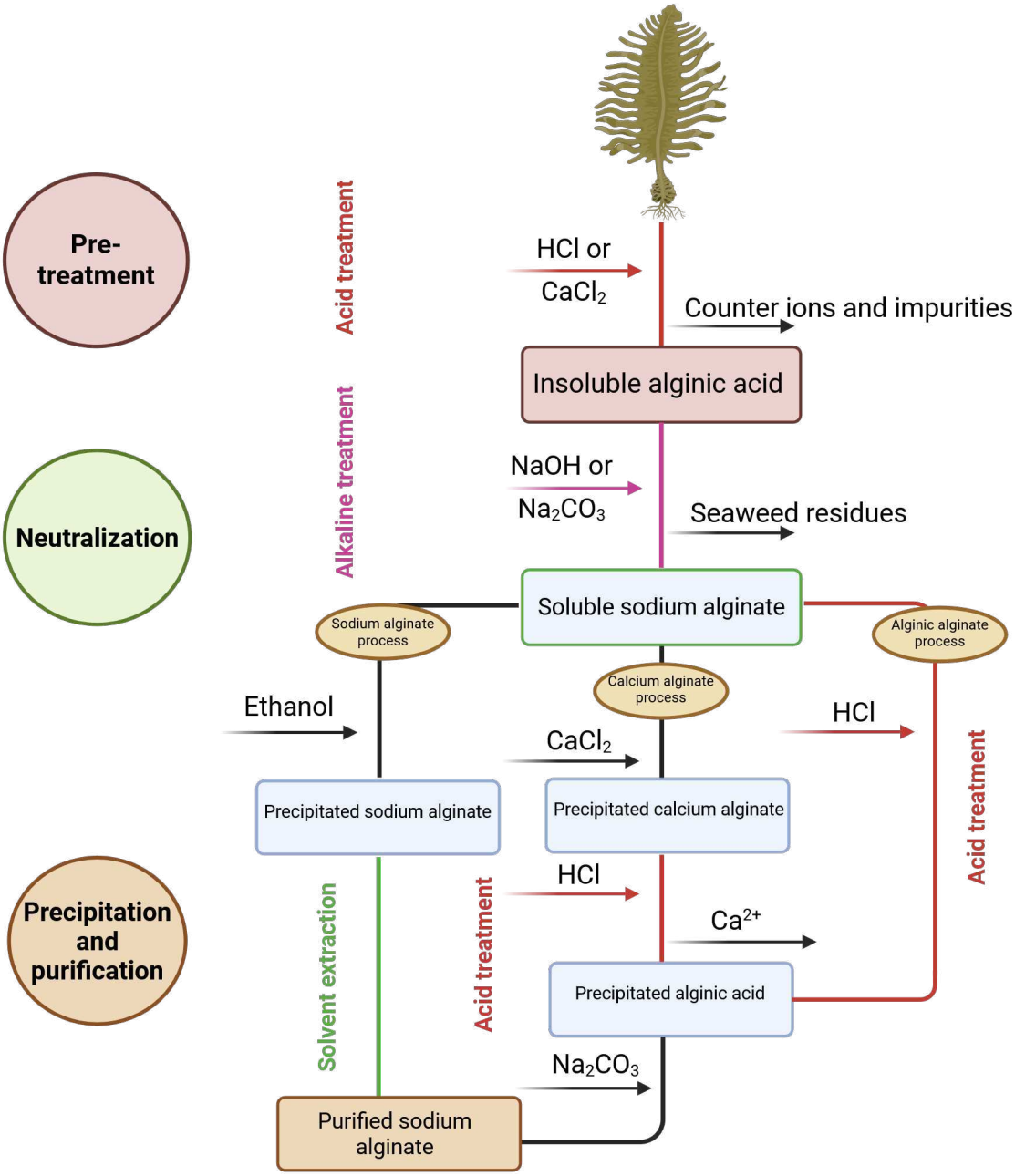

Figure 2.3: Scheme flow chart of sodium alginate extraction and other alginates from brown seaweed

selective precipitation with barium ions or solvent extractions. For biomedical or pharmaceutical applications, stricter purification protocols are adopted, although these are often kept confidential by companies. Finally, the material is subjected to **drying and milling**. Industrial drying is typically performed in fluidized bed dryers, after which the alginate is ground using hammer or turbine mills to achieve the required particle size. The dried powders are then marketed as sodium alginate or converted into other salts such as calcium, potassium, or magnesium alginates, as well as functional derivatives such as propylene glycol alginate (PGA) [109].

Alginate-based materials are known for their adsorption properties and have been used in a variety of wastewater treatment applications. The adsorption capacity of alginate is influenced by several factors, including the type of alginate, the presence of other materials in the wastewater, and the pH of the solution. They are typically more effective at adsorbing organic contaminants than inorganic ones. Alginate possesses several intrinsic properties that make it particularly suitable for wastewater treatment [110]:

- Effectively removes suspended solids and oils from wastewater.
- Improves the settleability of sludge.
- Adsorbs heavy metals and other pollutants from wastewater.
- Is a natural, biodegradable product that is environmentally safe.
- Possesses thermal stability.
- Low cost (approximately 3000 tons of alginate are produced annually from about 85,000 tons of algae).

Due to its biocompatibility, non-toxicity, and ability to form crosslinked networks with polyvalent cations, alginate has been extensively used for encapsulation and immobilization of chemical and biological species. Applications span agriculture, food technology, pharmaceuticals, cosmetics, chemical and environmental engineering, as well as tissue engineering and biomedical fields. Alginate-based hydrogels are particularly attractive for drug delivery, cell scaffolding, biosensors, and as materials capable of selectively removing toxic metals from aqueous environments. Hydrogels can be prepared under mild conditions, typically at room temperature, and the polymer can be easily crosslinked to produce mechanically stable and thermally resistant materials [111].

Among the many physical cross-linking methods, ionic cross-linking is the most commonly used technique for the preparation of alginate hydrogel materials due to its mild reaction conditions and ease of operation. When divalent or trivalent metal ions (M^{n+}) enter the alginate polymer chain, they interact with carboxylate ($-COO^-$) and oxygen atoms along the backbone, forming alginate hydrogel spheres with a three-dimensional network structure, which constitutes the well-known "egg-box" model illustrated in Figure 2.4 [112, 113].

The metal ions are predominantly coordinated within the GG-block regions, while the MM-blocks contribute to the flexibility and elasticity of the network. A near-membrane structure surrounding the GG-blocks further enhances the mechanical strength of the hydrogel. These hydrogels can react directly with metal ions and other pollutants through ion exchange and can be easily recovered via simple filtration, making them highly effective for water pollution treatment. The relative binding capacities of alginate hydrogels toward divalent metal cations follow the order: $Pb^{2+} > Cu^{2+} > Cd^{2+} > Ba^{2+} > Sr^{2+} > Ca^{2+} > Co^{2+}$, Ni^{2+}, $Zn^{2+} > Mn^{2+}$ [48].

A particularly effective technique for forming these hydrogels is ionotropic gelation, in which a solution of sodium alginate is extruded dropwise into a gelation bath containing soluble cal-

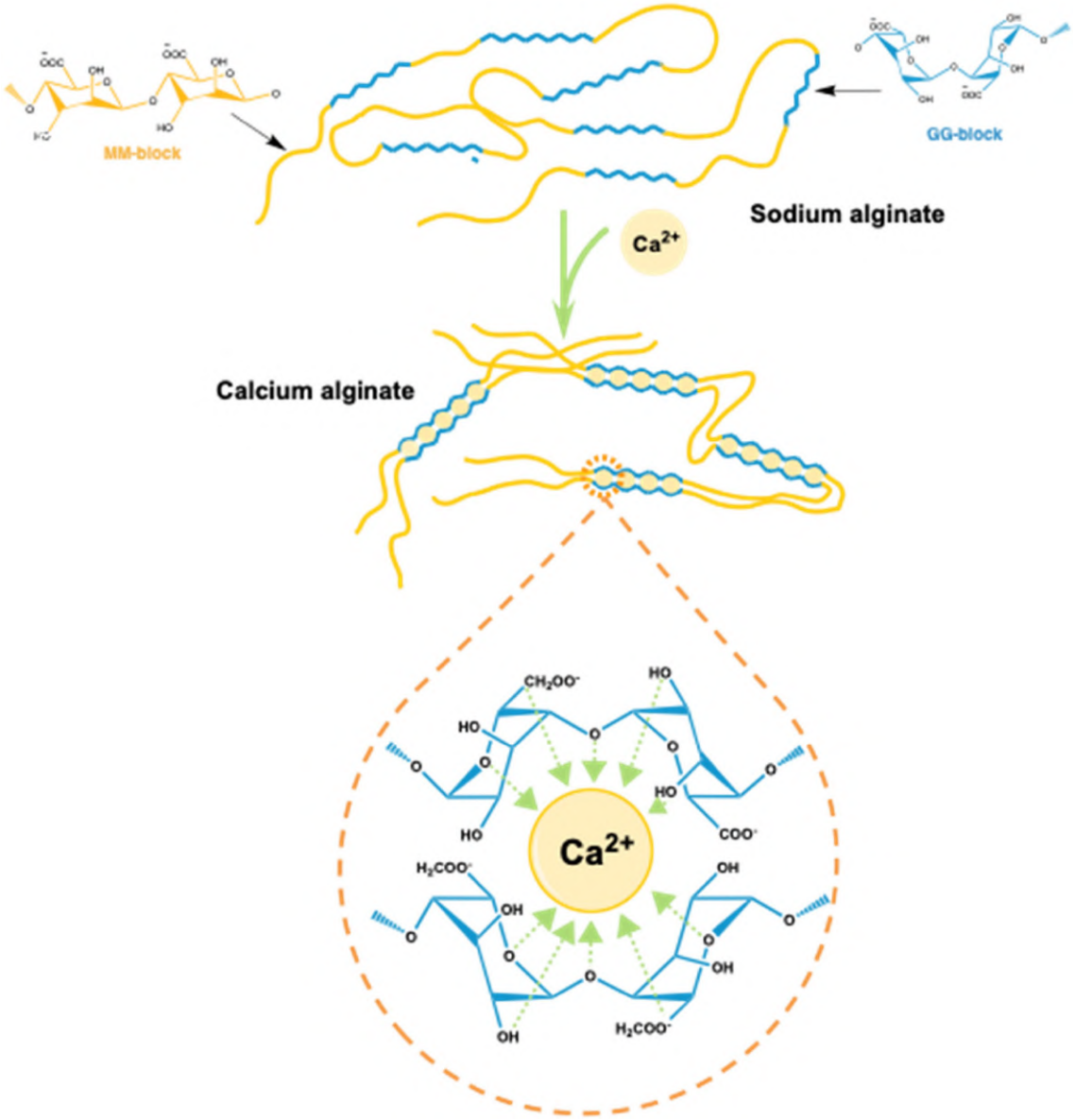

Figure 2.4: Schematic representation of the calcium-induced gelation of alginate in accordance with the "egg-box" model [104]

cium salts, such as $CaCl_2$. Calcium ions replace sodium ions in the GG blocks, forming a stable three-dimensional crosslinked network known as calcium alginate (CA). Gelation occurs rapidly, preserving the spherical shape of the droplets and producing hydrogel beads with tunable size, porosity, and mechanical properties. The presence of abundant carbonyl and hydroxyl groups along the polymer chains enhances the anchoring capacity for a wide variety of heavy metals, while the three-dimensional network prevents excessive swelling or dissolution in aqueous environments.

In addition to ionic crosslinking, covalent crosslinking can be introduced by reacting the carboxyl (-COOH) groups of alginate with primary amine groups through dehydration condensation reactions, forming amide bonds. The combination of ionic and covalent crosslinking results in hydrogels with superior structural stability, mechanical strength, and pollutant-binding efficiency. By tuning the ratio of ionic to covalent crosslinking, adjusting the G/M block composition, and controlling the bead size and porosity, alginate hydrogels can be optimized for maximal adsorption and immobilization of heavy metals, while remaining easily recoverable, reusable, and stable under a range of environmental conditions.

Alginate materials exhibit not only high adsorption and flocculation capacity but also remarkable porosity, with interconnected pore structures ranging from 5 to 200 nm. This porosity allows selective filtration, high water permeability, and effective transport of ions and small molecules, which is essential for applications in water treatment and purification systems. By adjusting the proportion of G residues in the polymer, the network can become more open and less prone to shrinkage, providing additional control over the mechanical and filtration properties of gels [114]. The combination of biodegradability, non-toxicity, renewability, and reusability makes alginate-based hydrogels highly attractive for sustainable wastewater treatment.

Overall, alginate-based materials, ranging from native polysaccharides to functionalized nanocomposites, provide a versatile platform for adsorption, flocculation, filtration, and catalytic applications. Their ability to selectively bind and remove heavy metals, coupled with tunable porosity, biocompatibility, and chemical stability, makes them highly suitable for a broad spectrum of environmental and industrial applications. The integration of alginate with nanostructured and zero-valent metal components further expands their functional capabilities, enabling simultaneous adsorption and catalytic degradation of organic and inorganic pollutants, while maintaining sustainability, cost-effectiveness, and ease of operation.

2.1.2 Active nanomaterials and nanoadsorbents

Nowadays, nanomaterials have attracted considerable attention as adsorbents for wastewater decontamination due to their large specific surface area and the abundance of active groups available for binding heavy metals [115, 116, 117]. Moreover, nanostructured adsorbents can be reused and recycled multiple times, making them cost-effective and highly appealing. However, their difficult removal from treated water and the challenges associated with their regeneration have limited their commercial application. Therefore, current research efforts are focused on addressing these issues through the functionalization of nanoparticles [118]. Among the most studied nanomaterials for remediation we find: **Carbon-based Nanoparticles** Carbon-based nanomaterials, including activated carbon, biochar, carbon black, and carbon nanotubes (CNTs), are among the most extensively studied adsorbents for wastewater treatment [119]. Activated carbon remains

the most widely applied, particularly for the removal of heavy metals and organic compounds, though its production is energy-intensive and costly. As a more sustainable alternative, biochar derived from agricultural residues has gained attention due to its low cost, porosity, and surface reactivity, serving as an effective substitute for coal-based activated carbon [120]. CNTs combine high mechanical strength, large surface area (up to 3000 m^2/g), and tunable porosity, making them powerful adsorbents for heavy metals, dyes, and organic pollutants [121]. Functionalization with carboxyl, hydroxyl, or amine groups further improves their affinity towards cationic pollutants by providing active binding sites [120]. However, despite their excellent performance, CNTs face challenges related to aggregation in aqueous solutions, limited selectivity, and toxicity concerns. Pristine CNTs often display low sorption capacities for certain metal ions because of their inert graphitic walls [122].

Nano Zero-Valent Iron (nZVI) Nanoscale zero-valent iron (nZVI) is one of the most promising nanomaterials for remediation, due to its strong reducing capacity and ability to degrade or immobilize a broad spectrum of pollutants. nZVI particles exhibit a high specific surface area and abundant reactive sites, allowing rapid interaction with metal ions such as Ni, Cd, Cr, Pb, Zn, Cu, and As, with removal efficiencies ranging between 40 and 99% depending on the system [123]. Their reactivity is attributed to their core–shell structure: a reactive metallic Fe^0 core surrounded by an oxidized Fe(II)/Fe(III) shell, which participates in redox reactions [124]. Compared with traditional sorbents like zeolites or ion-exchange resins, nZVI offers superior performance; for example, Ni adsorption can reach 130 mg/g, significantly higher than conventional materials. Moreover, nZVI can be directly injected into contaminated aquifers as a colloidal suspension, allowing in-situ treatment [125]. Despite these advantages, nZVI suffers from aggregation and passivation, reducing its mobility and reactivity in natural environments.

Silica-based Nanoparticles Silica nanoparticles (SiO_2) are widely used in environmental applications due to their tunable porosity, surface functionalization potential, and chemical stability. Their high surface area and abundant hydroxyl groups enable easy modification with amine, thiol, or phenyl groups, enhancing binding affinity towards heavy metals such as Cu(II), Hg(II), Pb(II), and As(III) [126]. Bi-functionalized silica has been shown to outperform mono-functionalized systems by offering synergistic binding effects. Hybrid silica-based composites further expand their functionality. For example, mesoporous silica-coated magnetite nanoparticles combine high adsorption capacity with magnetic separability, enabling efficient pollutant removal and easy recovery [127]. Similarly, graphene oxide-coated silica nanocomposites display strong adsorption for Pb(II) and As(III), benefiting from the combined surface functionalities of both components [128]. Nevertheless, challenges remain in scaling up laboratory-scale methods to real-world applications. While many studies report high efficiencies in dye or heavy metal removal under controlled conditions, fewer have demonstrated success in complex environmental systems. Further research into stability, regeneration, and cost reduction is required to fully exploit silica-based nanomaterials for wastewater treatment [129].

Nanocomposites Nanocomposites integrate multiple nanomaterials into a single platform, enhancing performance by combining complementary properties. Their large surface-to-volume ratios, abundant reactive sites, and catalytic potential make them particularly suitable for pollutant adsorption and degradation [130]. Chitosan-modified CNTs, for example, have been developed for dye adsorption (e.g., Congo red), heavy metal detection, and biosensing applications. Similarly,

polymer-clay nanocomposites offer low-cost, scalable solutions with high adsorption capacity due to their layered structure and intercalated nanoparticles.

Polymeric Nanoparticles Polymeric nanoparticles represent a versatile class of adsorbents, offering structural tunability, biocompatibility, and ease of synthesis. Conjugated polymers, due to their electronic properties, have also been explored as fluorescent sensors, capable of signal amplification and selective detection of electron-deficient pollutants [131]. Their incorporation onto nanoparticle surfaces enhances both adsorption and sensing functions, enabling dual-purpose materials. Compared with CNTs, polymeric nanoparticles are simpler to synthesize, often via precipitation methods using inexpensive precursors [132]. Functional groups such as carboxyl, amine, and sulfonate moieties can be easily introduced, enabling high selectivity towards specific contaminants. Polyrhodanine, containing sulfur and oxygen donor atoms, has attracted attention for its strong affinity towards heavy metals. Magnetic Fe_2O_3/poly-rhodanine nanoparticles synthesized in one step have shown excellent adsorption capacity, combining magnetic separability with efficient pollutant removal [133].

Ceramic Nanoparticles and Membranes Ceramic nanoparticles and membranes offer robust mechanical, thermal, and chemical stability, making them suitable for harsh operational environments. Compared with polymeric membranes, ceramic membranes demonstrate higher flux, reduced fouling, and longer lifetimes, albeit at higher initial costs [134]. Applications include dye removal, oil–water separation, and heavy metal remediation. Ceramic pot filters (CPFs), composed of clay and agricultural residues, represent low-cost point-of-use technologies capable of removing pathogens and turbidity. Modified CPFs impregnated with colloidal silver have shown partial removal of Cr(VI), organic dyes, and bacteria [135]. Advanced ceramic hollow fiber membranes synthesized from rice husk ash exhibit $>$99% removal efficiency for toxic metals at acidic pH values, highlighting the potential of waste-derived materials for high-performance membranes. Despite their advantages, the high fabrication costs and lack of large-scale deployment remain challenges.

Metal Oxide Nanoparticles In recent years, metallic and metal oxide nanoparticles have emerged as promising materials for the removal of heavy metal ions. Bare metallic nanoparticles are less commonly used as adsorbents because they tend to agglomerate, and their separation from wastewater is often complicated. Consequently, capping or functionalization of these nanostructured adsorbents is required to enhance their stability and to simplify the separation process. With their ability to adsorb a wide range of pollutants, magnetic properties, and functional versatility, magnetic nanoparticles (MNPs) have recently become crucial in water purification efforts [136, 137, 138]. They exhibit diverse behaviors, including magnetic, electrical, and optical properties, as well as high reaction efficiency, strong chemical activity, exceptional flexibility, and superior adsorptive potential [139]. The unique properties of MNPs are determined by their chemical composition, size, shape, and morphology, which enable effective interactions with pollutants and make them valuable for environmental remediation. By tuning these parameters, it is possible to optimize their magnetic traits, thereby enhancing performance in environmental and industrial processes, ensuring more efficient pollutant removal and resource management. Consequently, MNPs can be tailored to meet specific needs in various applications. This feature is particularly useful for enhancing the efficiency of purification, separation, and chemical processes, making MNPs an invaluable tool in modern technologies [140]. Structurally, MNPs often incorporate magnetic

metals such as iron, nickel, and cobalt, as well as oxides including magnetite, maghemite, cobalt ferrite, and chromium dioxide [141]. Iron oxide nanoparticles, particularly magnetite (Fe_3O_4), maghemite (γ-Fe_2O_3), and hematite (α-Fe_2O_3), are among the most widely studied nanomaterials for wastewater remediation due to their unique magnetic and surface properties. Depending on the synthetic method, Fe_3O_4 nanoparticles (MNPs) can combine large surface area, superparamagnetism, uniform size distribution, chemical stability, and cost-effectiveness, making them attractive for adsorption and catalytic processes [142, 143]. Their magnetic nature enables easy separation and recovery using external fields, minimizing secondary pollution and reducing operational costs, particularly in developing countries [144]. Surface modification strategies such as silylation, polymer coating, or surfactant adsorption enhance their reactivity, stability, and selectivity toward heavy metals and dyes. These nanoparticles exhibit tunable morphology (spherical, tubular, or wire-like), crystalline or amorphous structures, and adjustable surface chemistry, all of which influence adsorption capacity and reusability [145]. Core–shell polymer-coated magnetic nanoparticles (MNPs) are particularly attractive, as the polymer shell enhances dispersion, prevents aggregation, and introduces specific binding sites for targeted adsorption [146]

Beyond wastewater treatment, iron oxide nanoparticles have applications in catalysis, sensing, biomedicine, and energy storage, but environmental remediation remains one of their most promising one due to their high efficiency. More broadly, metal oxide nanostructures such as ZnO and SnO_2 also demonstrate strong potential in contaminant removal. Their large surface-to-volume ratios, high catalytic activity, and functionalizable surfaces enable efficient interactions with heavy metal ions and dyes [147]. Despite their promise, challenges remain regarding large-scale synthesis, stability after regeneration, and long-term performance in complex wastewater matrices. Nevertheless, iron- and other oxide-based nanoparticles continue to represent a cornerstone in the development of advanced, sustainable nanotechnology-enabled purification systems [148, 149].

2.1.3 Graphene oxide

Ideal graphene is a single-atom-thick two-dimensional (2D) sheet of sp^2 hybridized carbon atoms arranged in a hexagonal lattice through sigma and pi bonds. It serves as a fundamental building block for other carbon allotropes, including carbon nanotubes and fullerenes. Based on the preparation method (physical or chemical from graphite), graphene exists in several forms, at different degrees of oxidation. Among these, graphene oxide (GO) has appeared as very interesting in terms of versatility and potential for wastewater treatment applications. GO can be synthesized via chemical exfoliation of graphite under oxidizing conditions, resulting in a 2D sheet densely decorated with oxygenated functional groups on both its basal plane and edges. The presence of these functional groups disrupts the π-conjugated network of graphene, increasing water dispersibility and reducing aggregation between individual sheets. This characteristic makes GO particularly suitable as a precursor for bulk production of graphene-based nanomaterials and enhances its applicability in adsorption-based wastewater treatment. The choice of synthesis technique plays a decisive role in determining both the quality and scalability of the resulting graphene oxide, thereby directly influencing its suitability for various industrial applications. Broadly, graphene oxide is mainly produced by top-down approaches. These methods involve the disintegration of bulk graphite into individual graphene sheets. The chemical exfoliation of graphite into GO is generally carried out

in a two-step process. Initially, interlayer spacing is increased by oxidation, which reduces van der Waals forces between the graphite layers. Subsequently, a rapid heating process or ultrasonication is applied to exfoliate the material into single or few-layer graphene oxide sheets. For example, ultrasonication is commonly used to achieve monolayer GO. Several established synthetic routes for GO exist, including the Brodie, Staudenmaier, and Hummers methods, along with various advanced modifications of these approaches [150]. In particular, the Hummers method involves the oxidation of graphite using strong acids and oxidizing agents (e.g., $KMnO_4$). This process introduces abundant oxygen-containing functional groups that are essential for adsorption efficiency. In fatc, functional groups such as hydroxyl and carboxyl markedly enhance the adsorption capacity of GO toward a broad range of pollutants in wastewater treatment [151]. To further improve the properties of GO, the modified Hummers method has been developed (Figure 2.5). This approach incorporates additional steps to optimize the oxidation process, yielding graphene oxide with enhanced functionalization and improved adsorption capabilities. Compared to the original method, the Modified Hummers Method introduces several key improvements. Some variants eliminate or reduce the use of $NaNO_3$, significantly decreasing the formation of toxic gases such as NO_2 and N_2O_4. In addition, $KMnO_4$ and other oxidants are often added gradually, while the reaction temperature is carefully controlled, enhancing both safety and reaction efficiency [152]. These modifications also promote more complete oxidation of graphite, producing GO with fewer residual graphite particles and a higher concentration of oxygen-containing functional groups. The resulting material exhibits more organized graphene structures and a highly porous network, which directly translate into superior adsorption performance. Consequently, GO produced via the Modified Hummers Method demonstrates improved efficiency in pollutant removal and other environmental applications, such as catalysis and wastewater treatment [153].

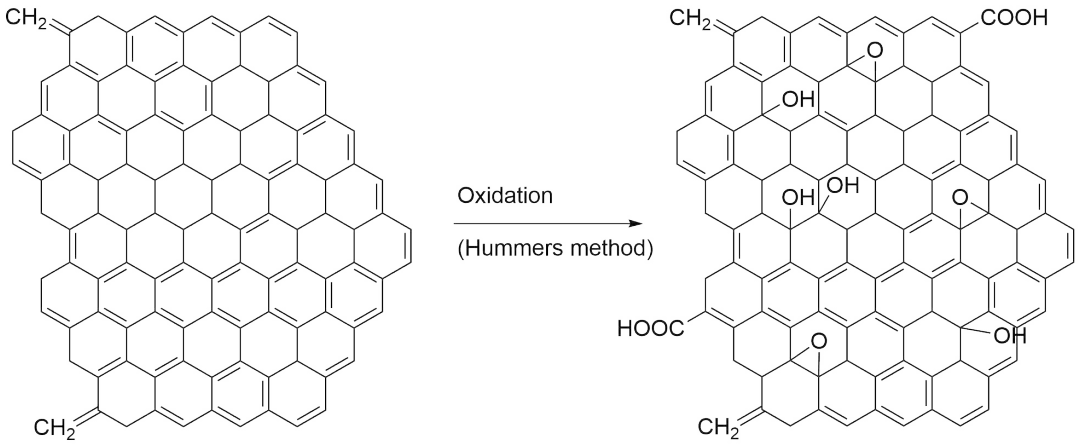

Figure 2.5: Graphene and graphene oxide structure

Because of its relatively large specific area, rich functional groups, and exceptional mechanical strength, graphene oxide (GO) is a promising material for the adsorption of heavy metal ions. The oxygen-containing functional groups on its surface confer a high negative charge density and hydrophilicity, making GO highly effective in removing various heavy metal ions from aqueous solutions, such as Pb(II), Cu(II), Co(II), Cd(II), and Cr(VI). With a typical pore size of roughly 0.9

nm, GO emerges as one of the most cost-effective graphene-based adsorbents. While activated carbon exhibits a metal uptake capacity of up to ∼260 mg/g [154], and biochar reaches values as high as ∼600 mg/g [155, 156], graphene oxide (GO) and its derivatives demonstrate significantly higher adsorption capacities, in the range of ∼900 mg/g for heavy metals such as Pb^{2+} and Cd^{2+}, i.e., 3–5 times greater than conventional sorbents [151]. This superior performance arises from several factors: (i) the tunable surface chemistry enabled by oxygenated functional groups (e.g., –COOH, –OH), which allows selective binding through mechanisms such as electrostatic attraction; (ii) the exceptionally high theoretical surface area of GO (∼2600 m^2/g) [157]; and (iii) the mechanical stability of GO, which enables regeneration over at least six cycles with less than 10% efficiency loss [158].

Table 2.1 summarizes representative graphene-based adsorbents that have been investigated for the removal of various heavy metals, highlighting their compositions, targeted contaminants, and corresponding references.

Table 2.1: Graphene-based adsorbents for heavy metal removal.

Adsorbent used	**Heavy Metal Type**	**Ref.**
GO with hydrophilic groups	Pb^{2+}, Cd^{2+}, Hg^{2+}	[159]
MGO	Pb(II), Hg(II)	[160]
Biochar–GO composites	Cd(II), Cr(VI), As(III)	[161]
Graphene-derived agricultural waste adsorbents	Pb(II), Hg(II), Zn(II)	[162]
Chitosan/graphene nanocomposites	Pb(II), Cd(II), Hg(II)	[163]
EDTA-functionalized GO	Pb(II), Cd(II)	[164]
GO membranes	Pb(II), Cr(VI)	[165]
Graphene-supported iron composites	Cr(VI), As(V)	[166]
rGO	Cd(II), Pb(II)	[10]
Sulfonated magnetic GO	Pb(II), Cd(II), Hg(II)	[167]
CNPs with graphene	Pb(II), Zn(II), Ni(II)	[168]
Chitosan/graphene nanocomposites	Pb(II), Cd(II), Hg(II)	[10]
Activated carbon–graphene composites	As(III), Cr(VI)	[10]
EDTA–GO	Pb(II), Cd(II)	[168]
rGO/Fe_3O_4	Pb(II), Cd(II), Cu(II)	[169]
Graphene oxide–ordered mesoporous silica	Hg(II), Cd(II)	[170]
3D graphene macrostructures	Cr(VI)	[171]
Graphene oxide–polypyrrole composites	Cr(VI)	[10]
Sulfur-doped graphene	Hg(II), Pb(II)	[146]
Graphene oxide–alginate beads	Cu(II), Pb(II)	[165]
Graphene oxide–cellulose nanocrystal composites	Cd(II), Pb(II)	[172]

The regeneration and reusability of adsorbents are critical for the commercial application of

the material. Several studies have shown that using strong acids (e.g., HCl) or strong bases (e.g., NaOH) allows the desorption of the metal ions or contaminants to restore the adsorption capacity of graphene-based materials. For instance, magnetite/non-oxidative graphene composites (M-nOG) retained more than 92% of their initial As(V) adsorption capacity after five regeneration cycles, highlighting their cost-effectiveness and durability. Chemisorption on GO involves the surface complexation of heavy metal ions by the oxygen-containing groups, which can share electron pairs. Although pristine GO exhibits some adsorption capacity, it suffers from limitations such as easy agglomeration due to strong intermolecular forces and a restricted adsorption capacity. To overcome these drawbacks, functionalized graphene-based materials have been developed. Modifications with organic molecules containing O, N, and S functional groups enhance the number and variety of active sites on GO, thereby improving its heavy metal adsorption efficiency. Common functionalizations include oxidation (–CO–, –OH, –COH, –COOR), nitrogenation (–NH, –NH_2, CN–R, –CNH, –CONH), and sulphuration (–S–, –SH, CS, –$CSNH_2$, COSH, –CSSH) [56]. Furthermore, hybrid nanomaterials combining GO with polymers or metal oxides have been developed to exploit the synergistic effects of the components. These materials exhibit exceptional structural properties and multifunctional capabilities, enhancing the overall adsorption performance and broadening the range of applications in heavy metal removal from wastewater.

2.2 State of art

Heavy metals adsorption using alginate The interaction between pristine alginate hydrogels and HMs depends strongly on the chemical properties of the metal ions as well as on operational parameters such as pH. As seen before, HMs are generally adsorbed through multiple mechanisms, including:

- **Ion exchange** between Na^+, Ca^{2+} and other exchangeable ions present on the adsorbent surface and metal ions. In general, ions with higher charge are more readily adsorbed, while for ions of equal charge, those with smaller hydration radii are preferentially taken up [173]. Moreover, the ionotropic gelation of alginate can be regarded as a rapid ion-exchange process in which divalent cations replace Na^+ and bind to the COO^- groups of the alginate. The gelation ability of alginate with metal ions therefore depends on the availability of carboxylic groups. For instance, Wang *et al.* [174] reported the direct gelation method of sodium alginate aqueous solutions with metal ions, enabling effective removal and recovery of Pb^{2+}, Cu^{2+}, and Cd^{2+} from industrial wastewater.

- **Chelation** between hydroxyl/carboxyl groups and metal ions. The affinity of alginate chains for divalent cations generally follows the order [113]: Pb(II) $>$ Cu(II) $>$ Cd(II) $>$ Ba(II) $>$ Sr(II) $>$ Ca(II) $>$ Co(II) $\sim$ Ni $\sim$ Zn $>$ Mn(II).

- **Reduction of heavy metals** in high oxidation states (e.g., Cr(VI)) to lower oxidation states through electron donation from hydroxyl groups in alginate chains. During this process, OH groups are often oxidized to carbonylic and carboxylic groups [175].

- **Electrostatic interactions** between deprotonated oxygen-containing groups and charged metal ions. This mechanism is pH-dependent: as the pH increases, carboxylic groups become

less protonated or fully deprotonated, thereby generating more active sites and enhancing adsorption efficiency.

- **Hydrogen bonding**, which is particularly relevant for oxoanion species such as chromate/dichromate (CrO_4^{2-}, $HCrO_4^-$) and arsenate ($H_2AsO_4^-$, $HAsO_4^{2-}$), where protonation equilibria determine their predominant aqueous forms.
- **Physical adsorption** processes, including pore-filling effects. For instance, hydrogel porosity can be reduced after drying (depending on the drying method), but pores may re-form upon swelling in water, thereby influencing the diffusion pathways of metal ions.

The use of alginate gels, predominantly in the form of beads, as adsorbents for heavy metals has been widely reported in recent studies. For example, the adsorption of Ni(II), Pb(II), and Zn(II) onto calcium alginate beads from aqueous solutions was investigated in a single-component system [176]. The maximum adsorption capacities were 97.9 mg g^{-1}, 261.9 mg g^{-1}, and 88.65 mg g^{-1} for Ni(II), Pb(II), and Zn(II), respectively, as determined by inductively coupled plasma mass spectrometry (ICP–MS), at pH 5, with an adsorbent dose of 8 mg and a contact time of 90 min. Wang *et al.* proposed a novel method based on the direct gelation of sodium alginate solutions with target metal ions (Pb(II), Cu(II), and Cd(II)) from industrial wastewater [177]. The higher gelation affinity of alginate towards Pb(II), compared with Cu(II) and Cd(II), was attributed to differences in ionic charge, radius, and electronegativity. Furthermore, FTIR and XPS analyses confirmed that –OH and $–COO^-$ groups on alginate served as the primary binding sites in the gelation mechanism. In another study, alginate microspheres were employed as adsorbents for the removal and recovery of Sr(II) ions from seawater, demonstrating an adsorption capacity of 110 mg g^{-1} at pH 7–8 [178]. Similarly, Tahtat *et al.* examined Pb(II) adsorption in simulated gastric fluid using both dry and hydrated alginate gel beads [179]. The maximum adsorption capacities were 83.33 mg g^{-1} for dry beads and 93.37 mg g^{-1} for hydrated beads, obtained at 37 °C, pH 2.5, and a contact time of 90 min. Although the preparation of alginate gels by ionic crosslinking is simple and can be performed under mild conditions, the resulting gels often suffer from poor mechanical strength [2]. This intrinsic weakness significantly limits the large-scale application of alginate as an adsorbent. Parameters such as the type and concentration of crosslinking ions, the alginate concentration, and the solution pH must be carefully optimized, as these factors strongly influence the stability, mechanical strength, and morphology of the alginate gel.

Alginate based-materials Several reviews have discussed the adsorption mechanisms involved in the removal of heavy metals using alginate-based composite adsorbents [180, 181, 45].

A comprehensive review of the literature shows that several types of materials have been encapsulated in alginate matrices for environmental applications, including activated carbon (AC), biochar, carbon nanotubes (CNTs), graphene oxide (GO), nanoparticles, magnetic materials, and microorganisms [182]. The selection of the encapsulated material depends on its functionality and the intended application, with the aim of achieving synergistic benefits in the composite. While alginate-based composites are well known for improving mechanical and physical properties in bioengineering applications, additional benefits for environmental applications are also noteworthy. The main advantages of encapsulating different functional materials into alginate matrices can be summarized as follows:

- **Carbon-based adsorbents:** Alginate beads serve as a stable and easily separable matrix for adsorbents that typically occur as fine powders, such as AC, biochar, CNTs, and GO [183, 184]. Activated carbon has long been used in wastewater treatment, but its powdered form is difficult to separate and regenerate, resulting in adsorbent losses. Biochar, considered a cost-effective alternative to AC, can be ball-milled to increase its surface area; however, fine biochar powders are also difficult to recover from water [185]. CNTs and GO are efficient in removing organic and inorganic pollutants due to their unique structures and large surface areas [186]. Yet, GO disperses very well in water and CNTs form small aggregates, both of which complicate separation [187]. Encapsulation into alginate beads or hydrogels resolves this issue by enabling easy recovery and regeneration of the adsorbent.

- **Magnetic and nanoparticle composites:** Incorporating nanoparticles or magnetic materials into alginate not only improves adsorption performance but also reduces the environmental risks associated with free nanoparticles [188]. Alginate/nanomaterial composites thus combine the benefits of nanotechnology with the separation advantages of alginate matrices [189]. Moreover, embedding magnetic nanoparticles into alginate allows the fabrication of so-called "magsorbents," which can be efficiently recovered by applying an external magnetic field [113]. For example, maghemite-incorporated alginate beads facilitate isolation and recovery during treatment processes [190]. This approach provides simple operation, efficient separation, and excellent reusability.

- **Microorganism carriers:** Alginate is also widely used to immobilize microorganisms for environmental and agricultural applications [191]. Compared with conventional suspension systems, alginate–microorganism composites show advantages such as higher biomass retention, increased metabolic activity, and improved resistance to toxic compounds [192]. Additionally, immobilized microorganisms within alginate beads can be reused multiple times without significant loss of activity. These features make alginate immobilization technology highly attractive for wastewater treatment.

In general, the encapsulation of carbonaceous adsorbents, MNPs, or microorganisms into alginate matrices provides a versatile strategy for combining the structural stability of alginate with the functional properties of the encapsulated materials, resulting in composites that are efficient, recoverable, and sustainable for environmental remediation.

Recent research has focused on composite materials that combine alginate with functional nanomaterials such as carbon nitride (g-C_3N_4) to further enhance adsorption and catalytic performance. In these systems, g-C_3N_4 is dispersed in sodium alginate, followed by gelation in calcium ion solutions to form Alg-CNBs (alginate-carbon nitride beads). These beads can then be treated with metal salts and reduced using $NaBH_4$ to produce composites enriched with zero-valent metals (Ag^0, Ni^0, Fe^0, Cu^0). Such metal-functionalized beads exhibit catalytic activity for the degradation of hazardous organic pollutants, including dyes and nitrophenol derivatives. For example, Cu-containing beads (Cu / Alg-CNBs) efficiently catalyze the reduction of 4-nitrophenol (4-NP) to 4-aminophenol (4-AP) and degrade dyes such as methyl orange (MO) and congo red (CR). The performance of these composites depends on several parameters, including dye concentration, catalyst loading, and $NaBH_4$ dosage. Notably, Cu/Alg-CNBs achieved 97–99% reduction of 4-NP in gravity-driven column reactors, demonstrating scalability and robustness. Importantly,

these catalytic beads are simple to fabricate, reusable, and maintain high activity over multiple cycles, confirming their potential as sustainable and efficient materials for water purification and environmental remediation [101].

Wang et al. (2021) [193] synthesized magnetic sodium alginate (SA) based polyelectrolyte nanospheres via Ca^{2+} ion crosslinking reactions and electrostatic interactions between SA and amino modified Fe_3O_4 nanoparticles. They characterized and discussed the chemical structure, surface properties and morphology of the new magnetic polyelectrolyte. The tests and modelling of the Pb(II) adsorption were conducted, and the recovery performance was evaluated. Isothermal adsorption curves were drawn to determine the maximum Pb(II) ion adsorption content. Based on ion uptake, the thermodynamic characteristics of the adsorbent were investigated by modelling of the adsorption curves. Freundlich and Langmuir models were used for deriving the adsorption isotherms. Micromorphology of the magnetic nanoparticles (MNPs), amino-based magnetic nanoparticles (AM), and magnetic SA-based polyelectrolyte nanosphere (SA@AM) were investigated by TEM. The MNPs were spherical and uniform in size, and those particles tended to be clustered. The surface of 3-amnopropyl-trimethoxysilane (APTES) modified nanosphere (AM) become compact, irregular, and amorphous, with MNP cores darker because of their high electron density. It was proved that APTES was successfully grafted onto the MNPs for yielding AMs. Regular circular nanosphere were detected by TEM for the SA@AM, possessing smooth surfaces and uniform sizes ranged between 15 and 22 nm. According to the BET analysis, the surface areas of the products MNP, AM, and SA@AM were 58.72, 72.69 and 104.85 m2/g, respectively. Compared with the original magnetic particles MNP, the specific surface area of the final product SA@AM was greatly increased, and the chance of contact with ions higher, which provides more opportunities for ion coordination and chelation. Therefore, the adsorption capacity was improved. Concerning the adsorption capacity of SA@AM for Pb(II), it was increased by 50.1% compared to the SA control without MNP core. Through the comparison of Pb(II) adsorption with other magnetic adsorbents, it was learned that, in this case, it was much higher than the others, i.e. from 20% to 150%. This was probably due to the abundant surface groups (-COO and -OH) from the SA shells, which could strongly adsorb Pb(II) ions. Further studies demonstrated that the Langmuir model well fits the Pb(II) isothermal adsorption of SA@AM and showed a pseudo second-order for its kinetic adsorption. Using the Langmuir linear fitting results, the SA@AM demonstrated maximum Pb(II) adsorption capacity at 105.8 mg/g. The equilibrium Pb(II) adsorption of SA@AM was 91.7 mg/g, which was 47.0% higher than that of SA (62.4 mg/g), demonstrating a great enhancement after the SAs being coated onto MNPs. The magnetic sodium alginate polyelectrolyte microspheres have good magnetic separation performance, which resulted from the modified magnetic particles coated in the sodium alginate micro-spheres. With the increase of adsorption-desorption cycles, the adsorption performance was gradually decreased from 92.3% (first cycle) to 77.3% (fifth cycle). It was confirmed that the recycling performance of SA@AM was good, benefiting the repeated adsorption of heavy metal ions. This research can provide a reference for the subsequent development of magnetic adsorption materials.

Wang et al. (2020) [194] synthetised a novel bio-adsorbent hydrogel composite named SA-PAM/GO through free radical polymerization. Under optimal conditions, the maximum adsorption capacity of Cu(II) and Pb(II) were 68.76 mg/g and 240.69 mg/g, respectively. In addition, the kinetics and isotherms displayed that the pseudo-second-order kinetic model and the Langmuir

isotherm model fitted the data well. Chemical adsorption accompanying the ion exchange process was confirmed as the principal adsorption mechanism. Furthermore, the adsorbent still maintained good adsorption capacity after 5 cycles of adsorption-regeneration. Therefore, the SA-PAM/GO hydrogel composites have potential to be applied in the removal of heavy metal ions from water bodies effectively.

Table 2.2 summarizes representative alginate-based adsorbents that have been investigated for the removal of various heavy metals from aqueous solutions, reporting their maximum adsorption capacities under different experimental conditions.

Table 2.2: Adsorption capacities of alginate-based adsorbents for the removal of heavy metals from aqueous solutions.

Adsorbent	**Metal ion**	**pH**	q_{max} **(mg g^{-1})**	**Ref.**
Magnetic alginate beads	Pb(II)	2.3–6	93.5	[195]
Carboxylated cellulose nanocrystal/-sodium alginate hydrogel beads	Pb(II)	5	838.98	[196]
Silica nanoparticles/alginate composite	Pb(II)	5	113.34	[197]
Iron-oxide modified sericite alginate beads	As(V)	5	261.61	[181]
Activated carbon–alginate composite	Hg(II)	6	35.85	[198]
Phosphate-embedded calcium alginate beads	Pb(II)	5	15.7	[199]
Tetraethylenepentamine functionalized alginate beads	Pb(II)	4.2	234.77	[200]
Chitosan coated calcium alginate	Cr(VI)	2	76.92	[201]
Glycine-functionalized magnetic nanoparticles entrapped calcium alginate beads	Pb(II)	5	108.4	[202]
Silica modified calcium alginate–xanthan gum hybrid bead	Pb(II)	5	555.5	[203]
Alginate–calcium carbonate composite	Pb(II)	5	18.9	[204]
Halloysite/alginate nanocomposite beads	Cu(II)	3	10.2	[205]
Alginate–carboxymethylcellulose gel beads	Pb(II)	3	325	[206]
Alginate graft polyacrylonitrile beads	Pb(II)	4	270.3	[207]
Alginate–graphene oxide hybrid gel beads	Cd(II)	4	454	[208]
Magnetite graphene oxide encapsulated in alginate beads	Pb(II)	4	609	[209]
Montmorillonite/alginate composite	Cd(II)	4	247.16	[210]
Activated carbon–alginate	Sr(II)	7	45.65	[211]
ZrO_2/alginate bentonite	Cu(II)	5	90.1	[212]
Graphite nano carbon/alginate	Pb(II)	6	60.99	[213]
Alginate/hydroxyapatite/carbon nanotube	Pb(II)	5	86.9	[214]
Titania-coated silica/alginate	Pb(II)	6	120	[215]

Table 2.2 (continued)

Adsorbent	Metal ion	pH	q_{max} (mg g^{-1})	Ref.
Sodium alginate/graphene oxide composite	Pb(II)	6	227.1	[216]
Chitosan microspheres/sodium alginate hybrid beads	Hg(II)	5	217.39	[217]
–	Cr(VI)	2	218.4	[218]

Chemical alginate modification and chemical cross-linking Sodium alginate (SA) contains abundant hydroxyl and carboxyl functional groups, which offer versatile sites for chemical modification [219, 181, 220]. Through suitable reactions, new functionalities such as amides, imines, and hydrazones can be introduced [221]. In particular, hydrazone moieties are well known for their strong and selective coordination ability towards a wide range of metal ions, which makes them attractive for environmental applications. Hydrazide-based modifications have already been reported for several natural polymers, including guar gum [222, 223, 224], cellulose [225], and chitosan [226], showing promising performance in the removal of dyes, heavy metal ions, and oily wastewater.

In this context, Shi *et al.* [227] reported the synthesis of hydrazide-modified sodium alginate (denoted as DSA-AAD@Ca^{2+}). The material was prepared by dehydrative condensation of adipic acid dihydrazide (AAD) with dialdehyde sodium alginate (DSA) through Schiff-base formation. This modification strategy plays a dual role: on the one hand, it introduces hydrazone groups capable of efficiently coordinating with heavy metal ions, and on the other hand, it grafts dihydrazide moieties onto the alginate backbone, which increases the molecular weight and reduces water solubility. In addition, Ca^{2+} ions act as secondary cross-linkers by exchanging with sodium ions in the alginate matrix, further stabilizing the structure and contributing to the ion-exchange removal of heavy metals from aqueous solution. The adsorption process of DSA-AAD@Ca^{2+} was well described by the Freundlich isotherm model and followed pseudo-second-order kinetics. The equilibrium adsorption capacities for Hg^{2+}, Pb^{2+}, Cd^{2+}, and Cu^{2+} were 7.833, 2.036, 4.766, and 3.937 mmol g^{-1}, respectively, while the maximum adsorption capacities reached 8.633, 1.968, 5.062, and 4.068 mmol g^{-1}, respectively.

Shi *et al.* [228] reported the preparation of biphthalate dihydrazide–modified sodium alginate (DSA-BDD@Ca^{2+}) using biphthalate dihydrazide (BDD) and dialdehyde sodium alginate (DSA) to introduce functional hydrazone structures capable of sensitively capturing heavy metal ions. The maximum adsorption capacities based on chemical and monolayer adsorption were determined as 668.42, 472.37, and 200.10 mg g^{-1} for Pb^{2+}, Cd^{2+}, and Cu^{2+}, respectively. The adsorption data conformed to a pseudo-second-order kinetic model, with the rate-determining step attributed to the interaction between the adsorbate and the surface adsorption sites. Thermodynamic analysis indicated that the adsorption process was both endothermic and spontaneous under ambient conditions. The highly effective and selective removal of Pb^{2+}, Cd^{2+}, and Cu^{2+} was facilitated by a combination of ion exchange, chelation via hydrazone groups, and electrostatic interactions, with hydrazone coordination confirmed as a key mechanism through DFT calculations. These results demonstrate that hydrazone-modified sodium alginate, using rigid carbon-chain dihydrazides,

represents a promising strategy for the practical removal of heavy metal ions from wastewater.

Huang *et al.* [219] reported the preparation and characterization of Ethylenediamine-Modified Calcium Alginate Aerogel (ECAA) beads, obtained by freeze-drying using a lyophilizer. The beads were applied for the adsorption of Pb^{2+} and Cu^{2+}, showing rapid removal of both metal ions with maximum adsorption capacities of 219.3 mg g^{-1} for Pb^{2+} and 87.83 mg g^{-1} for Cu^{2+}. The adsorption kinetics followed a pseudo-second-order model, while the equilibrium data fitted the Langmuir isotherm, indicating monolayer adsorption. Further insights from X-ray photoelectron spectroscopy (XPS) and regeneration studies suggested that the adsorption mechanism involved a combination of complexation and cation-exchange processes.

Cordova *et al.* [229] reported the successful two-step chemical modification of alginate (Alg) using thiosemicarbazide (TSC), producing a new material denoted as AlgOx–TSC. The synthesis involved first partially oxidizing Alg with sodium periodate ($NaIO_4$) to obtain oxidized alginate (AlgOx), followed by reacting AlgOx with TSC at 40–45 °C in the presence of sodium borohydride ($NaBH_4$). Although the primary aim of TSC incorporation was to introduce sulphur atoms capable of coordinating Pb^{2+} ions, characterization revealed that the carboxylate groups of alginate played the main role in Pb^{2+} sorption. Nonetheless, the TSC modification proved crucial for enhancing metal ion uptake, likely acting as a crosslinking agent between polymeric chains, which improved the accessibility of carboxylate groups for binding. AlgOx–TSC exhibited high sorption capacities, reaching a maximum adsorption of 950 mg g^{-1} for Pb^{2+} at pH 3 and 300 mg g^{-1} for Cd^{2+} at pH 7. The detailed characterization of alginate and its derivatives provided insights into the sorption behavior, confirming that despite the presence of TSC, carboxylate groups remained the principal active sites for Pb^{2+} removal.

3 Preparation of Alginate-based Nanoadsorbents

In this section, the preparation of magnetite nanoparticles (MNPs), the development of magnetic nanostructured adsorbents (MNAs), and their incorporation into alginate beads are described. The starting point was the synthesis of Fe_3O_4 nanoparticles by a coprecipitation route, which provided stable magnetic particles with good dispersion in aqueous media. Building on this system, MNAs were subsequently obtained by carrying out the same coprecipitation in the presence of graphene oxide (GO), so that Fe_3O_4 nanoparticles nucleated and grew directly on the GO sheets. This procedure yielded hybrid nanocomposites combining the large surface area and functional groups of GO with the magnetic properties of Fe_3O_4, thus improving their potential adsorption capacity. To facilitate handling and recovery, both MNPs and MNAs were embedded in sodium alginate hydrogels, resulting in the formation of three types of beads. The first system, named BGO, consisted of alginate beads containing GO nanosheets decorated with Fe_3O_4 nanoparticles. In parallel, two additional bead types, B1 and B2, were prepared using only Fe_3O_4 nanoparticles; their difference lies in the Ca^{2+} concentration employed during the cross-linking step, which was adjusted to modulate beads structural properties. The overall preparation process is schematically illustrated in Figure 3.1, which shows the synthesis of magnetic materials, their dispersion in alginate solution, and the final gelation into spherical beads.

This sequential approach, starting from simple MNPs, progressing to GO-based MNAs, and culminating in the formation of alginate beads, provides a rational strategy for the development of scalable, efficient, and reusable adsorbents for water treatment applications. In the following sections, the experimental procedures, material characterization, and adsorption tests are presented in detail.

3.1 Materials and method

3.1.1 Analytical techniques

Transmission electron microscopy (TEM) analysis

The morphology and microstructure of the samples were characterized by transmission electron microscopy (TEM) and high-angle annular dark-field (HAADF) scanning transmission electron microscopy (HAADF-STEM) using TEM JEOL F200 operated at 200 kV. Elemental analysis and mapping were performed using a JEOL 100 mm^2 silicon drift energy dispersive X-ray spectrometer (EDX). Carbon supported copper grids, 400 mesh size, were used for the preparation of the sample. All measurements were performed at the Department of Chemical Science (DISC) of the University of Padua by Dr. Andrea Basagni.

Environmental Scanning Electron Microscopy (ESEM) analysis

Environmental Scanning Electron Microscopy (ESEM) analysis was performed using a *FEI Quanta 200* variable pressure environmental scanning electron microscope, equipped with a backscattered electron (BSE) detector and an energy dispersive X-ray spectroscopy (EDX) system (EDAX

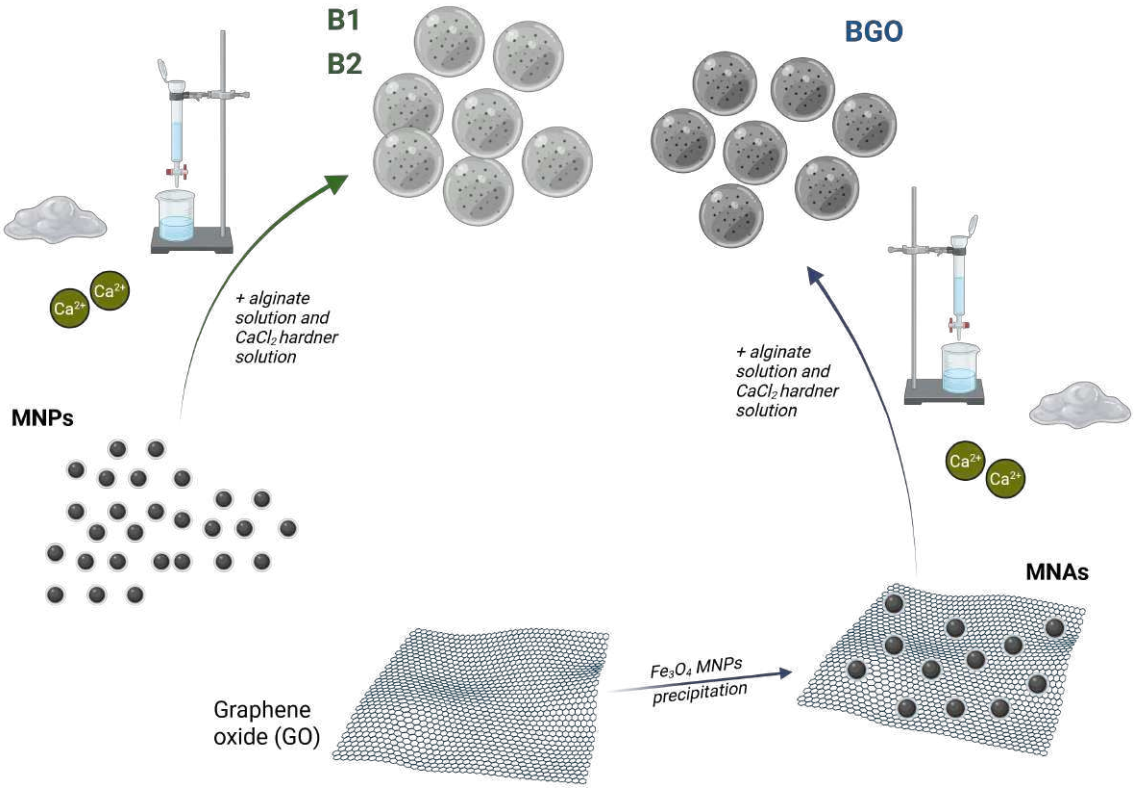

Figure 3.1: Beads preparation: (i) preparation of GO nanosheets decorated with magnetic nanoparticles by coprecipitation; (ii) mixing of magnetic materials (MNPs or MNAs) with dissolved sodium alginate; (iii) formation of the beads by cross-linking with a Ca^{2+} solution

Table 3.1: Materials used

Material	**Chemical formula**	**Purity**	**Producer**
Ammonium hydroxide	NH_4OH	28–30%	Sigma-Aldrich
Calcium chloride dihydrate	$CaCl_2 \cdot 2\,H_2O$	98%	Normapur
Cobalt(II) chloride hexahydrate	$CoCl_2 \cdot 6\,H_2O$	98%	Sigma-Aldrich
Chromium(III) chloride	$CrCl_3 \cdot 6\,H_2O$	99%	Sigma-Aldrich
Copper(II) chloride dihydrate	$CuCl_2 \cdot 2\,H_2O$	98%	Carlo Erba
Copper(II) nitrate trihydrate	$Cu(NO_3)_2 \cdot 3\,H_2O$	99%	Sigma-Aldrich
Copper(II) sulfate pentahydrate	$CuSO_4 \cdot 5\,H_2O$	99%	Sigma-Aldrich
Dichloromethane	CH_2Cl_2	>=99.8%	Honeywell
2,6-Pyridinedicarboxylate dichloride	$C_7H_3Cl_2NO_2$	97%	Sigma-Aldrich
Ethanol	C_2H_6O	>99.8%	Scharlau
Expanded graphite	–	–	ECOPHIT
Hydrazine monohydrate	$NH_2NH_2 \cdot H_2O$	98%	Sigma-Aldrich
Hydrochloric acid	HCl	37%	Sigma-Aldrich
Iron(II) chloride tetrahydrate	$FeCl_2 \cdot 4\,H_2O$	>=99%	Sigma-Aldrich
Iron(III) chloride hexahydrate	$FeCl_3 \cdot 6\,H_2O$	>=99%	Honeywell Fluka
Isophthaloyl chloride	$C_7H_3Cl_2NO_2$	>=99%	Sigma-Aldrich
Malonyl chloride	$CH_2(COCl)_2$	97%	Sigma-Aldrich
Methanol, anhydrous	CH_3OH	99.8%	Sigma-Aldrich
Methanol	CH_3OH	>=99.8%	Honeywell
Nickel(II) chloride hexahydrate	$NiCl_2 \cdot 6\,H_2O$	99%	Sigma-Aldrich
Potassium permanganate	$KMnO_4$	>=99%	Sigma-Aldrich
Sodium alginate	$(C_6H_7O_6Na)n$	90.8–106%	BioChemica
Sodium periodate	$NaIO_4$	>=99.8%	Sigma-Aldrich
Sulfuric acid	H_2SO_4	98%	Sigma-Aldrich
Tetrahydrofuran	C_4H_8O	>=99.9%	Sigma-Aldrich
Triethylamine	$C_6H_{15}N$	Analytical grade	Scharlau

Element-C2B). The instrument was operated under variable pressure conditions, allowing for the direct observation of non-conductive solid samples without the need for conductive coating. The BSE detector provided compositional contrast based on atomic number differences, while the EDX detector enabled elemental analysis and mapping of the sample surfaces. Elemental compositions were obtained by collecting EDX spectra from selected regions of interest (ROIs). All measurements were carried out under optimized accelerating voltages (typically 15–20 kV), ensuring adequate spatial resolution and elemental sensitivity. These combined techniques allowed for the morphological and semi-quantitative elemental characterization of the powder samples. All measurements were performed at Centro di Analisi e Servizi per la Certificazione (CEASC - UniPd) of the University of Padua by Dr. Federico Zorzi.

Magnetic measurements

The magnetic characterization of the samples was performed by means of a Physical Properties Measurement System (PPMS) by Quantum Design equipped with a Vibrating Sample Magnetometer (VSM). The PPMS has a superconductor magnet that reaches a DC magnetic field of 90,000 Oe and can perform measurements in a temperature range from 1.9 K to 400 K. The samples were characterized by studying the magnetization as a function of both the applied DC field, $M(H)$, and temperature, $M(T)$. The $M(H)$ curves were measured at 300 K and 5 K by varying the applied field from 0 Oe to 90,000 Oe, then by looping it from 90,000 Oe to $-90,000$ Oe and back to 90,000 Oe. The $M(T)$ measurements were performed with an applied DC field of 100 Oe and by varying the temperature from 5 K to 300 K. Before both measurements, the trapped field in the superconductor magnet was reduced by following the procedure described in reference. The $M(T)$ curves were acquired with both Zero Field Cooling (ZFC) and Field Cooling (FC) protocols. For the ZFC protocol, the temperature was reduced after field zeroing, then a magnetic field of 100 Oe was applied, and the magnetization was measured by increasing the temperature to 300 K. Once 300 K was reached, to follow the FC protocol, the magnetization was acquired by reducing the temperature to 5 K without turning off the applied field [230]. All measurements were performed at the Department of Physics of the University of Salerno by Professor Massimiliano Polichetti.

Inductively Coupled Plasma Optical Emission Spectroscopy (ICP) analysis

Ion oncentration measurements were carried out by Inductively Coupled Plasma Optical Emission Spectroscopy (ICP-OES) using a Perkin Elmer Optima 4200DV (Perkin Elmer Italia S.p.A., Milano, Italy). The aqueous samples were diluted with ultrapure water and acidified with ultrapure nitric acid to ensure the stability of metal ions in solution. The instrument operates with a radio-frequency generated argon plasma, which excites the analyte atoms and ions, producing characteristic optical emission lines. The emitted radiation was dispersed by the spectrometer of the Optima 4200DV and detected at element-specific wavelengths, allowing quantitative determination of metal concentrations after calibration with certified multi-element standard solutions. The measurements were performed at the Department of Environmental Engineering of the University of Padua by Dr. Sabrina Copelli.

3.2 Experimental - Preparation of Magnetic Nanoadsorbents (MNAs)

The MNAs were synthesized through a low-cost coprecipitation process involving iron(II/III) salts (e.g. chlorides), ammonium hydroxide solutions, and graphene oxide (GO), which was obtained from graphite by a modified Hummers' method at room temperature (Figure 3.2). The morphology and size of the materials were examined by transmission electron microscopy (TEM). The adsorbents were tested against different metal ions, such as copper(II), chromium(III), and nickel(II). Metal ions concentrations were determined by inductively coupled plasma optical emission spectroscopy (ICP-OES), and adsorption isotherms were determinated. The main advantage of the proposed system, compared to other state-of-the-art carbon-based adsorbents [56], lies in the use of a very simple synthetic procedure that employs GO and nanoparticles (NPs) without further functionalization. While additional functionalization can impart specific affinity toward certain heavy metals, it also increases the complexity of the synthesis and limits its scalability [231].

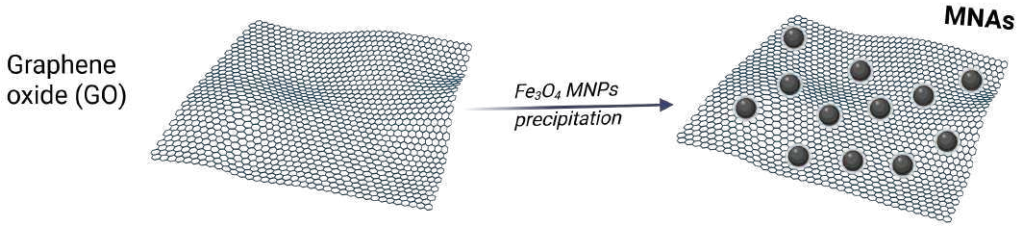

Figure 3.2: General scheme of MNAs preparation

3.2.1 Sinthesis of Graphene Oxide (GO)

The graphene oxide was obtained through a modified Sun method, based on [232]. 5 g of expanded graphite and 15 g of potassium permanganate powders were mixed and stirred in a beaker until homogeneity. The beaker was placed in an ice bath, adding slowly and under vigorous mechanical stirring 100 mL of $H_2{\cdot}SO_4$ until a petrol-dark green liquid sludge was obtained. The system was left reach room temperature under continuous stirring for about 30 min, until a foam-like material was formed. The beaker was placed again in the ice bath, and 400 mL of distilled water was added very slowly to avoid any uncontrolled temperature increase. The liquid was then placed in a 90°C water bath for 1 h and a dark suspension was obtained. The suspension was filtered on paper in a Buchner funnel and washed subsequently with 500 mL of distilled water, 200 mL of HCl for removing any manganese traces, and finally again with 500 mL of distilled water to reach neutrality.

3.2.2 Synthesis of Magnetite Nanoparticles (MNPs)

Magnetite nanoparticles were synthetised through a coprecipitation method based on [233], starting from iron salts in basic conditions. Making use of both Fe(II) and Fe(III) chlorides, the coprecipitation requires that the two salts are in the stoichiometric proportion 2:1 (Fe(III)/Fe(II)). Their mixing has to be carried out in aqueous solution, without oxygen to avoid Fe(II) oxidation,

with the successive precipitation in presence of a strong base. In an example, 1.03 g of $FeCl_2 \cdot 4H_2O$ and 2.78 g of $FeCl_3 \cdot 6H_2O$ were mixed in a 250 mL balloon with two necks under N_2 atmosphere. The solution obtained adding 100 mL of water was magnetically stirred for 20 minutes until the dissolution of the iron salts. Under a nitrogen flow, 12 mL of ammonia hydroxide (25% in water) were added in order to increase rapidly the pH over 11 and provoke the precipitation of Fe_3O_4. The mixture was left stirring at ambient temperature, for 1 h. The equation of the reaction that describes the formation of magnetite, starting from the iron (II/III) chlorides with NH_4OH as precipitating agent, is:

$$2\,FeCl_3 + FeCl_2 + 8\,NH_4OH \longrightarrow Fe_3O_4 + 4\,H_2O + 8\,NH_4Cl$$

Successively, the magnetic stirring was stopped, and the system was left decanting over a permanent magnet, for 1 h. The supernatant was removed with a pipette and the nanoparticles were washed with deionized water for three times and separated every time by centrifugation (80000 rpm per 5 min two times and 80000 rpm per 15 min). After two more washings with ethanol (8000 rpm for 15 min and for 5 min), the product was dried in a desiccator.

3.2.3 Production of Magnetic Nanoadsorbents (MNAs)

The magnetic nanoadsorbents of Fe_3O_4–NPs-decorated GO are prepared by a simple coprecipitation method in the presence of graphene oxide. Figure 3.3 schematically reports the MNAs production procedure. In a typical procedure, 0.340 g of $FeCl_2 \cdot 4H_2O$ and 0.965 g of $FeCl_3 \cdot 6H_2O$ (resulting in 0.350 g of Fe_3O_4) were mixed with 5 mL of GO suspension (10 g/L, 50 mg) in 50 mL of distilled water. The mixture was stirred for 30 min at room temperature to completely dissolve the iron salts and then treated with 7 mL of NH_4OH solution (25% in water) under vigorous stirring, to rapidly increase the pH to 11. After 1 h of continuous stirring, the nanocomposite was magnetically separated from the solution, washed with distilled water until neutrality, then with ethanol to remove the water and dried under vacuum.

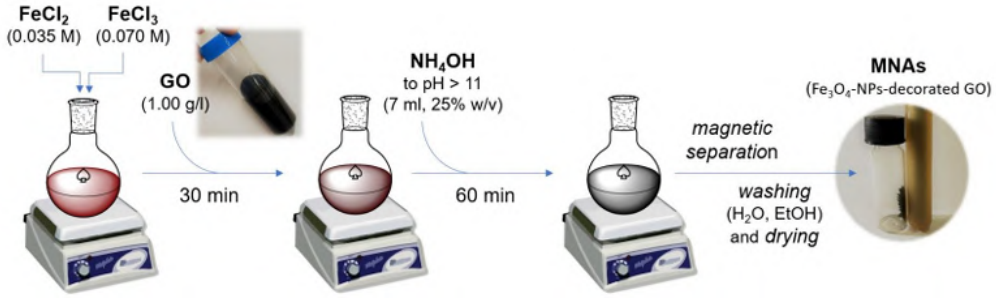

Figure 3.3: MNAs production procedure

As detailed in Section 3.1.1, all the magnetic nanomaterials were characterized in terms of morphology, using Transmission Electron Microscopy (TEM) and Environmental Scanning Electron Microscopy (ESEM) analyses, as well as in terms of their magnetic properties.

3.2.4 Adsorption tests

The MNAs developed were tested with three different heavy metal ions:

- Cu^{2+} (copper(II) sulphate, $CuSO_4 \cdot 5H_2O$)
- Ni^{2+} (nickel(II) chloride, $NiCl_2 \cdot 6H_2O$)
- Cr^{3+} (chromium(III) chloride, $CrCl_3 \cdot 6H_2O$)

Such pollutants are typical of the textile industry, and they are subject of many recent literature works [234, 235, 236]. MNAs were tested with different sets of concentrations. In particular, for chromium(III) 500, 600, 1000, 2000, and 5000 $\mu g\,L^{-1}$ concentrations were tested; for copper(II) 300, 500, 700, 1000, 2000, and 6000 $\mu g\,L^{-1}$ concentrations were tested; and, finally, for nickel(II) 1000, 2000, 4000, and 5000 $\mu g\,L^{-1}$ concentrations were used. These concentrations were chosen to reflect those typically found in textile industry wastewaters, which also accounts for the non-standardized range of the values tested. Tests were performed in a stirred lab glass flask (100 mL nominal volume for chromium and 50 mL for nickel and copper) at 298 K. Keeping stirring speed as low as possible is an important aspect, as MNAs structure may be compromised by an excessive mechanical stress. For chromium tests, 50 mL of solution was used. For nickel and copper, 20 mL of solution was treated. MNAs content was 1 $g\,L^{-1}$ for each test. After loading the MNAs in the solution, the vessel was kept at 298 K and stirred for 30 min. MNAs separation was finally carried out by using a classic neodymium magnet. The treated liquid was also filtered to eliminate the eventual traces of adsorbents. Each test was performed according to the following protocol: (a) preparation of the solution at the target concentration, (b) preparation of the blank sample for the starting concentration measurement, (c) loading of MNAs, (d) stirring at 100 rpm for 30 min (to ensure reaching the equilibrium of adsorption), (e) separation of MNAs (magnet + filtration) and (f) preparation of the sample for final concentration measurement. Finally, the removal efficiency was determined in six mixtures obtained mixing the three ions at different concentrations. For each mixture 20 mL of solution was treated as for the tests of single ion solutions, using MNAs at 1 $mg\,L^{-1}$.

3.2.5 Adsorption isotherm

Based on the difference between initial and final ion concentrations, the corresponding adsorption isotherms were constructed. All adsorption parameters were derived from the experimental data using a Langmuir model, which is expected to provide a reliable description of the adsorption process, even though the model was originally developed for gas adsorption on solid surfaces, such as activated carbons. According to Langmuir theory, adsorption onto a solid surface is governed by a kinetic principle in which molecules continuously collide with the surface and desorb (or evaporate) from it, resulting in a net zero accumulation rate at equilibrium. In practical terms, the rates of adsorption and desorption are equal under equilibrium conditions. This adsorption model is highly versatile and can be readily extended to characterize various adsorption processes, including the adsorption of metal ions from aqueous solutions onto MNAs.

The standard Langmuir isotherm model is usually described by Equation 3.1.

$$\eta_{\mathrm{end}} = \frac{Q_{\max} \cdot K_L \cdot C_{\mathrm{end}}}{1 + K_L \cdot C_{\mathrm{end}}} \tag{3.1}$$

where $Q_{\max}$ and K_L are constants, C_{end} is the equilibrium concentration of the chemical to be removed from the fluid phase and η_{end} is the equilibrium load of the same compound onto the adsorbent. Anyway, obtaining effective equilibrium conditions (both for fluid and solid phases) is difficult to be achieved experimentally inside a batch system, as it requires a constant concentration in the fluid phase until the reaching of the maximum load onto the solid phase at that compound concentration. Due to this fact, alternative definitions of the equilibrium load are found in the literature for analogous systems, where the initial pollutant concentration lowered overtime until the equilibrium with the adsorbent was reached.

Particularly, referring to the adsorption of a generic i-th metal ion on MNAs dispersed into an aqueous solution, Equation 3.1 can be modified as follows 3.2 [237]:

$$\eta_{\mathrm{end},i} = \frac{Q_{\max,i} \cdot K_{L,i} \cdot C_{0,i}}{1 + K_{L,i} \cdot C_{0,i}} = \frac{(C_{\mathrm{end},i} - C_{0,i}) \cdot V_{\mathrm{sol}}}{m_{\mathrm{MNAs},i}} \tag{3.2}$$

where $Q_{\max,i}$ and $K_{L,i}$ are constants, $C_{0,i}$ represents the initial concentration of the metal ion(s) (µmol/L) into the analyzed solution (fluid phase), $C_{\mathrm{end},i}$ is the concentration of the metal ion(s) in the fluid phase at the end of the treatment, V_{sol} is the volume of the aqueous solution (L), $m_{\mathrm{MNAs},i}$ is the mass of MNAs used for a single treatment (mg), and $\eta_{\mathrm{end},i}$ is the final load of metal ion(s) which is adsorbed onto the MNAs (µmol/mg).

The removal (or adsorption) efficiency, χ, can be therefore evaluated using 3.3:

$$X_i = \frac{C_{0,i} - C_{\mathrm{end},i}}{C_{0,i}} \tag{3.3}$$

Isotherm-specific parameters were optimized using a modified non-dominated sorting genetic algorithm (NSGA-II) [238], which incorporates periodic migration of sub-populations. The design variables, $Q_{\max}$ and K_L, are the Langmuir coefficients in equation 3.2. Two objective functions equation 3.4 and equation 3.5 were minimized:

$$f_1 = \sum_{i=1}^{N} \Big(X_{m,i}([C_{0,i}]) - X_{f,i}([C_{0,i}]) \Big)^2 \tag{3.4}$$

$$f_2 = \max_{i=1,\ldots,N} \Big| X_{m,i}([C_{0,i}]) - X_{f,i}([C_{0,i}]) \tag{3.5}$$

where X_m and X_f are the experimental and model-predicted values, respectively.

The initial population consisted of $N_i = 40$ individuals, which, combined with child populations generated from the two design variables ($N_d = 2$), produced up to $2N_i$ individuals. Selection retained the best 40 individuals based on f_1 and f_2, and the process was iterated for 200 generations. The resulting Pareto front represents the optimal solutions balancing the two objectives.

3.3 Results and discussion - Magnetic Nanoadsorbents (MNAs)

In the following section, the results concerning the characterization and the application of the MNAs are reported.

3.3.1 TEM analysis

The transmission electron microscopy (TEM) images (Figures 3.4 and 3.6) illustrate the morphological characteristics of the synthesized materials.

The magnetite (Fe_3O_4) nanoparticles in Figure 3.4 exhibit a nearly spherical to slightly polyhedral morphology. The particles are relatively uniform in size, with diameters predominantly in the range of 5–10 nm. However, a certain degree of agglomeration is observed, which can be attributed to magnetic dipole–dipole interactions and the high surface energy typical of nanoscale materials.

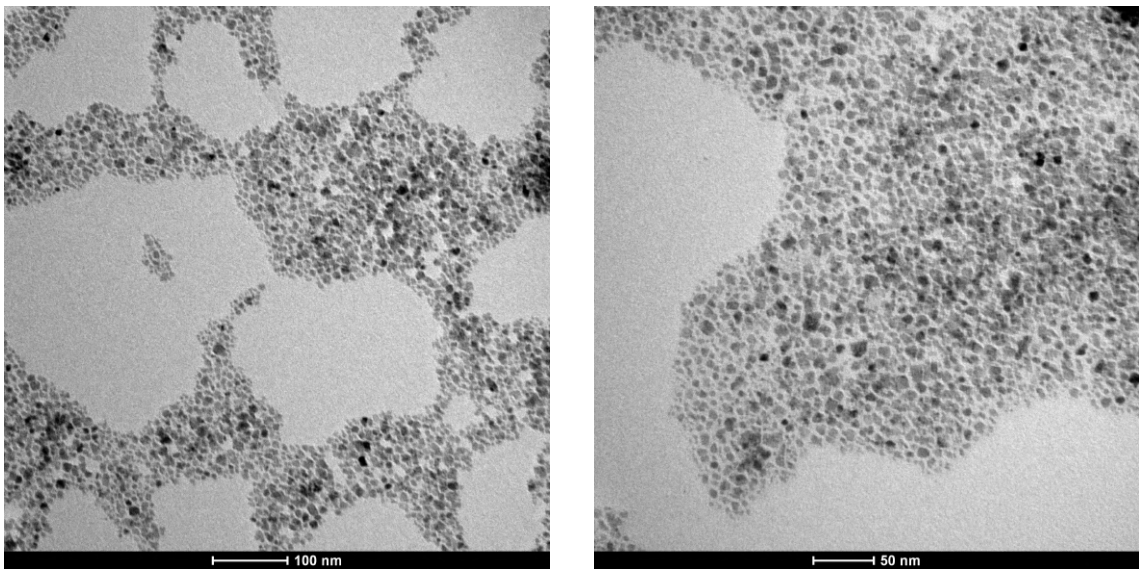

Figure 3.4: TEM images of MNPs at different magnification

Figure 3.5 shows the size distribution of the MNPs, which is centered at 7.2 nm with a standard deviation of 2.4 nm, based on measurements of approximately 300 individual particles.

TEM analysis of the magnetic nanocomposites (MNAs), composed of graphene oxide (GO) sheets decorated with magnetite nanoparticles (Figure 3.6), reveals a well-defined structural organization. The GO nanosheets exhibit irregular shapes with lateral dimensions of 200–500 nm, appearing as semi-transparent, wrinkled layers that serve as a two-dimensional support for the nanoparticles. Magnetite nanoparticles are attached to the GO sheets in small clusters, predominantly located near the sheet edges. Large areas of the GO surface remain uncovered, preserving accessible sites for adsorption. Thus, even if some agglomeration of the nanoparticles occurs, the GO matrix provides anchoring points that limit excessive clustering and enhance spatial stabilization of the composite structure.

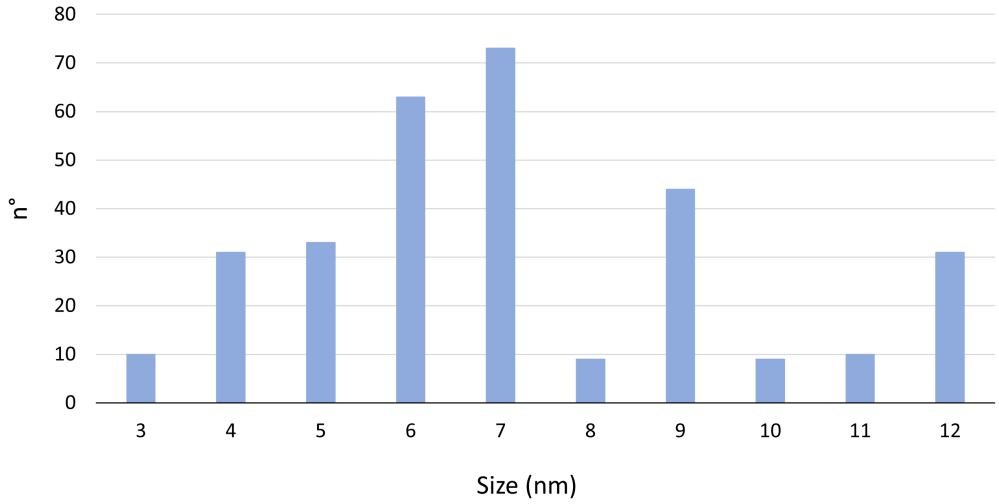

Figure 3.5: Size distribution of Fe_3O_4 magnetic nanoparticles

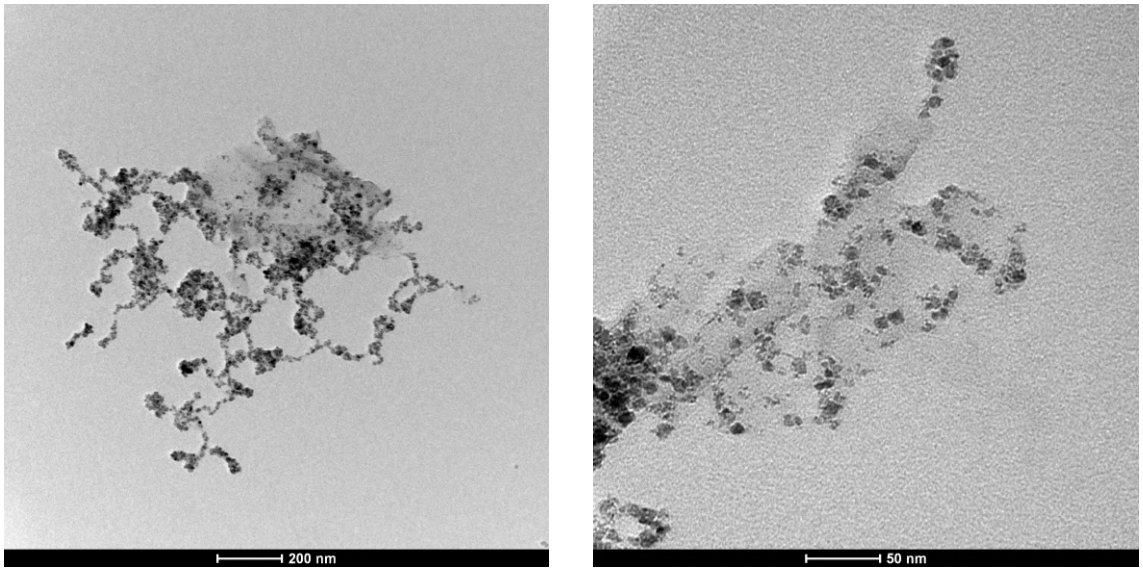

Figure 3.6: TEM images of MNAs at different magnification

These observations confirm the successful decoration of graphene oxide with magnetite nanoparticles and highlight the morphological differences between pure magnetite nanoparticles and their composite form.

3.3.2 Adsorption tests

The MNAs developed were tested for the adsorption of three heavy metal ions: copper(II), chromium(III) and nickel(II), which are commonly found in textile industry effluents. The experiments were carried out using different initial concentrations, selected to reflect typical levels in textile wastewater. All tests were performed in triplicate at 298 K, as described in Section 3.2.4.

Table 3.2 reports in details the results for chromium(III). With ion concentrations below 1100 $\mu g\,L^{-1}$, the adsorption efficiency was always above 0.97, showing that the equilibrium state was reached at higher removal-efficiency values. Above 1100 $\mu g\,L^{-1}$, χ decreased progressively till reaching values of less than 0.45 for 5000 $\mu g\,L^{-1}$ (where a maximum load of 2.23 mg/g was reached). Compared to other studies using different adsorbents [232, 234], the adsorption capacity observed in the present work was relatively low. However, those studies investigated much higher concentrations, up to 50 ppm, whereas the present work focused on concentrations up to 5 ppm. At lower concentrations, the driving force for mass transfer is reduced, which typically leads to lower adsorption capacities; therefore, the observed values are consistent with expectations under these conditions. In addition, all tests were performed at neutral pH, so it was not necessary to adjust it to achieve optimal adsorption.

Table 3.2: Concentrations, load, and removal efficiency for chromium(III) tests

Cr^{3+}	#1	#2	#3	#4	#5
C_0 [$\mu g\,L^{-1}$]	440±1	580±1	1060±10	1810±10	4990±10
C_{end} [$\mu g\,L^{-1}$]	10±1	10±1	17±1	370±1	2760±10
η_{end} [$mg\,g^{-1}$]	0.43	0.57	1.04	1.44	2.23
X [–]	0.977	0.983	0.984	0.796	0.447

For copper(II), the main results are reported in Table 3.3. Results were similar to chromium, but efficiency appeared to be lower at low starting concentrations. At 6.43 mg/L of Cu^{2+} concentration, the adsoprtion capacity was 4.56 mg/g, with a removal efficiency equal to 0.710. The adsorption capacity was comparable to other works [235], considering the neutral pH.

Table 3.3: Concentrations, load, and removal efficiency for copper(II) tests

Cu^{2+}	#1	#2	#3	#4	#5	#6
C_0 [$\mu g\,L^{-1}$]	296±1	501±1	690±1	1020±10	2000±10	6430±10
C_{end} [$\mu g\,L^{-1}$]	26±1	45±1	49±1	54±1	185±1	1865±10
η_{end} [$mg\,g^{-1}$]	0.27	0.46	0.64	0.97	1.81	4.56
X [–]	0.912	0.910	0.930	0.947	0.907	0.710

Finally, results for nickel(II) are reported in Table 3.4. Adsorption efficiency steadily increased with initial concentrations, with 0.914 at 935 $\mu g\,L^{-1}$ and 0.566 at 5120 $\mu g\,L^{-1}$ starting concentrations. The maximum load achieved of nickel (II) ions was found to be 2.90 mg/g, which was higher than that of chromium at similar starting concentrations. Even in this case, the results were similar to those reported in other works [235].

Table 3.4: Concentrations, load, and removal efficiency for nickel(II) tests

Ni^{2+}	#1	#2	#3	#4
C_0 [$\mu g\,L^{-1}$]	935±1	1900±10	3980±10	5120±10
C_{end} [$\mu g\,L^{-1}$]	80.4	298	1700	2220
η_{end} [$mg\,g^{-1}$]	0.85	1.60	2.28	2.90
X [–]	0.914	0.843	0.573	0.566

3.3.3 MNAs Isotherm Evaluation

For the selected ions, the isotherms were experimentally evaluated. This study was carried out in collaboration with the University of Insubria and with the contribution of Dr. Sabrina Copelli and Dr. Marco Barozzi. Based on the experimental results of adsorption efficiency, the parameters of Equation 3.2 were determined by solving the corresponding optimization problem. The Pareto fronts for the three analyzed elements (Cu, Ni, and Cr) were obtained using the NSGA-II algorithm and normalized to the maximum value of the objective function obtained by minimizing the functions in equations 3.4 and 3.5. Each point in the Pareto front corresponds to a specific set of design variable values, with the trade-offs among the design variables clearly represented. The values of two selected design variables are reported in Table 3.5 and were used to fit the experimental data using the Langmuir adsorption model. The Langmuir function showed excellent agreement with the experimental results, with the minimizing function f_1 always below 2×10^5. The correlation coefficients were consistently equal to or greater than 0.99, confirming the suitability of the Langmuir model to describe a single-layer adsorption process. The maximum monolayer adsorption capacities ranged between 3.42 and 31.3 mg/g of MNAs, with the highest adsorption load observed for copper(II), indicating a particularly strong affinity of the nanoparticles for this ion.

Figure 3.7 shows the fitting of the experimental data with the Langmuir isotherm. The results, consistent with the Langmuir hypothesis, highlight monolayer adsorption as the dominant mechanism for the tested adsorbent. According to these results, it is reasonable to assume that the copper adsorption capacity could further increase at higher concentration values.

As a preliminary validation of the reliability of the previously proposed isotherms, six different mixtures containing the three tested ions were prepared. Table 3.6, Table 3.7, Table 3.8 summarize the initial composition of the mixtures and the results obtained after treatment with 1 mg/mL of MNAs.

A comparison between the experimental data (see Table 3.6, Table 3.7, Table 3.8) and the values predicted for the ion load on our MNAs was carried out. All the equilibrium loads, previously

Table 3.5: Langmuir and fitting parameters from NSGA-II optimization algorithm for the investigated ions

	Cr^{3+}	**Cu^{2+}**	**Ni^{2+}**
Q_{max} [mg/g(MNA)]	3.42	31.3	5.45
K_L [L/mg]	0.38	2.75×10^{-2}	0.20
f_1	3.92×10^{-6}	1.74×10^{-5}	1.39×10^{-5}
f_2	1.21×10^{-3}	2.86×10^{-3}	2.44×10^{-3}
R^2	0.9978	0.9987	0.9900

Table 3.6: Removal and equilibrium load for mixed solutions (tests #1–#2)

	#1			**#2**		
	Cr^{3+}	Cu^{2+}	Ni^{2+}	Cr^{3+}	Cu^{2+}	Ni^{2+}
C_0 [µg L^{-1}]	430±1	293±1	937±1	1830±10	316±1	1030±10
η_{end} [mg g^{-1}]	0.42	0.63	0.81	1.625	0.140	0.665
X [–]	0.977	0.927	0.859	0.888	0.809	0.645

Table 3.7: Removal and equilibrium load for mixed solutions (tests #3–#4)

	#3			**#4**		
	Cr^{3+}	Cu^{2+}	Ni^{2+}	Cr^{3+}	Cu^{2+}	Ni^{2+}
C_0 [µg L^{-1}]	1860±10	500±1	1850±10	4540±10	1050±10	5090±10
η_{end} [mg g^{-1}]	1.51	0.222	0.997	2.06	0.157	0.85
X [–]	0.812	0.827	0.539	0.454	0.680	0.167

Table 3.8: Removal and equilibrium load for mixed solutions (tests #5–#6)

	#5			**#6**		
	Cr^{3+}	Cu^{2+}	Ni^{2+}	Cr^{3+}	Cu^{2+}	Ni^{2+}
C_0 [µg L^{-1}]	4690±10	317±1	1060±10	1830±10	987±1	5100±10
η_{end} [mg g^{-1}]	2.25	0.052	0.354	1.55	0.461	1.45
X [–]	0.480	0.769	0.334	0.849	0.854	0.284

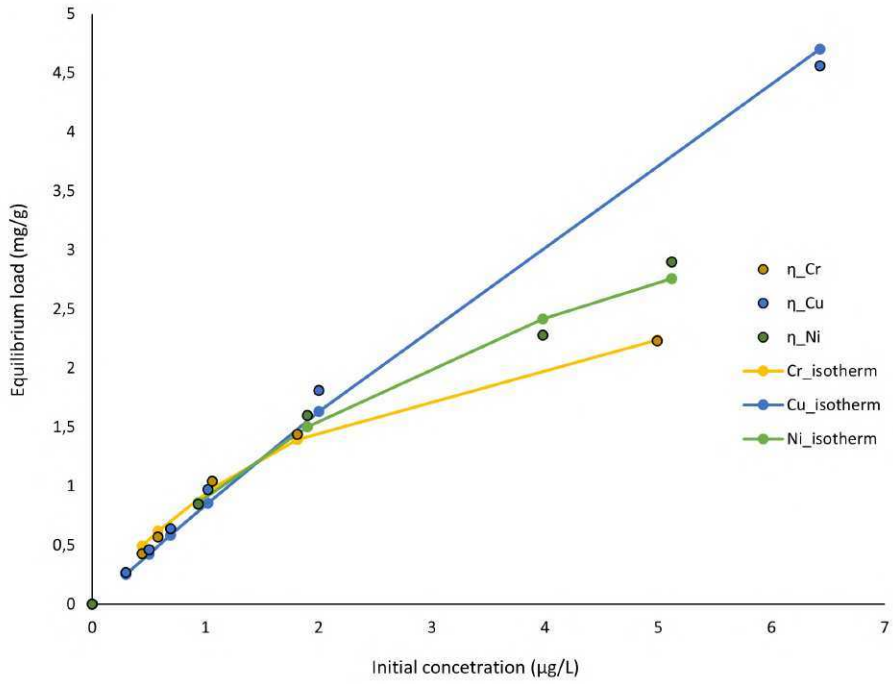

Figure 3.7: Fitting of the Langmuir isotherm of the experimental data, for the three different metal ions

predicted using the competitive Langmuir isotherm found for the three ions, were found to be within the experimental uncertainty (assumed to be 50% of the measured value). Minor deviations were observed only for copper, specifically in mixtures (#1) and (#5), where the Langmuir model predicted respectively lower and higher loads compared to the experimental results. This behavior could be attributed to the high affinity of copper ions for the proposed MNAs.

3.4 Experimental - Alginate beads production

Previously developed MNAs, together with magnetite nanoparticles, were embedded in alginate beads to improve their handling and recovery in aqueous solutions. In fact, encapsulation within the alginate matrix transforms the system from a two-dimensional arrangement of individual nanoparticles into a three-dimensional bead structure. This 3D structure not only reduces nanoparticle aggregation, but also enhances adsorption performance by providing a wide and interconnected porous network that facilitates ion diffusion throughout the bead. Moreover, the inherent magnetic properties of the nanoparticles enable easy and rapid recovery of the beads from aqueous solutions using an external magnetic field, combining effective adsorption with convenient handling and recovery. These properties are particularly advantageous for real-world applications such as wastewater treatment.

This approach resulted in three magnetic beads types, labeled BGO, B1, and B2, which can be easily separated from the treated solution or directly incorporated into adsorption columns.

Specifically, BGO consists of nanocomposite beads containing graphene oxide (GO) sheets decorated with magnetite (Fe_3O_4) nanoparticles, prepared through a straightforward coprecipitation method in the presence of GO. For comparison, B1 and B2 were synthesized by dispersing only magnetite nanoparticles into alginate beads, with different Ca^{2+} concentrations in the cross-linking solution to modulate the bead structure (Figure 3.8). The performance of these three beads types was evaluated for the removal of Cr^{3+}, Ni^{2+}, and Cu^{2+} ions under various concentrations at 25°C. The main objective was to characterize the adsorption efficiency at short contact times, which is critical for potential industrial applications, without relying on classical adsorption isotherms.

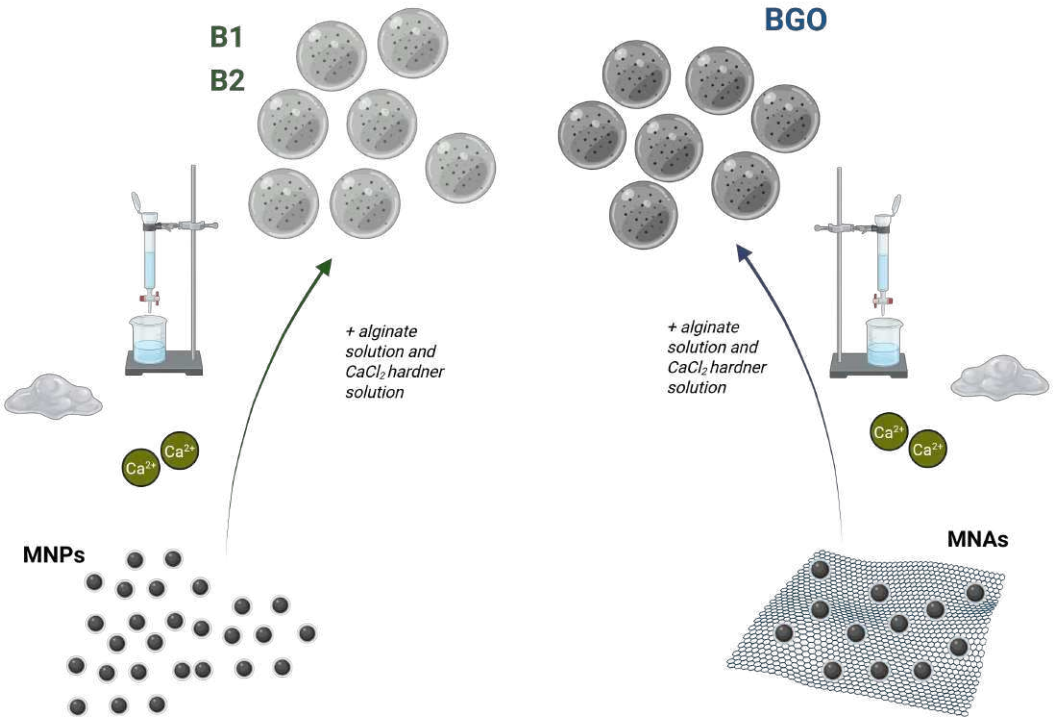

Figure 3.8: Beads preparation: (i) preparation of GO nanosheets decorated with magnetic nanoparticles by coprecipitation; (ii) mixing of magnetic materials (MNPs or MNAs) with dissolved sodium alginate; (iii) formation of the beads by cross-linking with a Ca^{2+} solution

3.4.1 Sodium alginate solution

In 300 mL of deionized water, 3 g of sodium alginate powder were added (10.0 g/L). At this point the mixture was heated at 40°C and mechanically mixed by stirring for 1 h, until a homogeneous solution was obtained.

3.4.2 Beads production

The production of beads involved the incorporation of MNAs or magnetite nanoparticles into a sodium alginate solution, followed by crosslinking in a calcium chloride hardener solution. During

this process, the alginate/nanomaterials suspension is transformed into a three-dimensional structure. The resulting beads were recovered, washed, and stored in deionized water prior to use. The detailed procedures for the preparation of the beads containing magnetite nanoparticles (B1 and B2) and of the beads containing MNAs (BGO) are described below.

Embedding of MNPs - B1 and B2 Beads B1 and B2 were prepared as follows:

1. Dispersion of the pristine magnetite MNPs (5.0 mg/mL) in the sodium alginate solution, previously prepared by dissolving the compound in deionized water at a concentration of 10.0 g/L.
2. Drop-wise addition of the previously prepared suspension into a cross-linking solution, obtained by dissolving either 10.0 g/L (for B1) or 30.0 g/L (for B2) of calcium chloride in deionized water. During the addition, the Ca^{2+} solution was kept under constant magnetic stirring.
3. Mechanical recovery from the solution, followed by four washing steps with deionized water, and storage in deionized water.

Embedding of MNAs - BGO The beads BGO are prepared as follows:

1. Dispersion of the MNAs (2.5 mg/mL) in the sodium alginate ($C_6H_9NaO_7$) solution, previously prepared by dissolving the compound in deionized water at a concentration of 10.0 g/L.
2. Drop-wise addition of the previously prepared suspension into a cross-linking solution, obtained by dissolving 10.0 g/L of calcium chloride ($CaCl_2$) in deionized water. During the addition, the Ca^{2+} solution was kept under constant magnetic stirring.
3. Mechanical recovery from the solution, followed by four washing steps with deionized water, and storage in deionized water.

3.4.3 Adsorption tests

According to the previous section 3.2.4, the three types of beads were tested on artificially polluted water samples, prepared by dissolving the corresponding inorganic salts in deionized water. Three different heavy metal ions, commonly found in industrial effluents, were selected:

- Cu^{2+} (copper(II) nitrate, $Cu(NO_3)_2{\cdot}3H_2O$);
- Ni^{2+} (nickel(II) chloride, $NiCl_2{\cdot}6H_2O$);
- Cr^{3+} (chromium(III) chloride, $CrCl_3{\cdot}6H_2O$).

The beads were tested with different sets of concentrations. In particular, for chromium(III) 100, 200 300, 400, 600, and 2000 $\mu g\,L^{-1}$ csolutions were tested; for copper(II) 100, 300, 600, 800, 3000, and 5000 $\mu g\,L^{-1}$ solutions were tested; and, finally, for nickel(II) 400, 1000, 2000, 4000, and 5000 $\mu g\,L^{-1}$ solutions were used. These concentrations were chosen to reflect those typically found in

textile industry wastewaters, which also accounts for the non-standardized range of the values tested.

All the prepared solutions were subsequently treated with BGO, B1, or B2 to evaluate their adsorption removal efficiencies. The experimental protocol followed for each test (#i, $i = 1 : 6$ for all metal ions) was as follows:

1. A flask containing 1 mL of deionized water was prepared;
2. Five beads (B1, B2, or BGO, depending on the test) were manually added;
3. Subsequently, 1 mL of the tested salt solution (#i, at double concentration) was added to reach the target initial concentration;
4. The flask was then mechanically shaken for 10 min at 25 °C. This contact time may appear rather short, but it was chosen to ensure the feasibility of a real industrial application of the embedded nanoadsorbents, which must operate far from equilibrium conditions (typically characterized by poor adsorption kinetics). It was observed that this time was sufficient to reach a "quasi-equilibrium" concentration for copper with each beads type; therefore, it was adopted as the reference contact time for all ions, allowing direct comparison among the different adsorption beads performances;
5. At the end of the experiment, 1.5 mL of solution was transferred with a micropipette into a 2 mL vial for ICP analysis. All final sample concentrations were determined by ICP-OES measurements.

The pH of all the metal ion stock solutions was measured and found to be in the range of 5.2–6.0.

3.4.4 Adsorption Isotherm Definition

From the ICP-OES concentration data, the different adsorption performances were analyzed. As discussed in Section 3.2.5, adsorption data were evaluated using the Langmuir isotherm framework (3.2), suitably adapted for batch experiments. While continuous-flow systems typically maintain a constant inlet concentration and reach equilibrium when the outlet concentration matches the inlet one, batch systems differ in two main aspects:

1. The starting concentration is not maintained; hence, the concentration gradient between the two phases is lower compared to continuous systems;
2. Equilibrium is established between the adsorbent and the final concentration, rather than the initial concentration as in continuous-flow conditions.

In this work, only the concept of final load, $\eta_{\mathrm{end},i}$ (see Equation 3.2), was applied, linking it to the experimental ion concentrations measured. The beads were always used in their hydrated form to avoid changes in their adsorption properties. However, some water—difficult to quantify—was trapped inside the alginate matrix, slightly altering the removal efficiency of the system. For

this reason, the direct application of Equation 3.2 was not considered fully reliable for isotherm determination.

Another useful parameter for evaluating the adsorption properties of the different beads is the removal efficiency, X_i, already defined in Equation 3.3. It is important to note that, according to this definition alone, it is not possible to separate the contributions of the individual bead components (MNA, GO, alginate). Therefore, the system is treated as a pseudo-mono-adsorbent.

3.4.5 Metal ion speciation in water

To ascertain the nature of the metal ion species in solution at the tested concentrations and pH, a speciation analysis was performed using the freeware software Visual MINTEQ Version 4.0 (developed by J. P. Gustafsson). The percent molar distribution of copper(II), nickel(II), and chromium(III) species in solution was evaluated at their specific pH values at 25 °C.

The results confirmed that, under the tested conditions, the entire amount of metal ions remains in solution, with no evidence of aggregation or precipitation. In the cases of Ni(II) and Cu(II), the M^{2+} cation is the predominant species in solution. Conversely, for Cr(III), the metal is more distributed among various hydroxo-species, with the bis-cationic $[Cr(OH)]^{2+}$ being the most relevant.

3.5 Results and discussion - Alginate beads

In the following section, the results concerning the characterization and the application of the beads are reported.

3.5.1 Beads composition

The three samples of magnetic nanocomposite beads, namely BGO, B1, and B2, were prepared by mixing previously synthesized magnetic nanomaterials with sodium alginate. BGO was obtained using GO nanosheets decorated with magnetic nanoparticles synthesized by coprecipitation, while B1 and B2 were prepared with only MNPs and alginate, with B2 differing from B1 by the higher concentration of Ca^{2+} used during the cross-linking step (Figure 3.8). To provide a reference for comparison with the nanocomposite beads, the composition of the alginate-only beads (BA) was also examined.

Table 3.9 reports the average composition of the different beads used. Since the beads must remain wet to avoid irreversible drying and shrinking, their composition was calculated as the mean of the alginate and nanoparticle masses used in the preparation process, divided by the number of beads produced.

In order to properly assess the equilibrium load of all the beads, the net mass of adsorbing material had to be determined. Since the produced alginate beads were in the form of hydrogel, composed of up to 95% water, a sample of 20 to 40 beads per type was taken and lyophilized for 24 h. Table 3.10 reports the weight of random samples of beads, used to assess the reliability of the composition based on the mass balance (Table 3.9). As can be seen from the table, the estimated average weights are comparable to the experimental results, taking into account the standard

Table 3.9: Estimated average composition of the beads tested

	B1	**B2**	**BGO**	**BA**
Composition	MNPs+Alg.	MNPs+Alg.	MNPs+GO+Alg.	Alg.
Average Weight [mg/bead]	0.74	0.75	0.64	0.9
MNPs [mg/bead]	0.22	0.22	0.10	-
GO [mg/bead]	-	-	0.01	-
Alginate [mg/bead]	0.52	0.52	0.53	0.88

deviation. When comparing wet and lyophilized beads, the former contain water corresponding to 97.0–97.5% of their total mass. In the case of BA, water accounts for about 94% of the total weight, while the remaining 6% corresponds to the alginate polymer. The lower water fraction, compared to the magnetic beads, is due to the absence of magnetite nanoparticles or MNAs: the solid phase is entirely alginate, which is heavier than the nanomaterials employed in the composites. In contrast, in the nanocomposite formulations part of the alginate is replaced by lightweight fillers such as magnetite nanoparticles or MNAs. As a result, the total solid mass is reduced and water becomes the dominant component, reaching 97.0–97.5% of the bead weight.

Table 3.10: Wet and dry mass of the different beads

	B1		**B2**		**BGO**		**BA**	
State	Wet	Dry	Wet	Dry	Wet	Dry	Wet	Dry
N. of Beads	27	27	29	29	34	34	20	20
Average Weight [mg]	23.4	0.7	23.1	0.7	22.6	0.6	15.9	0.91
Std. Dev. [mg]	2.5	0.1	1.6	0.1	3.6	0.1	0.91	0.060
Std. Dev. (%)	10.5	12.4	6.80	13.1	16.0	13.4	5.74	12.0

3.5.2 Beads characterization

Stereomicroscope characterization

The beads were characterized in terms of morphology using a stereomicroscope. Figure 3.9 shows stereoscopic images of the hydrated beads on a white background, highlighting their regular spherical shape and smooth surface. In the magnified images (Figure 3.9 b-d-f), the magnetic nanomaterial is clearly visible within the beads as black spots, uniformly distributed. Since the size of the spots is considerably larger than that of individual nanomaterials [239], aggregation of the magnetic material within the alginate matrix likely occurred during the cross-linking process.

The wet bead diameters were also estimated using ImageJ software on stereoscopic images. B1 exhibits an average diameter of 3.63 mm with a standard deviation of 0.18 mm (5.0%), B2 shows an average diameter of 3.44 mm with a standard deviation of 0.17 mm (4.9%), and BGO has an average diameter of 3.40 mm with a standard deviation of 0.25 mm (7.3%).

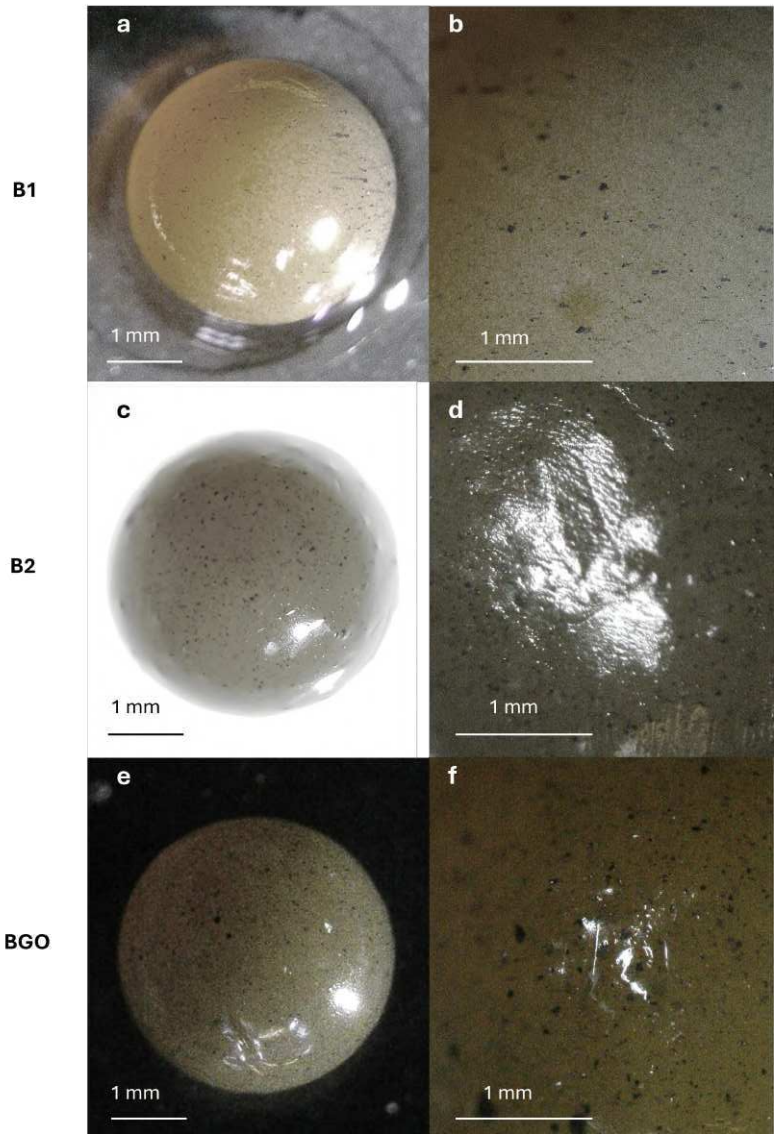

Figure 3.9: Stereoscope images of the wet beads

The beads were also lyophilized for 24 h, and stereoscopic images of the dried beads are shown in Figure 3.10. The diameters of the beads were considerably reduced due to shrinkage (from 3.4–3.6 mm to approximately 2 mm). While B1 and B2 maintained a spherical shape, BGO collapsed during drying (Figure 3.10c), suggesting a less compact internal structure. In all images, the bead surfaces appear corrugated, but remain compact. Varying the Ca^{2+} concentration in the cross-linking solution did not produce any discernible effect on the morphology of the beads, as observed by comparing B1 and B2.

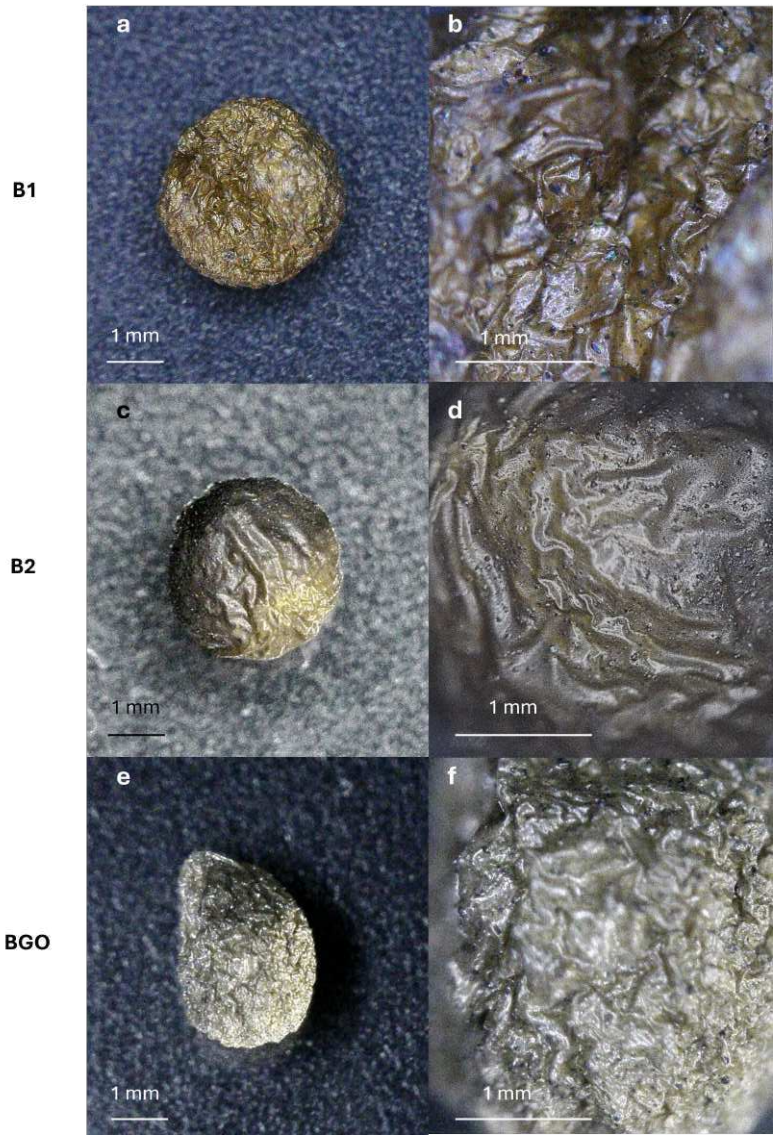

Figure 3.10: Stereoscope pictures of lyophilized beads

ESEM-EDX analysis

Although ESEM is a technique that allows the presence of water vapor in the sample chamber [240], we observed a rapid evaporation of the water phase in the beads after vacuum application, which consequently led to structural contraction. Nevertheless, the ESEM images collected show a homogeneous distribution of the magnetic material (visible as lighter spots in Figure 3.11) also on the bead surfaces. Beads B1 (Figure 3.11 a-b) exhibit a more regular surface and shape, while B2 (Figure 3.11 c-d), obtained using a three-fold higher concentration of Ca^{2+} in the cross-linking solution, exhibit cracks and inward folding on the surface.

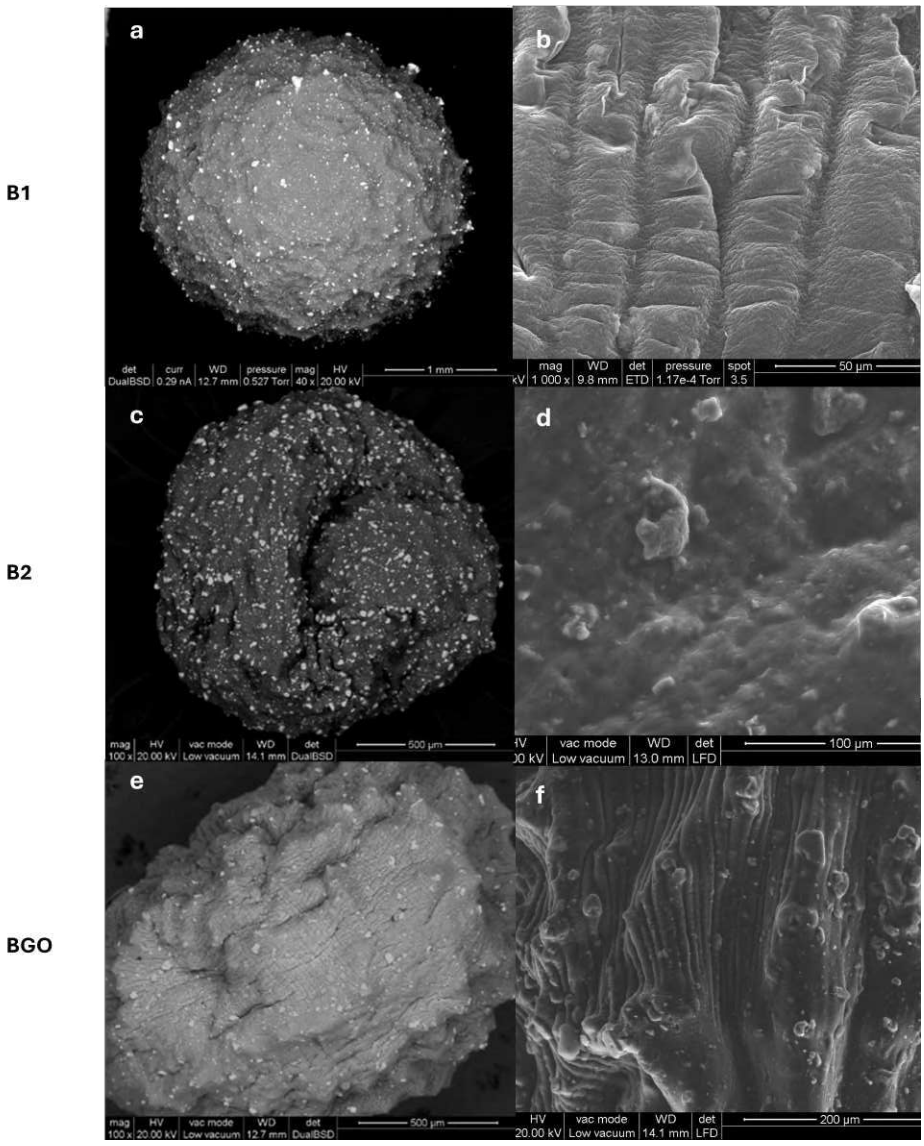

Figure 3.11: ESEM characterization of the beads

The oblong shape (as observed in the lyophilized sample of the same type showed in Figure 3.10e-f) and the rough surface of BGO are likely due to the presence of the 2D graphene oxide

sheet structure, which can interfere with the organization of the polymer fibers and their ionic interactions.

To provide a reference for comparison with the nanocomposite beads, also the morphology of the alginate-only beads (BA) was examined using Environmental Scanning Electron Microscopy (ESEM). Figure 3.12 shows two representative ESEM images of BA beads at different magnifications.

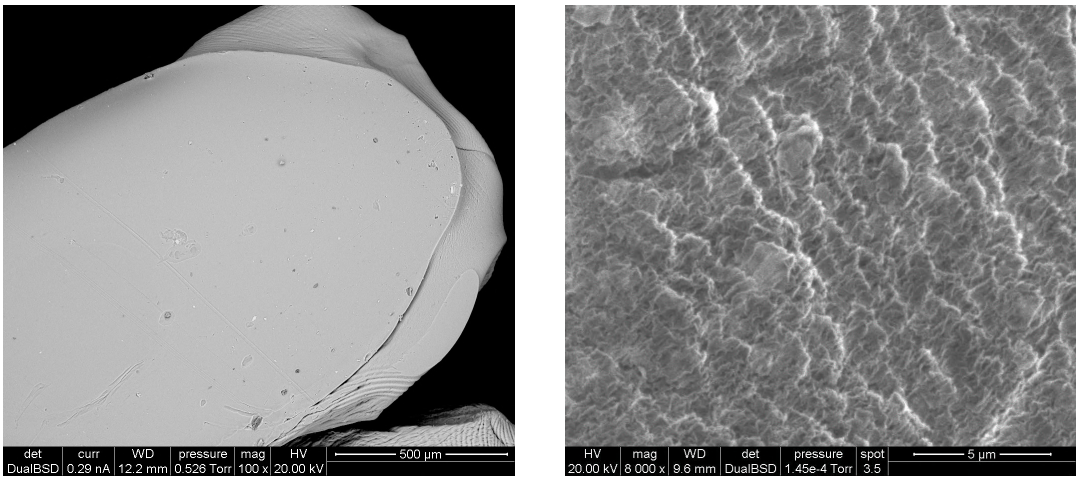

Figure 3.12: ESEM images of alginate-only beads (BA), used as reference for comparison with nanocomposite beads

At low magnification, the beads appear homogeneous and maintain a nearly spherical shape. At higher magnification, the surface morphology can be observed in greater detail, confirming the absence of magnetic nanoparticles and highlighting the smooth texture typical of pure alginate beads.

The elemental composition of the three samples, determined by Energy Dispersive X-Ray Spectroscopy (EDX, model EDAX Element-C2B), is reported in Table 3.11.

Table 3.11: EDX elemental analysis on the bead surfaces

Element	**Weight %**			
	B1	**B2**	**BGO**	**BA**
C	22.08	26.05	12.77	51.6
O	61.65	55.57	83.21	38.3
Ca	5.87	5.62	2.03	10.1
Fe	10.40	12.76	1.99	-

The surface composition of B1 and B2 is consistent with the material ratios used during their preparation, taking into account the presence of some residual water in their structure. In contrast, BGO shows a much lower iron concentration, which reflects the smaller amount of

magnetite employed, but also a relatively high oxygen content, suggesting a higher hydration level compared to the other beads. This behavior could be attributed to the presence of GO, which can strongly interact with water molecules through hydrogen bonding with its oxygenated functional groups [241].

Magnetic characterization

The magnetic properties of the nanoadsorbents are of paramount importance in their separation and use. Thus, the magnetic properties are a key factor to be investigated. The incorporation of MNPs not only facilitates an easy separation of the adsorbent from the aqueous medium under an external magnetic field, but also influences their dispersion stability and overall handling during adsorption experiments. For practical applications, a sufficiently high magnetization is essential to ensure a rapid and complete recovery of the adsorbent after use, minimizing losses and improving reusability. At the same time, the adsorption of heavy metal ions, such as Cu(II), may alter the magnetic response of the embedded nanoparticles, either by surface interactions or by partial shielding of magnetic moments. Understanding these variations is therefore fundamental, as a reduction in magnetization could compromise the efficiency of bead recovery and limit their applicability in dynamic water treatment systems. Moreover, monitoring the magnetic signal provides a non-destructive method to indirectly assess the adsorption process, potentially offering a simple way to track adsorbent loading during operation. For these reasons, systematic magnetic measurements were carried out both on pristine Fe_3O_4 nanoparticles and on alginate beads incorporating them, before and after copper adsorption, to establish a direct correlation between structural modifications, adsorption performance, and magnetic behavior. The measurements have been carried out as described in Section 3.1.1.

The curves obtained by performing the M(H) measurements on the powder of Fe_3O_4 magnetic nanoparticles at 5 K and 300 K are reported in Figure 3.13. The value of the mass magnetization at 90000 Oe (M_s) was about $70\,\mathrm{emu\,g^{-1}}$ at 300 K and about $78\,\mathrm{emu\,g^{-1}}$ at 5 K. These values are comparable to those reported in the literature for Fe_3O_4 nanoparticle samples [242, 243, 244]. The increasing of mass magnetization at 5 K and the change of coercivity field from a value below 2 Oe at 300 K to a value about 250 Oe at 5 K suggested the presence of a superparamagnetic behavior at the highest temperatures. In fact, despite the absence of coercive field, which is expected for a paramagnet, the shape of the loop at 300 K showed a rapid increase of magnetization below a field intensity of 10000 Oe, as expected for the signal of a ferromagnet.

To better investigate the transition from a blocked state to a superparamagnetic behavior for the powder of Fe_3O_4 magnetic nanoparticles, the study of magnetization versus temperature with 100 Oe of applied field was performed and the curves obtained are reported in Figure 3.14. The inset reveals that the ZFC curve reaches its maximum (T_{max}) at a temperature of 205 K. This T_{max} represents the mean blocking temperature for the sample of magnetic nanoparticles, indicating a transition to a superparamagnetic behavior. In fact, as observed in Figure 3.14, at temperatures below T_{max} the ZFC and FC curves were completely separated, as expected for a sample of magnetic nanoparticles in a blocked state. For temperatures above T_{max} the separation between ZFC and FC curves suggested that not all the nanoparticles were in a superparamagnetic state. The two curves had an overlap near room temperature indicating that the sample had a reversible behavior. This

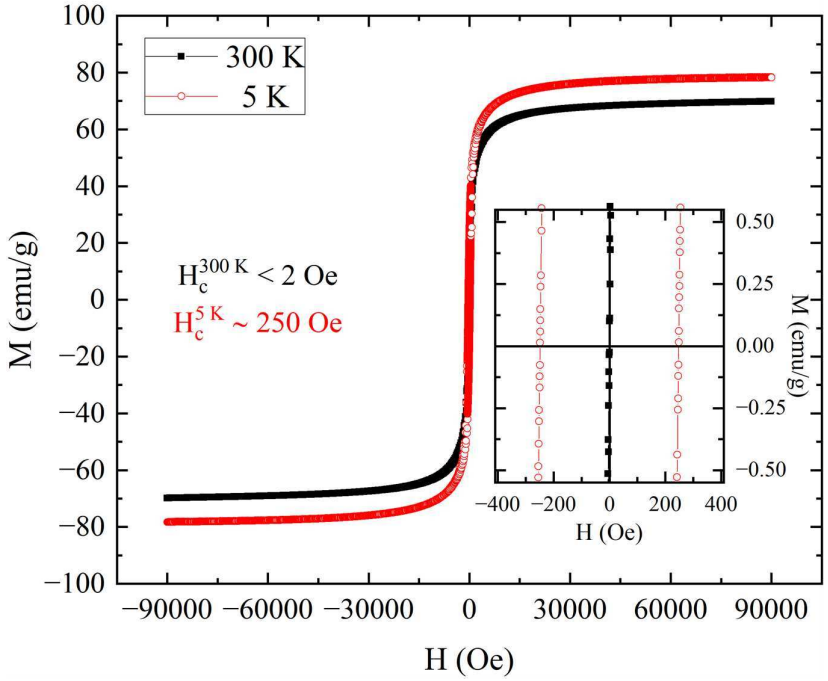

Figure 3.13: M(H) loops performed at 5 K (red opened circles) and 300 K (black closed squares) for the powder of Fe_3O_4 magnetic nanoparticles

was an indication of the complete transition to the superparamagnetic state, and it is in accordance with the absence of hysteretic behavior at 300 K (see inset of Figure 3.13).

To compare the magnetic properties of the pristine nanoparticles with those of their alginate composite beads, the same magnetic characterizations performed on Fe_3O_4 nanoparticles were also carried out on bead B1. This would allow to highlight the effect of the embedment in the polysaccharide matrix. The M(H) loops obtained for the dried bead at 300 K and 5 K are reported in Figure 3.15. The mass magnetization was obtained by normalizing the magnetic moment with the mass of magnetic nanoparticles embedded in the sodium alginate. The mass ratio between magnetic nanoparticles and the total mass of the bead, used to evaluate the mass magnetization, was obtained considering the proportion between magnetic nanoparticles and sodium alginate in the synthesis process of the bead. Thus, considering the mass proportion between magnetic nanoparticles and sodium alginate determined for B1 in Table 3.9, the mass of the former was estimated as 1/3 of the total dry mass of the bead.

The first observation that can be made from Figure 3.15 is that the saturation magnetization at 300 K was lower than that at 5 K. Furthermore, from the inset which showed the data around zero field, it was possible to evaluate the coercivity of the sample. In particular, the coercive field at 5 K was about 280 Oe while the coercive field at 300 K was lower than 2 Oe. This reduction in coercivity suggests that magnetic nanoparticles retained their superparamagnetic behavior also when they were embedded in the bead. Despite this, there was a difference in the mass magnetization at 90000 Oe both at 5 K and 300 K for the two samples. From Figure 3.15, the mass magnetization reached a maximum of $54\,\mathrm{emu\,g^{-1}}$ at 300 K and of $62\,\mathrm{emu\,g^{-1}}$ at 5 K. Comparing these values

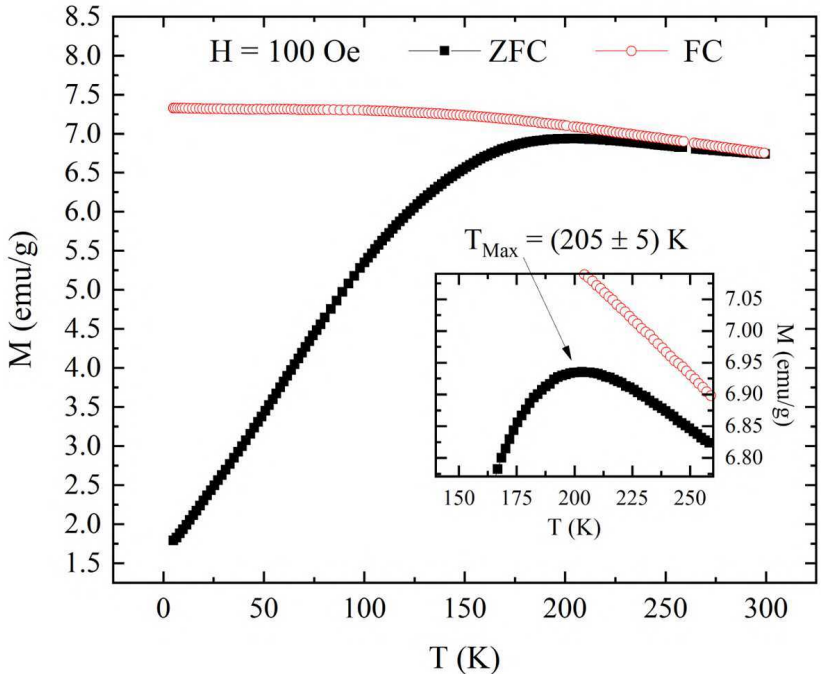

Figure 3.14: Magnetization versus temperature measured with an applied field of 100 Oe in the ZFC (black closed squares) and FC protocol (red opened circles) for a powder of Fe_3O_4 magnetic nanoparticles.

with those measured in Figure 3.13 for the powder of magnetic nanoparticles ($70\,\mathrm{emu\,g^{-1}}$ at 300 K and $78\,\mathrm{emu\,g^{-1}}$ at 5 K), it was possible to see a difference of around $16\,\mathrm{emu\,g^{-1}}$ at each temperature (reduction of 23% at 300 K and of 21% at 5 K). Considering the fact that, the 1/3 fraction is an average value, but could slightly change when considering a single bead, this could explain the difference between the M_s of the pure powder of magnetic nanoparticles and the bead. Another possible explanation could be the presence of an alternating surface anisotropy due to the incorporation of nanoparticles in the sodium alginate matrix. Despite this, the value obtained for M_s was comparable to that reported in literature for similar types of beads [244] produced for wastewater remediation.

3.5.3 Adsorption tests

The adsorption properties of the nanostructured adsorbent beads were analyzed as described in section 3.4.3. Each test was carried out at 25 °C using the same volume of metal-polluted solution (2 mL), the same number of beads (5), and a contact time of 10 min.

The effective starting concentration of the solution were determined by Inductively Coupled Plasma Optical Emission Spectroscopy (ICP-OES). Table 3.12 reports all the heavy metal starting concentrations tested.

Tables 3.13, 3.14 and 3.15 report the initial concentrations of copper(II) and the corresponding final concentrations after treatment with B1, B2, and BGO, respectively.

Figure 3.16 reports the adsorption performance of the different types of beads investigated,

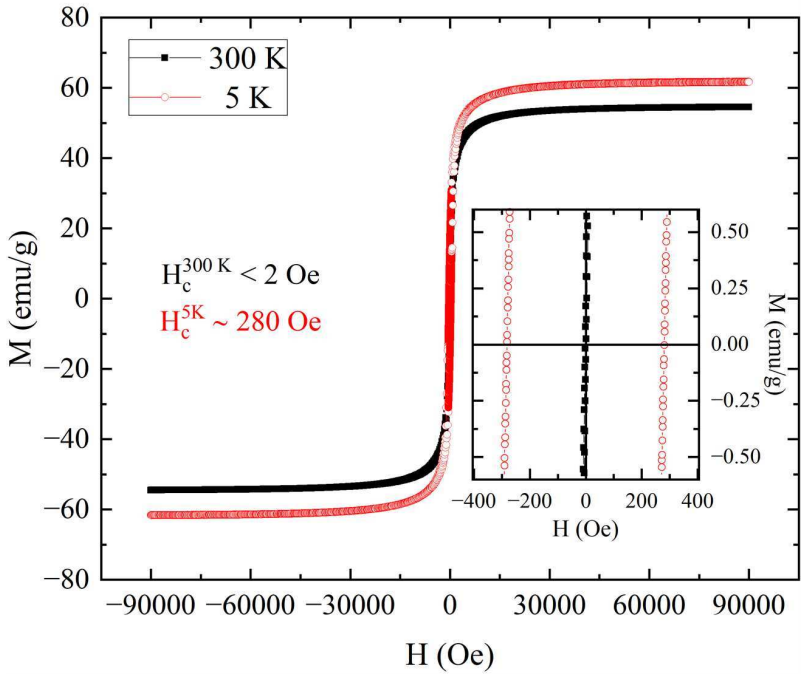

Figure 3.15: M(H) loops performed at 5 K (red opened circles) and 300 K (black closed squares) for B1

expressed as removal efficiency. The histogram allows a straightforward comparison, highlighting how the structural and compositional differences among the beads influence their ability to capture copper ions.

For copper(II), all three bead types exhibited high removal efficiencies, particularly in low-concentration samples. Beads B1 and B2 both showed very effective adsorption, especially in samples #1 to #4, where final Cu concentrations remained below 2 µmol/L. For copper(II), the results were generally similar across the different bead types. At higher initial concentrations (above 2700 $\mu g\,L^{-1}$), BGO exhibited slightly higher final concentrations compared to B1 and B2, which may be attributed to its smaller size and lower surface area relative to the other beads.

Tables 3.16, 3.17 and 3.18 report the initial concentrations of nickel(II) and the corresponding final concentrations after treatment with B1, B2, and BGO, respectively.

Table 3.16: Results for adsorption of Ni(II) with **B1** beads

Sample	#1	#2	#3	#4	#5
Initial Ni Conc. (μg/L)	443 ± 1	1060 ± 1	2120 ± 1	4394 ± 10	5123 ± 10
(mmol/L)	7.55	18.1	36.1	74.9	87.3
Final Ni Conc. (μg/L)	82 ± 1	193 ± 1	364 ± 1	1053 ± 1	982 ± 1
(mmol/L)	1.40	3.29	6.20	17.9	16.7

Table 3.12: Theoretical and effective concentrations ($\mu g\,L^{-1}$) of heavy metal ions in the tested samples

Ion	Type	#1	#2	#3	#4	#5	#6
Cu^{2+}	Theoretical	100	300	600	800	3000	5000
	Effective	123 ± 1	302 ± 1	587 ± 1	838 ± 1	2770 ± 10	4820 ± 10
Ni^{2+}	Theoretical	400	1000	2000	4000	5000	–
	Effective	443 ± 1	1060 ± 10	2120 ± 10	4394 ± 10	5123 ± 10	–
Cr^{3+}	Theoretical	100	200	300	400	600	2000
	Effective	139 ± 1	225 ± 1	273 ± 1	423 ± 1	605 ± 1	1915 ± 10

Table 3.13: Results for adsorption with Cu(II) polluted samples using **B1** beads

Sample	#1	#2	#3	#4	#5	#6
Initial Cu Conc. (μg/L)	123 ± 1	302 ± 1	587 ± 1	838 ± 1	2770 ± 10	4820 ± 10
(mmol/L)	1.94	4.75	9.24	13.2	43.6	75.8
Final Cu Conc. (μg/L)	24 ± 1	53 ± 1	88 ± 1	156 ± 1	383 ± 1	648 ± 1
(mmol/L)	0.377	0.833	1.38	1.81	4.70	10.2

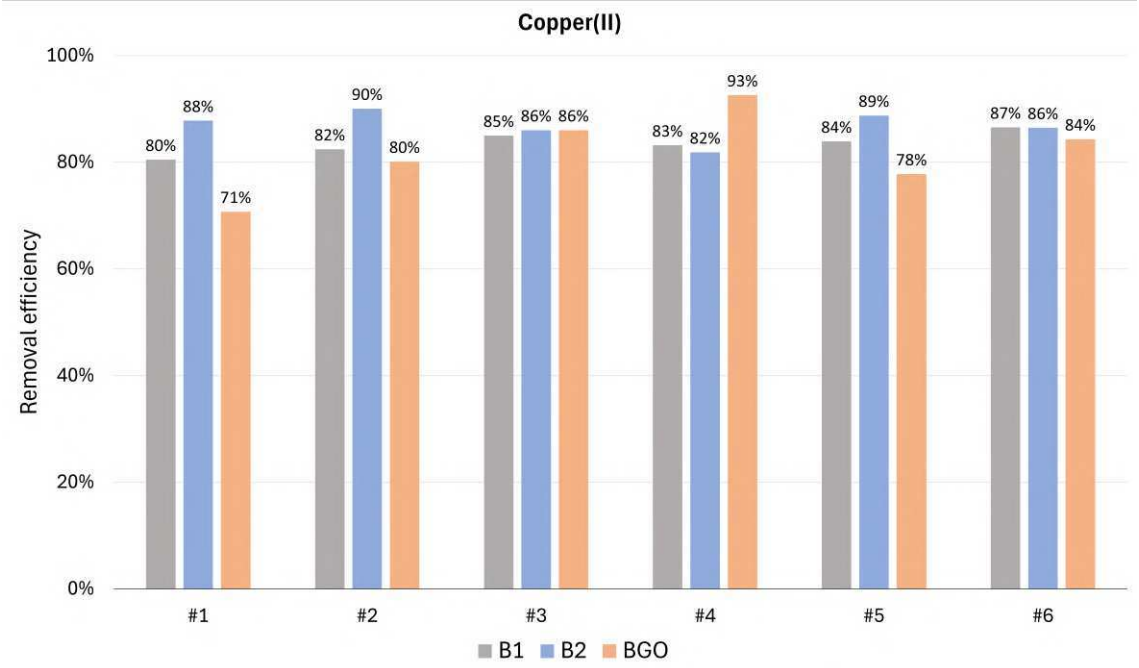

Figure 3.16: Comparison between the performance of different beads types for the adsorption of Cu(II)

Table 3.14: Results for adsorption with Cu(II) polluted samples using **B2** beads

Sample	#1	#2	#3	#4	#5	#6
Initial Cu Conc. (μg/L)	123 ± 1	302 ± 1	587 ± 1	838 ± 1	2770 ± 10	4820 ± 10
(mmol/L)	1.94	4.75	9.24	13.2	43.6	75.8
Final Cu Conc. (μg/L)	15 ± 1	30 ± 1	82 ± 1	152 ± 1	311 ± 1	652 ± 1
(mmol/L)	0.236	0.472	1.29	2.39	4.99	10.2

Table 3.15: Results for adsorption with Cu(II) polluted samples using **BGO** beads

Sample	#1	#2	#3	#4	#5	#6
Initial Cu Conc. (μg/L)	123 ± 1	302 ± 1	587 ± 1	838 ± 1	2770 ± 10	4820 ± 10
(mmol/L)	1.94	4.75	9.24	13.2	43.6	75.8
Final Cu Conc. (μg/L)	36 ± 1	60 ± 1	82 ± 1	62 ± 1	615 ± 1	755 ± 1
(mmol/L)	0.566	0.94	1.29	0.976	9.68	11.9

Table 3.17: Results for adsorption of Ni(II) with **B2** beads

Sample	#1	#2	#3	#4	#5
Initial Ni Conc. (μg/L)	443 ± 1	1060 ± 1	2120 ± 1	4394 ± 10	5123 ± 10
(mmol/L)	7.55	18.1	36.1	74.9	87.3
Final Ni Conc. (μg/L)	93 ± 1	415 ± 1	881 ± 1	2022 ± 1	2171 ± 1
(mmol/L)	1.58	7.07	15.0	34.4	37.0

Table 3.18: Results for adsorption of Ni(II) with **BGO** beads

Sample	#1	#2	#3	#4	#5
Initial Ni Conc. (μg/L)	443 ± 1	1060 ± 1	2120 ± 1	4394 ± 10	5123 ± 10
(mmol/L)	7.55	18.1	36.1	74.9	87.3
Final Ni Conc. (μg/L)	196 ± 1	172 ± 1	100 ± 1	621 ± 1	990 ± 1
(mmol/L)	3.34	2.93	1.70	10.6	16.9

Figure 3.17 reports the adsorption performance of the different types of beads investigated, expressed as removal efficiency.

In the case of nickel(II), differences among the adsorbents were more pronounced. Particularly, the highest final concentrations were found for all the solutions treated with B2, while B1 and BGO performances appeared to be quite similar. However, B1 again exhibited the best performance overall, particularly for samples #1 to #3. The final Ni concentrations dropped from 7.55 to 1.40 µmol/L in sample #1, and from 36.1 to 6.20 µmol/L in sample #3. B2, although less effective in the higher concentration samples (#4 and #5), maintained moderate efficiency in the lower ones. In

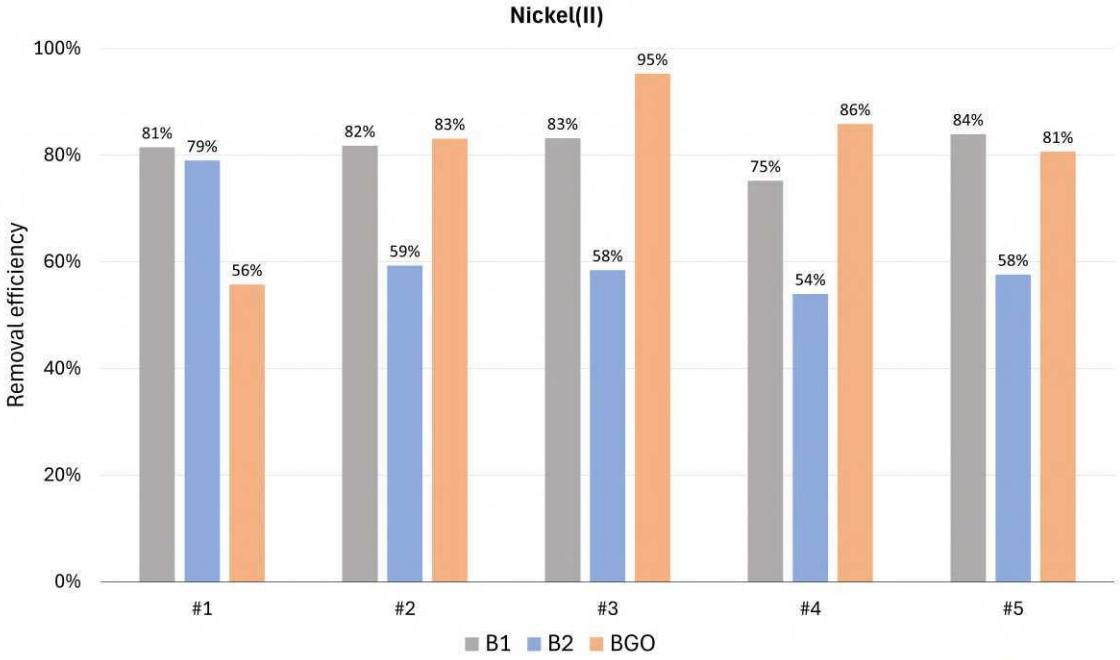

Figure 3.17: Comparison between the performance of different beads types for the adsorption of Ni(II)

contrast, BGO displayed excellent removal in samples #2 and #3, reducing the concentration from 18.1 to 2.93 µmol/L and from 36.1 to 1.70 µmol/L, respectively. This indicates that BGO might exhibit higher affinity for Ni(II) under moderate concentration ranges. However, for sample #5, its performance dropped (final: 16.9 µmol/L), suggesting a potential saturation effect or kinetic limitation.

Tables 3.16, 3.17 and 3.18 report the initial concentrations of chromium(III) and the corresponding final concentrations after treatment with B1, B2, and BGO, respectively.

Table 3.19: Results for adsorption of Cr(III) with **B1** beads

Sample	#1	#2	#3	#4	#5	#6
Initial Cr Conc. (μg/L)	139 ± 1	225 ± 1	273 ± 1	423 ± 1	605 ± 1	1915 ± 1
(mmol/L)	2.67	4.33	5.25	8.13	11.6	36.8
Final Cr Conc. (μg/L)	33 ± 1	35 ± 1	105 ± 1	18 ± 1	23 ± 1	67 ± 1
(mmol/L)	0.635	0.673	2.02	0.346	0.44	1.29

Table 3.20: Results for adsorption of Cr(III) with **B2** beads

Sample	#1	#2	#3	#4	#5	#6
Initial Cr Conc. (μg/L)	139 ± 1	225 ± 1	273 ± 1	423 ± 1	605 ± 1	1915 ± 1
(mmol/L)	2.67	4.33	5.25	8.13	11.6	36.8
Final Cr Conc. (μg/L)	29 ± 1	76 ± 1	26 ± 1	29 ± 1	15 ± 1	62 ± 1
(mmol/L)	0.558	1.46	0.500	0.558	0.288	1.19

Table 3.21: Results for adsorption of Cr(III) with **BGO** beads

Sample	#1	#2	#3	#4	#5	#6
Initial Cr Conc. (μg/L)	139 ± 1	225 ± 1	273 ± 1	423 ± 1	605 ± 1	1915 ± 1
(mmol/L)	2.67	4.33	5.25	8.13	11.6	36.8
Final Cr Conc. (μg/L)	65 ± 1	46 ± 1	45 ± 1	56 ± 1	71 ± 1	120 ± 1
(mmol/L)	1.25	0.885	0.865	1.08	1.36	2.31

Figure 3.18 reports the adsorption performance of the different types of beads investigated, expressed as removal efficiency.

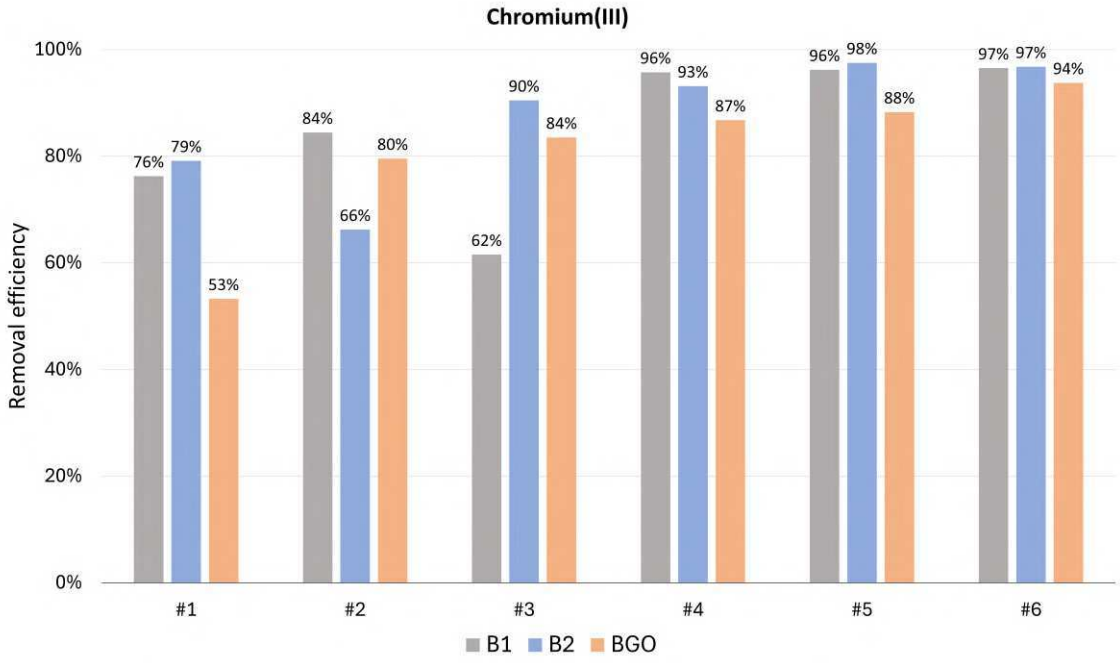

Figure 3.18: Comparison between the performance of different beads types for the adsorption of Cr(III)

For chromium(III), all adsorbents were highly effective, particularly at higher initial solution concentrations, with very low final concentrations consistently measured. B1 showed excellent

efficiency in high-concentration samples: from 36.8 to 1.29 µmol/L in sample #6, and from 11.6 to 0.44 µmol/L in sample #5. B2 showed particularly high efficiency in samples #3 to #6, with final concentrations as low as 0.288 µmol/L (sample #5), confirming a strong affinity toward trivalent chromium. Conversely, BGO demonstrated the lowest removal performance for Cr(III) overall, especially in the higher concentration samples (#5 and #6), with final Cr concentrations of 1.36 and 2.31 µmol/L, respectively. This could be due to the less favorable interaction of Cr(III) hydroxocomplexes with the graphene oxide-based surfaces. However, the comparison of starting and final concentrations alone is not sufficient, as adsorption strongly depends on the amount of adsorbent used (approximately 1.6–1.85 mg bead/mL). Therefore, removal efficiency must also be evaluated and discussed.

By looking at the data, it is possible to see that for copper and nickel the final concentration generally increases with the increase of the initial concentration, while for chromium, a general trend was not observed. This behavior is likely due to both the adsorption kinetics and chromium speciation: during the 10 min contact time, chromium adsorption does not reach equilibrium, considering the presence of different hydroxo species in solution that may require coordination exchange processes to bind to the beads. In fact, chromium(III), due to its more complex aqueous speciation (as confirmed by the Visual MINTEQ analysis), forms multiple hydroxospecies under the experimental pH conditions. This likely influences its interactions with the adsorbent surfaces.

In comparing the three types of beads:

- **B1** consistently performed well across all metals and concentration ranges. Its high efficiency and consistent results make it a promising universal adsorbent.
- **B2** displayed strong removal for Cu(II) and Cr(III), especially at high concentrations, and is particularly suitable for Cr(III) remediation.
- **BGO** performed variably. While highly efficient in certain Ni(II) and Cu(II) samples, its lower efficiency with Cr(III) limits its applicability for trivalent metal ions.

Overall, the findings suggest that while all beads are effective under certain conditions, a careful selection must be made based on the target pollutant and operating concentration. B1 offers the best all-around performance, B2 is ideal for Cr(III) in particular, and BGO performs well for divalent metals under moderate concentrations.

These results underline that the speciation and valence of the metal ions significantly affect adsorption efficiency:

- **Cu(II)** was the most effectively adsorbed metal overall, regardless of the adsorbent used. Its simple speciation and divalent charge promote efficient surface interaction.
- **Ni(II)** showed similar trends but slightly reduced efficiencies, potentially due to smaller hydrated radius or lower affinity in some systems.
- **Cr(III)** removal was more challenging, likely due to its hydrolyzed forms (e.g., $[Cr(OH)]^{2+}$), which may sterically hinder binding or limit access to adsorption sites.

3.5.4 Adsorption Isotherm Evaluation

The yield of removal (or, simply, removal efficiency), χ, is a useful parameter to evaluate how much of the pollutant was removed from the initial solution. It is well known that different metal ions exhibit different affinities toward a given adsorbent, as widely reported in the literature [237, 235, 245]. Based on the calculated yields, it was possible to compare the behavior of the adsorbents under different conditions. Each ion displayed a distinct trend: for copper, beads B1 and B2 showed a very similar affinity, resulting in almost identical removal efficiencies, whereas BGO exhibited a lower performance, especially at higher concentrations. In the case of nickel, the differences among the adsorbents became more evident: BGO appeared to be the most efficient, followed by B1 and then B2. For chromium, on the other hand, all beads displayed comparable removal efficiencies over the entire concentration range investigated. It should also be noted that, at low initial concentrations, the removal efficiency tended to increase with increasing pollutant concentration for most samples. The highest yields were observed for chromium, reaching up to 98% at an initial concentration of 605 μg L^{-1} (11.6 μmol L^{-1}). This suggests that the adsorption equilibrium had not yet been reached. The relatively large size of the beads, compared to functionalized nanoparticles, probably slowed the adsorption kinetics, introducing a sort of "microkinetic bottleneck." Further evidence of non-equilibrium operating conditions can be inferred from the trend of the final metal loading on the adsorbent, η_{end}, as a function of both the initial and the final solution concentration. The evolution of the final metal load on the adsorbent confirmed that the equilibrium state was not yet reached under the tested conditions. For all experiments, the load increased with the initial concentration, without showing any plateau region. This provides further evidence of non-equilibrium conditions, although for copper it can be reasonably assumed that the equilibrium state was relatively close, since the load consistently increased with the initial concentration. This aspect is of particular importance, as saturation time represents a crucial parameter in the design of real industrial adsorbers. When the load was analyzed as a function of the final concentration of the ions, which should theoretically correspond to the equilibrium concentration, the results indicated that equilibrium was still not achieved (with the exception of copper). In addition, the bead saturation was not observed: the loads increased with the final concentration but did not exhibit the typical plateau behavior that would indicate the complete occupation of active sites. Comparison with literature data highlights some interesting aspects. In a related study [235], an adsorbent composed of sawdust–chitosan nanocomposite beads was applied to the removal of copper and nickel from aqueous solutions. In that work, an adsorbent concentration of 20 mg mL^{-1} (1 g in 50 mL of solution) was used, with initial ion concentrations in the range of 20–200 mg L^{-1}. In the present work, the adsorbent concentration was significantly lower (1.6–1.8 mg mL^{-1}), and the ion concentration range was also lower (0.1–5 mg L^{-1}). Therefore, the adsorbent-to-pollutant ratios were comparable. According to the cited study, equilibrium was reached in 70 min. By contrast, in the present case, even after only 10 min of stirring, the removal yields were about 50% higher for each ion investigated.

3.5.5 Effects of adsorption on magnetic properties

Magnetic characterizations were first performed on pristine magnetite nanoparticles, in order to establish a reference for their intrinsic magnetic behavior. Subsequently, the same analyses were

carried out on bead B1, which contains magnetite nanoparticles embedded in the alginate matrix, to evaluate how the encapsulation process affects their magnetic properties (Section 3.5.2). This comparison allowed us to highlight the influence of the polymeric environment on the response of the nanoparticles. However, the study could not be limited to this stage, since the adsorption of metal ions is expected to further modify the magnetic behavior of the beads. In fact, the incorporation of adsorbed species not only alters the overall mass balance, but can also influence the local magnetic environment of the nanoparticles. For this reason, bead B1 was subjected to an additional characterization after copper adsorption. The results of this post-adsorption analysis, which provide insights into the evolution of the magnetic properties following the adsorption process, are reported in the following section.

Focusing on the possible application to the treatment of contaminated water, from which the adsorbent must be magnetically recovered, the magnetic properties of a bead of B1 type dried after adsorbing copper ions (in a 3.00 g/L Cu^{2+} solution) were analyzed by performing the M(H) measurements (Figure 3.19). Table 3.10 reports the mass of wet vs. dry beads. The average dried mass was used to evaluate the load of copper(II) per gram of bead.

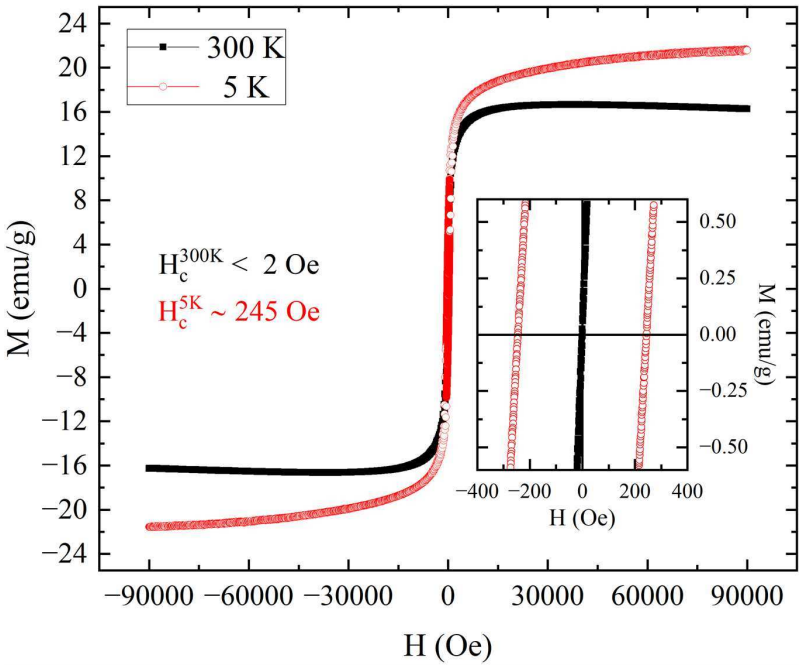

Figure 3.19: Magnetization versus field loops performed at 5 K (red opened circles) and 300 K (black closed squares) for B1 after copper ions adsorption

To maximize the metal effect on the adsorbent's magnetic signal, the B1 sample with the highest copper load was selected for this characterization. From the M(H) shown in Figure 3.19 it was possible to observe that the superparamagnetic behavior at 300 K remained also after the adsorption of copper ions. In fact, the coercive field changed from about 245 Oe at 5 K to a value below 2 Oe at 300 K. This difference was perfectly in accordance with the behavior observed in Figures 3.13 and 3.15. Despite this, the magnetic responses showed a difference in terms of signal

intensity. In fact, as it can be seen in Figure 3.19, the maximum of mass magnetization for the bead after adsorption was of $16\,\mathrm{emu\,g^{-1}}$ at 300 K and of $21\,\mathrm{emu\,g^{-1}}$ at 5 K with a difference of more than $40\,\mathrm{emu\,g^{-1}}$ with the data reported in Figure 3.15 (a reduction of 74% at 300 K and of 65% at 5 K). One possibility to explain the change in signal is to consider that the value of mass used to calculate mass magnetization in Figure 3.19 was higher than that used for Figure 3.15. In fact, the mass magnetization in Figure 3.19 was calculated by considering 1/3 of the mass of the dried bead after copper adsorption, exactly as in the case of a dried bead before adsorption, but in this case (after the adsorption) the total mass of the bead not only considered the presence of sodium alginate and of magnetic nanoparticles, but also of copper ions. So, there was an error in the estimation of the mass associated with magnetic nanoparticles due to the presence of copper. In fact, the average mass of a group of 20 beads before copper adsorption and of 20 beads after copper adsorption differed by around 0.5 mg. However, even rescaling the mass used for normalization in Figure 3.19 to the one used for the bead before adsorption (Figure 3.15), M_s would be of $21\,\mathrm{emu\,g^{-1}}$ at 300 K and of $27\,\mathrm{emu\,g^{-1}}$ at 300 K. Thus, the difference with the case of bead before adsorption would be more than $30\,\mathrm{emu\,g^{-1}}$ (a reduction of 55% at 300 K and of 47% at 5 K). Another possibility to explain this change could be the effect of the presence of copper inside the bead. Considering that the mass susceptibility of bulk copper at 300 K was of $-0.0830 \times 10^{-6}\,\mathrm{emu\,Oe^{-1}\,g^{-1}}$, and evaluating the signal associated to the estimated mass of 0.5 mg of copper at 300 K with an applied field of 90000 Oe, the contribution of copper would be of about $-4 \times 10^{-6}\,\mathrm{emu}$ and of about $-0.017\,\mathrm{emu\,g^{-1}}$ after the normalization with mass used for data in Figure 3.19. From this estimation, a reduction of about 0.03% of M_s for the bead after copper adsorption, compared to that before copper adsorption, is expected, but it is too low to explain the difference between the data in Figure 3.15 and Figure 3.19. After these evaluations, the difference in signal intensity obtained by comparing M(H) for the bead before and after copper adsorption cannot be explained by considering only the presence of copper ions or an underestimation of the mass of the magnetic component. Copper adsorption has also another effect, which can be observed in the behavior of magnetization at high fields at 300 K. In Figure 3.19, the magnetization associated with the B1 sample before adsorption shows a maximum around 58000 Oe and then decreases with the increasing of the field. This behavior is observed also for the sample of B1 after copper adsorption (see Figure 3.19). However, the maximum has reached around 37000 Oe. After this field value, magnetization starts to decrease until the maximum field is reached. This can be explained considering the diamagnetic behavior of the copper which is relevant when the signal of magnetic nanoparticles reduced its growth. In fact, this behavior is observed for the M(H) at 300 K, but not for the M(H) at 5K in which the magnetization does not reach a maximum both in the case before and after copper adsorption.

3.6 Comparison of GO-based adsorbents

Finally, a direct comparison can be drawn between the results obtained in section 3.5.3 on alginate beads and those reported in the previous section 3.3.2 on GO nanosheet decorated with magnetite nanoparticles. In fact, the earlier study essentially represented a preliminary assessment of the same MNAs later embedded within the beads. Among the tested formulations, BGO can be considered the closest system to MNAs, and therefore it was selected as the reference material for this comparison. In Figure 3.20, the schematic procedure for the production of both MNAs and

BGOs is presented.

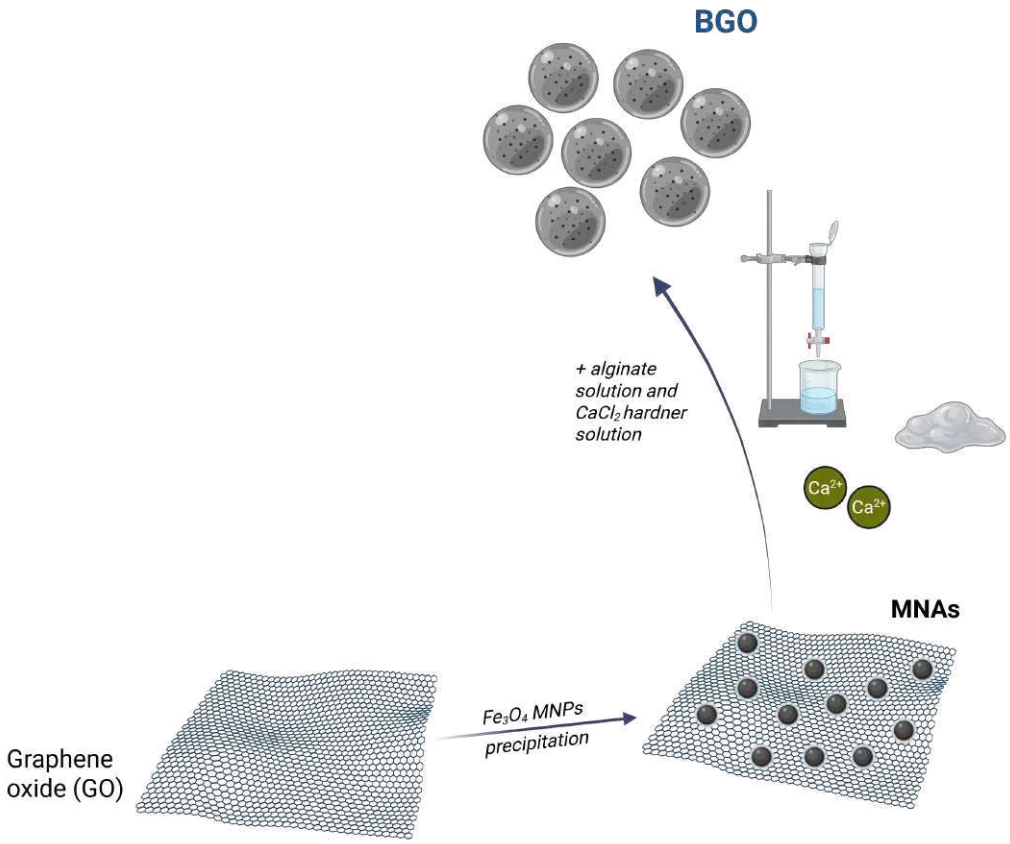

Figure 3.20: Preparation of the compared adsorbents. i) preparation of graphene oxide nanosheets decorated with the magnetic nanoparticles; ii) production of cross-linked alginate beads carrying magnetic GO-based nanosheets

In fact, a rapid analysis of the ion load as a function of concentration showed that with the beads, neither site saturation nor equilibrium were reached within the tested conditions. In contrast, for MNAs (where equilibrium was achieved), the loads displayed the expected plateau typical of saturation, while also increasing with the final concentration. This difference highlights the adsorption potential of the beads, which in the present study were tested with only 10 min of contact time. In terms of removal capacity, it was observed that for BGO the yield kept increasing in almost every test, confirming that the results were far from saturation. However, it should be emphasized that each load was estimated considering the total bead mass, which contained only 15–20% of MNAs. Since the loads and the yields were of the same order of magnitude, this indicates that MNAs were not the sole contributors to the adsorption process. This represents a crucial aspect that warrants further investigation. Since alginate is a linear anionic polysaccharide with the repeating units G and M arranged in different proportion, the polymer possess various structural domains depending on their distribution along the chain. When used to generate the beads, alginate is cross-linked by a hardening solution (typically $CaCl_2$) resulting in a three-dimensional

network that retains carboxylate and hydroxyl groups, which can act as potential active sites for adsorption [239].

It should be emphasized that the adsorption tests conducted with MNAs (Section 3.2.4) and BGOs (Section 3.4.3) differed in several fundamental aspects. In the case of 2-D MNAs, the contact time was fixed at 30 minutes, whereas for BGO it was reduced to 10 minutes due to the higher mixing efficiency associated with smaller solution volumes. The dosage also varied: MNAs were used at a concentration of 1 mg/mL, while BGOs were introduced at a fixed rate of five beads per 2 mL of solution, corresponding to approximately 0.27 mg/mL of MNAs. The separation procedure was different as well, since MNAs required magnetic recovery followed by filtration, whereas BGO could be collected directly without further steps. Finally, the concentration ranges tested diverged, with MNAs experiments limited to 5000–6000 µg/L, while for BGO values up to 10,000 µg/L were investigated in order to obtain reliable isotherm fitting.

Table 3.22 summarizes the comparison between the adsorption performance of MNAs and of BGO for the removal of Cu^{2+}, Ni^{2+}, and Cr^{3+}. The data clearly indicate that embedding MNAs into an alginate matrix substantially enhances adsorption performance compared to the 2-D nanosheets. Across all ions, the alginate beads exhibited equilibrium loads (n_{end}) and removal efficiencies (X) significantly higher than MNAs. For nickel, a 527% increase in equilibrium load was observed at $C_0 = 5000\ \mu\mathrm{g\,L^{-1}}$, whereas chromium showed a 137.5% increase at $C_0 = 2000\ \mu\mathrm{g\,L^{-1}}$. Even at lower concentrations, beads generally outperformed MNAs, though care must be taken when interpreting X values below $300\ \mu\mathrm{g\,L^{-1}}$ due to instrumental limitations. The enhancement is particularly evident when comparing specific concentrations and ions. For Cu^{2+}, at $C_0 = 1020\ \mu\mathrm{g\,L^{-1}}$, MNAs reached $n_{\mathrm{end}} = 0.97\ \mathrm{mg\,g^{-1}}$, whereas beads achieved $n_{\mathrm{end}} = 2.87\ \mathrm{mg\,g^{-1}}$, nearly tripling the adsorption capacity. At the maximum tested concentration ($C_0 = 10\,040\ \mu\mathrm{g\,L^{-1}}$), beads reached $n_{\mathrm{end}} = 29.85\ \mathrm{mg\,g^{-1}}$. Similar trends were observed for Ni^{2+} and Cr^{3+}, with beads maintaining high n_{end} values even at elevated concentrations, while MNAs showed a significant decrease in performance. Cr^{3+} on beads reached $n_{\mathrm{end}} = 19.96\ \mathrm{mg\,g^{-1}}$ and $X = 0.940$ at $C_0 = 9980\ \mu\mathrm{g\,L^{-1}}$, contrasting with lower capacity and efficiency on MNAs. The superior performance of beads arises from the combination of MNAs with the alginate matrix. Chemically, the abundant carboxyl and hydroxyl groups of alginate provide numerous binding sites for metal ions, complementing the adsorption properties of MNAs. Physically, the gel-like, hydrated, and porous structure of the beads enhances ion diffusion and accessibility to active sites, allowing for higher adsorption capacity and sustained removal efficiency across a broad concentration range. These findings are consistent with literature reports showing that alginate-based composites can increase adsorption capacity by an order of magnitude compared to planar 2-D nanocomposites [239]. In conclusion, alginate beads represent a highly effective platform for heavy metal removal from aqueous solutions, achieving higher n_{end} and more stable X values than MNAs alone, even at high initial pollutant concentrations.

In order to highlight the differences in the removal efficiency between the two materials, Figure 3.21 was constructed by selecting the experimental points that correspond to the same initial concentrations (C_0) for both MNAs and BGO. In this way, a direct comparison can be made, showing how the removal efficiency changes as a function of the ion concentration for the two adsorbents. As shown in Figure 3.21a, for copper ions MNAs display a consistently higher removal efficiency at lower concentrations, while BGO reaches higher absolute uptake values at increasing

Table 3.22: Comparison between removal efficiency of MNAs and BGO for the adsorption of Cu^{2+}, Ni^{2+} and Cr^{3+}

Ion	**MNAs**			**BGO**		
	C_0 (µg L^{-1})	n_{end} (mg g^{-1})	X [-]	C_0 (µg L^{-1})	n_{end} (mg g^{-1})	X [-]
Cu^{2+}	296 ± 1	0.27	0.912	123 ± 1	0.32	0.707
	501 ± 1	0.46	0.910	302 ± 1	0.90	0.801
	690 ± 1	0.64	0.930	587 ± 1	1.87	0.860
	1020 ± 10	0.97	0.947	838 ± 1	2.87	0.926
	2000 ± 10	1.81	0.907	2770 ± 10	7.98	0.778
	6430 ± 10	4.56	0.710	4820 ± 10	15.05	0.843
	–	–	–	10040 ± 10	29.85	0.803
Ni^{2+}	935 ± 1	0.85	0.914	443 ± 1	0.91	0.558
	1900 ± 10	1.60	0.843	1020 ± 10	3.14	0.831
	3980 ± 10	2.28	0.573	2120 ± 10	7.48	0.952
	5120 ± 10	2.90	0.566	4394 ± 10	13.97	0.856
	–	–	–	5123 ± 10	15.31	0.807
Cr^{3+}	440 ± 1	0.43	0.977	139 ± 1	0.35	0.532
	580 ± 1	0.57	0.983	225 ± 1	0.66	0.795
	1060 ± 10	1.04	0.984	273 ± 1	0.77	0.835
	1810 ± 10	1.44	0.796	423 ± 1	1.36	0.868
	4990 ± 10	2.23	0.447	605 ± 1	1.98	0.883
	–	–	–	1915 ± 1	6.65	0.934
	–	–	–	5120 ± 10	13.39	0.968
	–	–	–	9980 ± 10	19.96	0.940

C_0. A similar behavior is observed in the case of nickel (Figure 3.21b), where the efficiency of MNAs is markedly higher in the low-concentration regime, whereas BGO outperforms at larger initial concentrations. Finally, for chromium (Figure 3.21c), MNAs achieve very high efficiencies close to unity at moderate concentrations, while BGO shows a progressive increase in adsorption capacity with C_0, eventually surpassing MNAs at the highest investigated concentrations. Overall, these comparisons emphasize that MNAs are more efficient at removing trace amounts of heavy metals, making them particularly suitable for applications where very low residual concentrations are required, whereas BGO exhibits superior adsorption capacity under conditions of high pollutant load.

From these data, adsorption isotherms were constructed by plotting the equilibrium load (n_{end}) versus the initial pollutant concentration (C_0) for both MNAs and BGO (Figure 3.22. The analysis of these isotherms revealed distinct behaviors between the two nanoadsorbents. In the case of 2-D nanosheets, saturation was generally reached for most of the investigated ions within the tested concentration range. Moreover, the relative affinity of different ions remained consistent across MNAs and beads: Cu^{2+} consistently exhibited the highest adsorption capacity, whereas Cr^{3+} showed the lowest.

Langmuir isotherm parameters, obtained by fitting the experimental data (Table 3.23), highlight the remarkable enhancement of the adsorption capacity achieved by the presence of alginate in the beads.

Table 3.23: Langmuir isotherm parameters for MNAs and BGO

	Cu^{2+}			**Ni^{2+}**			**Cr^{3+}**		
	Q_{max} [mg/g]	b [L/mg]	R^2 [-]	Q_{max} [mg/g]	b [L/mg]	R^2 [-]	Q_{max} [mg/g]	b [L/mg]	R^2 [-]
MNAs	31.3	$2.75 \cdot 10^{-2}$	0.9987	5.45	0.20	0.9900	3.92	0.38	0.9978
BGO	659.55	$4.70 \cdot 10^{-3}$	0.9996	101.45	0.0354	0.9980	41.08	$9.48 \cdot 10^{-2}$	0.9997

For Cu^{2+} and Ni^{2+}, the maximum adsorption capacity (Q_{max}) increased by approximately 20-fold relative to MNAs, while for Cr^{3+}, Q_{max} was roughly 12 times higher. This substantial improvement can be attributed to the structural characteristics of the alginate matrix, which provides a high density of accessible binding sites and a porous, hydrated network that facilitates ion diffusion and accessibility to active sites. The observed ion-specific trends can be rationalized based on fundamental chemical and physical properties. Copper ions, with moderate hydrated radii and high affinity for oxygen-containing functional groups, interact strongly with both MNAs and alginate beads, leading to high Q_{max} values. Nickel(II) also exhibits good affinity, although slightly lower than copper, whereas Cr^{3+} presents a smaller hydrated radius and a stronger hydration shell, resulting in slower diffusion and steric limitations that reduce adsorption efficiency. These findings underscore the importance of considering both the chemical nature of the target ion and the structural properties of the adsorbent when designing efficient remediation systems. Overall, the Langmuir isotherm analysis confirms that alginate beads provide a significantly larger adsorption capacity and maintain effective removal across a wider concentration range compared to MNAs alone. The combination of abundant functional groups and a gel-like, hydrated architecture

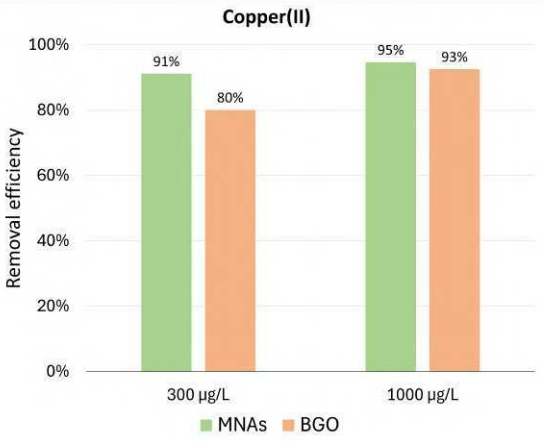

(a)

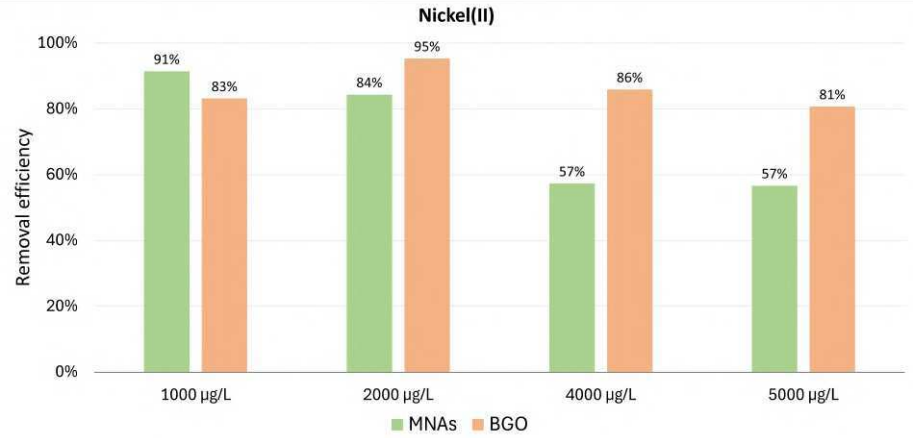

(b)

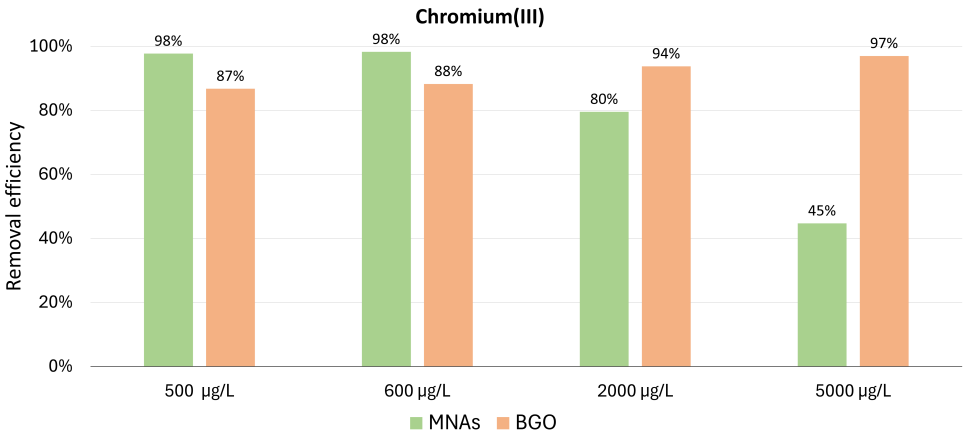

(c)

Figure 3.21: Comparison between the removal efficiency of MNAs and BGO for the adsorption of Cu^{2+}, Ni^{2+} and Cr^{3+} ions at the same initial concentrations

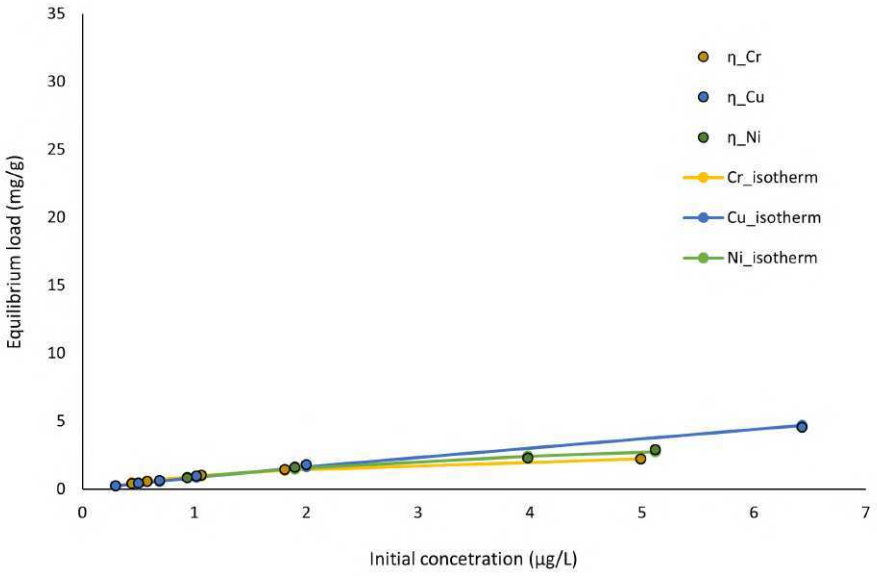

(a) MNAs

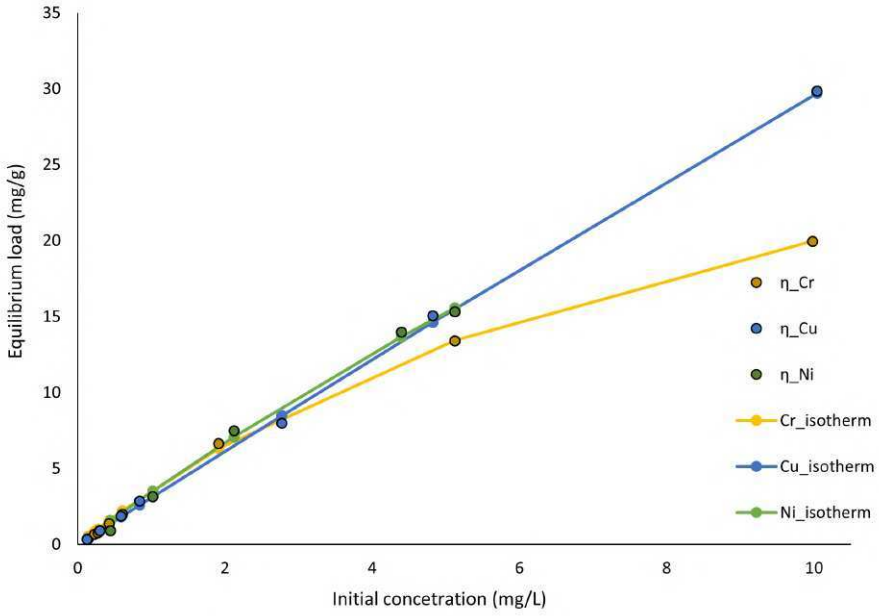

(b) BGO

Figure 3.22: Comparison between Langmuir isotherms for MNAs and BGO

allows for superior adsorption performance, highlighting the potential of alginate-based beads as highly effective adsorbents for environmental remediation applications.

3.7 Alginate functionalization with reticulating agents

Although unmodified alginate exhibits a good intrinsic ability to interact with metal ions, its adsorption efficiency is often limited by the number and nature of available functional groups. To overcome this drawback, chemical modification can be employed as a rational strategy to enhance both the density and the diversity of coordination sites. By introducing additional reactive moieties, it becomes possible not only to strengthen the affinity toward target contaminants but also to expand the range of metal species that can be effectively captured. At the same time, tailoring the chemical environment of the polymer contributes to improving stability and reusability, two crucial aspects for practical applications in water treatment. In this context, the adoption of selective oxidation and subsequent crosslinking offers a promising pathway to generate advanced alginate-based adsorbents with superior performance compared to the native material. The following section illustrates this approach and its relevance for the design of more efficient and robust adsorption systems. The general synthetic scheme is illustrated in Figure 3.23.

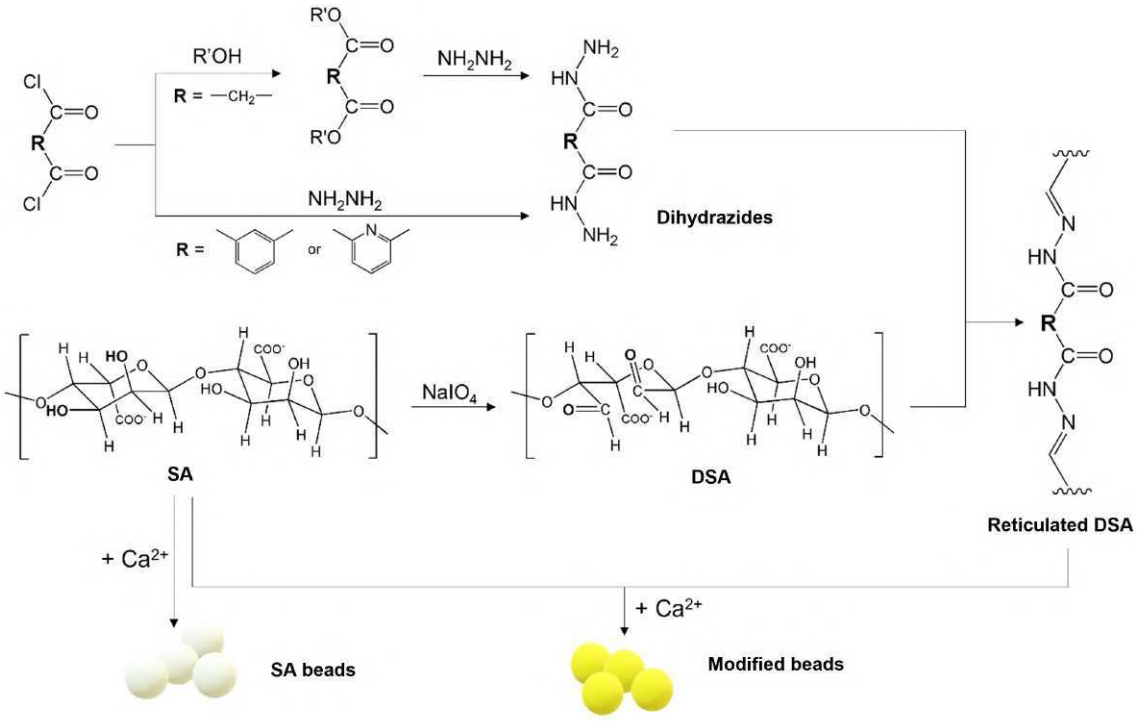

Figure 3.23: General procedure for the production of alginate-modified beads

Specifically, partial oxidation of alginate was carried out, introducing carbonyl groups that can subsequently be crosslinked through reaction with organic hydrazides. This approach involved first the partial oxidation of sodium alginate (SA) to introduce aldehyde groups, followed by

covalent crosslinking through reaction with hydrazide-based agents, forming hydrazone bonds. The final goal was the preparation of hydrogel beads via additional ionic crosslinking in a Ca^{2+} solution, which were then evaluated for adsorption and removal of transition metal contaminants.

The overall experimental sequence can be summarized as follows:

1. Partial oxidation of sodium alginate with sodium periodate to obtain dialdehyde sodium alginate (DSA).
2. Covalent crosslinking of DSA with hydrazide derivatives (isophthalic hydrazide, pyridine-2,6-dicarbohydrazide, and malonic hydrazide) to form hydrazone-linked polymers.
3. Preparation of composite alginate beads by mixing crosslinked DSA with unmodified SA.
4. Ionic crosslinking of the beads in Ca^{2+} solution to finalize hydrogel formation.
5. Evaluation of the beads for heavy metal adsorption from aqueous solutions.

This approach allows precise control over the degree of oxidation and crosslinking, providing a versatile platform for tuning hydrogel properties such as porosity, mechanical strength, and metal-binding capacity, which are crucial for efficient water purification.

3.7.1 Oxidation of Alginate

Alginate oxidation is a crucial step in the functionalization process with hydrazide crosslinkers, since these compounds readily react with free carbonyl groups to form the corresponding hydrazones. The degree of oxidation, corresponding to the number of aldehyde groups formed along the polymer chain, directly determines the extent of crosslinking that can potentially be achieved.

The synthesis of dialdehyde alginate (DSA) proceeds through the oxidation of the hydroxyl groups in the repeating units, in particular the guluronic (G) residues of the polymer chain. In these units, the anionic carboxyl group is located further from the site attacked by the negatively charged periodate ion. Specifically, the hydroxyl groups involved are located at the C2 and C3 positions.

Sodium periodate ($NaIO_4$), the oxidizing agent, interacts with the two hydroxyl groups of the same repeating unit, oxidizing the two carbon atoms, causing ring opening, and reducing iodine's oxidation state from +7 to +5.

Since the reaction preferentially targets guluronic (G) units, which are involved in the coordination of divalent metal centers and in crosslinking, the oxidation process significantly affects gel formation, mechanical properties, and adsorption capacity.

3.7.2 Reticulating agents

Crosslinking agents are generally small molecules bearing two functional groups suitable for covalent anchoring onto different chains of the polymer. The formation of interchain crosslinks affects the solubility of the resulting derivative. However, by an appropriate choice of the linker structure, it is also possible to introduce new functional groups, including coordinating moieties.

In the case examined in this work, hydrazide-based crosslinkers were selected. Hydrazide groups can readily react with the aldehyde functionalities of oxidized alginate, leading to the formation of the corresponding hydrazones.

This type of crosslinking was proposed by T. Shi *et al.* [227, 228], who employed the hydrazides, exploiting not only their crosslinking effect but also the potential coordinating contribution of the nitrogen atoms within the hydrazone groups. When comparing the metal adsorption capacity of unmodified alginate with that of alginate functionalized using different linkers, the latter exhibited a significantly higher adsorption performance. Moreover, crosslinking with terephthalic hydrazide improved the mechanical properties of alginate in comparison with the adipic linker. This enhancement can be mainly ascribed to the more rigid structure of the aromatic bridge relative to the aliphatic one. In that work, the formation of beads was not proposed, since the obtained materials were insoluble in water. Instead, spongy adsorbents were prepared, which may represent a limitation during separation from the aqueous matrix due to their irregular and undefined shape.

In our study, to investigate the role of different crosslinking structures on the performance of oxidized alginate, three hydrazide-based linkers were selected. The choice was made to include both aromatic and aliphatic bridges, in order to assess how the rigidity and electronic nature of the linker backbone influence the adsorption behavior and the overall stability of the resulting materials. Specifically, the linkers employed were isophthalic hydrazide, pyridine-2,6-dicarbohydrazide, and malonic hydrazide. Their structure are shown in Figure 3.24.

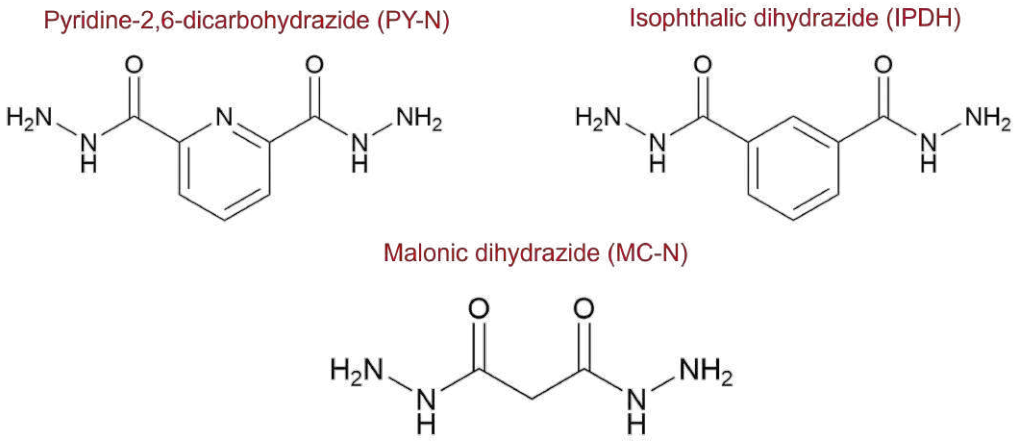

Figure 3.24: Linkers employed in alginate functionalization

Isophthalic hydrazide Isophthalic hydrazide is an aromatic linker containing two hydrazide groups positioned meta with respect to each other on the benzene ring. The rigidity of the aromatic backbone contributes to enhanced mechanical stability of the crosslinked alginate network, while the conjugated π-system may also play a role in modulating adsorption properties.

Pyridine-2,6-dicarbohydrazide Pyridine-2,6-dicarbohydrazide combines an aromatic heterocycle with two hydrazide functionalities located in positions 2 and 6. In addition to providing rigidity to the network, the nitrogen atom of the pyridine ring can potentially act as a coordinating site, offering further interactions with metal ions and therefore improving adsorption capacity.

Malonic hydrazide Malonic hydrazide is a small aliphatic linker characterized by two terminal

hydrazide groups attached to a short three-carbon chain. Unlike the aromatic linkers, its flexibility can facilitate chain mobility within the alginate matrix. Although less rigid, its bifunctional nature still enables efficient crosslinking while providing a useful comparison with aromatic analogues.

All the hydrazides investigated in this work were prepared from the corresponding acyl halides (Figure 3.25) through a nucleophilic substitution reaction with hydrazine. This straightforward synthetic route ensures good yields and allows the introduction of the hydrazide functionality in a wide range of acyl derivatives.

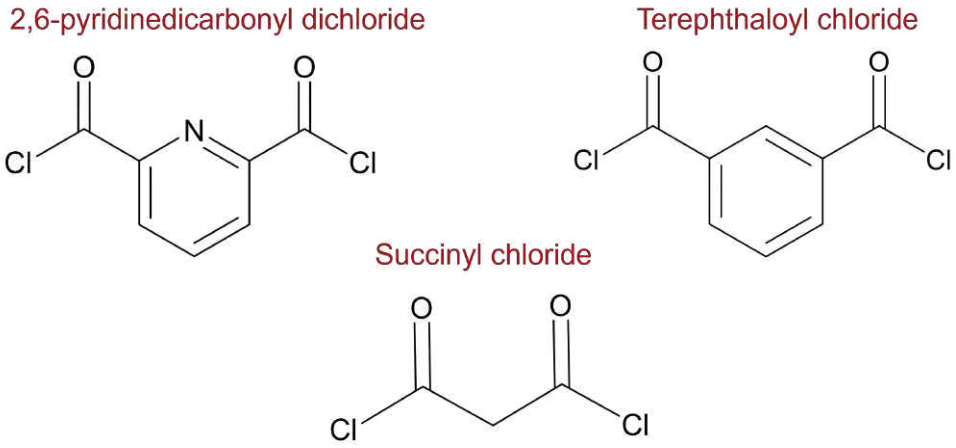

Figure 3.25: Acyl halides employed in hydrazide synthesis

Synthesis of isophthalic hydrazide (IPDH)

To obtain isophthalic hydrazide (IPDH), 0.512 g of isophthaloyl chloride (IPC) were dissolved in 15 mL of EtOH and treated with 1.0 mL of triethylamine (TEA) and 4.0 mL of hydrazine monohydrate (NH_2–NH_2). The mixture was stirred for a few minutes and reacted in a microwave reactor for 1 h at 85 °C under stirring at 600 rpm. After completion of the reaction, the solution was transferred into a 50 mL Falcon tube, cooled to room temperature, and stored at -20°C overnight. The precipitate was collected by filtration through a Gooch crucible, washed with 10 mL of ethanol, and dried in a vacuum desiccator for 12 h. This procedure afforded 0.387 g of IPDH as a crystalline white solid, corresponding to an 85% yield (theoretical yield: 0.453 g).

Synthesis of pyridine-2,6-dicarbohydrazide (PY-N)

To obtain pyridine-2,6-dicarbohydrazide (PY-N), 0.507 g of dichloro-2,6-pyridine dicarboxylate (PY-C) were dissolved in 15 mL of EtOH and treated with 1.0 mL of triethylamine (TEA) and 4.0 mL of hydrazine monohydrate (NH_2–NH_2). The mixture was stirred for a few minutes and reacted in a microwave reactor for 1 h at 85 °C under stirring at 600 rpm. After completion, the solution was transferred into a 50 mL Falcon tube, cooled to room temperature, and stored at -20°C overnight. The precipitate was collected by filtration through a Gooch crucible, washed with 10 mL of ethanol, and dried in a vacuum desiccator for 12 h, affording 0.408 g of PY-N as a crystalline white solid, corresponding to a 98% yield (theoretical yield: 0.414 g).

Synthesis of malonic hydrazide (MC-N)

Malonic hydrazide (MC-N) is the third and final crosslinking agent synthesized. Its precursor, malonyl chloride (MC), is an extremely reactive liquid that requires careful handling, since it cannot come into contact with water, alcohols, or other protic nucleophiles. For this reason, all reactions involving this compound were carried out under a nitrogen flow, either in a round-bottom flask or inside the microwave reactor tube. Because of its high reactivity toward oxygen- and nitrogen-containing nucleophiles, the corresponding reactions are usually highly exothermic and may cause overheating of the solution. This makes synthetic operations in alcoholic solvents, or the direct use of hydrazine hydrate, particularly difficult, not only due to the formation of vapors but also because of unwanted by-products such as malonic acid from hydrolysis. For these reasons, the direct route to the hydrazide was abandoned. Instead, a sequential approach was adopted: diethyl malonate (MC-E) was first synthesized and isolated as a stable intermediate, and only afterwards converted into the target hydrazide.

Thus, malonic hydrazide (MC-N) was prepared in two steps. First, 0.5 mL of malonyl chloride ($\rho = 1.44$ g/mL) were added to 20 mL of THF under constant stirring, followed by 15 mL of MeOH. The mixture was stirred at room temperature for 3 h. After addition of excess Na_2CO_3 to neutralize the reaction, the solvent was evaporated, and the residue was dissolved in CH_2Cl_2, filtered, and washed with 15 mL of dichloromethane. Evaporation of the solvent afforded 0.420 g of diethyl malonate (MC-E) as a colorless liquid, corresponding to an 88% yield (theoretical yield: 0.672 g). In the second step, 0.208 g of MC-E were dissolved in 15 mL of EtOH and treated with 1.0 mL of triethylamine (TEA) and 1.0 mL of hydrazine monohydrate (NH_2–NH_2). The mixture was stirred until homogeneous and reacted under microwave irradiation (100 °C, 30 min, 600 rpm). After cooling and storage at -20°C overnight, the precipitate was collected by filtration, washed with 10 mL of ethanol, and dried under vacuum to afford 0.188 g of malonic hydrazide (MC-N) as a crystalline white solid, corresponding to a 95% yield (theoretical yield: 0.130 g).

Synthesis of dialdehyde alginate (DSA)

Dialdehyde alginate (DSA) was prepared via partial oxidation of sodium alginate (SA) using sodium periodate ($NaIO_4$), as illustrated in Figure 3.26. Three reactions were performed using varying molar ratios of $NaIO_4$ to guluronic acid units (G) of SA: A (1:0.7), B (1:1.5), and C (1:3.2).

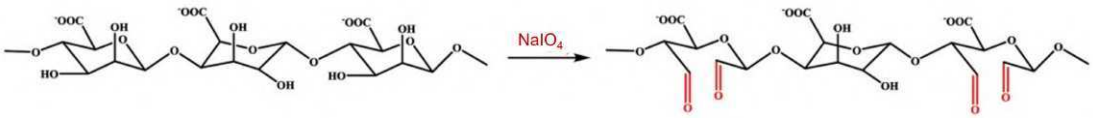

Figure 3.26: Oxidation of Sodium Alginate to DSA

Sodium alginate was weighed and dissolved in 100 mL of EtOH in a 250 mL flask completely wrapped in aluminum foil to avoid light exposure. Corresponding amounts of $NaIO_4$ were dissolved in water as follows:

- A: 10.103 g SA in 100 mL EtOH with 5.022 g $NaIO_4$ in 80 mL H_2O;
- B: 10.097 g SA in 100 mL EtOH with 2.513 g $NaIO_4$ in 40 mL H_2O;

- C: 10.122 g SA in 100 mL EtOH with 1.252 g $NaIO_4$ in 20 mL H_2O.

The aqueous $NaIO_4$ solution was added dropwise using a 50 mL glass burette under continuous magnetic stirring. After addition, the reaction mixture was stirred at 45 °C for 24 h. After completion, the precipitate was collected by filtration, washed multiple times with an ethanol/water solution (v/v = 5:4), and dissolved in 100 mL of deionized water. The solution was placed in a 3500 Da dialysis membrane within a 500 mL cylinder of deionized water and dialyzed for 3 days, changing the water every hour on the first day and twice daily on the following days. After dialysis, the membrane was removed, rinsed with deionized water, and the content was divided into 50 mL Falcon tubes, frozen at -80°C for at least 5 h, and lyophilized for 3 days (≤ 30 mL solution per tube is recommended). The resulting DSA was obtained as a white powder, ready for crosslinking reactions. All oxidation reactions gave an 85% yield, differing in the number of oxidized guluronic acid units.

3.7.3 Crosslinking of DSA with Hydrazides and Beads Formation

Crosslinking of DSA with Hydrazides

All crosslinking reactions were carried out on the oxidized derivative obtained in reaction A shown in the previous section.
DSA crosslinked with IPDH: In a 6 mL microwave vial (G10), 0.051 g of DSA were mixed with 0.032 g of IPDH and 5.0 mL of anhydrous MeOH, heated at 80 °C for 30 min under magnetic stirring at 600 rpm. After the reaction, the solution was transferred to a 15 mL Falcon tube, left in the freezer at -20°C overnight, filtered through a Gooch crucible with 10 mL of MeOH, and dried in a vacuum desiccator. 0.062 g of DSA-IPDH yellow solid were obtained (70% yield).
DSA crosslinked with PY-N: 0.051 g of DSA and 0.032 g of PY-N were treated under identical conditions. The solution was processed as above and 0.058 g of DSA-PY-N yellow solid were obtained (65% yield).
DSA crosslinked with MC-N: 0.053 g of DSA and 0.022 g of MC-N were treated under the same conditions. The solution was processed as above and 0.075 g of DSA-MC-N yellow solid were obtained (64% yield).

Formation of Beads with SA and Crosslinked DSA

To form beads through additional Ca^{2+} crosslinking, each crosslinked DSA derivative was mixed with unmodified sodium alginate (SA). In fact, the crosslinked derivatives of DSA turned out to be insoluble both in water and also in all other polar solvents miscible with it. This behavior made it impossible to prepare beads directly by Ca^{2+}-induced gelation through the standard dripping technique. To overcome this limitation, the idea was to disperse the crosslinked derivatives within a solution of unmodified sodium alginate (SA). Thanks to its intrinsic ability to gel into spherical structures upon contact with Ca^{2+} ions, SA could encapsulate the crosslinked material and generate composite beads, still suitable for the intended applications. Several preliminary trials were carried out to optimize the balance between the two components. In the first approach (mixtures A), equal weights of SA and crosslinked DSA were used (0.075 g each, dissolved in 15 mL of water). In a second approach (mixtures B), the proportion of crosslinked DSA was lowered (0.121 g of SA and

0.053 g of crosslinked DSA, in the same solvent volume). The preparation was tested for each derivative varying the ratio of SA to crosslinked DSA as follows:

Beads with DSA-IPDH:

- A: 15 mL deionized water, 0.153 g composite (0.075 g DSA-IPDH + 0.075 g SA), vortexed and sonicated for 2 h.
- B: 15 mL deionized water, 0.151 g composite (0.053 g DSA-IPDH + 0.121 g SA), vortexed and sonicated for 2 h.

Meanwhile, 5.13 g of $CaCl_2$ were dissolved in 100 mL of deionized water under stirring until clear. The alginate composite solution was added dropwise with a burette under constant stirring. Bead formation was observed only for the type B mixtures. Once obtained, the beads were left to stand in the beaker for approximately 1 h to allow complete gelation. They were then collected and transferred into 50 mL Falcon tubes, where a washing protocol was applied in order to remove the excess Ca^{2+} ions. This consisted of replacing the supernatant water three times per day over a period of three days, after which the beads were ready for further characterization and adsorption tests.

Beads with DSA-PY-N:

- A: 15 mL deionized water, 0.152 g composite (0.075 g DSA-PY-N + 0.075 g SA), vortexed and sonicated for 2 h.
- B: 15 mL deionized water, 0.151 g composite (0.051 g DSA-PY-N + 0.122 g SA), vortexed and sonicated for 2 h.

Meanwhile, 5.011 g of $CaCl_2$ were dissolved in 100 mL of deionized water under stirring until clear. The alginate solution was added dropwise under stirring. Beads formed only in case B and were processed as above.

Beads with DSA-MC-N:

- A: 15 mL deionized water, 0.151 g composite (0.075 g DSA-MC-N + 0.075 g SA), vortexed and sonicated for 2 h.
- B: 15 mL deionized water, 0.152 g composite (0.051 g DSA-MC-N + 0.101 g SA), vortexed and sonicated for 2 h.

Meanwhile, 5.141 g of $CaCl_2$ were dissolved in 100 mL of deionized water under stirring until clear. The solution was added dropwise under stirring. Beads formed only in case B and were processed as above.

Beads of SA alone: 0.152 g of SA were dissolved in 15 mL deionized water, vortexed and sonicated

for 2 h, then added dropwise to 100 mL of $CaCl_2$ solution (5.14 g) under stirring. Beads were left for 1 h, transferred to a 50 mL Falcon tube, and washed three times per day for 3 days to remove excess ions.

The results showed a clear difference between the two formulations. In mixtures A, the crosslinked component remained poorly dispersed, while in mixtures B the higher relative amount of SA favored mutual interactions in solution. Under these conditions, the crosslinked derivatives became more compatible with the medium, and the system turned homogeneous. Based on this evidence, the type B mixtures were chosen for further experiments, as they provided a stable and workable basis for bead formation.

3.7.4 ESEM characterization

The morphological structure of the composite beads can to play a significant role. Environmental scanning electron microscopy (ESEM) of sectioned beads revealed that PY-N beads are relatively compact and poorly porous, whereas IPDH beads exhibit a spongy and highly porous structure (Figure 3.27).

The higher porosity could facilitate the diffusion of divalent cations from the aqueous solution into the beads and vice versa, enhancing the overall adsorption capacity. Elemental analyses (EDX) of beads with DSA PY-N and DSA IPDH are reported in Figures 3.28 and Figure 3.29, respectively.

The higher chloride content observed in PY-N beads may be attributed to the greater difficulty in exchanging ions with the wash solution in the more compact beads compared to the more porous IPDH beads.

3.7.5 Adsorption tests with modified beads

To evaluate the adsorption capacity of the composite beads containing cross-linked DSA and unmodified SA to transition metal cations, preliminary tests were carried out using aqueous solutions of Cu^{2+} and Co^{2+}. Both ions absorb in the visible region, allowing their concentrations to be monitored by UV-visible spectroscopy. Absorption spectra were acquired in the visible range at the absorption maximum for Co^{2+}. In the case of Cu^{2+} solutions, since the absorption maximum occurs at wavelengths beyond the measurable range, a wavelength was selected that ensured a high absorbance-to-concentration ratio (i.e., a high molar extinction coefficient) while remaining within the linear range described by the Beer-Lambert law. For both ions, calibration curves were constructed at the chosen wavelengths. The calibration curve for copper(II) was obtained from absorbance measurements at 680 nm on four standard solutions of known concentration. Similarly, the calibration curve for cobalt(II) was determined from absorbance measurements at 508 nm using four standard solutions of known concentration. Figure 3.30 represents the general setup for the adsorption tests.

Copper(II) adsorption tests Adsorption tests with the composite beads were conducted by adding a defined mass of each adsorbent (approximately 0.500 g) to a fixed volume (3 mL) of the stock solution at an initial Cu^{2+} concentration C_0, equals to 0.62 mg/mL. The suspensions were stirred for 1 h, and the supernatant was then collected for UV-visible measurements.

Cobalt(II) adsorption tests Adsorption tests for Co^{2+} were conducted in a manner entirely analogous to those described for Cu^{2+}. Equal masses of each adsorbent type (approximately 0.500

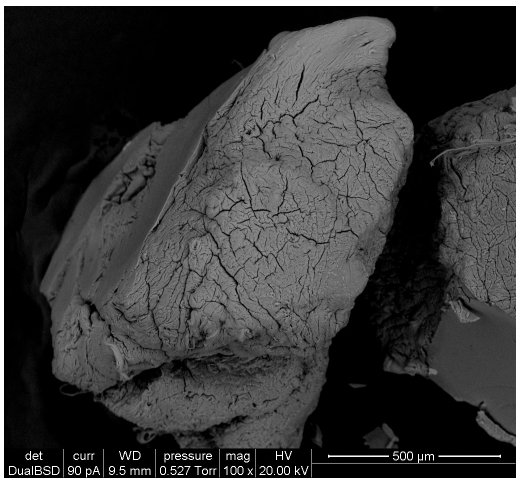

(a) ESEM 500 image SA+DSA-PY-N

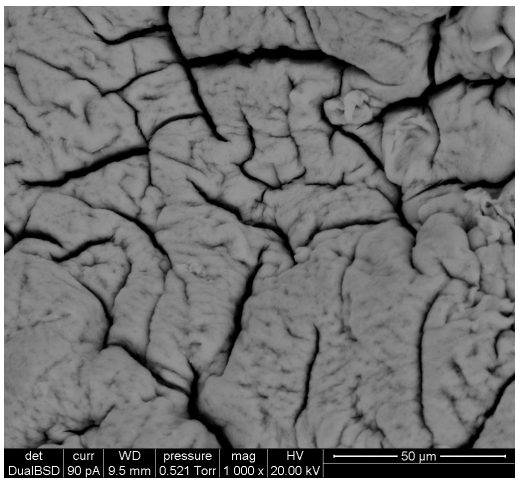

(b) ESEM 50 image SA+DSA-PY-N

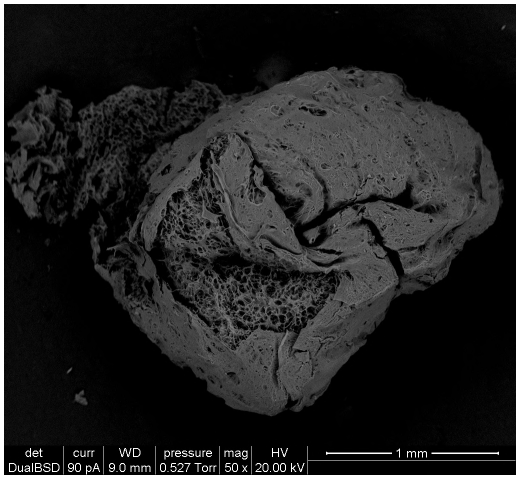

(c) ESEM 1 mm image SA+DSA-IPDH

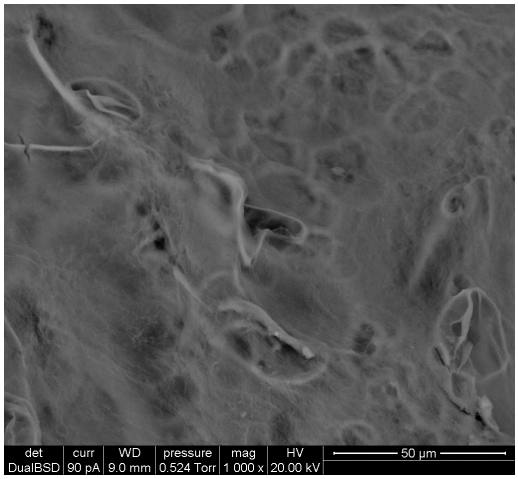

(d) ESEM 50 image SA+DSA-IPDH

Figure 3.27: ESEM images of modified beads

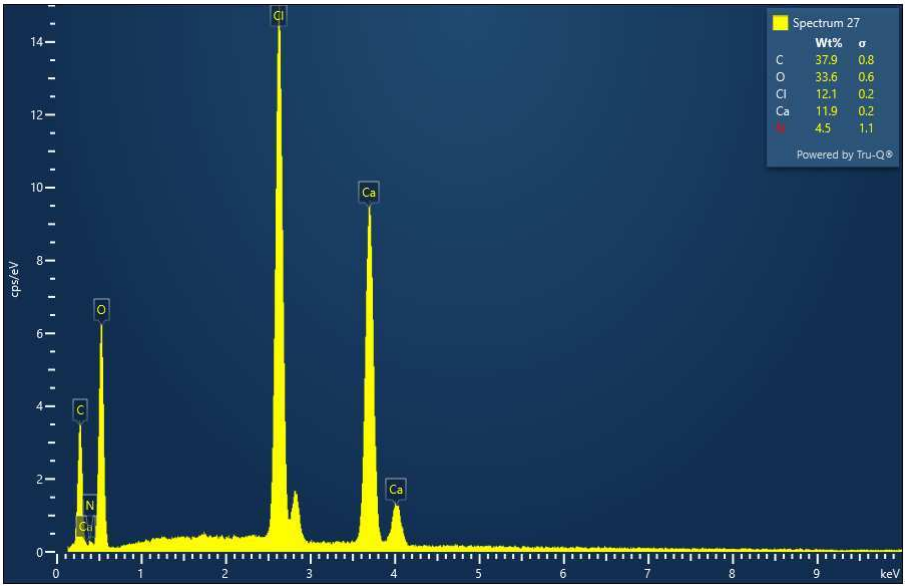

Figure 3.28: EDX PY-N bead

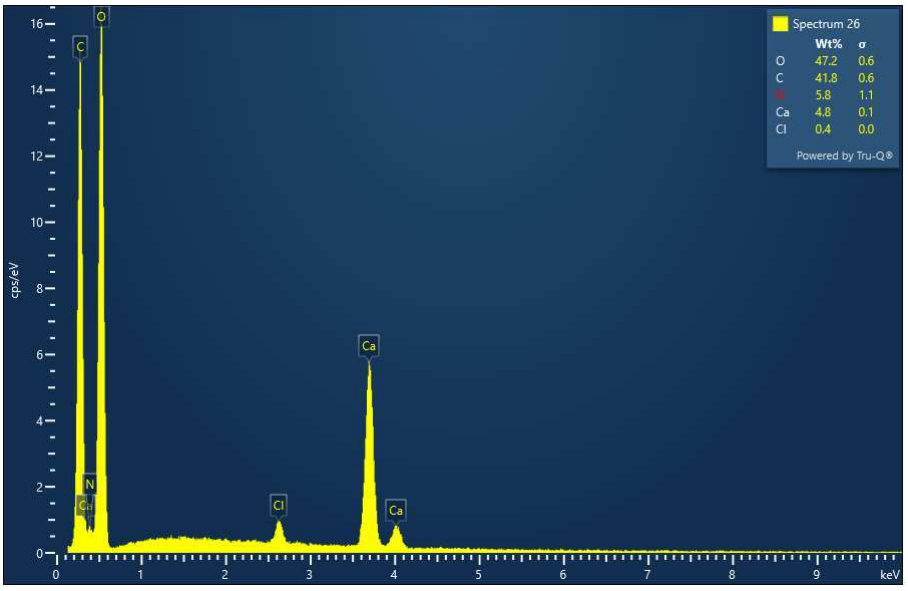

Figure 3.29: EDX IPDH bead

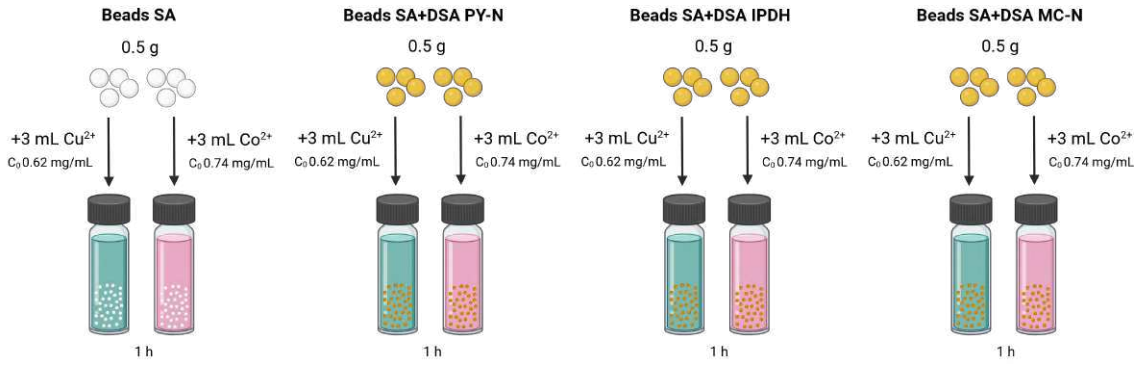

Figure 3.30: Schematic representation of the adsorption tests setup

g) were added to a defined volume (3 mL) of the stock solution at an initial Co^{2+} concentration C_0 , equals to 0.74 mg/mL. The suspensions were stirred for 1 h, after which the supernatants were collected and analyzed by UV-visible spectroscopy.

Table 3.24 summarizes the performance of the adsorbents produced by reporting the residual concentrations of Cu^{2+} and Co^{2+}, along with the corresponding removal efficiencies, for solutions treated with modified beads and with the sodium alginate beads (SA).

Table 3.24: Characterization of Cu^{2+} and Co^{2+} solutions treated with modified beads and sodium alginate (SA)

	Cu^{2+}		**Co^{2+}**	
Adsorbent	C_{final} (mg/mL)	Reduction %	C_{final} (mg/mL)	Reduction %
-	0.62	0	0.74	0
SA	0.38	38	0.60	20
SA+DSA PY-N	0.33	46	0.52	31
SA+DSA IPDH	0.28	55	0.46	38
SA+DSA MC-N	0.33	46	0.49	34

As shown in Table 3.24, the composite beads with crosslinked alginate generally exhibit a higher adsorption capacity for Cu^{2+} cations. In particular, the beads containing DSA IPDH (featuring an isophthalic bridge) reduce the Cu^{2+} concentration by more than 50%. A similar adsorption trend is observed for Co^{2+}, suggesting that the two metal cations follow a comparable adsorption mechanism. For cobalt as well, the beads containing DSA IPDH demonstrate the highest adsorption capacity among the tested adsorbents.

The composite beads containing hydrazone-crosslinked alginate exhibited an increased adsorption capacity for divalent cations compared to unmodified alginate. It can therefore be concluded that the presence of hydrazone groups promotes the complexation of transition metal centers, making these derivatives promising candidates for applications in the treatment of contaminated water. However, the hypothesis that the PY-N derivative could have a higher adsorption capacity

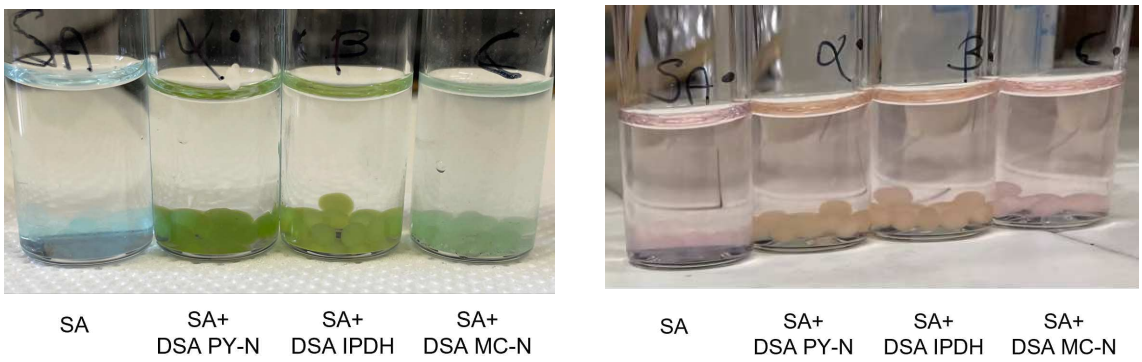

(a) Cu^{2+} adsorption tests

(b) Co^{2+} adsorption tests

Figure 3.31: Solutions after the ions adsorption tests

due to the presence of nitrogen in the pyridine ring, providing an additional coordination site, was not confirmed in comparison with the IPDH derivative. Nevertheless, it is in accordance with the observed more porous structure of the beads containing DSA IPDH, which can facilitate ion transport and coordination.

3.8 Conclusions

In this chapter, magnetic nanostructured adsorbents (MNAs) were developed and tested for the removal of different metal ions (Cr^{3+}, Ni^{2+}, and Cu^{2+}) at 298 K. From these experiments, single-ion adsorption isotherms were determined and subsequently applied to six different mixtures containing all three metal ions. The maximum adsorption efficiencies observed for single-ion solutions were over 98% for chromium(III), 94% for copper(II), and 91% for nickel(II). For the mixed-ion solutions, the maximum removal efficiency slightly decreased for nickel(II) (up to 86%), while the efficiencies for chromium(III) and copper(II) were largely unaffected. Thus, the proposed MNAs demonstrated good removal efficiency even for mixtures with highly varying concentrations of Cr^{3+}, Ni^{2+}, and Cu^{2+}, and the predictions of a competitive Langmuir model were confirmed by experimental results. The ability to remove a mixture of pollutants in a single step is particularly valuable for wastewater treatment, as real-world samples typically contain multiple contaminants rather than a single component.

Moreover, it was demonstrated that magnetic nanocomposite adsorbents, prepared by embedding magnetite nanoparticles and graphene oxide decorated with them into alginate beads, represent a promising class of materials for wastewater treatment. Specifically, three different types of beads have been produced. BGO consists of nanocomposite beads containing graphene oxide (GO) sheets decorated with magnetite (Fe_3O_4) nanoparticles, prepared through a straightforward coprecipitation method in the presence of GO. For comparison, B1 and B2 were synthesized by dispersing only magnetite nanoparticles into alginate beads, with different Ca^{2+} concentrations in the cross-linking solution to modulate the bead structure. Among these tested beads formulations, bead B1 showed the best overall performance across all investigated metal ions. The experiments confirmed that 10 min of contact time was not sufficient to reach equilibrium; nevertheless, com-

parison with literature data suggests that the equilibrium time should not be much longer. This aspect indicates that such adsorbents can achieve high removal yields within relatively short operating times, which is advantageous for industrial application. In addition to their adsorption performance, the beads exhibited favorable technological characteristics: they were homogeneous in shape and size, easy to reproduce, and cost-effective. Their suitability for implementation in packed columns makes them compatible with established adsorption technologies. Furthermore, their intrinsic magnetic behavior offers additional opportunities, such as magnetic stirring or induction heating, which could be exploited to enhance regeneration efficiency. Overall, these findings confirm the potential of the proposed magnetic nanocomposite beads as versatile and scalable adsorbents.

Moreover, alginate was chemically modified with the aim of improving its adsorption performance toward transition metal ions. To achieve this, sodium alginate was first partially oxidized to obtain dialdehyde sodium alginate (DSA), which was then covalently crosslinked with different hydrazide derivatives—namely isophthalic hydrazide, pyridine-2,6-dicarbohydrazide, and malonic hydrazide—forming hydrazone-linked polymers with an increased density and diversity of coordination sites. Composite hydrogel beads were subsequently prepared by blending the modified alginate with pristine SA and stabilized through ionic crosslinking with Ca^{2+}. A preliminary evaluation of the adsorption capacity of the prepared modified beads was carried out towards two transition metal ions, Cu^{2+} and Co^{2+}, and compared with that of pristine alginate, revealing a significant improvement. It can therefore be stated that the presence of crosslinking hydrazone groups leads to a positive modification of the adsorption capacity, making these derivatives good candidates for application in the treatment of contaminated water. Furthermore, it was found that alginate crosslinked with IPDH, by providing a porous structure to the beads, exhibits a higher adsorption capacity compared to the other derivatives analyzed.

4 Graphitic Carbon Nitride Derivatives For Wastewater Depuration

In the framework of sustainability, developing new technologies to improve the current linear water-use system is of increasing importance. Wastewater represents not only a disposal challenge but also a potential resource for the recovery of valuable materials, and when adequately treated, it can be almost entirely recycled, establishing the foundation for a circular economy in water management. Organic contaminants, such as synthetic dyes and emerging pollutants—particularly pharmaceuticals—pose significant challenges for conventional treatment methods due to their chemical stability, persistence, and low biodegradability. These compounds often resist biological degradation and can accumulate in the environment, causing ecological and human health risks even at trace concentrations [136]. In this context, photocatalysis has emerged as a promising strategy to overcome these limitations, as it can generate highly reactive species capable of mineralizing recalcitrant organic molecules. Graphitic carbon nitride (g-C_3N_4) is a particularly appealing photocatalyst, offering stability, abundance, non-toxicity, and straightforward preparation, while its electronic properties allow the effective production of radicals under visible light [246]. By enabling the degradation of both dyes and pharmaceutical residues, g-C_3N_4-based photocatalytic systems provide a sustainable solution to the persistent problem of organic pollutant removal, supporting water reuse and contributing to a circular economy in water management [247].

4.1 Introduction

g-C_3N_4 is a yellow solid with stacked nanosheet structure that can be synthesized from easily applicable, economic, and eco-friendly procedures, such as thermal condensation, starting from different low-cost nitrogenated precursors such as urea, melamine, dicyandiamide, and thiourea.

In response to the increasing demand for efficient and sustainable photocatalytic materials, graphitic carbon nitride (g-C_3N_4) has emerged as a particularly promising candidate for photodegradation applications of contaminants of emerging concern. The start of carbon nitride research dates back to 1834, when Liebig first synthesized a polymer with a linear structure of heptazine units linked by secondary nitrogen, termed "melon". Later, Teter and Hemley [248] reported five possible structures of C_3N_4: graphitic, α-C_3N_4, β-C_3N_4, cubic, and pseudocubic. Among these, triazine (C_3N_3) and tri-s-triazine/heptazine (C_6N_7) rings constitute the two main building units of g-C_3N_4 allotropes. It was subsequently demonstrated that the tri-s-triazine-derived structure is the most stable under ambient conditions, in agreement with density functional theory (DFT) calculations [249]. The polymeric nature of g-C_3N_4 allows for straightforward tuning of its surface properties at the molecular level. Furthermore, g-C_3N_4 exhibits remarkable physicochemical stability and an interesting electronic structure with a moderate band gap of 2.7 eV. The material favors the formation of C–N bonds while suppressing electron delocalization in the π system. Thermogravimetric analysis (TGA) further confirms that g-C_3N_4 is thermally stable up to 600 °C, chemically inert, and insoluble in organic solvents, alkali, and acids, thereby presenting it as a resilient material under ambient conditions [250].

The intrinsic structure of the precursor, along with the type of thermal processing, exerts a decisive influence on the physicochemical properties of graphitic carbon nitride, enabling the preparation of g-C_3N_4-based materials with tailored functionalities such as light absorption, surface charge, porosity, and photoluminescence. Different synthetic strategies have yielded a wide variety of morphologies, including nanosheets, nanorods, nanotubes, and nanowires [251]. Despite its numerous advantages, g-C_3N_4 also presents several drawbacks, such as a relatively low specific surface area, structural disorder, limited visible-light absorption range, and poor processability in bulk form, which reduce its dispersibility in both aqueous and organic media. To overcome these limitations, multiple strategies have been explored, including morphological modification [252], surface grafting [253], non-covalent doping [254], and copolymerization [255]. Functionalization by introducing organic species, surfactants, or polymers through covalent and non-covalent approaches has proven effective in enhancing the physicochemical performance of g-C_3N_4. In particular, molecular doping and chemical derivatization represent some of the most widely employed approaches to tune its electronic properties, exploiting the reactivity of C–N linkages as well as the free –NH_2 groups present in the g-C_3N_4 network.

The main precursors used in this work is melamine ($C_3H_4N_6$) also called 1,3,5-triazine-2,4,6 triamine), a white powder mainly used as a starting material for the manufacture of synthetic resins. In fact, g-C_3N_4 can be synthesized from different low-cost nitrogen-rich compounds, but the use of melamine allows for a higher mass yield compared to using for instance urea. Melamine is obtained by conversion of calcium cyanamide into dicyandiamide, that when heated above its melting point, produces melamine. These precursors are subjected to calcination at temperatures ranging from 500 to 600°C in air or an inert atmosphere, resulting in a yellow powder with a lamellar morphology. By pyrolysis, polycondensation reactions take place, leading to the formation of longer chains with the elimination of small molecules. In the case of melamine, tri-s-triazine units are produced, with the elimination of NH_3 molecules in each polycondensation reaction, forming a packed-sheets structure of graphitic carbon nitride. The reaction is shown in figure 4.1.

4.2 State of art

Graphitic carbon nitride (g-C_3N_4) has emerged in recent years as one of the most promising metal-free photocatalysts, due to its unique combination of physicochemical stability, visible light photoactivity, and tunable electronic structure. Structurally, g-C_3N_4 is a polymeric semiconductor composed entirely of carbon and nitrogen atoms arranged in a layered architecture analogous to graphite. However, unlike graphite, where carbon atoms form a continuous hexagonal network, g-C_3N_4 is built from tri-s-triazine (heptazine) units interconnected by planar amino bridges, forming a two-dimensional network with strong in-plane covalent bonding and weak interlayer van der Waals forces [256].

The electronic structure of g-C_3N_4 features a medium band gap of approximately 2.7 eV, which makes it responsive to visible light up to around 460 nm [257]. This enables it to act as a promising photocatalyst under solar illumination. Moreover, the valence and conduction band positions are suitably aligned for engaging in redox reactions, including water splitting and organic pollutants degradation. Its thermal and chemical stability are also remarkable, withstanding temperatures up to 600°C in air and maintaining integrity in acidic and basic environments [258]. These features

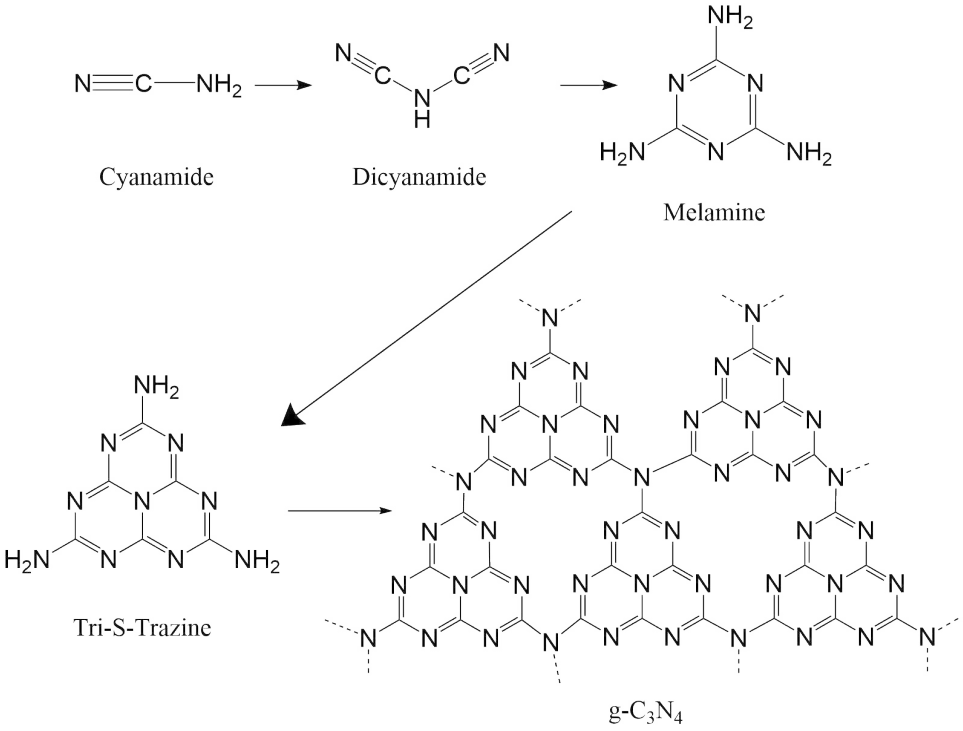

Figure 4.1: Mechanism of the synthesis of g-C_3N_4 from different precursors

position g-C_3N_4 as a durable and environmentally benign material for photocatalytic applications. The synthesis of g-C_3N_4 is straightforward and cost-effective, typically carried out via thermal polycondensation of nitrogen-rich precursors. Despite the simplicity of this method, bulk g-C_3N_4 often suffers from low surface area and poor charge carrier mobility, prompting the development of various strategies to enhance its properties.

The electronic structure of g-C_3N_4 can be understood by examining its highest occupied molecular orbital (HOMO) and lowest unoccupied molecular orbital (LUMO) [259]. The HOMO is largely dominated by nitrogen 2p and 2s orbitals, with smaller contributions from carbon 2p and 2s orbitals, while the LUMO is mostly formed by carbon 2p and nitrogen 2p orbitals [260]. Computational studies suggest that two primary electronic transitions are present in g-C_3N_4: the π-π^* transition and the n-π^* transition (Figure 4.2), which correspond to absorption edges around 460 nm and 600 nm, respectively [261].

The characteristic absorption bands of g-C_3N_4 arise predominantly from interactions between the lone pairs of nitrogen atoms and the p orbitals of carbon and nitrogen [262]. The π-π^* transition involves the excitation of electrons from bonding π orbitals to anti-bonding π^* orbitals, producing an absorption edge near 460 nm and defining a bandgap of approximately 2.7 eV [263, 264]. This transition is crucial for the material's ability to harvest visible light, thereby enabling its photocatalytic activity. Additionally, the sp^2-hybridized nitrogen atoms in the tri-s-triazine units possess lone pairs with energies higher than the π bonding orbitals (Figure 4.2). These high-energy lone pairs can contribute to additional electronic transitions, further influencing the optical

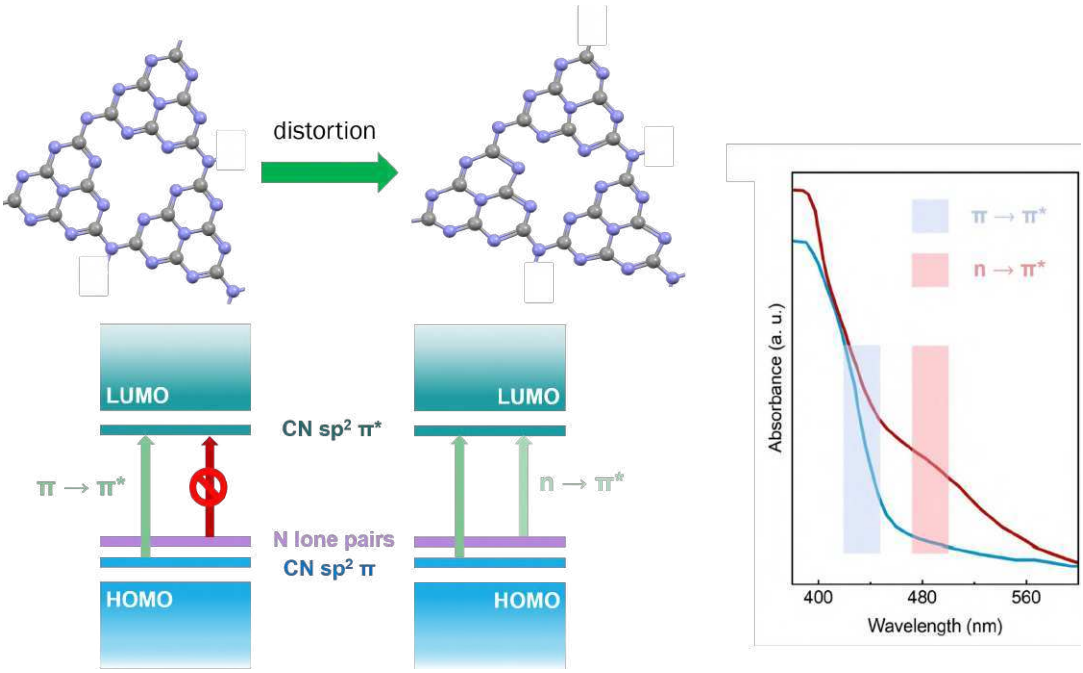

Figure 4.2: Electronic transitions in g-C_3N_4 for planar (left panel) and corrugated (right panel) tri-s-triazine units. The optical absorption spectra correspond to the π-π^* and n-π^* electronic transitions [259]

properties and photocatalytic efficiency of g-C_3N_4.

In recent years, research has focused on modifying to overcome its intrinsic limitations, particularly the rapid recombination of photogenerated electron–hole pairs and limited absorption of the visible spectrum. Techniques such as exfoliation into nanosheets, template-assisted synthesis of porous structures, and heteroatom doping have been extensively explored. Non-metal dopants (e.g., oxygen, sulfur, phosphorus) can introduce mid-gap states or shift the band positions, thereby extending visible-light absorption and improving charge separation [265]. Metal doping or the incorporation of metal atoms at specific sites has also been investigated to enhance surface activity and tailor catalytic behavior.

The photocatalytic applications of g-C_3N_4 are diverse. One of its most significant uses is in photocatalytic hydrogen evolution from water, where it can act as a hydrogen evolution photocatalyst, especially when coupled with suitable cocatalysts such as platinum or molybdenum sulfide [256]. Another crucial application is the photoreduction of CO_2 into value-added fuels like carbon monoxide or methane, a process that benefits from the suitable electronic structure of g-C_3N_4 and can be further improved through heterojunction formation with other semiconductors. Additionally, g-C_3N_4 has demonstrated efficient performance in the photodegradation of organic pollutants, including dyes and pharmaceuticals, due to its ability to generate reactive oxygen species under illumination.

Cutting-edge research is now exploring advanced designs such as Z-scheme heterojunctions that mimic natural photosynthesis by spatially separating oxidation and reduction processes,

thereby reducing recombination losses [266, 267]. Furthermore, the use of graphitic carbon nitride as a support for single-atom catalysts is gaining attraction, leveraging its nitrogen-rich structure to anchor isolated metal atoms that serve as highly active catalytic centers [268].

Despite these advances, challenges remain in fully exploiting the potential of g-C_3N_4. The bulk material still suffers from limited surface area, and improving the crystallinity and electronic conductivity is a priority. In fact, in its pristine state, graphitic carbon nitride possesses a relatively wide band gap, which restricts visible-light absorption. This limitation arises from its lamellar architecture, which governs the electronic interactions between stacked nanosheets. Perturbation of this planar order —-by defects, structural distortions, or heteroatom incorporation —- leads to band-gap narrowing and enhanced light-harvesting capability. Such modifications may be introduced mechanically, for example, through exfoliation, or chemically. Chemical modification is most commonly achieved during thermal synthesis, permitting direct incorporation of dopants into the polymeric framework. Alternatively, post-synthesis functionalization offers a versatile route, enabling the preparation of a uniform pristine material that can subsequently be subjected to targeted doping or functionalization for specific catalytic applications.

Exfoliation of g-C_3N_4 The transformation of g-C_3N_4 into nanosheets is highly efficient in enhancing photocatalytic activity due to the significant increase in specific surface area. Protonated exfoliation and hydrothermal decomposition processes have been investigated over the past decades; however, these methods are often complex and costly [131]. Thermal exfoliation, by contrast, represents one of the most effective approaches to overcome the limitations associated with other techniques.

In 2020, Mathew *et al.* reported the synthesis of three different forms of g-C_3N_4 through thermal condensation of urea, melamine, and dicyandiamide, producing UCN, MCN, and DCN, respectively. A comparative analysis of these thermally exfoliated polymeric carbon nitrides (PCNs) revealed that UCN exhibits a high porosity with a surface area of 179 m^2/g. This structural feature significantly enhances the separation efficiency of photogenerated charge carriers, thereby resulting in superior photocatalytic degradation performance of rhodamine B (RhB) dye under sunlight irradiation [269].

Ganesan *et al.* [270] reported the thermal exfoliation of g-C_3N_4 by heat treatment of bulk g-C_3N_4 at $550\,^{\circ}\mathrm{C}$. Brunauer–Emmett–Teller (BET) surface area analysis and scanning electron microscopy (SEM) confirmed the enhanced porosity and high surface area of the thermally exfoliated g-C_3N_4 (TE-g-C_3N_4). This material was demonstrated as a promising photocatalyst for the degradation of dyes such as methylene blue (MB), methyl orange (MO), and rhodamine B (RhB). It was further observed that the exfoliation temperature is directly correlated with the degradation efficiency. Moreover, TE-g-C_3N_4 retained its photocatalytic performance over five consecutive recycling cycles, exhibiting negligible loss in efficiency.

Das *et al.* [122] characterized exfoliated graphitic carbon nitride (GCNX) prepared through a two-step heat treatment technique. In the presence of hydrogen peroxide (H_2O_2), GCNX efficiently photodegraded rhodamine B (RhB) dye within $30\,\mathrm{min}$. The catalytic degradation efficiency was systematically investigated under different reaction conditions, including pH, catalyst loading, dye concentration, and H_2O_2 dosage.

Exfoliated g-C_3N_4 tends to agglomerate, resulting in a loss of specific surface area and consequently reduced photocatalytic activity. As reported by Dongling Ma *et al.* [271], ultra-thin

porous g-C_3N_4 nanosheets successfully overcame these limitations by achieving $96\,\%$ degradation of methyl orange (MO) within $30\,\mathrm{min}$ of visible-light irradiation. Acid-assisted ultrasonication enabled the formation of ultra-thin, porous g-C_3N_4 nanosheets with a controlled pore structure, effectively preventing aggregation.

In 2022, Kim *et al.* [143] reported the synthesis of few-layered porous g-C_3N_4 via a simple molecular self-assembly process. The resulting porous g-C_3N_4 exhibited a higher density of active sites, which promoted more efficient charge separation and consequently enhanced photocatalytic activity compared to conventional g-C_3N_4. Notably, $97.46\,\%$ of rhodamine B (RhB) dye was degraded within $1\,\mathrm{h}$ under visible-light irradiation.

In 2023, Gogoi *et al.* [272] reported a facile and sustainable solvothermal synthesis of g-C_3N_4 nanospheres (g-CNNS). The adsorption performance of g-CNNS was evaluated for four different dyes, revealing a significantly higher affinity for the cationic dye methylene blue (MB). This was attributed to the strong electrostatic interactions between MB molecules and the surface of g-CNNS.

Functionalizzation of g-$\mathbf{C_3N_4}$ One important strategy for tailoring the electrical characteristics of graphitic carbon nitride, narrowing its band gap, enhancing visible-light absorption, and improving photocatalytic efficiency is element doping. Metal doping is typically achieved by thermal treatment of a precursor mixed with a metal-soluble salt solution. Alkali-metal incorporation has been shown to enhance redox processes and promote photogenerated charge carrier transfer. By modifying the band structure of the photocatalyst, this approach increases light absorption and is frequently employed, even with non-metallic elements, to improve the optical properties associated with the band-gap structure [273, 274]. Non-metal doping reduces the band gap and strengthens the visible-light absorption of g-C_3N_4. Modulation through non-metal incorporation, or by combining g-C_3N_4 with other narrow-band-gap photocatalysts to construct composites, effectively broadens its absorption across the visible spectrum [275]. Doping with non-metal elements also preserves the metal-free nature of g-C_3N_4. Typical non-metal dopants include nitrogen, boron, carbon, sulfur, phosphorus, and oxygen [276]. These elements can also be introduced through post-synthesis treatments, enabling their incorporation into the pristine framework in a controlled manner. Such an approach allows the preparation of a uniform stock material that can subsequently undergo targeted doping or functionalization for specific catalytic applications.

Chegeni et al. [277] reported the preparation of phosphorus-doped graphitic carbon nitride (P-g-C_3N_4) via a straightforward approach using phosphoric acid and melamine. The resulting material was characterized by Fourier-transform infrared spectroscopy (FT-IR), X-ray diffraction (XRD), scanning electron microscopy (SEM), and Brunauer–Emmett–Teller (BET) surface area analysis. This synthesis route was noted for its simplicity, efficiency, and ease of implementation compared to other methods. The as-prepared P-g-C_3N_4 was evaluated for the adsorption of methylene blue. Adsorption data were analyzed using both Langmuir and Freundlich isotherms, with the Langmuir model providing the best fit (R^2 = 0.98). From the Langmuir isotherm, the maximum adsorption capacity (q_{max}) was determined to be 100 mg g^{-1} under the following conditions: pH 8, adsorbent dosage 0.07 g, initial methylene blue concentration 8 ppm, contact time 60 min, and temperature 18 °C. The adsorption kinetics followed a pseudo-second-order model. These results indicate that P-g-C_3N_4 is a promising material for efficient methylene blue removal from aqueous solutions. Similarly, Paul *et al.* [247] functionalized graphitic carbon nitride

(g-C_3N_4) with silver nanoparticles (AgNPs). The photocatalytic activity of the resulting material was assessed for the degradation of organic dye pollutants, including rose Bengal (RB), crystal violet (CV), and methylene blue (MB).

Changlin Yu *et al.* [278] developed porous g-C_3N_4 nanosheets synthesized through thermal oxidation of sodium hypophosphite (SHP) and porous g-C_3N_4, with the materials placed at the downside of the furnace to enable the element doping process. SHP and porous g-C_3N_4 nanosheets were used in a 40:1 mass ratio, leading to the formation of two different nanosheets depending on the mass ratio applied. These nanosheets were tested as photocatalysts for RhB degradation under visible light, achieving a photodegradation ratio of 99.5% and a reaction rate constant of 0.120 min^{-1}, which is significantly higher than that of undoped g-C_3N_4 (0.031 min^{-1}). The mechanism analysis suggested the involvement of reactive species such as $O_2^{\bullet -}$ and $OH^{\bullet}$ in the degradation process.

Syed Ghulam Musharraf *et al.* [279] reported the synthesis of sulfur-doped g-C_3N_4 (SGCN) via thermal polymerization of thiourea, which was subsequently applied to the photodegradation of the industrial dye Acid Orange (AO-7). The SGCN photocatalyst exhibited a degradation efficiency of 98%, markedly higher than the 45% achieved by pristine g-C_3N_4 under visible light irradiation within 70 min. In addition, SGCN demonstrated considerable photocatalytic activity toward both cationic and anionic dyes. Radical trapping experiments indicated that O_2^- species were the main active contributors, while $OH\cdot$, e^-, and h^+ also participated in the process. Furthermore, SGCN achieved degradation efficiencies of 70% for methylene blue (MB) and 81% for Congo red (CR), highlighting its broad-spectrum photocatalytic performance.

Fengfu Fu and *et al.* [94] reported the synthesis of boron-doped g-C_3N_4 (B-g-C_3N_4) nanosheets with thicknesses of one monolayer to 5 monolayer and lateral sizes ranging from 50 nm to 200nm. These thin-layered B-g-C_3N_4 nanosheets exhibited remarkable photocatalytic activity, achieving efficient degradation of various organic dyes, including eosin Y (EY), rhodamine B (RhB), methylene blue (MB), and methyl orange (MO), under visible-light irradiation. Complete degradation of the dyes was achieved within 5 to 20 minutes. The enhanced photocatalytic activity of the thin-layer B-g-C_3N_4 nanosheets was attributed to their larger BET surface area and reduced optical band gap.

Luo et al. [280] reported that the photocatalytic performance of boron-doped graphitic carbon nitride (BCN and KBCN) exceeded that of pristine graphitic carbon nitride (g-C_3N_4) in the selective oxidation of cinnamaldehyde (a planar molecule containing an aldehyde functional group) to benzaldehyde under visible-light irradiation. Potassium tetraborate tetrahydrate ($K_2B_4O_7 \cdot 4\,H_2O$) and potassium borohydride (KBH_4) were employed as boron sources to prepare BCN and KBCN, respectively, via calcination under an inert atmosphere. These boron dopants not only introduced boron atoms into the g-C_3N_4 framework but also generated nitrogen vacancies on the catalyst surface, enhancing adsorption of both oxygen and cinnamaldehyde and thereby improving the catalytic activity. The conversion of cinnamaldehyde and the selectivity toward benzaldehyde increased by 10% and 11% with BCN, and by 25% and 34% with KBCN, respectively, compared to pristine g-C_3N_4. Further studies on four different substrates indicated that the introduction of a carbonyl group conjugated with a carbon-carbon double bond enhanced the conversion rate by a factor of 1.8–2.4. Moreover, the benzaldehyde selectivity was primarily governed by the substrate's adsorption capability on the catalyst surface, demonstrating that both electronic structure

modifications and surface interactions contribute to the overall photocatalytic performance.

Jiao *et al.* [281] synthesized g-C_3N_4 as a potential photocatalyst for pollution control and energy conversion, although its performance was limited by poor light absorption and inefficient photocarrier transport and separation. To address these issues, they employed a one-pot thermal polymerization strategy involving ammonium bicarbonate and urea, which enabled molecular homogenization, lamellar separation, polycondensation, and urea recrystallization, ultimately yielding a porous g-C_3N_4 with abundant nitrogen vacancies and oxygen heteroatoms. The resulting material exhibited extended visible-light absorption, interconnected charge-transport pathways, and a high density of active sites. Structural modifications arising from nitrogen vacancies and oxygen heteroatom incorporation significantly altered the electronic configuration, thereby improving photocatalytic performance. The optimized g-C_3N_4 derivative demonstrated photodegradation efficiencies of 97.5% and 99% for RhB (C_0 = 50 mg L^{-1}) after 90 min of visible-light and sunlight irradiation, respectively, highlighting its potential as a porous photocatalyst for environmental remediation and energy conversion.

Hussain *et al.* [282] investigated the thermal doping of carbon nitride from urea using a series of non-metallic precursors. For instance, g-C_3N_4-P was obtained by introducing ammonium dihydrogen phosphate, resulting in a bandgap of 2.56 eV. Similarly, thiourea was employed to produce g-C_3N_4-S, which exhibited a narrower band gap of 2.40 eV. The latter derivative demonstrated superior solar light absorption, leading to enhanced photocatalytic activity.

Bresolin *et al.* [283] address the limitations of low charge transport efficiency and chemical instability, a cesium/bismuth-based perovskite was anchored onto g-C_3N_4 nanosheets to prepare a composite photocatalyst stabilized by nitrogen–iodine chemical bonding. Among the different lead-free halide perovskite loadings, the CNCSBI001 composite (g-C_3N_4:$Cs_3Bi_2I_9$, 10:0.1 w%) demonstrated superior stability and an outstanding yield in the photocatalytic degradation of organic compounds in aqueous solution under visible light irradiation.

In another study, Bresolin *et al.* [284] reported the thermally induced copolymerization of melamine with 2-bromobenzonitrile, yielding a g-C_3N_4-Br derivative with a band gap of 2.55 eV. This material displayed promising photocatalytic efficiency in the degradation of Rhodamine B.

In addition to non-metals, metal atoms can also be incorporated into the g-C_3N_4 lattice, taking advantage of the high donor capability of nitrogen functionalities within the framework. Ma *et al.* [285] synthesized an Fe-doped graphitic carbon nitride through the thermal condensation of melamine in the presence of ferric nitrate nonahydrate. The resulting catalyst exhibited significantly improved photocatalytic activity compared to pristine g-C_3N_4.

Graphitic carbon nitride (g-C_3N_4) and metal oxide (MO_x) based nanocomposites (g-C_3N_4-MO_x) are photocatalysts that provide interesting results in terms of charge transfer capacity, redox capabilities, and charge recombination inhibition. The degradation of common antibiotics such as amoxicillin (AMX), azithromycin (AZM), cefixime (CFM), ciprofloxacin (CIP), and tetracycline (TC) using g-C_3N_4-MO_x nanocomposites has been investigated [286]. Sun *et al.* reported that a g-C_3N_4/ZnO nanocomposite with a 3D/2D petal-like microstructure, prepared via a simple solvothermal method, effectively degraded three sulfonamides. In situ modification of g-C_3N_4 with ZnO nanoparticles improved its visible light responsiveness, oxidation potential, and charge-transfer efficiency. Consequently, sulfamethoxazole (SMX) degradation reached 96.91% with the nanocomposite, compared to 60.34% and 43.53% for pure g-C_3N_4 and ZnO nanoparticles, respec-

tively, after 80 minutes of visible-light irradiation [77].

Singh *et al.* [287] reported that a CuO-g-C_3N_4 composite, synthesized via a solution combustion process, efficiently degraded tetracycline (TC) under solar irradiation within 30 minutes. The maximum degradation reached 88% in the presence of H_2O_2 and 32% without it. The enhanced performance is attributed to increased surface area, additional trap states, and improved electron-hole separation. The catalyst maintained high stability over three cycles with only minor efficiency loss.

Hunge *et al.* [288] similarly highlighted that H_2O_2 improves charge carrier dynamics and degradation efficiency, while the composite exhibits superior electron-hole separation and reusability compared to pure CuO or g-C_3N_4. Nonetheless, the reliance on H_2O_2 as co oxidant limits practical large-scale applications. Ni *et al.* [289] prepared g-C_3N_4/TiO_2 (TCNT) composites with 2%, 4%, and 6% g-C_3N_4 via grinding and step-scheme heterojunction formation. The 4% composite exhibited the highest degradation of tetracycline hydrochloride (TCH), reaching 96.53% under UV light within 50 minutes.

5 Preparation of Heteroatom-doped g-C_3N_4 Derivatives

In this section, the attention is focused on the preparation of photocatalytic materials derived from graphitic carbon nitride (g-C_3N_4). Pristine g-C_3N_4 is a promising polymeric semiconductor, yet its practical use is limited by fast electron–hole recombination and restricted light absorption. To address these shortcomings, a series of non-conventional derivatives was designed through different doping strategies involving bromine, phosphorus, and boron. Each of these modifications was conceived to tailor the electronic structure and surface chemistry of the material, thereby enhancing its photocatalytic efficiency under visible-light irradiation. Taken together, they provided access to a family of doped g-C_3N_4 materials with distinct structural and chemical features. By progressing from the pristine semiconductor to bromine-, phosphorus-, and boron-modified derivatives, photocatalytic tests were carried out for the degradation of dyes and pharmaceutical pollutants.

In the following sections, the preparation procedures, characterization techniques, and photocatalytic tests are described in detail, with the aim of elucidating how different dopants influence the structure–property relationships of g-C_3N_4 and ultimately govern its performance.

5.1 Materials and method

Table 5.1: Materials used

Composites	Chemical formula	Purity	Producer
2-Bromobenzonitrile	C_7H_4BrN	99.9%	Merck-Schuchardt
4-Bromo N,N-dimethylaniline	$BrC_6H_4N(CH_3)_2$	99.9%	Sigma-Aldrich
Ammonium Hydroxide	NH_4OH	28.0–30.0%	Sigma-Aldrich
Boric acid	H_3BO_3	99.5–100.5%	Scharlau
Boron trifluoride diethyl etherate	$BF_3 \cdot O(C_4H_{10})_2$	$\geq$ 98.0%	TCI
Dichloromethane	CH_2Cl_2	$\geq$ 99.9%	Honeywell
Dimethylformamide	C_3H_7NO	$\geq$ 99.8%	Honeywell
Ethanol	C_2H_6O	99.9%	Scharlau
Hydrobromic acid aq. solution	HBr	48.0%	Carlo Erba Analyticals
Melamine	$C_3H_6N_6$	99.9%	Alfa Aesar
Methanol	CH_3OH	$\geq$ 99.8%	Sigma-Aldrich
N,N-Diisopropylethylamine	$(C_3H_7)_2NCH_2CH_3$	$\geq$ 99.0%	Sigma-Aldrich
Rhodamine-B	$C_{28}H_{31}ClN_2O_3$	$\geq$ 95.0%	Sigma-Aldrich
Sodium Hydroxide	NaOH	$\geq$ 98.0%	Sigma-Aldrich
Sulfuric acid	H_2SO_4	96.0%	Carlo Erba Reagents
Sulfamethoxazole	$C_{10}H_{11}N_3O_3S$	98%	Alfa Aesar
Tetracycline	$C_{22}H_{24}N_2O_8$	98.0–102.0%	Sigma-Aldrich
Triphenylphosphine	$P(C_6H_5)_3$	99%	Aldrich

5.1.1 Analytical techniques

Transmission electron microscopy (TEM) analysis

The morphology and microstructure of the samples were characterized by transmission electron microscopy (TEM) and high-angle annular dark-field (HAADF) scanning transmission electron microscopy (HAADF-STEM) using TEM JEOL F200 operated at 200 kV. Elemental analysis and mapping were performed using a JEOL 100 mm^2 silicon drift energy dispersive X-ray spectrometer (EDX). A carbon supported copper grids, 400 mesh size, were used for preparation of the sample. All measurements were performed at the Department of Chemical Science (DISC) of the University of Padua by Dr. Andrea Basagni.

Environmental Scanning Electron Microscopy (ESEM) analysis

Environmental Scanning Electron Microscopy (ESEM) analysis was performed using a *FEI Quanta 200* variable pressure environmental scanning electron microscope, equipped with a backscattered electron (BSE) detector and an energy dispersive X-ray spectroscopy (EDX) system (EDAX Element-C2B). The instrument was operated under variable pressure conditions, allowing for the direct observation of non-conductive solid samples without the need for conductive coating. The BSE detector provided compositional contrast based on atomic number differences, while the EDX detector enabled elemental analysis and mapping of the sample surfaces. Elemental compositions were obtained by collecting EDX spectra from selected regions of interest (ROIs). All measurements were carried out under optimized accelerating voltages (typically 15–20 kV), ensuring adequate spatial resolution and elemental sensitivity. This combined technique allowed for the morphological and semi-quantitative elemental characterization of the powder samples. All measurements were performed at Centro di Analisi e Servizi per la Certificazione (CEASC - UniPd) of the University of Padua by Dr. Federico Zorzi.

Fourier-Transform Infrared Spectroscopy (FTIR) analysis

Fourier-transform infrared (FTIR) spectra of the solid samples were collected using a *PerkinElmer Spectrum 100* spectrophotometer, equipped with a DTGS detector and operated in the range of 4000–400 cm^{-1}. The measurements were performed in attenuated total reflectance (ATR) mode using a diamond/ZnSe crystal, which allows direct analysis of powders without the need for additional sample preparation, such as pellet formation. Each spectrum was acquired by averaging 32 scans at a resolution of 4 cm^{-1} to ensure optimal signal-to-noise ratio. Background spectra were collected before each measurement and automatically subtracted from the sample spectrum to remove atmospheric contributions (e.g., CO_2, H_2O). The FTIR spectra were used to identify functional groups and assess chemical interactions, structural changes, or the presence of specific bonds characteristic of the sample composition.

Diffuse reflectance spectra (DRS) analysis

Diffuse reflectance spectra (DRS) analysis was carried out using a *PerkinElmer Lambda 365+* UV-Vis spectrophotometer, operating in the 300–7000 nm spectral range, which allows coverage from

the ultraviolet to the near-infrared region. The measurements were performed on solid powder samples, which were finely ground in an agate mortar and uniformly spread onto suitable sample holders (e.g., quartz plates) to guarantee a consistent optical path, surface homogeneity, and reproducibility of the reflectance signal. Diffuse reflectance data were acquired using an integrating sphere accessory, which enhances the accuracy of the measurements by collecting both specular and diffuse components of the reflected light. This configuration is particularly important for powdered and heterogeneous materials, where scattering phenomena strongly influence the measured intensity. The raw reflectance spectra were subsequently converted into absorbance-like data by means of the Kubelka–Munk function 5.1, which establishes a proportionality between the reflectance and the absorption coefficient of the sample:

$$F(R) = \frac{(1-R)^2}{2R} \tag{5.1}$$

where R is the measured reflectance. The use of the Kubelka–Munk transformation provides a reliable approximation of the absorption properties of highly scattering samples and is widely adopted in the optical characterization of powders and polycrystalline solids. To determine the optical band gap (E_g), Tauc plots were constructed by plotting $[F(R)h\nu]^n$ versus $h\nu$, where h is Planck's constant, ν is the photon frequency, and n is a constant that depends on the nature of the electronic transition, being $n = \frac{1}{2}$ for direct allowed transitions and $n = 2$ for indirect ones. The band gap energy was obtained by extrapolating the linear portion of the Tauc plot to the photon energy axis ($h\nu$), corresponding to the onset of strong absorption. This procedure enables the distinction between direct and indirect band gaps, thus offering valuable insights into the electronic band structure of the investigated materials. Overall, the combination of diffuse reflectance spectroscopy with the Kubelka–Munk and Tauc methodologies represents a powerful approach for the optical characterization of solid-state powders. It provides quantitative information on the band gap energy, while also allowing the detection of sub-band-gap states associated with structural defects, dopants, or surface modifications. This makes DRS particularly well suited for the study of semiconducting materials, photocatalysts, and other functional solids where the optical response plays a key role in their technological applications.

X-ray Diffraction (XRD) analysis

X-ray diffraction (XRD) spectra were recorded to characterize samples using a PANalytical X'Pert Pro diffractometer equipped with a Co X-ray tube and a real-time multiple strip (RTMS) detector (X'Celerator). X-ray diffraction (XRD) relies on the interaction between incident X-rays and the periodic lattice of crystalline materials. When a monochromatic X-ray beam impinges upon a crystalline specimen, it is scattered by the electrons surrounding the atoms. Constructive interference of these scattered rays occurs only at specific angles, producing a diffraction pattern that satisfies Bragg's Law:

$$n\lambda = 2d\sin\theta \tag{5.2}$$

where:

- n is an integer (order of diffraction),

- λ is the wavelength of the incident X-rays,
- d is the interplanar spacing of the crystal lattice,
- θ is the angle of incidence.

The resulting diffraction peaks provide a "fingerprint" of the crystal structure, allowing identification of crystalline phases and determination of lattice parameters. XRD data is typically represented as a diffractogram, i.e., a plot of diffracted intensity versus the diffraction angle (2θ). The key information obtained includes:

- **Phase Identification:** Comparing experimental patterns with standard reference data (e.g., PDF-4+ database) enables phase determination.
- **Crystallite Size:** Estimated using the Scherrer equation:

$$D = \frac{K\lambda}{\beta \cos\theta} \tag{5.3}$$

  where:

  - D = average crystallite size,
  - K = shape factor (typically $\sim$0.9),
  - λ = X-ray wavelength,
  - β = full width at half maximum (FWHM) of the peak in radians,
  - θ = Bragg angle.

- **Lattice Parameters and Strain:** Accurate peak positions enable calculation of unit cell dimensions, while peak broadening can reveal microstrain.
- **Preferred Orientation and Texture:** Deviations from expected peak intensities may indicate texture, which can be analyzed using pole figures or Rietveld refinement.

In this research, XRD was employed to analyze the structural properties of doped graphitic carbon nitride (g-C_3N_4) materials. The technique was crucial in:

- Identifying the crystalline phases present before and after doping;
- Estimating the impact of different dopants (P, B, Br) on interlayer spacing and crystallite size;
- Monitoring structural changes induced by thermal treatments or chemical modification.

The results of XRD analysis were correlated with photocatalytic activity and optical properties to elucidate structure-property relationships. All measurements were performed at Centro di Analisi e Servizi per la Certificazione (CEASC - UniPd) of the University of Padua by Dr. Federico Zorzi.

X-ray photoelectron spectroscopy (XPS) analysis

X-ray photoelectron spectroscopy (XPS) was carried out by means of a Perkin Elmer PHI 5600ci Multi Technique System, using AlKα radiation (1486.6 eV) working at 250 W. The spectrometer was calibrated by assuming the binding energy (BE) of the 4f 7/2 line to be 84.0 eV with respect to the Fermi level. Both extended and detailed spectra were collected. The standard deviation in the BE value of the XPS line is 0.1 eV. The atomic percentage, after a Shirley-type background subtraction was evaluated by using the PHI sensitivity factors. The peak positions (referred to NIST database) were corrected for the charging effects by considering the C 1s peak at 285.0 eV and evaluating the BE differences. All measurements were performed at the Department of Chemical Science (DISC) of the University of Padua by Professor Antonella Glisenti.

UV-Visible Spectroscopy and Photocatalytic Efficiency Calculation

UV-Vis analysis was carried out using a *PerkinElmer Lambda 365+* UV-Vis spectrophotometer, operating in the 200–7000 nm spectral range. The UV-Vis spectrum represents the absorbance of a material as a function of the wavelength (nm) of the incident electromagnetic radiation in the ultraviolet and visible regions. The absorbance (A) quantifies the fraction of light energy absorbed by a given thickness of material and is related to the transmittance (T)–the ratio between the intensity of the light transmitted through the sample and the incident intensity–according to the following equation:

$$A = -\log T \tag{5.4}$$

The absorbance of a solution can be linearly related to the concentration of the analyte by the Beer-Lambert law:

$$A = \varepsilon c l \tag{5.5}$$

where ε is the molar absorptivity ($\mathrm{L\,mol^{-1}\,cm^{-1}}$), c is the molar concentration of the analyte ($\mathrm{mol\,L^{-1}}$), and l is the optical path length (cm).

This relation was employed to determine the concentration of dye in solution and to calculate the photocatalytic degradation efficiency of the investigated samples. The efficiency was calculated as follows:

$$\text{Photodegradation efficiency (\%)} = \left(1 - \frac{C}{C_0}\right) \times 100 = \left(1 - \frac{A}{A_0}\right) \times 100 \tag{5.6}$$

Considering that all parameters in the Beer-Lambert law remain constant except for the concentration, the efficiency can be equivalently expressed in terms of absorbance. Here, C_0 and A_0 represent the initial dye concentration and absorbance (i.e., those of the stock solution), respectively. It is important to note that C, C_0, A, and A_0 must refer to the same wavelength in the absorption spectrum to ensure consistency.

Calibration Curve The calibration curve describes the relationship between the absorbance and the concentration of the dye. If the Beer-Lambert law holds within the concentration range studied, this relationship is expected to be linear.

To establish the calibration curve for Rhodamine-B (RhB), a series of dye solutions with known concentrations was prepared by diluting a stock solution with a concentration of $20\,\mathrm{mg/L}$. The concentrations prepared were: $2\,\mathrm{mg/L}$, $4\,\mathrm{mg/L}$, $6\,\mathrm{mg/L}$, $8\,\mathrm{mg/L}$, and $10\,\mathrm{mg/L}$. According to the Beer-Lambert Law (Equation 5.5), the slope of the experimental calibration curve is equal to the product of the molar absorption coefficient (ε) and the optical path length (l). Since both parameters remain constant throughout the measurements, this value can be inferred directly from the slope of the linear fit, as shown in Figure 5.1.

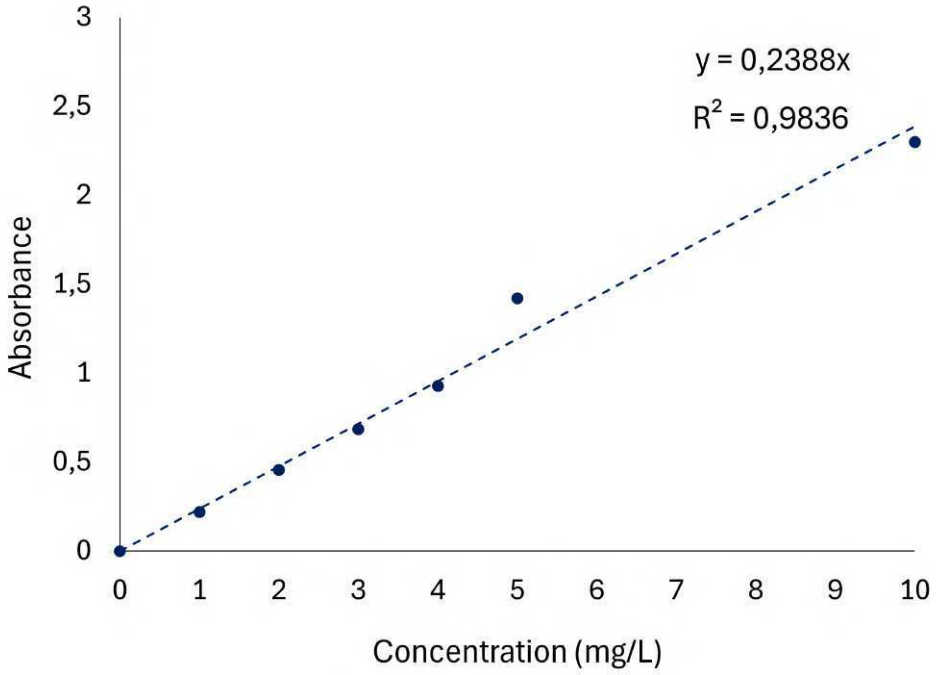

Figure 5.1: Calibration curve of Rhodamine B between 0–10 mg/L. A linear fit is shown for the range where the Beer-Lambert law is valid

High-Performance Liquid Chromatography (HPLC) analysis

High-performance liquid chromatography HPLC (UFLC, Shimadzu, equipped with a diode array detector), was used for the determination of each pharmaceutical concentration along the reaction time. The specifications regarding the column type, solvents, operating temperature, and other conditions used for the determination of pharmaceuticals by HPLC are reported in section 5.2.6. All measurements were performed at the Chemical Engineering and Renewable Resources for Sustainability (CERES) research centre, at the Faculty of Science and Technology of the University of Coimbra (FCTUC), Portugal, under the supervision of Professor Rui C. Martins.

5.2 Experimental

In this section, the synthesis of graphitic carbon nitride (g-C_3N_4) and its chemical modification through heteroatom doping will be discussed. Graphitic carbon nitride was prepared by thermal polymerization of melamine, chosen as a precursor for its higher mass yield compared to urea. The undoped material was obtained by pyrolysis at 550 °C for 2 h, yielding a yellow powder that was subsequently ground and stored. To improve visible-light absorption and photocatalytic performance, different doping strategies were explored. As illustrated in Figure 5.2, doped g-C_3N_4 can be obtained either by post-synthesis functionalization of the undoped material or by co-pyrolysis in the presence of a suitable doping reagent. Bromine doping was first investigated, starting from brominated precursors or elemental bromine; phosphorus doping was achieved by co-pyrolysis with triphenylphosphine; and boron doping was carried out using boric acid or boron trifluoride diethyl etherate. This general scheme highlights how chemical modifications can be introduced during or after thermal treatment, allowing a direct comparison between different dopants and their effects on the structure and photocatalytic behavior of g-C_3N_4.

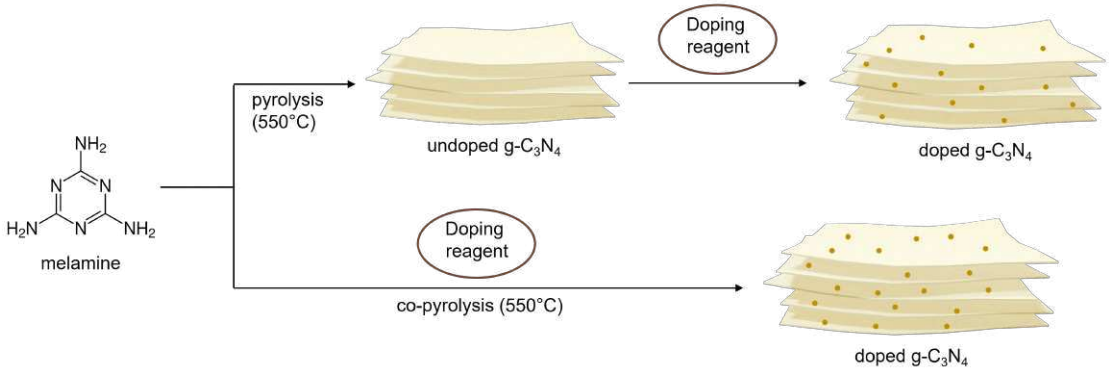

Figure 5.2: Mechanism of the synthesis of g-C_3N_4

5.2.1 Synthesis of g-C_3N_4

g-C_3N_4 was synthesized by placing 10 g of melamine in a ceramic crucible covered with aluminium foil, to reduce the mass loss. The crucible was placed for 2 h at 550 ° C, in a pyrolizer, with a N_2 constant flow of 1 mL/s. The sample was left cooling down to ambient temperature, obtaining a yellow sample that was grinded on an agate mortar.

5.2.2 Synthesis of bromine functionalized g-C_3N_4

Five different doped g-C_3N_4 have been synthesized with different bromine precursors: hydrobromic acid, 2-bromobenzonitrile, 4-bromo-N,N-dimethylaniline, elemental bromine (Br_2). Their chemical structures are shown in Figure 5.3. The doped samples were called BrN (with N the type of precursor).

Table 5.2 summarizes the nomenclature of the Br-doped g-C_3N_4 samples, the dopant reagents employed, the corresponding atomic percentage of bromine incorporated (calculated based on the

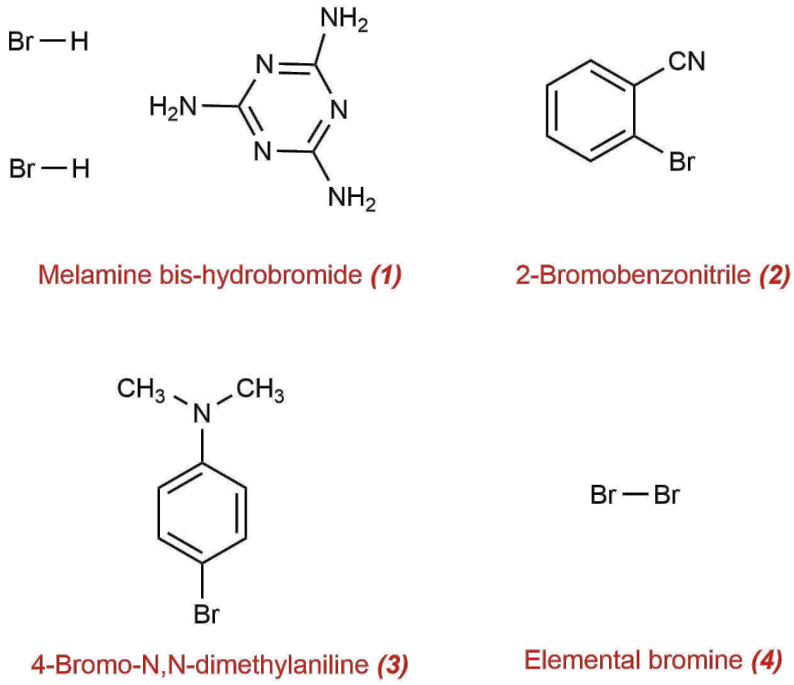

Figure 5.3: Brominated precursors used

synthesis stoichiometry), as well as the adopted synthetic procedure. In particular, the CP-labelled samples were obtained by co-pyrolysis, i.e., by mixing the dopant precursor with melamine prior to thermal condensation, whereas the PP-labelled samples were prepared by post-pyrolysis functionalization through direct reaction of pre-synthesized g-C_3N_4 with the dopant reagent.

Table 5.2: Nomenclature and atomic % content of the dopant element in the Br-doped g-C_3N_4 samples

Sample	**Dopant reagent**	**Mass % dopant elem.**[‡]
Br1-CP*	$C_9H_8N_6^{2+}\cdot 2Br^-$	1.1
Br2-CP	C_6H_4BrCN	0.9
Br3-CP	$BrC_6H_4N(CH_3)_2$	0.8
Br4-CP	Br_2	22.4
Br4-PP**	Br_2	19.0

* co-pyrolysis doping procedure
** post-pyrolysis doping procedure
‡ according to the synthesis stoichiometry

Synthesis of Br1-CP

The first Br-doped photocatalyst was called Br1-CP, and was prepared by adding melamine bis-hydrobromide, obtained by reaction with hydrobromic acid (HBr), to melamine and subsequently subjected to co-pyrolysis. The synthesis was based on the work of Msalmi *et al.* [290], which prepared a similar species using HI. In this case, a white powder of melamine bis-ammonium salt $\left(C_3H_8N_6^{2+}\right)\left(Br^-\right)_2$ was produced by reaction of pure melamine with excess HBr in dimethylformamide (DMF) according to the Equation 5.7.

$$C_3H_6N_6 + 2\ HBr \rightarrow C_3H_8N_6^{2+} \cdot 2\ Br^- \tag{5.7}$$

In detail, 0.695 g of melamine was dissolved in 25 mL of DMF, and the obtained solution was then treated with 5 mL of HBr. The crystals salts were formed after partial evaporation of the solvent under reduced pressure. Afterward, 30 mL of ethanol were added, provoking the complete precipitation of the bis-hydrobromide salt, which was filtered on a filter paper, and dried on a desiccator under vacuum [290]. The salt obtained was then used in the preparation of Br1-CP: 10 g of melamine and 0.2 g of ammonium salt were mixed in an agate mortar. The mixed powders were grinded, placed in a ceramic crucible and pyrolyzed at 550 °C for 2 h, under inert atmosphere. After 2h, the pyrolyzer was switched off and the product was slowly cooled to ambient temperature, obtaining a yellow sample that was grinded on an agate mortar and stored in a vial.

Synthesis of Br2-CP

The second Br-doped photocatalyst was called Br2-CP. It was prepared by mixing in an agate mortar 0.2 g of C_7H_4BrN (2-bromobenzonitrile) with 10 g of melamine. The mixed powders were ground, placed in a ceramic crucible, and subjected to co-pyrolysis at 550 °C for 2 h under inert atmosphere. After the thermal treatment, the furnace was turned off and the product was slowly cooled to ambient temperature, yielding a yellow solid that was ground in an agate mortar and stored in a vial. This synthesis was based on the work of Bresolin *et al.* [284] in which 4-bromobenzonitrile was employed to introduce organic motifs into g-C_3N_4 networks through a convenient one-pot thermally induced process.

Synthesis of Br3-CP

As the last brominated reagent, $BrC_6H_4N(CH_3)_2$ (4-Bromo-N,N-dimethylaniline) was used to produce Br3-CP. The same co-pyrolysis approach of the synthesis of Br2-CP was followed to produce it.

Synthesis of Br4-CP

Br4-CP was synthesized following a procedure adapted from the literature [291]. In a typical synthesis, 0.833 g of melamine was dissolved in 1.0 g of NaOH in 5 mL of deionized water. Bromine (Br_2) was added slowly dropwise until a total volume of 1 mL was reached. The mixture was stirred at room temperature for 2 h, then the solid residue was centrifuged, with deionized water and dried, yielding a yellow solid. For the co-pyrolysis, 0.2 g of the obtained brominated melamine was mixed with 10.0 g of pristine melamine. The mixture was pyrolyzed at 550 °C for

2 h. After cooling, the resulting solid was ground with a mortar, collected in a vial, and stored for further use.

Synthesis of Br4-PP

Figure 5.4 shows the schematic synthesis procedure followed for Br4-PP. Unlike the Br4-CP sample, which was obtained via bromination of melamine prior to thermal condensation, Br4-PP was synthesized through an innovative post-pyrolysis treatment. In this procedure, 150 μL of elemental bromine (Br_2) were added to a 50 mL round bottom flask containing 2 g of pre-synthesized g-C_3N_4, dispersed in 20 mL of chloroform, under stirring and nitrogen flux. After 2 h of continuous stirring, the suspension was centrifuged and washed twice with chloroform (5 min at 10000 rpm). The obtained material was finally dried and stored in air. This post-pyrolysis approach represents a novel strategy, as it enables the direct functionalization of the carbon nitride framework after its formation, rather than during the condensation of melamine.

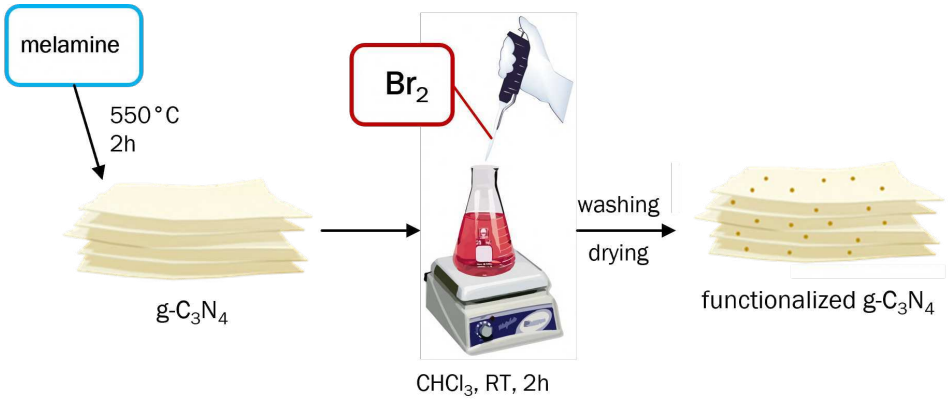

Figure 5.4: Schematic synthesis procedure of Br4-PP

5.2.3 Synthesis using triphenylphosphine

The phosphorous-doped samples have been obtained using triphenylphospine as precursor (Figure 5.5).

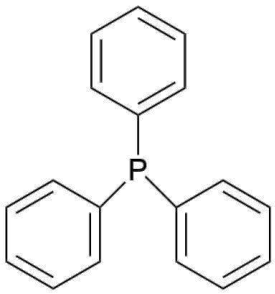

Figure 5.5: Phosphine used as precursor

P 0.1%-CP was synthetized by mixing 10 g of melamine with 0.1 g of triphenylphosphine in a mortar. The mixed powder was put in a ceramic crucible inside a pyrolizer, under inert atmosphere. The system was heated at 550°C for 2h and left cooled at ambient temperature, keeping the nitrogen flux inside the furnace. P 1.2%-CP was synthetized following the same procedure. This time the amount of triphenylphospine added to the melamine was 1 g.

Table 5.3 summarizes the nomenclature of the samples, the dopant reagents employed, and the corresponding atomic percentage of phosphorous incorporated, calculated based on the synthesis stoichiometry.

Table 5.3: Nomenclature and atomic % content of the dopant element in the P-doped g-C_3N_4 samples

Sample	Dopant reagent	Mass % dopant elem.‡
P 0.1%-CP	$P(C_6H_5)_3$	0.1
P 1.2%-CP	$P(C_6H_5)_3$	1.2

‡ according to the synthesis stoichiometry

5.2.4 Synthesis of boron functionalized g-C_3N_4

In the synthesis of boron-doped g-C_3N_4 derivatives, two different boron precursors were employed: boron trifluoride diethyl etherate ($BF_3 \cdot OEt_2$), used for the preparation of fluorescent molecules such as BODIPY [292], and boric acid (H_3BO_3), a more conventional boron source for g-C_3N_4 doping [293, 294, 295]. These reagents were introduced using two distinct synthetic strategies: co-pyrolysis with melamine and post-pyrolysis functionalization of pre-formed g-C_3N_4. In both cases, different precursor-to-melamine mass ratios were tested in order to evaluate their influence on the extent of boron incorporation into the carbon nitride framework. The chemical formulas of the boron precursors used in this study are summarized in Figure 5.6.

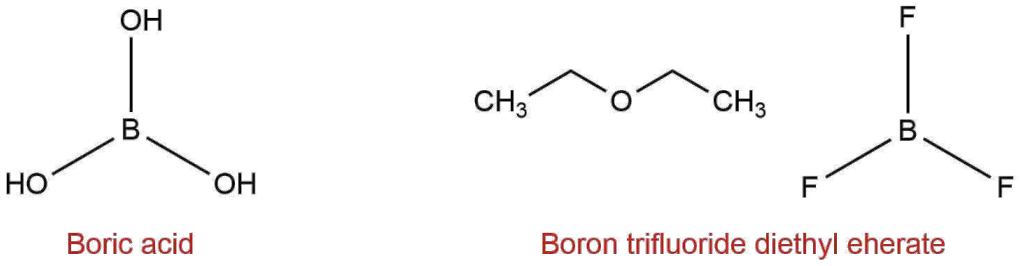

Figure 5.6: Boronated precursor used

Table 5.4 summarizes the nomenclature of the samples, the dopant reagents employed, and the corresponding atomic percentage of bromine incorporated, calculated based on the synthesis stoichiometry.

Table 5.4: Nomenclature and atomic % content of the dopant element in the B-doped g-C_3N_4 samples

Sample	Dopant reagent	Mass % dopant elem.‡
B 0.6%-PP*	$BF_3{\cdot}OEt_2$	0.6
B 1.2%-PP*	$BF_3{\cdot}OEt_2$	1.2
B 5.8%-PP*	$BF_3{\cdot}OEt_2$	5.8
B 0.9%-CP**	H_3BO_3	0.9
B 0.9%-PP*	H_3BO_3	0.9

* post-pyrolysis doping procedure
** co-pyrolysis doping procedure
‡ according to the synthesis stoichiometry

Synthesis using boron trifluoride diethyl etherate

Figure 5.7 shows the schematic synthesis procedure followed for the samples obtained with a post pyrolisis tratment with trifluoride diethyl etherate. This synthetic procedure was adapted from the work of Groves *et al.* [292]. B 0.6%-PP was synthetized by dissolving 2 g of g-C_3N_4 in 70 mL of dichloromethane in a ballon, at ambient temperature, at inert atmosphere. The system was kept agitated for 30 minutes to obtain a complete dispersion. At this point, 0.14 mL of N,N-Diisopropylethylamine (DIPEA) and 0.14 mL of boron trifluoride diethyl etherate were added, under nitrogen flux. The system was stirred in an inert atmosphere overnight. B 1.2%-PP was synthesized following the same synthetic procedure. In this case, the volume of DIPEA and of $BF_3 \cdot OEt_2$ added was doubled. 0.28 mL respectively of DIPEA and of $BF_3 \cdot OEt_2$ were added to the system, under stirring. In the case of B 5.8%-P the volume of DIPEA and of $BF_3 \cdot OEt_2$ was decuplicated, thus 1.40 mL of DIPEA and 1.40 mL of $BF_3 \cdot OEt_2$ were added respectively.

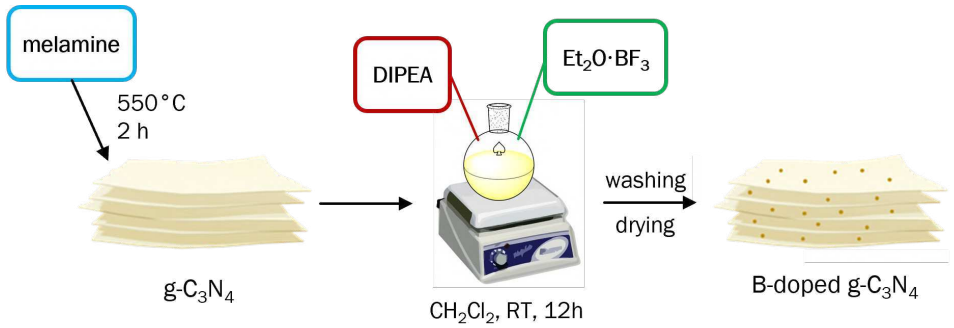

Figure 5.7: Schematic synthesis procedure of post-pyrolisis boron samples

Synthesis using boric acid

B 0.9%-CP was synthetized by mixing 10 g of melamine with 0.5 g of boric acid (H_3BO_3) in a mortar. The mixed powder was put in a ceramic crucible inside a muffle. The system was heated at

550°C for 2 h and left cooled at ambient temperature. This synthetic procedure was adapted from the work of Singh *et al.* [294]. B 0.9%-PP was synthetized following the same procedure. The only differences were that this time 0.25 g of boric acid was added to 2.5 g of g-C_3N_4 already obtained.

5.2.5 Testing procedure for dyes identification

As a model dye we chose Rhodamine-B (RhB) to evaluate and compare the photodegradation capacity of the photocatalysts prepared in this work (Figure 5.8).

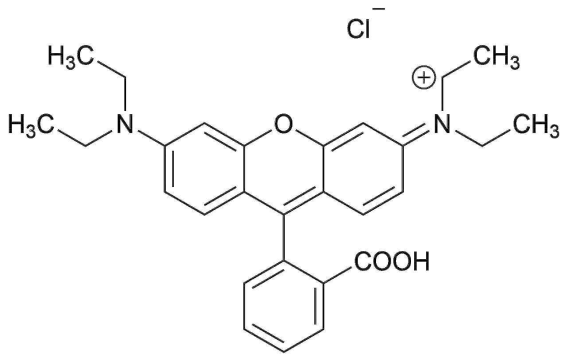

Figure 5.8: Chemical structure of Rhodamine-B

RhB is a cationic dye that gives strong pink solutions in water and is widely used in the textile, paint, leather, plastic, coatings, and paper industries. However, due to its high chemical stability, it is harmful to the environment, with easy accumulation and long-lasting effects, and can also cause allergic reactions, irritation, and damage to the eyes and skin [296, 297, 298]. For this reason, its removal from aqueous effluents is necessary in wastewater treatment. Photocatalytic experiments were performed by dispersing 62.5 mg of photocatalyst in 100 mL of a RhB solution with a concentration of 4 mg L^{-1}, corresponding to 0.400 mg of dye (i.e. 8.3×10^{-7} mol). The suspension was magnetically stirred in a beaker and kept in the dark for 30 minutes to reach adsorption–desorption equilibrium. After this period, the lamp was switched on to initiate photocatalysis. At regular time intervals, aliquots were withdrawn, filtered to remove suspended catalyst, and analyzed by UV–Vis spectrophotometry (*PerkinElmer Lambda 365+*). Samples were measured in quartz cuvettes with a 1 cm optical path, and the absorbance of the RhB band in the visible region was monitored to evaluate the photocatalytic degradation. Before the photocatalytic tests, blank measurements of pure deionized water were performed to exclude any interference from the matrix or the cuvettes.

5.2.6 Testing procedure for pharmaceutical identification

Sulfamethoxazole (SMX) and atenolol (AT) were selected as model pharmaceutical pollutants for photocatalytic degradation studies. Their chemical strcture is shown in Figure 5.9 and in Figure 5.10, respectively.

Both compounds are of environmental concern due to their persistence in water and potential harmful effects on ecosystems and human health [299, 40]. Photocatalytic experiments were conducted by dispersing 62.5 mg of photocatalyst in 200 mL of pollutant solution with an initial

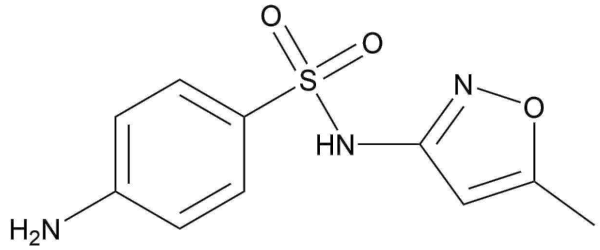

Figure 5.9: Chemical structure of sulfamethoxazole

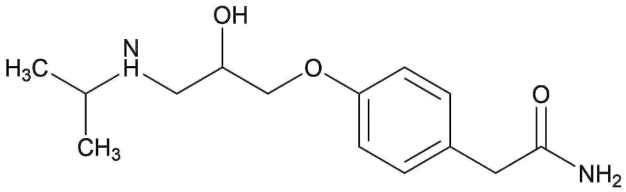

Figure 5.10: Chemical structure of atenolol

concentration of 1 mg L^{-1}. This corresponds to 0.200 mg of pollutant, i.e. 7.9×10^{-7} mol for SMX and 5.2×10^{-7} mol for AT. The suspensions were stirred and left in the dark for 30 minutes to allow adsorption equilibrium. Afterwards, the lamp was switched on to start the reaction, and aliquots were withdrawn at fixed intervals, filtered, and analyzed by high-performance liquid chromatography (HPLC, UFLC Shimadzu). For SMX analysis, 100 μL of each sample was injected into the system using a mobile phase (1 mL min^{-1}) composed of 50% methanol and 50% acidic water (0.1% orthophosphoric acid). A C18 (SiliaChrom) column was maintained at 40 °C, and detection was carried out at 280 nm. For AT analysis, 100 μL of each sample was injected with a mobile phase (1 mL min^{-1}) consisting of 10% acetonitrile and 90% acidic water (0.1% orthophosphoric acid). The same C18 column was used at 40 °C, with detection at 230 nm. These analytical conditions enabled accurate monitoring of the residual concentration of both pharmaceuticals during the photocatalytic process.

5.2.7 Scavenger tests

To investigate the role of reactive oxygen species in the photocatalytic degradation of pharmaceuticals, scavenger tests were carried out using atenolol (AT) as model pollutant. The experiments were performed in 200 mL of aqueous AT solution with an initial concentration of 1 mg/L. A mass of 62.5 mg of photocatalyst was dispersed in the solution under constant stirring, yielding a catalyst loading of 312.5 mg/L. Prior to irradiation, the suspension was kept in the dark for 30 minutes to evaluate adsorption of the pollutant onto the photocatalyst surface. After this equilibration period, scavenger molecules were introduced to selectively quench the formation of reactive species. Isopropanol (IPA, 20 mmol/L) was used as a hydroxyl radical (·OH) scavenger, corresponding to a final amount of 4 mmol (approximately 240 mg) in the reactor. p-Benzoquinone (BQ, 0.05 mmol/L) was employed as a superoxide radical anion ($O_2^{\cdot -}$) scavenger, corresponding to a final amount of 0.01 mmol (approximately 1.08 mg) in the solution. Following the addition of the scavengers,

the photocatalytic tests were initiated by turning on the visible-light source. During irradiation, aliquots were withdrawn at fixed time intervals, filtered, and analyzed by high-performance liquid chromatography (HPLC). Atenolol was quantified by injecting 100 μL of each sample with a mobile phase (1 mL min^{-1}) consisting of 10% acetonitrile and 90% acidic water (0.1% orthophosphoric acid). A C18 column was used at 40 °C, with detection at 230 nm. The procedure allowed direct comparison of atenolol photodegradation kinetics in the absence and presence of scavengers, thereby identifying the predominant reactive species involved in the photocatalytic process.

5.3 Material characterization

In this section, the results obtained from the synthesis and characterization of the samples are presented and discussed. The main focus is on comparing the effects of different doping strategies on the structural and chemical properties of g-C_3N_4, highlighting how each dopant modifies crystallinity, layer stacking, and surface characteristics.

5.3.1 Pristine g-C_3N_4

The pristine graphitic carbon nitride powder obtained from melamine at 550°C shows a brownish tone (Figure 5.11). The pyrolysed sample yielded about 40%.

Figure 5.11: Pristine graphitic carbon nitride synthesized

ESEM-EDX analysis

As described in subsection 5.1.1, ESEM analyses were carried out to study the morphology of the synthesized materials. Figure 5.12 reports representative ESEM images of pristine g-C_3N_4, which reveal an open and porous morphology with a sponge-like structure and interconnected voids. This indicates that the pyrolysis process promotes the formation of a porous microstructure, likely resulting from the rapid gas evolution and decomposition during thermal treatment, which can induce exfoliation and prevent dense stacking of the layers.

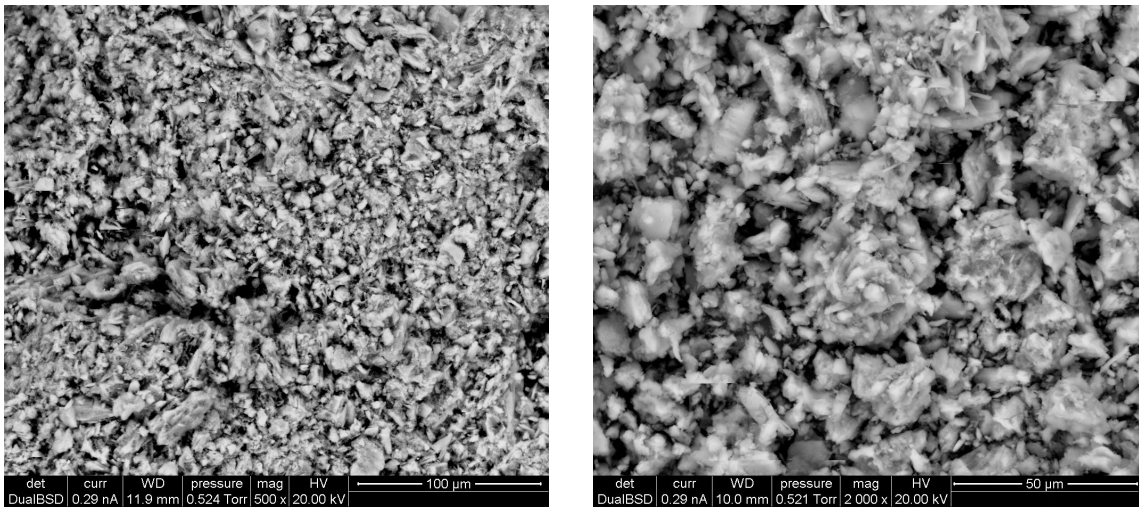

Figure 5.12: ESEM images of g-C_3N_4

The chemical composition of the pristine g-C_3N_4 sample was investigated through energy-dispersive X-ray spectroscopy (EDX) in order to evaluate the elemental distribution of the material surface. The results of the analysis, summarized in Table 5.5, show that the sample is predominantly composed of nitrogen (61.6 wt%) and carbon (35.2 wt%), in line with the theoretical stoichiometry of graphitic carbon nitride. The detection of a small amount of oxygen (3.2 wt%) can be associated with the presence of surface-adsorbed molecules or with partial oxidation processes occurring during the thermal treatment and handling of the material.

Table 5.5: Surface composition of pristine g-C_3N_4 determined by EDX analysis

Sample	**C (wt%)**	**N (wt%)**	**O (wt%)**
g-C_3N_4	35.2	61.6	3.2

TEM analysis

As described in subsection 5.1.1, the TEM analyzes were also carried out. The TEM images provide further insight into the nanostructure of g-C_3N_4.

The sample obtained from pyrolyzed melamine (Figure 5.13) exhibits a compact and aggregated morphology. The sheets appear thick and densely packed, suggesting an high degree of condensation or restacking. However, some lamellar features are still visible, indicating that the layered nature of g-C_3N_4 is retained. Thus, the pyrolysis treatment promotes the condensation and eventually the graphitization.

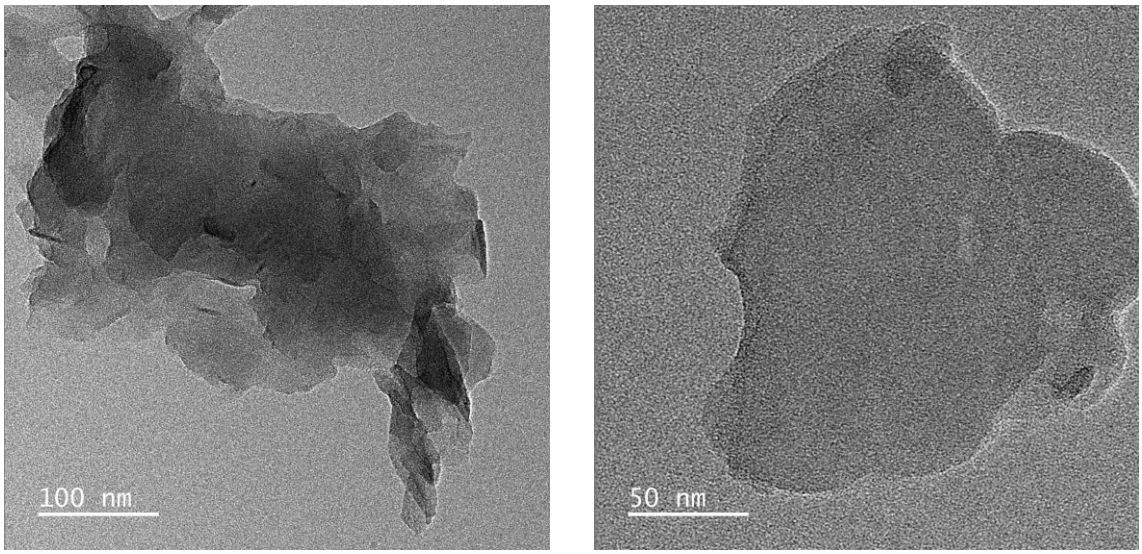

Figure 5.13: TEM images of g-C_3N_4

FTIR characterization

In the FTIR spectrum of g-C_3N_4 (Figure 5.14), it is possible to recognize the characteristic features of graphitic carbon nitride.

The broad absorption band in the region of 3000–3300 cm^{-1} is attributed to the N–H stretching vibrations, likely from residual –NH_2 or –NH groups. Multiple peaks appear in the 1200–1650 cm^{-1} region, corresponding to C–N and C=N stretching vibrations in the heterocyclic aromatic structure of tri-s-triazine units, a hallmark of g-C_3N_4. The sharp peak around 810 cm^{-1} is associated with the out-of-plane bending mode of triazine rings, confirming the preservation of the g-C_3N_4 framework.

XPS analysis

To investigate the surface composition and chemical bonding states, the XPS spectra of pristine carbon nitride were analyzed. Table 5.6 summarizes the elemental composition obtained from XPS quantification. The pristine sample exhibits a composition of 44.9% C, 53.3% N, and 1.8% O, corresponding to a C/N ratio of 0.84. These values are consistent with the expected stoichiometry of graphitic carbon nitride and confirm the structural integrity of the triazine/heptazine network, which is the typical framework of g-C_3N_4.

Table 5.6: Surface composition of pristine g-C_3N_4 determined by XPS analysis

Sample	C (%)	N (%)	O (%)	C/N
g-C_3N_4	44.9	53.3	1.8	0.84

The high-resolution C 1s spectrum of pristine g-C_3N_4 (Figure 5.15) shows a dominant peak

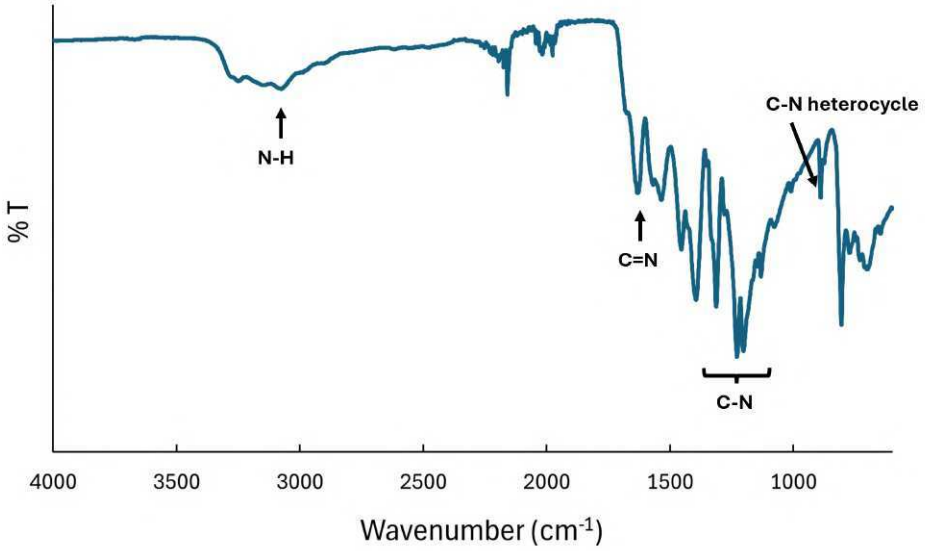

Figure 5.14: IR graph of g-C_3N_4

centered at ∼288.2 eV, which corresponds to sp^2-hybridized carbon atoms bonded to nitrogen in the N–C=N environment typical of triazine and heptazine rings. A shoulder at lower binding energy (∼286.5 eV) can be assigned to carbon in C–N bonds, whereas a minor component near 284.6 eV is associated with adventitious carbon contamination (C–C/C–H species) on the surface. In addition, a weak contribution at higher binding energies (∼291 eV) is observed, which can be interpreted either as a π–π^* satellite feature, characteristic of conjugated aromatic systems, or as an indication of oxygen-containing carbon species (such as carboxyl or carbonate functionalities). These assignments are consistent with both the intrinsic bonding states of g-C_3N_4 and the presence of minor surface oxidation. The high-resolution N 1s spectrum of pristine g-C_3N_4 (Figure 5.16) can be deconvoluted into two or three main components depending on the adopted fitting model. In agreement with most reports in the literature, peaks are typically observed at ∼398.6 eV (sp^2-bonded nitrogen in C=N–C), ∼399.7 eV (tertiary nitrogen, N–$(C)_3$), and ∼401.0–401.2 eV (terminal amino groups such as –NH_2 or –NH). In our fitting procedure, the spectrum can be satisfactorily described by two main contributions: a dominant peak at ∼399.0 eV, which is consistent with nitrogen involved in amine-type functionalities (–NH_2, –NHR, –NR_2), and a secondary component at higher binding energy (∼400.8 eV), attributable to nitrogen species interacting with oxygen (N–O). The slight differences in the binding energy positions and peak assignment reflect both instrumental calibration and the presence of surface oxygen, but overall the results are consistent with the bonding environments expected for g-C_3N_4. The O 1s spectrum of pristine g-C_3N_4 (Figure 5.17) reveals a relatively weak but detectable signal, in line with the low oxygen content obtained from XPS quantification (Table 5.6). The main contribution is centered at ∼531.5–532.0 eV and can be attributed to oxygen atoms bound to carbon in C=O or C–O species, likely originating from surface oxidation or adsorbed oxygen-containing groups. A minor component at higher binding energies (∼533.0 eV) may arise from physisorbed water or residual solvent species. These

oxygen-related features are not intrinsic to the g-C_3N_4 framework but are commonly observed in carbon nitride materials due to their high surface reactivity and tendency to react with atmospheric oxygen or moisture.

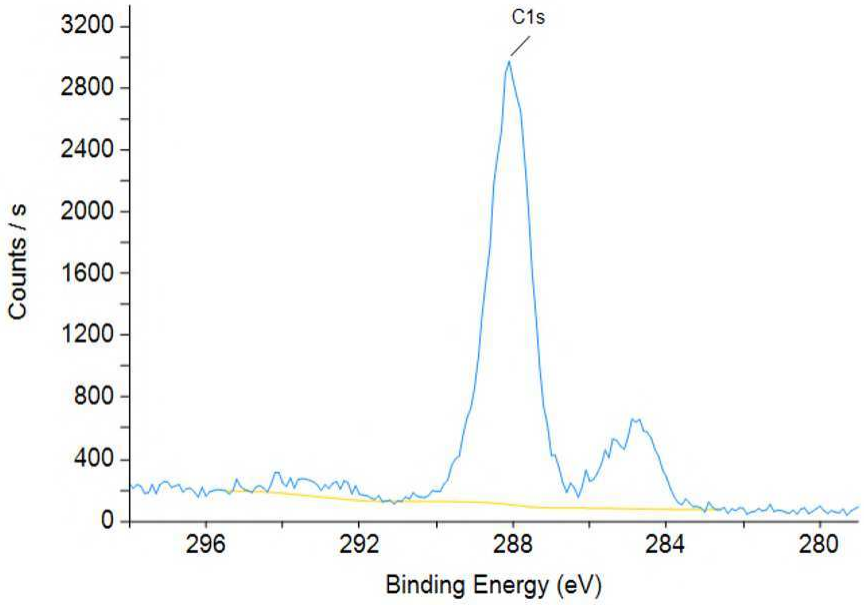

Figure 5.15: High-resolution C 1s spectrum of pristine g-C_3N_4

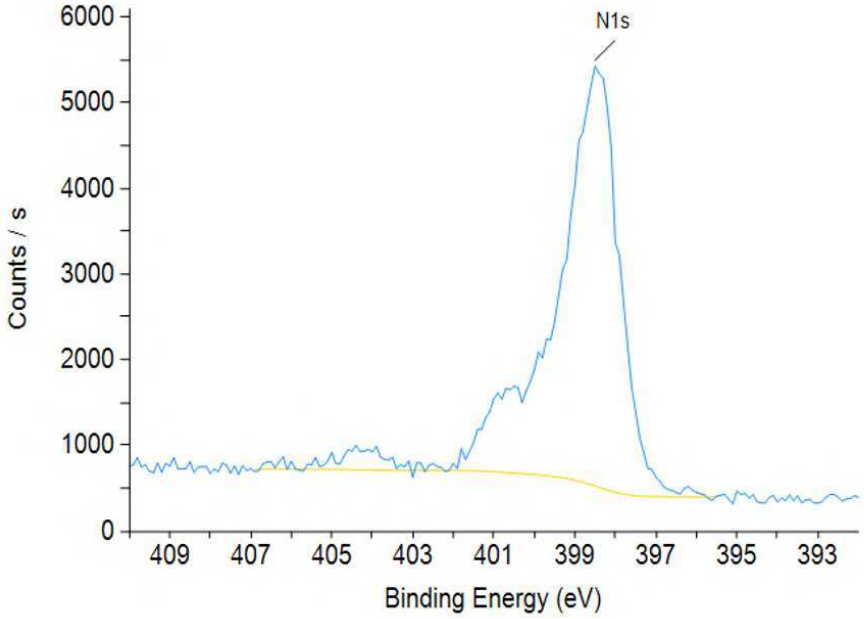

Figure 5.16: High-resolution N 1s spectrum of pristine g-C_3N_4

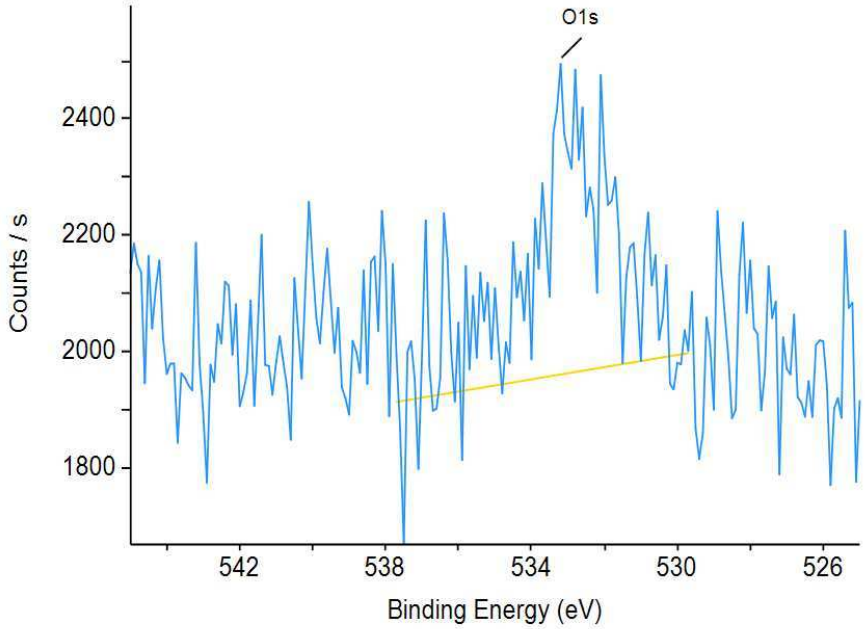

Figure 5.17: High-resolution O 1s spectrum of pristine g-C_3N_4

Overall, the XPS analysis confirms that pristine g-C_3N_4 exhibits the expected bonding environments and surface composition. The C/N ratio is close to the theoretical value. These results validate the use of pristine g-C_3N_4 as a reliable reference sample. In the following sections, the XPS analysis of heteroatom-doped samples (Br, P, B) will be presented, where the C 1s, N 1s, and O 1s spectra remain largely consistent with the pristine material, while additional contributions associated with dopant elements are highlighted.

XRD analysis

Figure 5.18 shows the X-ray diffraction (XRD) patterns of pristine g-C_3N_4.

The pattern exhibits the characteristic diffraction peaks of graphitic carbon nitride. The most intense peak, centered around 27.5° (2θ), corresponds to the (002) plane, associated with the interlayer stacking of the conjugated aromatic systems. In addition to this, a weaker reflection can be observed at approximately 13° (2θ), which is assigned to the (100) plane. This peak arises from the in-plane structural periodicity of the tri-s-triazine units, highlighting the ordered arrangement within the aromatic framework. The relative intensity of this reflection is lower compared to the (002) peak, reflecting the limited degree of long-range order parallel to the layers. The sharpness and position of the (002) peak provide useful information on the stacking of the layers: a well-defined peak indicates efficient π–π stacking, whereas a broader signal suggests structural disorder or incomplete condensation. The interlayer distance d_{002}, around 0.32–0.33 nm, can be calculated from the peak position using Bragg's law, while the width of the peak can be exploited to estimate the crystallite size along the stacking direction. Shifts of the (002) reflection towards higher or lower angles may indicate compression or expansion of the interplanar spacing, often linked to

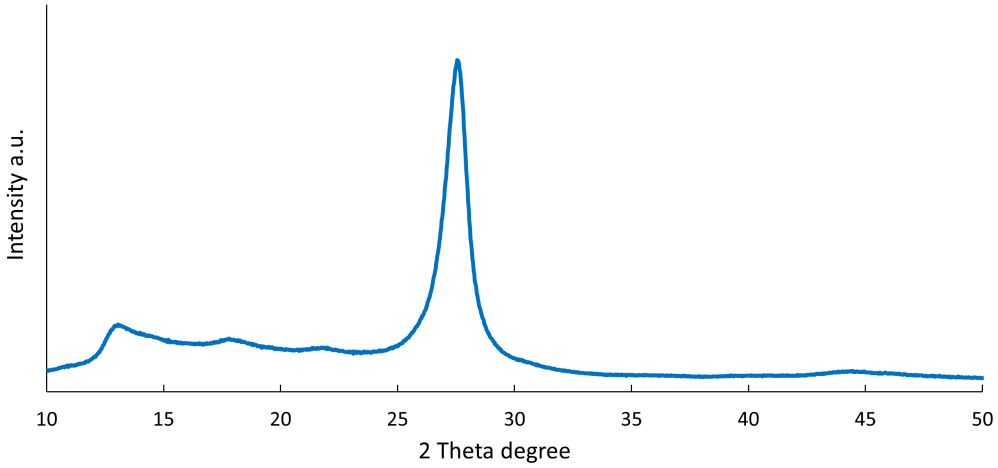

Figure 5.18: XRD graph of pristine g-C_3N_4

defects or the incorporation of foreign atoms and groups. Similarly, the absence or weakening of the (100) reflection can be interpreted as a loss of in-plane periodicity, possibly due to distortions or a reduced degree of condensation. Overall, the XRD pattern of g-C_3N_4 reflects its partially ordered layered structure, where the strong stacking along the c-axis coexists with a more limited ordering within the planar direction.

Band gap analysis

The band gap of the material was estimated from diffuse reflectance spectra (DRS) measurements, as described in Subsection 5.1.1. Figure 5.19a reports the DRS curve for pristine g-C_3N_4, where the absorption edge can be clearly identified and related to the onset of electronic transitions between the valence and conduction bands.

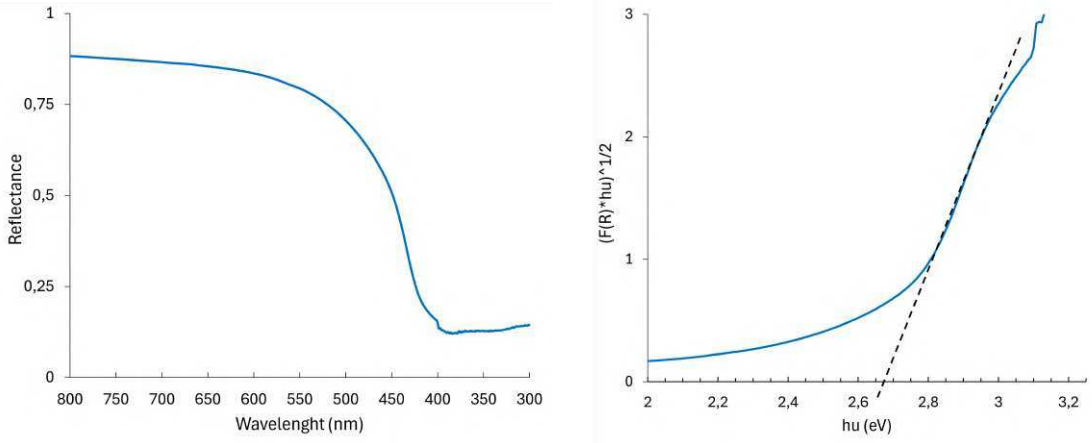

(a) Diffuse reflectance spectrum (DRS)

(b) Tauc plot

Figure 5.19: Band gap analysis of pristine g-C_3N_4

However, in order to determine the band gap energy more precisely, the Tauc method was applied by transforming the reflectance data according to the Kubelka–Munk function. The corresponding Tauc plot is shown in Figure 5.19b, where the linear portion of the curve was extrapolated to the energy axis, leading to a band gap value of 2.68 eV. This value is in good agreement with those typically reported in the literature for pristine g-C_3N_4, thereby confirming the reliability of the synthesis procedure. In summary, while the DRS spectrum provides the experimental basis to visualize the optical absorption edge, the Tauc plot allows the quantitative determination of the band gap energy.

5.3.2 Bromine doping

Five bromine-doped g-C_3N_4 samples were synthesized using different bromine sources and labeled as Br1-CP, Br2-CP, Br3-CP, Br4-CP, and Br4-PP, where CP indicates co-pyrolysis and PP indicates post-pyrolysis treatment. The samples display distinct coloration, ranging from light yellow to dark brown and orange, reflecting differences in the bromine precursors and the applied thermal treatments. Such visual variations are indicative of changes in the electronic structure and optical properties of the materials. Images of all samples are shown in Figure 5.20.

Figure 5.20: Bromine-doped g-C_3N_4 samples synthesized

Table 5.7 summarizes the synthesis conditions for the different bromine-doped g-C_3N_4 samples obtained, including the initial mass, the bromine source, the mass of the isolated product and the corresponding yield.

Synthetic yields varied depending on the bromine source and the synthetic strategy. The first three samples (Br1-CP, Br2-CP, Br3-CP) were prepared via co-pyrolysis with melamine bis-hydrobromide or organic bromides and delivered consistent yields around 43–44%, indicating that this approach is reproducible and allows for recovery of the product without significant loss. Br4-CP, synthesized via co-pyrolysis with elemental bromine, showed a lower yield (39%). Br4-PP, prepared through a post-pyrolysis treatment with elemental bromine, represents a completely different synthetic pathway and achieved a higher yield (81%), reflecting the efficiency of this method in preserving the structural integrity of g-C_3N_4. Overall, these observations highlight that the yield of Br-doped g-C_3N_4 is strongly influenced by both the bromine source and the specific synthetic approach.

Table 5.7: Synthesis conditions and yields of bromine-doped g-C_3N_4 samples

Sample	Mass (g)	Dopant reagent	Mass obtained (g)	Yield (%)
Br1-CP	10 melamine	$C_9H_8N_6^{2+}\cdot 2Br^-$	4.41	43
Br2-CP	10 melamine	C_6H_4BrCN	4.43	43
Br3-CP	10 melamine	$BrC_6H_4N(CH_3)_2$	4.52	44
Br4-CP	10 melamine	Br_2	3.99	39
Br4-PP	2 g-C_3N_4	Br_2	2.0	81

ESEM-EDX analysis

As described in subsection 5.1.1, the SEM analyzes were carried out, as represented in the Figure 5.21.

The EDX elemental analysis reported in Table 5.8 confirms that all bromine-doped $\mathrm{g\text{-}C_3N_4}$ samples maintain the typical stoichiometric balance between nitrogen (62–64 wt%) and carbon (34–35 wt%). The oxygen content is low (1.6–3.2 wt%), mainly arising from surface oxidation and exposure to air.

Table 5.8: EDX elemental analysis on the surface of bromine-doped $\mathrm{g\text{-}C_3N_4}$ samples

Element	Weight %				
	Br1-CP	Br2-CP	Br3-CP	Br4-CP	Br4-PP
N	62.5	63.5	63.2	63.0	62.4
C	34.2	34.4	34.2	34.1	34.6
O	3.2	2.1	2.6	2.9	1.6
Br	–	–	–	–	1.4

Although EDX analysis is useful for elemental characterization, it is known to have limited sensitivity, especially for light elements. No bromine is detected in the Br1-CP, Br2-CP and Br3-CP samples, obtained respectively from hydrobromic acid, 2-bromobenzonitrile and 4-bromo-N,N-dimethylaniline as precursors. Similarly, the Br4-CP sample, synthesized by co-pyrolysis with elemental bromine, does not exhibit a measurable Br signal. In contrast, bromine is clearly detected (1.4 wt%) in the Br4-PP sample, where Br_2 was introduced after pyrolysis through a post-pyrolytic treatment. This suggests that bromine incorporation is less efficient under high-temperature co-pyrolysis conditions, but becomes significant when Br_2 interacts with preformed $\mathrm{g\text{-}C_3N_4}$ surfaces. Therefore, post-pyrolysis functionalization appears to be the most effective strategy for introducing bromine atoms. These results highlight how the choice of precursor and synthesis pathway strongly influences bromine retention.

TEM analysis

As described in subsection 5.1.1, the TEM analyzes were carried out, as represented in Figure 5.22.

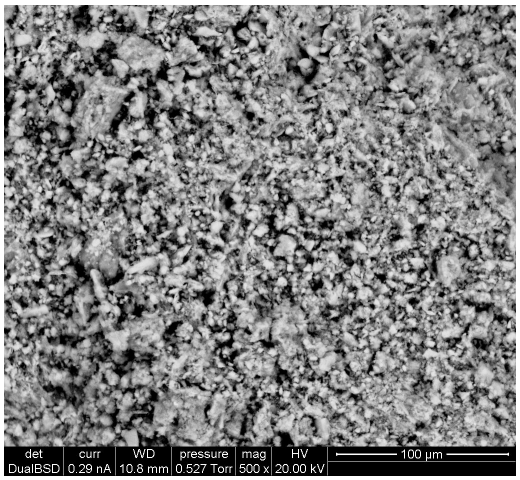

(a) Br1-CP

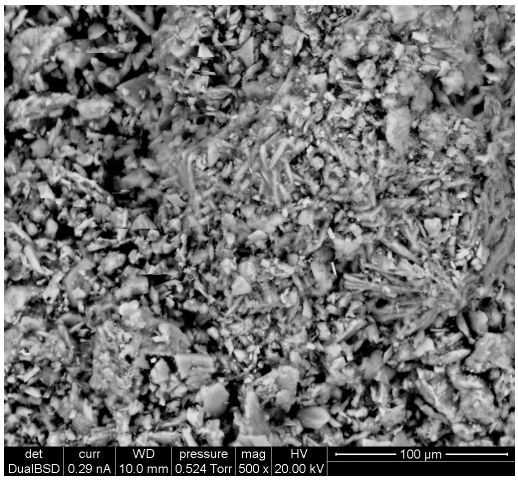

(b) Br2-CP

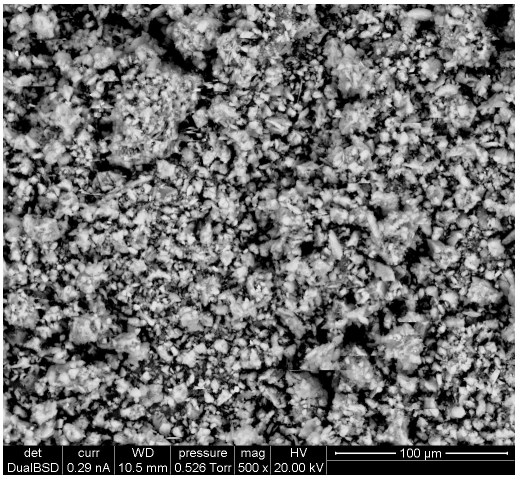

(c) Br3-CP

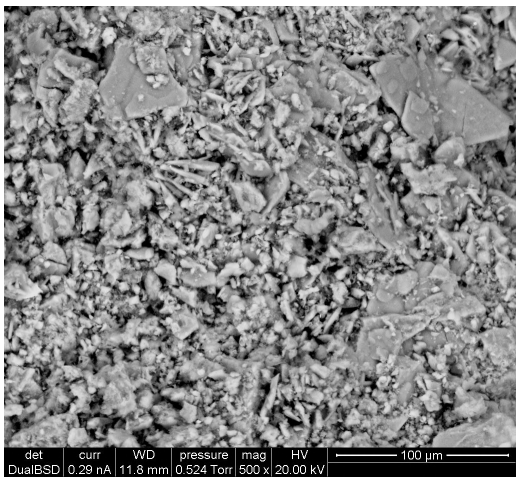

(d) Br4-CP

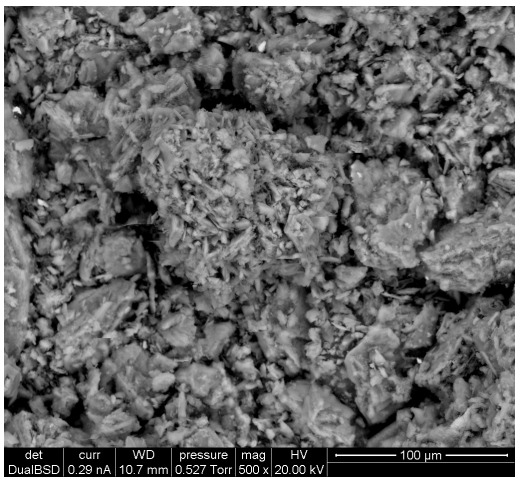

(e) Br4-PP

Figure 5.21: ESEM images of bromine-doped g-C_3N_4 samples

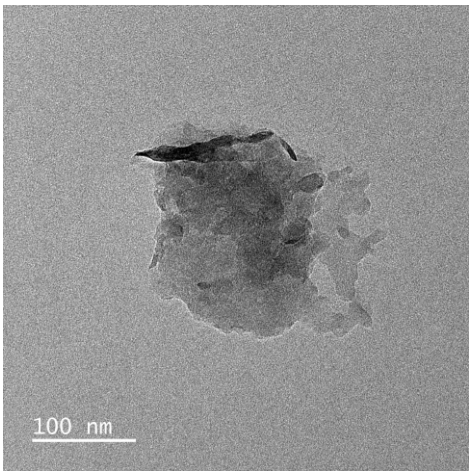

(a) Br1-CP

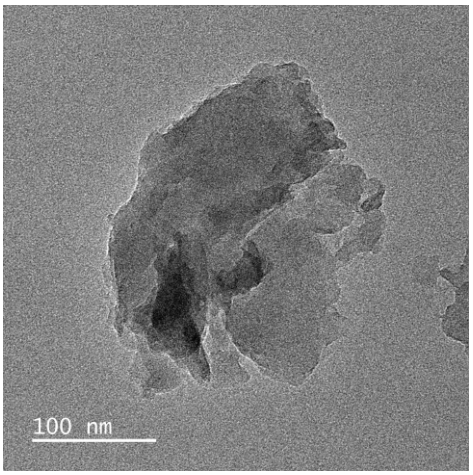

(b) Br2-CP

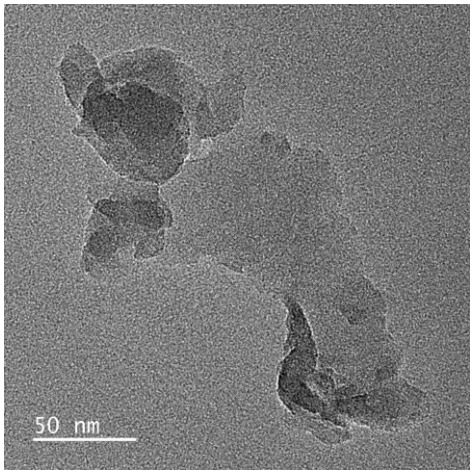

(c) Br3-CP

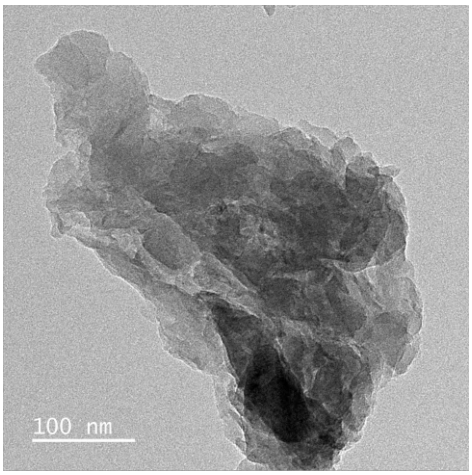

(d) Br4-CP

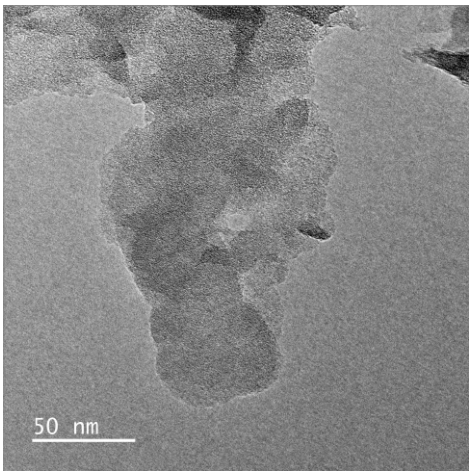

(e) Br4-PP

Figure 5.22: TEM images of bromine-doped g-C_3N_4 samples

FTIR characterization

The infrared spectra of the bromine-doped g-C_3N_4 samples are reported in Figure 5.23.

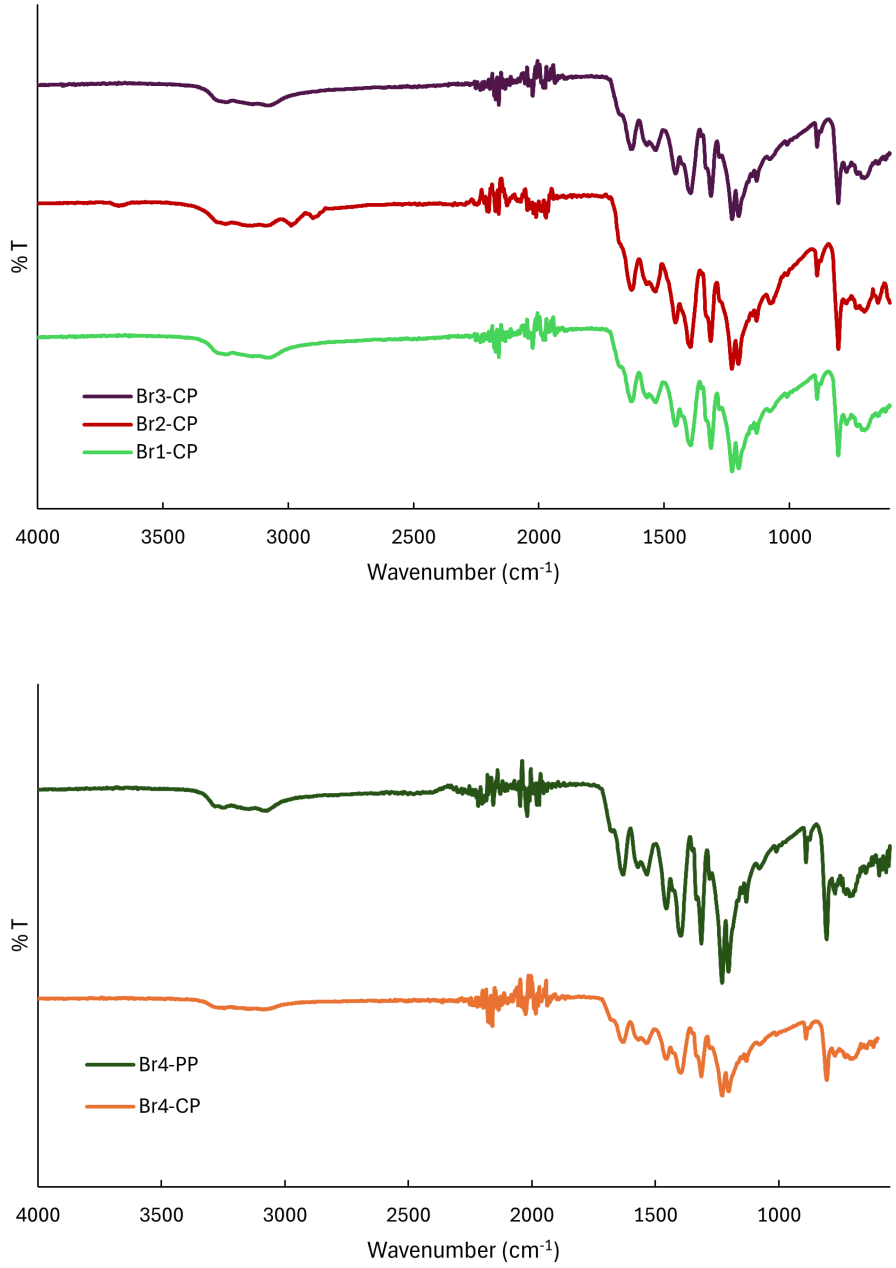

Figure 5.23: IR graph of bromine-doped g-C_3N_4 samples

The spectra allow a direct comparison of the chemical environment of the carbon nitride framework after doping. All samples show the characteristic vibrational features of the heptazine-

based structure, including the stretching modes of C–N and C=N bonds. Minor shifts in band positions are observed depending on the precursor employed, reflecting the different interactions between bromine and the polymeric network. In particular, the post-pyrolyzed Br4-PP sample displays subtle modifications, consistent with the EDX evidence of bromine incorporation. These results confirm that the doping route has a measurable effect on the surface functionalization.

XPS analysis

The XPS spectra of the two bromine-doped g-C_3N_4 samples, Br3-CP and Br4-PP, display overall features for C 1s, N 1s, and O 1s that are similar to those of pristine g-C_3N_4 (see Section 5.3.1). This indicates that the general polymeric structure of g-C_3N_4 is largely preserved upon bromination. The bromine-doped carbon nitride samples were obtained by post-synthetic functionalization of pyrolyzed g-C_3N_4 using elemental bromine (Br_2) for Br4-PP, while Br3-CP was prepared via co-pyrolysis with 4-nitrodimethylaniline. XPS analysis confirms successful bromine incorporation in Br4-PP, which displays a Br content of 0.9 at.% (Table 5.9).

Table 5.9: Surface composition of Br-doped g-C_3N_4 samples (XPS analysis)

Sample	**C (%)**	**N (%)**	**O (%)**	**Br (%)**	**C/N**
Br3-CP	42.9	55.2	1.9	–	0.8
Br4-PP	41.0	56.0	2.1	0.9	0.7

In contrast, Br3-CP shows no detectable Br signal, suggesting either low doping levels or loss of bromine during the thermal treatment procedure. Compared to the undoped reference, both bromine-doped samples exhibit slightly lower C/N ratios (0.7–0.8), which could reflect partial oxidation, retention of nitrogen, or structural perturbations due to Br incorporation. Oxygen levels remain modest (1.9–2.1 at.%), indicating limited surface oxidation and preservation of the g-C_3N_4 framework. The detection of bromine by XPS confirms that the halogenation process effectively modifies the surface chemistry of g-C_3N_4, particularly with a post-pyrolisis, process with sufficient Br_2 loading. Bromine incorporation is expected to introduce electron-withdrawing effects, altering the local electronic environment and potentially enhancing photocatalytic activity. The high-resolution Br 3d spectrum of Br4-PP (Figure 5.24) shows a peak at 68.2 eV, indicative of bromine present as bromide species.

This signal was acquired in high-sensitivity, low-resolution mode to improve the signal-to-noise ratio, as compared to the high-resolution scans of the C 1s, N 1s, and O 1s regions.

XRD analysis

Figure 5.25 shows the XRD patterns of bromine-doped graphitic carbon nitride synthesized using two different approaches.

The blue curve corresponds to the sample doped by copyrolysis using 4-bromo-N,N-dimethylaniline (Br3-CP), while the orange curve refers to the material post-synthetically treated with elemental bromine (Br4-PP). Both patterns exhibit the characteristic (002) diffraction peak at approximately 27.5° (2θ), which is attributed to the interlayer stacking of the conjugated aromatic units in the

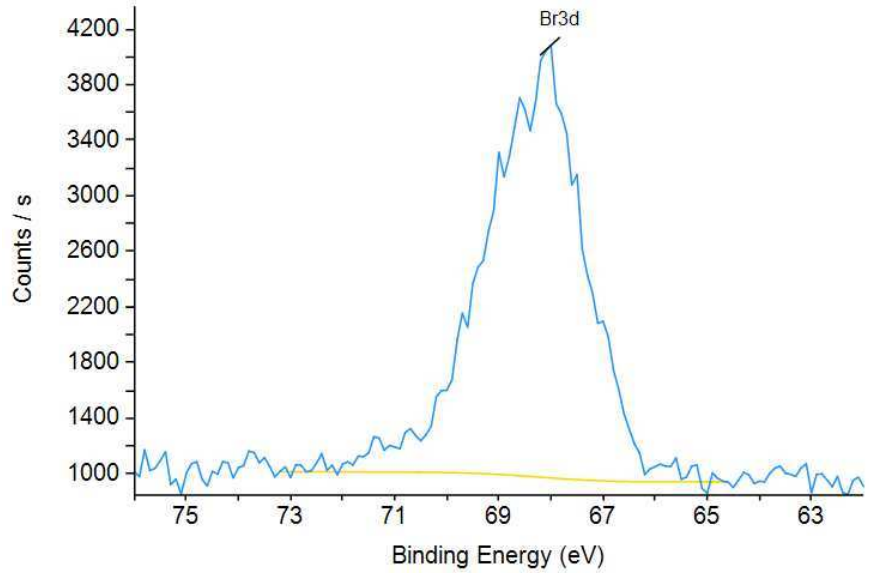

Figure 5.24: High-resolution Br 3d spectrum of Br4-PP

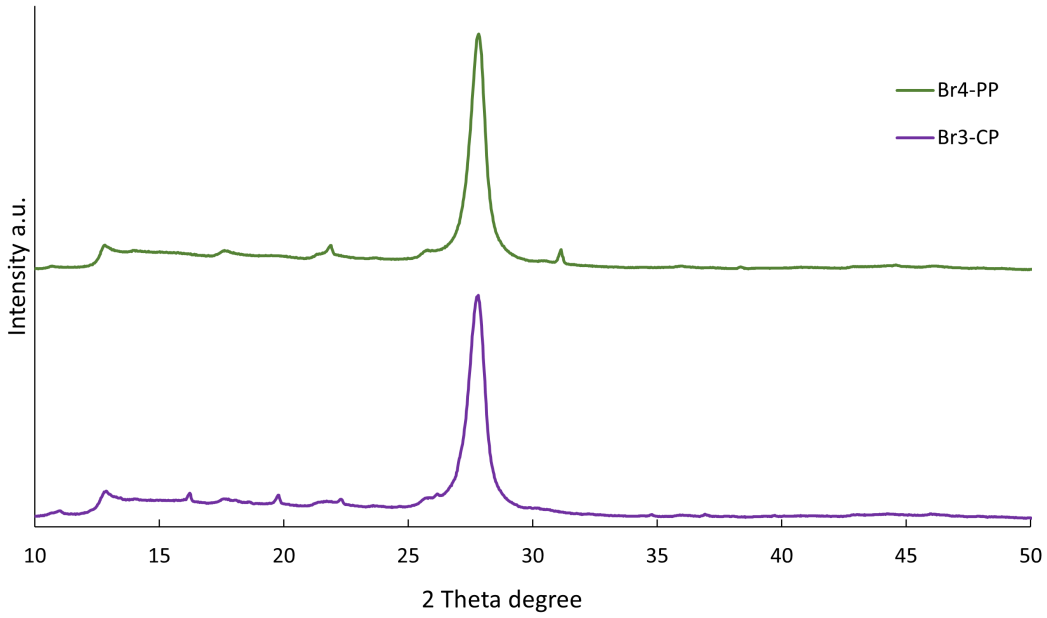

Figure 5.25: XRD graph of bromine-doped g-C_3N_4

g-C_3N_4 framework. Notably, the Br3-CP sample displays a sharper and more intense (002) peak, indicating a higher degree of crystallinity and a more ordered lamellar structure. This suggests that the use of a molecular bromine-containing precursor during synthesis promotes a more homogeneous and controlled incorporation of dopant into the framework. Conversely, the sample treated with elemental bromine post-synthetically shows a broader and less intense (002) reflection, pointing to a partial disruption of the interlayer order and a lower crystallinity. This effect is likely due to the aggressive oxidative nature of elemental bromine, which may induce structural defects, fragmentation, or even partial exfoliation of the g-C_3N_4 layers during treatment. Additionally, the (100) peak near 13°, typically associated with in-plane structural packing, is barely visible or absent in both samples, indicating that bromine doping—regardless of the method—has a limited effect on the in-plane structural order. Overall, the XRD analysis confirms that bromine doping can influence the crystallinity of g-C_3N_4, with the in situ method (Br3-CP) being more effective in preserving and even enhancing the structural ordering of the material. These structural modifications are expected to impact the optical and electronic properties of the materials, as discussed in the following sections. The small peaks observed in the XRD pattern of Br4-PP sample analysed before being washed with water correspond to ammonium bromide residues. In fact, during the synthesis, liquid bromine can react with the amorphous regions of graphitic carbon nitride, causing an etching process. This reaction involves the electrophilic attack of bromine molecules on defect sites and nitrogen-rich moieties within the amorphous domains, breaking C–N bonds and causing structural degradation. Consequently, this chemical erosion leads to material loss, which explains the lower mass yield compared to the initial amount of carbon nitride precursor used.

Band gap analysis

The optical properties of bromine-doped g-C_3N_4 samples were investigated using diffuse reflectance spectroscopy (DRS) to determine the corresponding band gap energies.

The DRS spectra (Figures 5.26a and 5.27a) reveal a noticeable red-shift in the absorption edge compared to pristine g-C_3N_4 (Figure 5.19a), suggesting modifications in the electronic structure. In fact, in bromine-doped samples electronic perturbations arise from the presence of Br atoms, which can alter the local electronic environment, slightly reducing the band gap and enhancing visible-light absorption. The band gap values were calculated using Tauc plots derived from the DRS data (Figures 5.26b and 5.27b), assuming an indirect allowed transition, which is typical for g-C_3N_4. The results are summarized in Table 5.10.

Table 5.10: Band gap values obtained from DRS measurements for bromine-doped g-C_3N_4 samples

Sample	Band gap value (eV)
Br1-CP	2.56
Br2-CP	2.60
Br3-CP	2.45
Br4-CP	2.45
Br4-PP	2.53

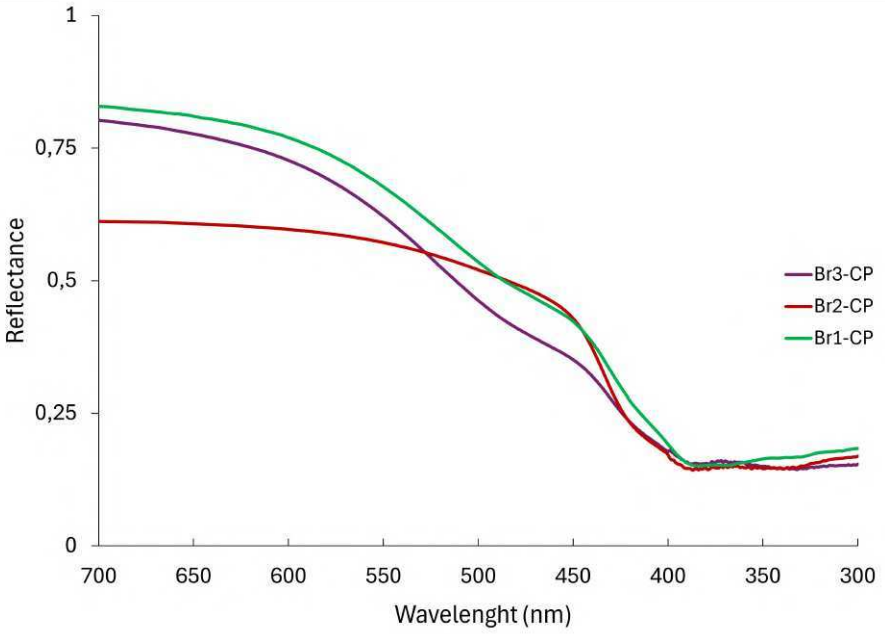

(a) Diffuse reflectance spectra (DRS) for Br1-CP, Br2-CP, Br3-CP

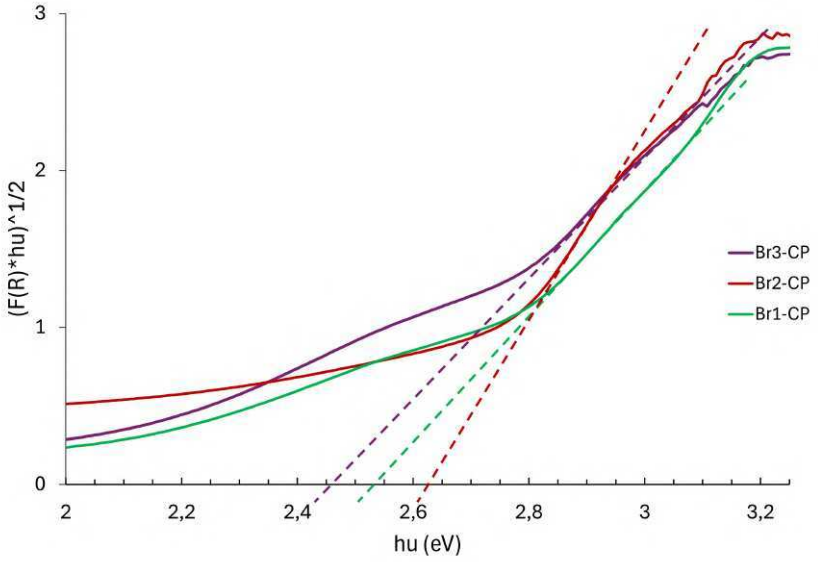

(b) Tauc plots for Br1-CP, Br2-CP, Br3-CP

Figure 5.26: DRS and Tauc plot analysis of Br1-CP, Br2-CP, and Br3-CP

Among the bromine-doped samples, the band gap ranges from 2.45 eV (Br3-CP) to 2.60 eV (Br2-CP), with Br4-PP exhibiting 2.53 eV. The slight reduction in the band gap relative to undoped g-C_3N_4 indicates an enhanced absorption in the visible region, which is particularly beneficial for photocatalytic processes.

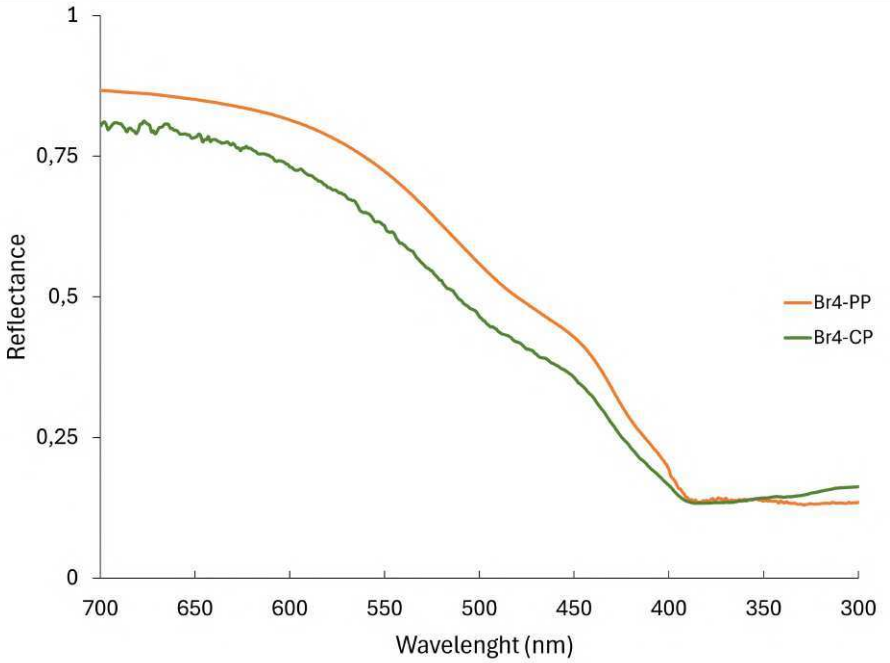

(a) Diffuse reflectance spectra (DRS) for Br4-CP and Br4-PP

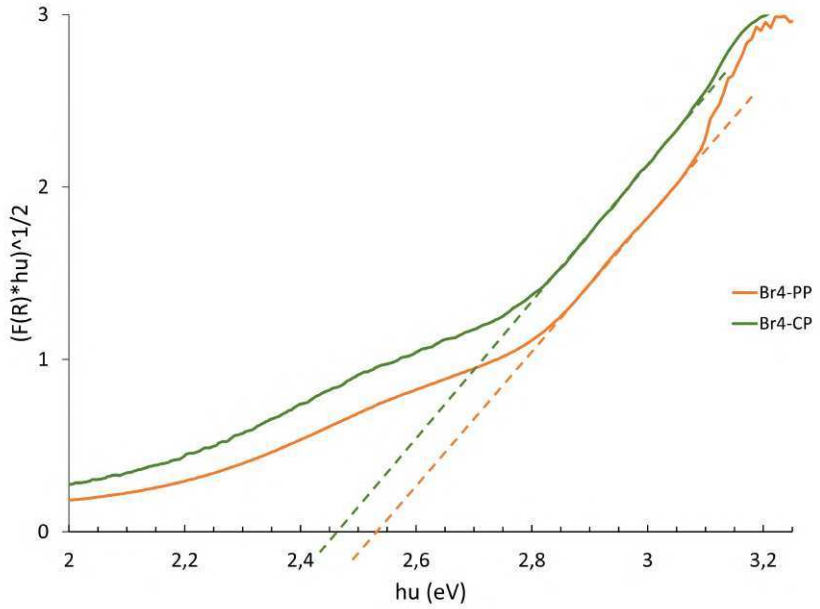

(b) Tauc plots for Br4-CP and Br4-PP

Figure 5.27: DRS and Tauc plot analysis of Br4-CP and Br4-PP

5.3.3 Phosphorous doping

The obtained phosphorous-doped g-C_3N_4 samples exhibit quite a similar color (Figure 5.28).

Figure 5.28: Phosphorous-doped g-C_3N_4 samples synthesized

In particular, two different materials are shown, corresponding to P 0.1%-CP and P 1.2%-CP, synthesized with increasing amounts of triphenylphosphine (PPh_3) as the phosphorus source. Despite the variation in functionalization degree, both powders appear to have an almost identical yellowish shade, typical of carbon nitride derivatives. No clear macroscopic differences can be distinguished by simple visual inspection, suggesting that the phosphorus incorporation does not significantly affect the overall aspect of the final solids. This observation is in line with previous reports where only subtle optical variations could be detected upon heteroatom doping.

Table 5.11 reports the synthesis data for two phosphorus-functionalized carbon nitride samples.

Table 5.11: Synthesis conditions and yields of phosphorus-doped g-C_3N_4 samples

Sample	Melamine mass (g)	P reagent (g)	Mass obtained (g)	Yield (%)
P 0.1%-CP	10	0.1	4.69	46.9
P 1.2%-CP	10	1.0	4.72	47.2

Both materials were prepared starting from 10 g of melamine, varying the amount of phosphorus reagent introduced in the reaction. In the first case, only 0.1 g of P reagent was used, corresponding to a nominal functionalization degree of 0.1%. The obtained solid mass after synthesis was 4.69 g, which represents a yield of 46.9%. The second sample was prepared with a larger amount of phosphorus reagent (1.0 g). After synthesis, the recovered mass was 4.72 g, very close to that of the previous material. The yield in this case was slightly higher, reaching 47.2%.

ESEM-EDX analysis

Figure 5.29 shows the ESEM images of phosphorus-doped graphitic carbon nitride (P-g-C_3N_4) samples synthesized with different amounts of triphenylphosphine. The ESEM images reveal a significant change in the surface morphology with increasing phosphorus content. The P 0.1%-CP sample exhibits a rough, porous structure composed of aggregated particles, indicating a typical g-C_3N_4 morphology. In contrast, the P 1.2%-CP sample shows a more compact and homogeneous surface, suggesting that a higher phosphorus doping level may influence the polymerization or condensation process during the thermal treatment, resulting in denser packing and reduced porosity. These morphological differences are consistent with variations in chemical composition and may affect the photocatalytic or electronic properties of the material.

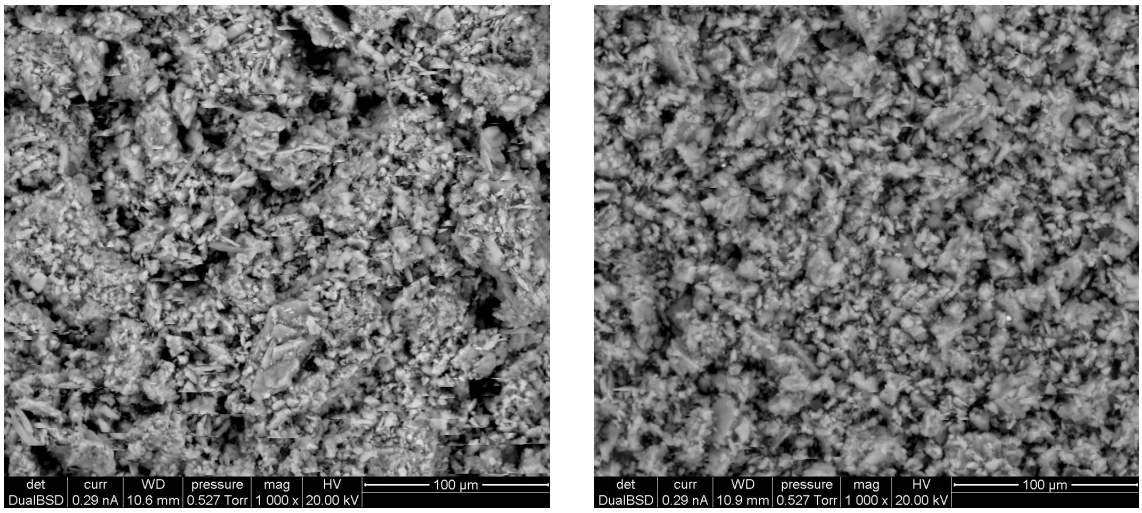

(a) P 0.1%-CP (b) P 1.2%-CP

Figure 5.29: ESEM images of P 0.1%-CP and P 1.2%-CP

Table 5.12 reports the surface composition of phosphorus-doped g-C_3N_4 samples as determined by EDX analysis. Compared to the pristine sample in Table 5.5, the incorporation of phosphorus slightly decreases the nitrogen content while increasing both carbon and oxygen contributions. However, no phosphorus signal was detected in either sample, confirming that the low doping level lies below the detection limit of the EDX technique.

Table 5.12: EDX elemental analysis on the surface of phosphorous-doped g-C_3N_4 samples

Sample	N (wt%)	C (wt%)	O (wt%)	P (wt%)
P 0.1%-CP	62.7	35.7	1.6	–
P 1.2%-CP	60.7	36.8	2.4	–

TEM analysis

Transmission electron microscopy (TEM) was employed to investigate the morphology of the phosphorous-doped g-C_3N_4 samples. Figure 5.30 presents representative TEM micrographs of P 0.1%-CP (Figure 5.30a) and P 1.2%-CP (Figure 5.30b).

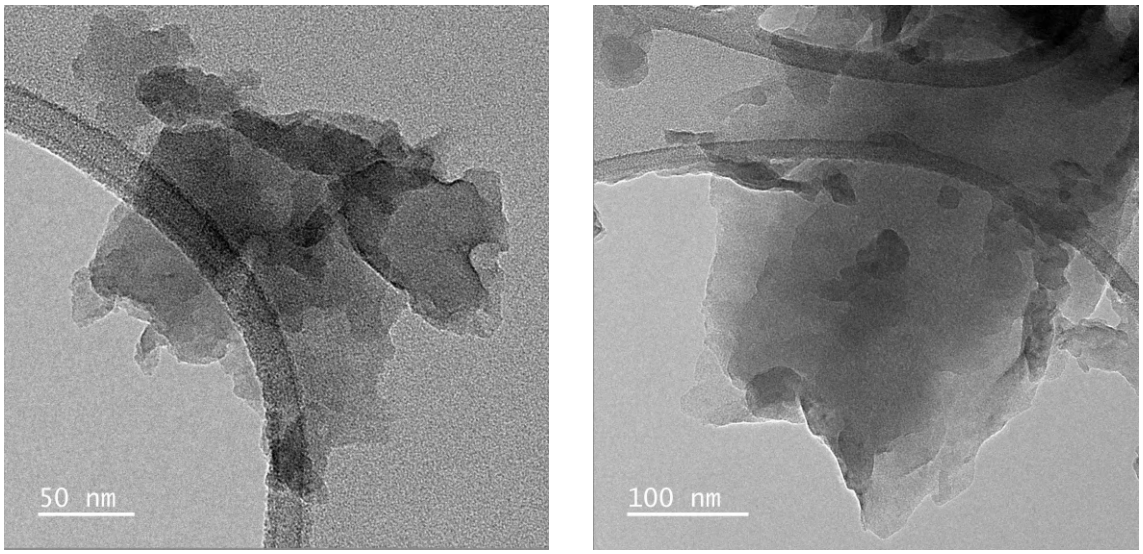

(a) P 0.1%-CP (b) P 1.2%-CP

Figure 5.30: TEM images of P 0.1%-CP and P 1.2%-CP

Both images reveal the typical layered structure of carbon nitride, appearing as thin and irregularly stacked sheets. The nanosheets exhibit a wrinkled morphology, which is commonly observed for g-C_3N_4 due to its graphitic nature. No significant morphological differences are detected between the two samples at this magnification.

FTIR characterization

Figure 5.31 shows the FTIR spectra of phosphorus-doped g-C_3N_4 samples, containing different amount of triphenylphosphine (PPh_3) as the phosphorus source.

Both spectra display the typical absorption features of graphitic carbon nitride. The broad band in the 3000–3300 cm^{-1} region is attributed to N–H and O–H stretching vibrations, likely from surface amine groups or adsorbed water. The region between 1200 and 1650 cm^{-1} contains several bands associated with C–N and C=N stretching vibrations within the heptazine units, while the sharp peak near 810 cm^{-1} corresponds to the breathing mode of the tri-s-triazine rings — confirming the integrity of the g-C_3N_4 framework. No significant differences are observed in these regions between the two samples, suggesting that phosphorus doping, even at higher content (1.2%), does not markedly affect the bulk chemical structure of the g-C_3N_4 matrix. Minor changes may occur in the 1000–1150 cm^{-1} region, but no new bands clearly attributable to P–N or P–O vibrations are distinguishable in these spectra, likely due to overlapping signals or low doping levels.

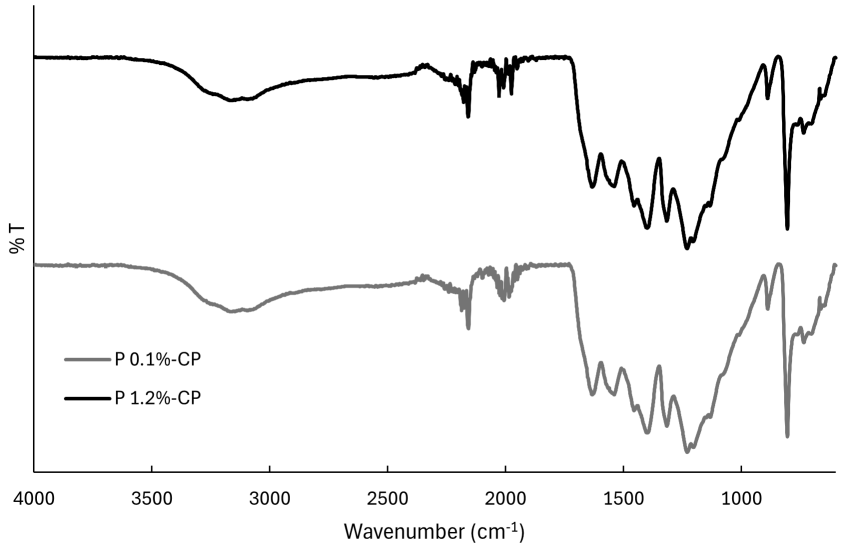

Figure 5.31: IR graph of phosphorous-doped g-C_3N_4 samples

XPS analysis

The XPS survey spectra of phosphorus-doped g-C_3N_4 samples (P 0.1%-CP and P 1.2%-CP) show overall features similar to those observed for pristine g-C_3N_4 in Section 5.3.1, indicating that the polymeric network is largely preserved upon doping. The high-resolution C 1s, N 1s, and O 1s spectra display comparable shapes and peak positions to the undoped references, suggesting that the local bonding environments of carbon and nitrogen are mostly maintained.

Table 5.13: Surface composition and C/N ratio of phosphorus-doped g-C_3N_4 samples (XPS analysis)

Sample	C (at.%)	N (at.%)	O (at.%)	P (at.%)	C/N
P 0.1%-CP	40.9	57.5	1.6	–	0.7
P 1.2%-CP	42.0	56.8	1.3	–	0.7

Although phosphorus was not detected in the survey spectra, likely due to its low concentration or incorporation in chemical environments not distinguishable from the carbon nitride matrix, some changes in the elemental composition are observed. Both P 0.1%-CP and P 1.2%-CP exhibit lower C/N ratios (0.7) compared to pristine g-C_3N_4 (0.8–0.9), suggesting an increase in nitrogen-rich sites or structural rearrangements that reduce the relative carbon content. Oxygen levels remain low (1.3–1.6 at.%), indicating limited surface oxidation and the preservation of the condensed g-C_3N_4 framework. These findings are consistent with the successful incorporation of low levels of phosphorus, even if it is below the XPS detection limit. Overall, the XPS results indicate that phosphorus doping does not significantly disrupt the g-C_3N_4 network but introduces modifications

in the elemental composition that could influence electronic and photocatalytic properties.

XRD analysis

Figure 5.32 presents the XRD patterns of carbon nitride samples doped with phosphorus using triphenylphosphine (PPh_3) as the phosphorus source.

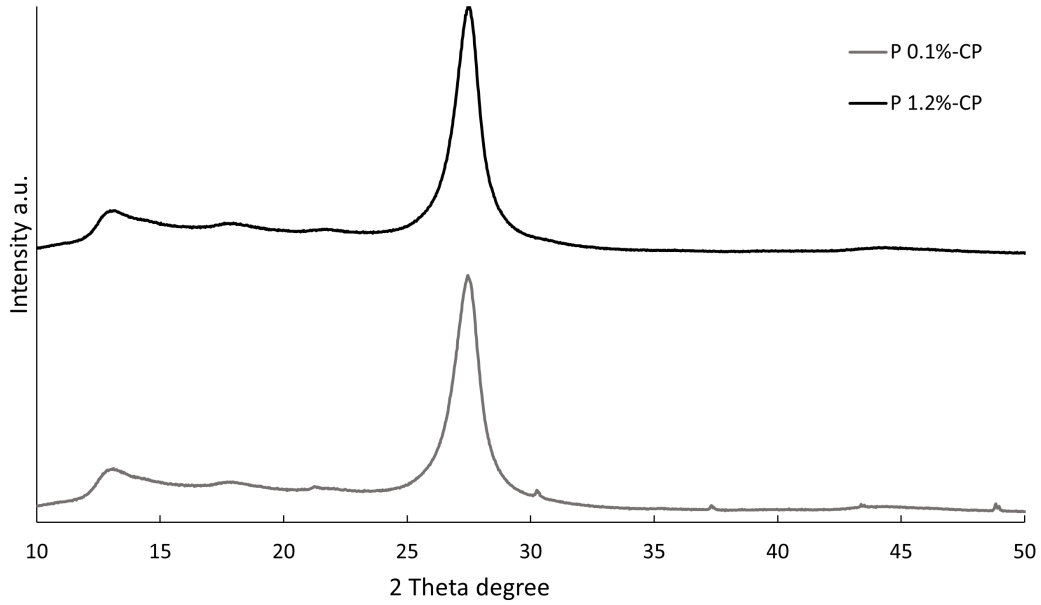

Figure 5.32: XRD graph of phosphorous-doped g-C_3N_4

Two doping levels are shown: 0.1% P (gray curve) and 1.2% P (black curve). Both samples display the typical diffraction features of polymeric carbon nitride: a minor reflection near 13° (100) and a strong peak around 27.4° 2θ (002), which corresponds to the interlayer stacking of the conjugated aromatic systems. These features confirm the successful synthesis of the carbon nitride framework. Notably, sample P 0.1%-CP exhibits a sharper and more intense (002) reflection, suggesting a higher degree of crystallinity and well-preserved stacking order. In contrast, P 1.2%-CP shows a significant broadening and intensity decrease of the (002) peak, indicative of increased structural disorder. This is likely caused by excessive phosphorus loading, which perturbs the interlayer interactions and introduces defects.

Band gap analysis

The optical properties of the phosphorous-doped samples were evaluated by diffuse reflectance spectroscopy (DRS), following the same procedure described in subsection 5.1.1. Figure 5.33a shows the DRS spectra of P 0.1%-CP and P 1.2%-CP, in which the absorption edges are clearly visible and indicate a band gap transition similar to that of pristine g-C_3N_4. To quantitatively estimate the band gap values, the reflectance data were first converted into the Kubelka–Munk

function and then analyzed using the Tauc method. The resulting plots are shown in Figure 5.33b, where the linear regions of the curves were extrapolated to the energy axis.

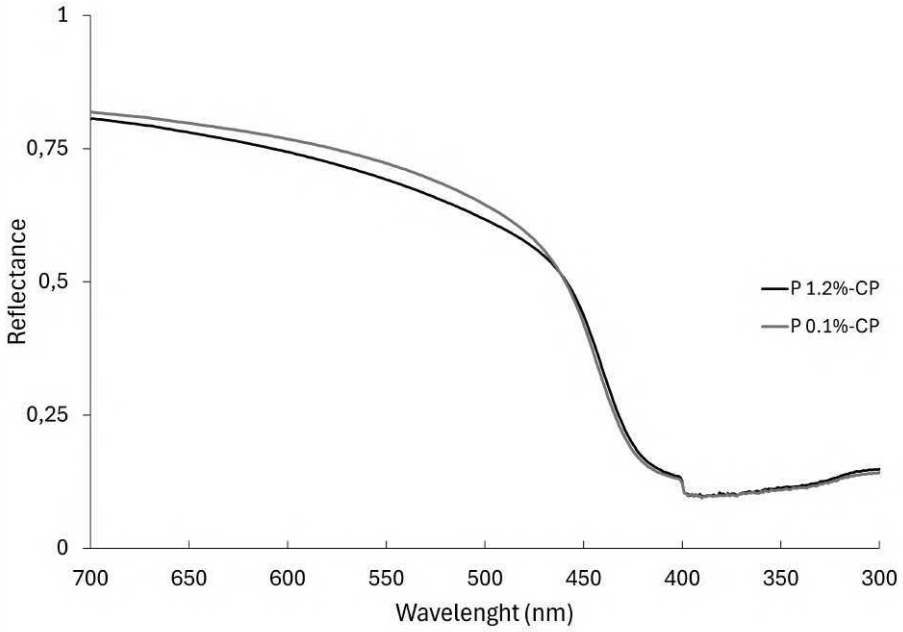

(a) Diffuse reflectance spectrum (DRS)

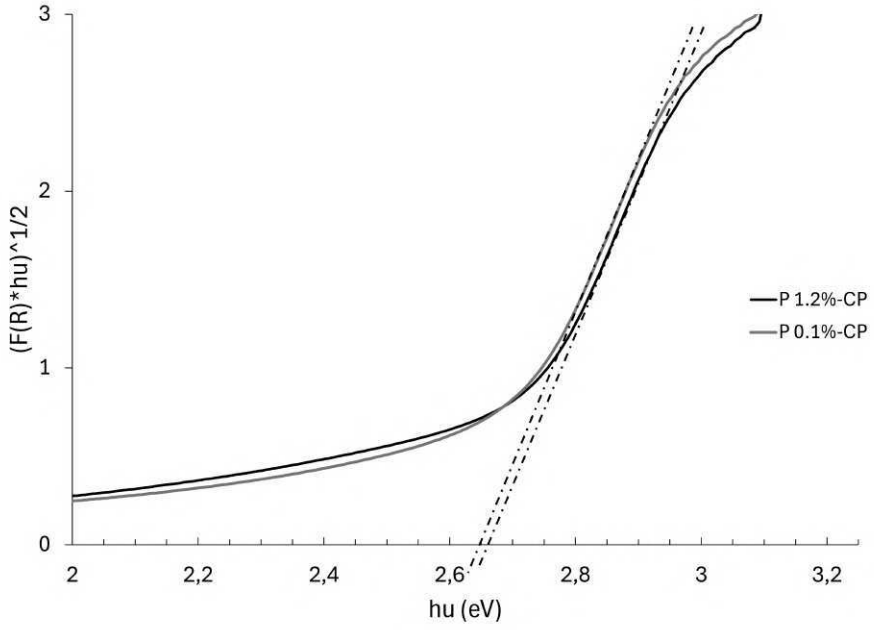

(b) Tauc plot

Figure 5.33: Band gap analysis of phosphorous-doped g-C_3N_4

The obtained band gap value was very similar, as summarized in Table 5.14.

Table 5.14: Band gap values obtained from DRS measurements

Sample	Band gap value (eV)
P 0.1%-CP	2.64
P 1.2%-CP	2.66

This result confirms that the introduction of phosphorus, even at different functionalization degrees, does not significantly affect the electronic structure of g-C_3N_4. Overall, the DRS analysis demonstrates that the band gap of the doped materials remains comparable to that of pristine g-C_3N_4, suggesting that phosphorus incorporation mainly influences surface and structural features rather than bulk electronic transitions.

5.3.4 Boron doping

In the synthesis of boron-doped g-C_3N_4 derivatives, two different boron precursors were employed. Boron trifluoride diethyl etherate ($BF_3 \cdot OEt_2$), a reagent used in the preparation of fluorescent molecules such as BODIPY [292], was chosen to exploit the potential photoluminescent properties of the boron-containing species that can coordinate to nitrogen atoms within the g-C_3N_4 framework. Coordination of boron to the electron-rich nitrogen sites can induce local electronic modifications, potentially enhancing charge separation and transfer under light irradiation, and thus improving the photocatalytic performance of the material. Additionally, the incorporation of boron in this manner could introduce new optically active sites, which might interact with visible light and contribute to photoluminescent emission, a property that could be leveraged for photocatalytic applications. On the other hand, boric acid (H_3BO_3) was employed as a simpler and less reactive boron source, serving primarily as a benchmark to assess the effects of different boron precursors on the material properties. Unlike $BF_3 \cdot OEt_2$, which can form coordination bonds with nitrogen atoms in the extended conjugated g-C_3N_4 network and potentially interact with fluorescent moieties such as BODIPY, H_3BO_3 undergoes incorporation primarily through condensation reactions during thermal treatment, resulting in substitutional or interstitial boron doping. This approach allows for a more controlled and predictable modification of the carbon nitride framework, without introducing additional photoluminescent species, making it ideal for isolating the effect of boron itself on the photocatalytic and structural characteristics of the material.

Boron trifluoride diethyl etherate doping

The obtained powders, shown in Figure 5.34, exhibit a similar yellowish color, indicating that boron incorporation does not significantly alter the macroscopic appearance of the material.

Table 5.15 reports the main characteristics and synthetic yields of the boron-doped g-C_3N_4 samples.

All materials were obtained starting from 2 g of g-C_3N_4, introducing increasing amounts of boron precursor to achieve different functionalization degrees. B 0.6%-PP and B 1.2%-PP show relatively high yields, 79.5% and 81.7%, respectively, whereas B 5.8%-PP presents a lower yield of 47.7%.

Figure 5.34: $BF_3 \cdot OEt_2$-doped g-C_3N_4 samples synthesized

Table 5.15: Synthesis conditions and yields of $BF_3 \cdot OEt_2$-doped g-C_3N_4 samples

Sample	Mass g-C_3N_4 (g)	B reagent (g)	Mass obtained (g)	Yield (%)
B 0.6%-PP	2.0	0.16	1.72	79.5
B 1.2%-PP	2.0	0.32	1.80	81.7
B 5.8%-PP	2.0	1.61	1.73	47.7

ESEM-EDX analysis The ESEM images (Figure 5.35) display the surface morphology of boron-doped graphitic carbon nitride (B-g-C_3N_4) as a function of increasing boron content: 0.6%, 1.2%, and 5.8%.

At 0.6% B doping, the material exhibits a relatively uniform surface. When the boron content increases to 1.2%, the structure appears more compact. At the highest doping level (5.8%), the morphology becomes markedly more heterogeneous, with visible particle agglomeration and denser clusters. These changes in morphology, as observed by ESEM, indicate that boron incorporation influences the surface texture and aggregation behavior of g-C_3N_4, which may have an impact on its photocatalytic activity.

Table 5.16 reports the surface composition of g-C_3N_3 samples treated with $BF_3 \cdot OEt_2$, as determined by EDX analysis.

Table 5.16: EDX elemental analysis on the surface of $BF_3 \cdot OEt_2$-doped g-C_3N_4 samples

Sample	N (wt%)	C (wt%)	O (wt%)	B (wt%)
B 0.6%-PP	61.5	36.4	2.1	–
B 1.2%-PP	43.1	43.0	1.5	12.4
B 5.8%-PP	61.4	34.6	4.0	–

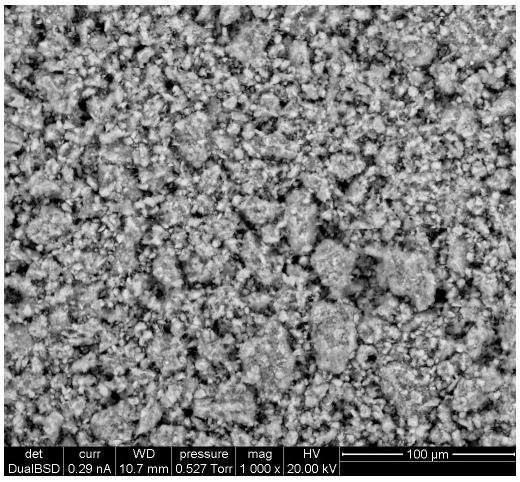

(a) B 0.6%-PP

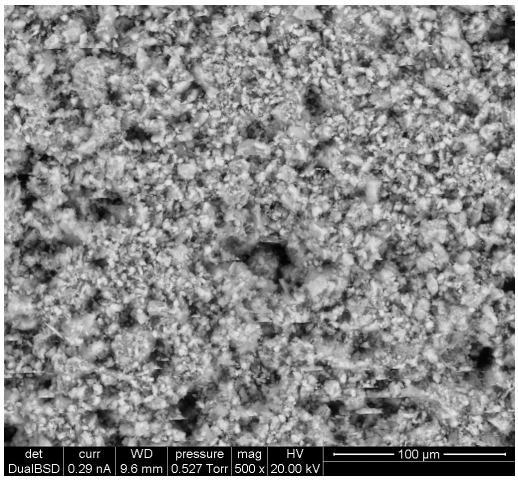

(b) B 1.2%-PP

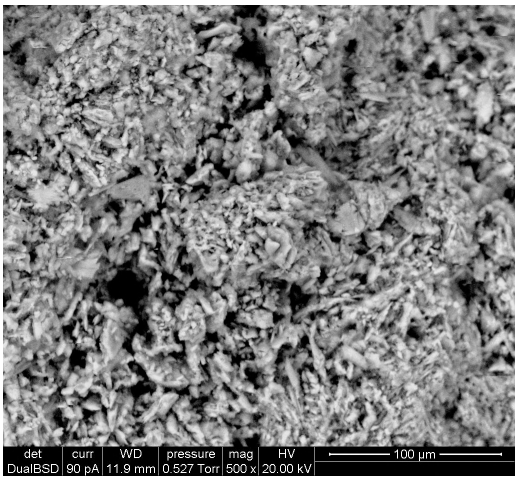

(c) B 5.8%-PP

Figure 5.35: ESEM images of boron-doped g-C_3N_4 samples with increasing B content: 0.6%, 1.2%, and 5.8%.

Compared to the pristine material (Table 5.5), the boron-doped samples show variations in the nitrogen and carbon contents, while oxygen remains a minor component. A clear boron signal (12.4 wt%) is detected only in the B 1.2%-PP sample, whereas for B 0.6%-PP and B 5.8%-PP the dopant lies below the detection limit. These findings illustrate the challenges of quantifying light elements such as boron by EDX.

TEM analysis The TEM images (Figure 5.36) show the morphological evolution of boron-doped graphitic carbon nitride (g-C_3N_4) with increasing B content: 0.6%, 1.2%, and 5.8%.

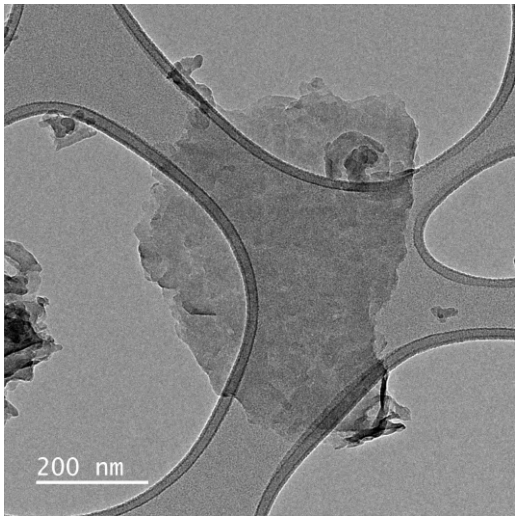

(a) B 0.6%-PP

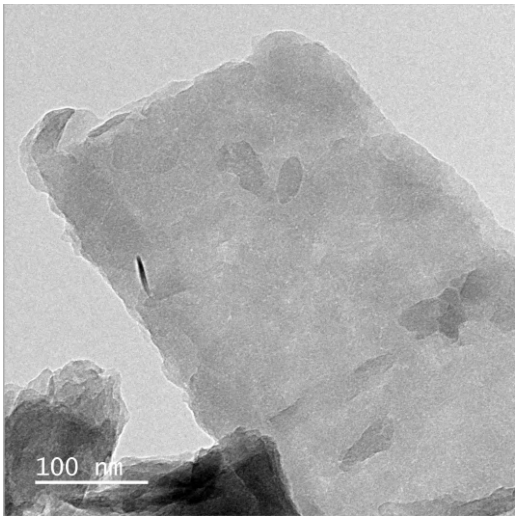

(b) B 1.2%-PP

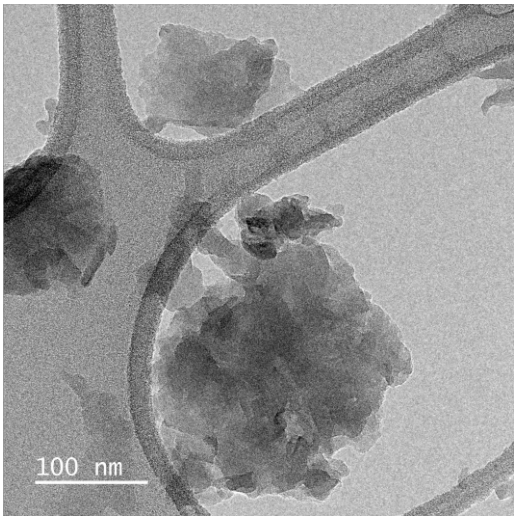

(c) B 5.8%-PP

Figure 5.36: TEM images of boron-doped $\mathrm{g\text{-}C_3N_4}$ samples with increasing B content: 0.6%-PP, 1.2%-PP, and 5.8%-PP.

At 0.6% B doping, the sample exhibits relatively thin and partially exfoliated nanosheets with a visible porous network, suggesting moderate structural disruption due to doping. At 1.2% B, the nanosheets appear more compact and aggregated, with smoother edges and reduced porosity, indicating a denser microstructure that may result from enhanced condensation or restacking processes promoted by higher boron incorporation. At 5.8% B, the structure shows further densification and a more amorphous appearance, possibly due to excessive loading altering the crystalline domains and inducing significant structural disorder. These observations demonstrate how increasing boron content influences the nanostructure of g-C_3N_4, with potential implications for its surface area, defect concentration, and photocatalytic properties.

FTIR characterization Figure 5.37 shows the infrared spectra of g-C_3N_4 samples doped with boron trifluoride diethyl etherate.

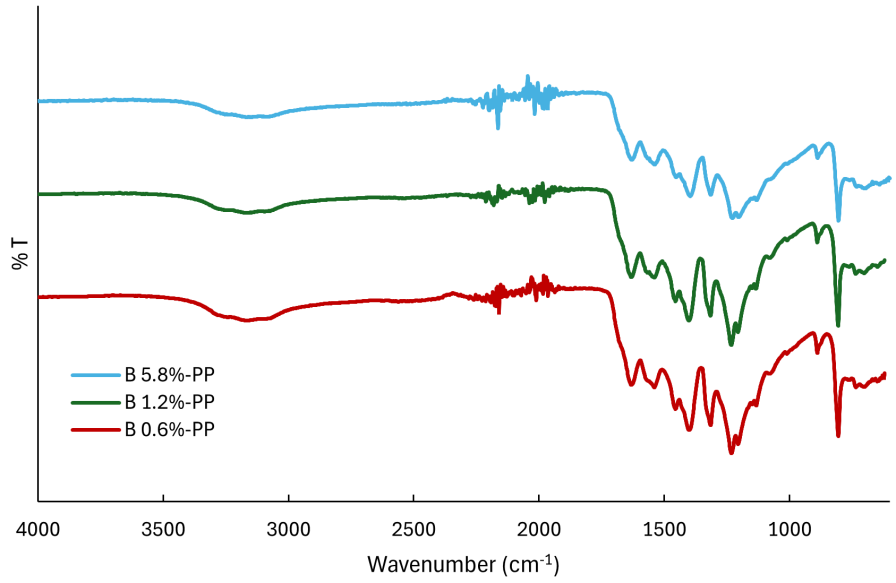

Figure 5.37: IR graph of boron $BF_3 \cdot OEt_2$-doped g-C_3N_4

The spectra provide information on the characteristic vibrational modes of the carbon nitride framework as well as possible modifications induced by boron incorporation. Comparing the different samples allows the identification of shifts or changes in intensity that may reflect the interaction between boron and the g-C_3N_4 structure.

Band gap analysis The optical properties of the boron-doped g-C_3N_4 samples synthesized with boron trifluoride diethyl etherate were investigated by UV-Vis diffuse reflectance spectroscopy. The spectra, reported in Figure 5.38a, show a strong absorption edge in the visible region, which is characteristic of g-C_3N_4-based materials. The corresponding Tauc plots (Figure 5.38b) were used to estimate the optical band gap values of the different samples.

The extracted values are summarized in Table 5.17, highlighting a small variation in the band

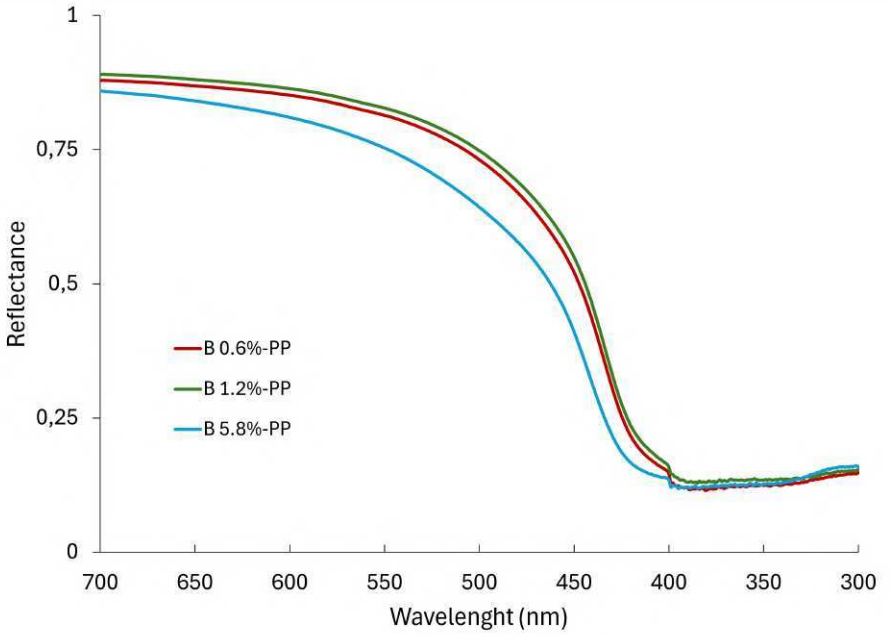

(a) Diffuse reflectance spectrum (DRS)

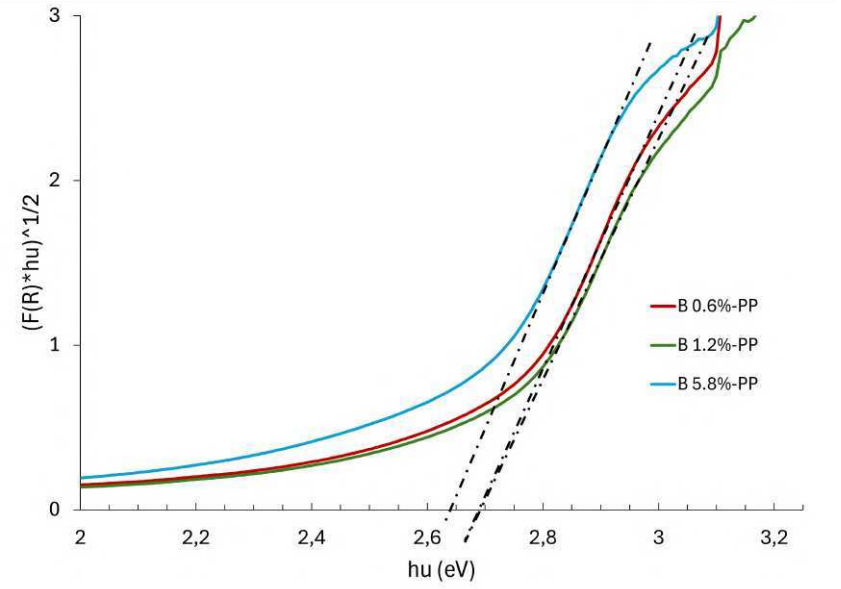

(b) Tauc plot

Figure 5.38: Band gap analysis of boron trifluoride diethyl etherate-doped g-C_3N_4

gap energy as the boron loading increases.

These materials, obtained with different boron loadings, display values in a narrow range between 2.62 and 2.70 eV. In particular, the samples with lower boron loading (0.6% and 1.2%)

Table 5.17: Band gap values of boron trifluoride diethyl etherate-doped g-C_3N_4 samples

Sample	Band gap value (eV)
B 0.6%-PP	2.68
B 1.2%-PP	2.70
B 5.8%-PP	2.62

show values around 2.68–2.70 eV, while the highly doped material (5.8%) exhibits a slightly reduced band gap of 2.62 eV, indicating a possible effect of excess boron incorporation on the electronic structure.

Boric acid doping

Two materials were obtained with the same boron loading of 0.9%, but following different procedures: co-pyrolysis (B 0.9%-CP) and post-pyrolysis (B 0.9%-PP), in order to investigate the influence of the synthesis route on the structural and chemical properties of the final material.

The powders, shown in Figure 5.39, exhibit a very similar yellowish color, indicating that the use of boric acid does not significantly affect the visual appearance of the samples.

Figure 5.39: H_3BO_3-doped g-C_3N_4 samples synthesized

Table 5.18 reports the main characteristics and synthetic yields of the boron-doped g-C_3N_4 samples prepared using boric acid as the dopant source. B 0.9%-CP presents a moderate yield of 63.6%, while B 0.9%-PP shows a higher yield of 84.3%.

ESEM-EDX analysis Environmental scanning electron microscopy (ESEM) was employed to investigate the morphology of the boron-doped g-C_3N_4 samples prepared with boric acid. Figure 5.40 presents representative micrographs of the two materials synthesized with the same nominal boron content (0.9%), but obtained through different procedures: co-pyrolysis (Figure 5.40a) and post-

Table 5.18: Synthesis conditions and yields of H_3BO_3-doped g-C_3N_4 samples

Sample	Mass (g)	B reagent (g)	Mass obtained (g)	Yield (%)
B 0.9%-CP	10	0.5	6.36	63.6
B 0.9%-PP	2.5 of g-C_3N_4	0.25	2.32	84.3

pyrolysis (Figure 5.40b). The images allow a direct comparison of the surface features and particle aggregation.

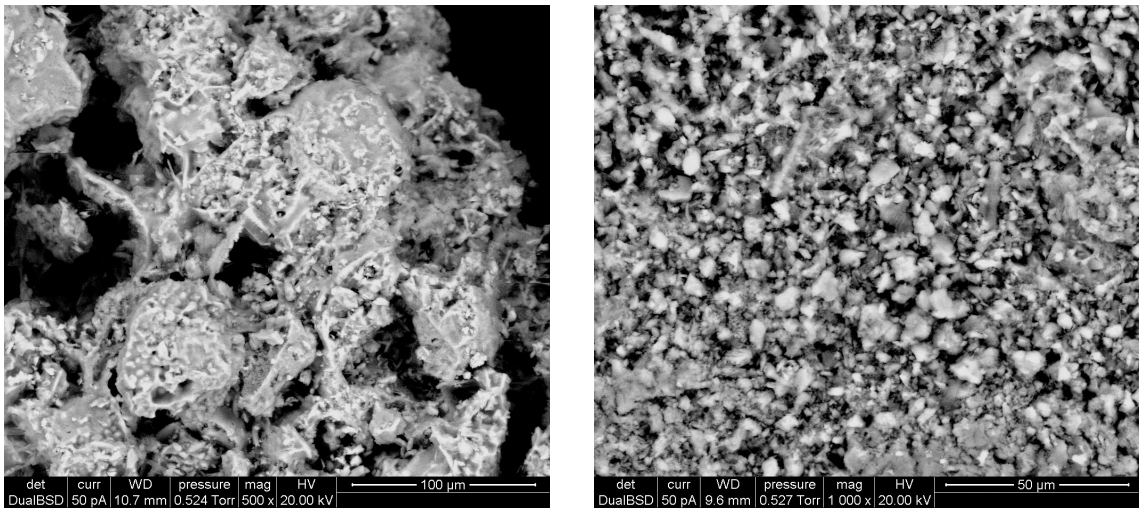

(a) B 0.9%-CP

(b) B 0.9%-PP

Figure 5.40: ESEM images of H_3BO_3-doped g-C_3N_4 samples

Table 5.19 reports the surface composition of H_3BO_3-doped g-C_3N_4 samples as determined by EDX analysis. Compared to the pristine material (Table 5.5), only minor changes are observed in the nitrogen, carbon, and oxygen contents. No boron signal was detected in either sample, indicating that the doping level is below the detection limit of the EDX technique.

Table 5.19: EDX elemental analysis on the surface of H_3BO_3-doped g-C_3N_4 samples

Sample	N (wt%)	C (wt%)	O (wt%)	B (wt%)
B 0.9%-CP	64.5	32.5	3.1	–
B 0.9%-PP	62.8	34.1	3.1	–

TEM analysis Transmission electron microscopy (TEM) was used to examine the nanostructure of the boron-doped g-C_3N_4 samples synthesized with boric acid. Figure 5.41 displays representative images of the two materials with identical boron loading (0.9%), obtained by different procedures:

co-pyrolysis (Figure 5.41a) and post-pyrolysis (Figure 5.41b). The TEM analysis provides direct insight into the sheet-like morphology and local structural organization.

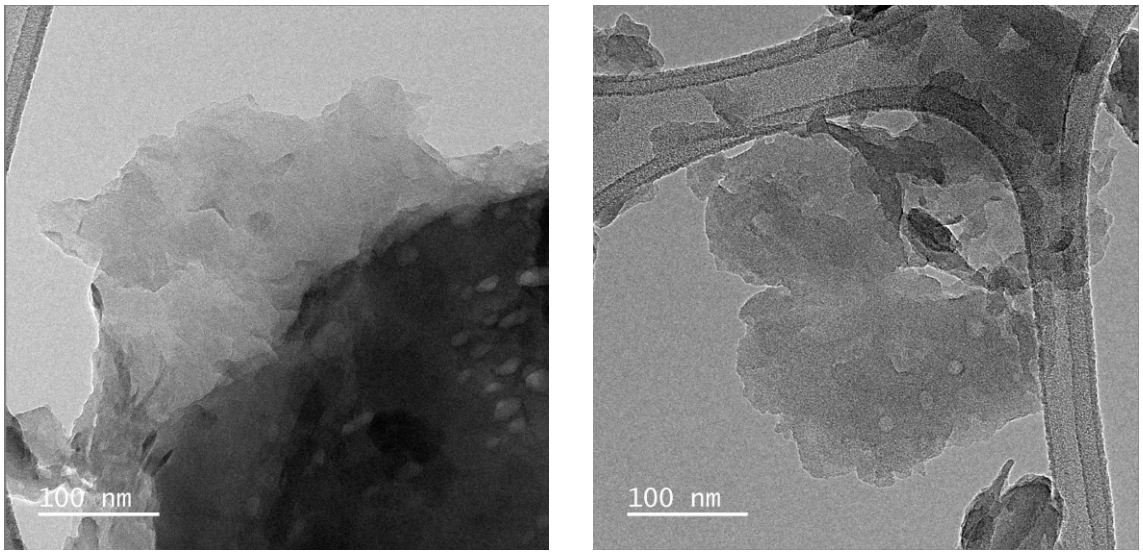

(a) B 0.9%-CP (b) B 0.9%-PP

Figure 5.41: TEM images of boric acid-doped g-C_3N_4 samples

FTIR characterization Fourier-transform infrared (FTIR) spectroscopy was employed to investigate the vibrational features of the boron-doped g-C_3N_4 samples obtained using boric acid as dopant. Figure 5.42 shows the IR spectra, where the characteristic bands of the g-C_3N_4 framework can be clearly identified.

Band gap analysis The optical band gap of the boron-doped g-C_3N_4 samples obtained using boric acid as precursor was investigated by UV-Vis diffuse reflectance spectroscopy. The spectra reported in Figure 5.43a display a distinct absorption edge in the visible region, confirming the semiconducting nature of the materials. To determine the band gap values more accurately, the Tauc method was applied, as illustrated in Figure 5.43b, where the extrapolation of the linear region provides the corresponding energy values.

The second group of boron-doped g-C_3N_4 materials, synthesized using both post- and co-pyrolysis approaches with the same nominal boron content (0.9%), is reported in Table 5.20.

Table 5.20: Band gap values of boron-doped g-C_3N_4 with 0.9% nominal content, prepared by post- and co-pyrolysis

Sample	**Band gap value (eV)**
B 0.9%-PP	2.63
B 0.9%-CP	2.63

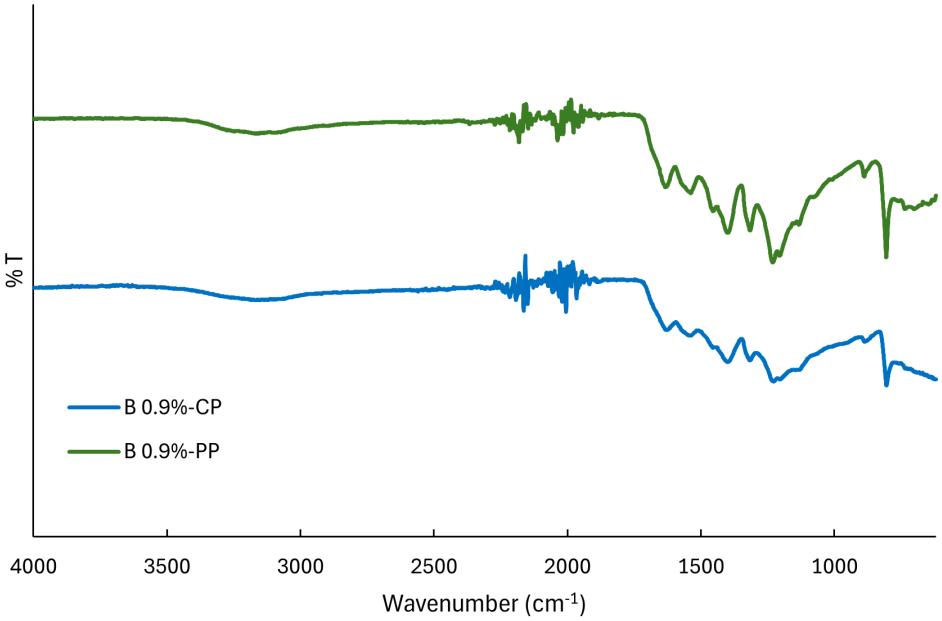

Figure 5.42: IR graph of H_3BO_3-doped g-C_3N_4

The measured band gaps are identical for the two samples, confirming that the synthesis route has no significant effect on the electronic structure.

XPS analysis of B-g-C_3N_4 samples

The XPS survey spectra of boron-doped g-C_3N_4 samples (B 0.6%-PP, B 1.2%-PP, B 0.9%-CP) show features comparable to pristine g-C_3N_4 in section 5.3.1, indicating that the polymeric structure is preserved upon a very little boron incorporation. High-resolution C 1s, N 1s, and O 1s spectra display similar shapes and binding energies as the undoped reference, suggesting that the local bonding environment of carbon and nitrogen remains largely unaffected.

Table 5.21: Surface composition of boron-doped g-C_3N_4 samples (XPS analysis)

Sample	C (at.%)	N (at.%)	O (at.%)	B (at.%)	C/N
B 0.6%-PP	43.0	54.7	2.4	–	0.8
B 1.2%-PP	45.5	50.8	3.6	0.1	0.9
B 0.9%-CP	42.6	53.5	2.8	1.1	0.8

Despite boron being a light element with low photoelectron cross-section, and thus difficult to detect in survey scans, subtle variations in the elemental composition provide indirect evidence of successful doping. C/N ratios remain between 0.8 and 0.9, similar to pristine g-C_3N_4, suggesting that boron incorporation occurs at localized sites such as surface defects or edge terminations,

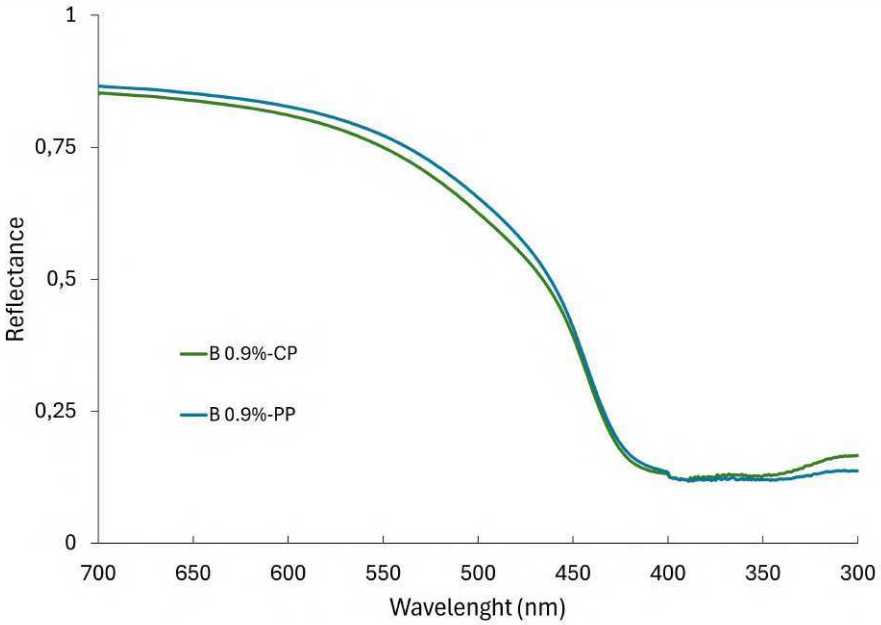

(a) Diffuse reflectance spectrum (DRS)

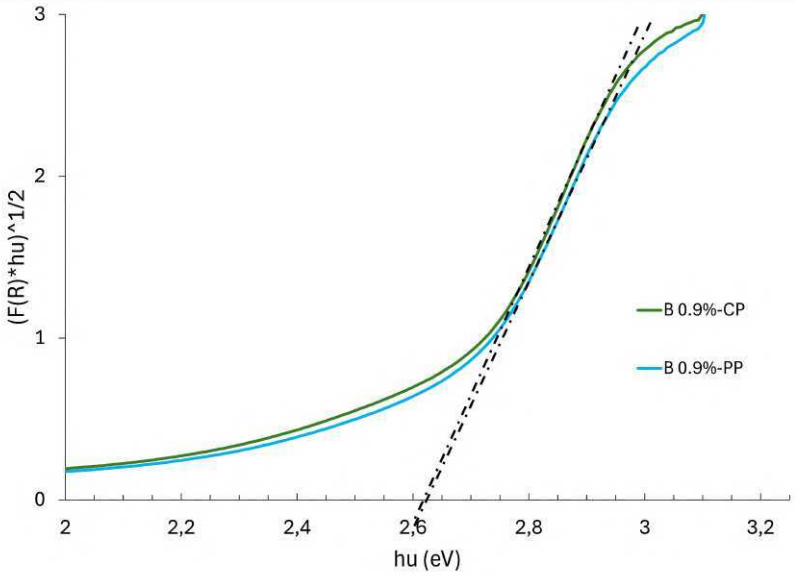

(b) Tauc plot

Figure 5.43: Band gap analysis of boric acid-doped g-C_3N_4

rather than through a wholesale restructuring of the polymer network. Minor variations in oxygen content hint at subtle surface chemistry changes, likely due to the use of boron trifluoride etherate ($BF_3{\cdot}OEt_2$) and DIPEA in dichloromethane, which may introduce functional groups or induce minor side reactions. High-resolution B 1s spectra (Figures 5.44 and 5.45) reveal peaks around 192–193 eV, indicative of boron species bound to oxygen (e.g., B_2O_3).

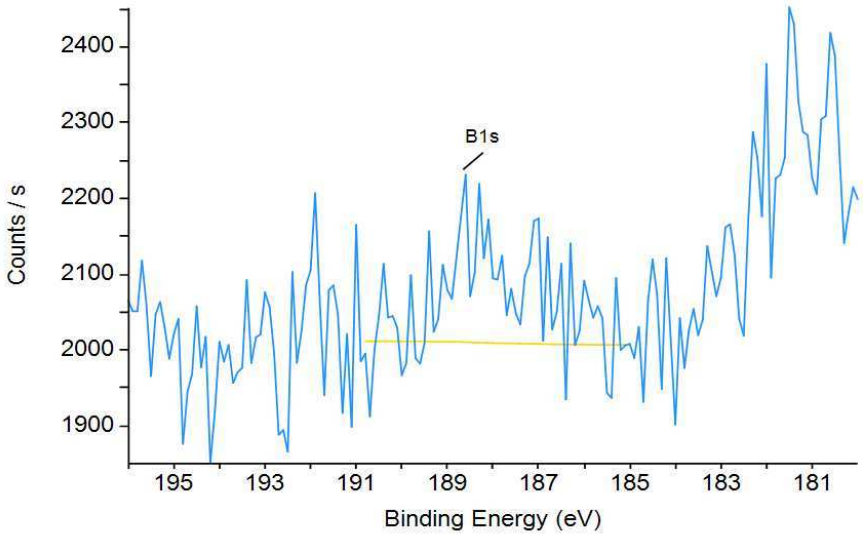

Figure 5.44: High-resolution B 1s spectrum of B 1.2%-PP

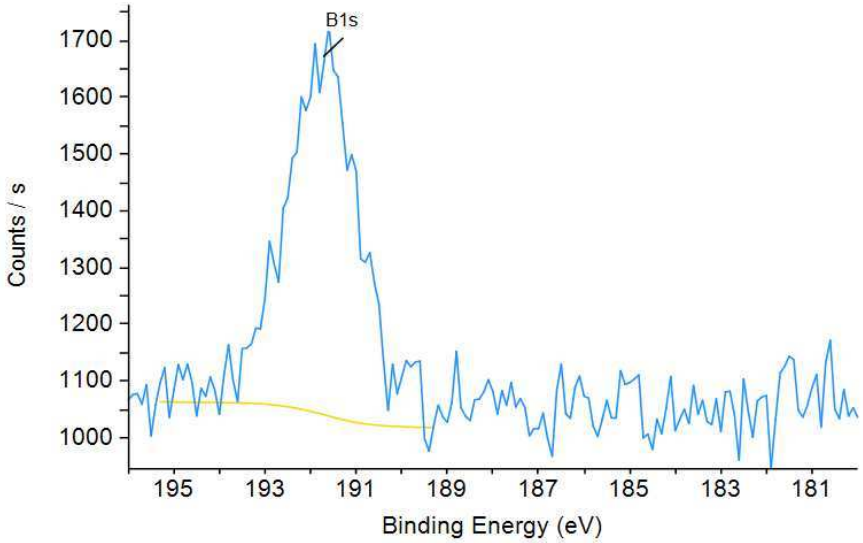

Figure 5.45: High-resolution B 1s spectrum of B 0.9%-CP

These spectra were acquired in high-sensitivity, low-resolution mode to improve the signal-to-noise ratio. Even though the boron loading is low, these results confirm surface modification and suggest potential effects on the electronic structure of g-C_3N_4, which can influence photocatalytic activity and charge-carrier dynamics.

XRD analysis of B-g-C_3N_4 samples

Figure 5.46 presents the X-ray diffraction (XRD) patterns of boron-doped graphitic carbon nitride samples synthesized with varying boron concentrations and dopant sources.

In particular, Figure 5.46a shows the diffraction patterns for samples doped with 0.6% and 1.2% B using boron trifluoride diethyl etherate ($BF_3{\cdot}OEt_2$) as the dopant precursor, while Figure 5.46b reports the XRD pattern for the sample doped with 0.9% B using boric acid as the dopant source. All samples exhibit the two characteristic diffraction peaks of graphitic carbon nitride: the (100) peak at approximately 13.1° 2θ, associated with the in-plane structural packing motif of tri-s-triazine units, and the (002) peak near 27.4° 2θ, corresponding to the interlayer stacking of conjugated aromatic systems.

Despite all samples sharing the same basic g-C_3N_4 structure, notable differences emerge depending on the dopant concentration and precursor:

- In Figure 5.46a, both the 0.6% and 1.2% B-doped samples ($BF_3{\cdot}OEt_2$-derived) display a sharp (002) peak at 27.4°, indicating a relatively ordered lamellar structure. However, increasing the boron concentration from 0.6% to 1.2% results in a noticeable increase in peak intensity and narrowing, suggesting improved crystallinity and enhanced layer stacking order.
- In contrast, sample B 0.9%-CP using boric acid (Figure 5.46b) also shows the typical g-C_3N_4 peaks, but the (002) peak is slightly broader and less intense compared to the $BF_3{\cdot}OEt_2$-derived counterparts, possibly indicating lower crystallinity or increased structural disorder, likely due to the different doping mechanism and incorporation behavior of boric acid.

These observations suggest that not only the concentration, but also the chemical nature of the dopant precursor significantly influences the crystallinity and structural order of boron-doped g-C_3N_4.

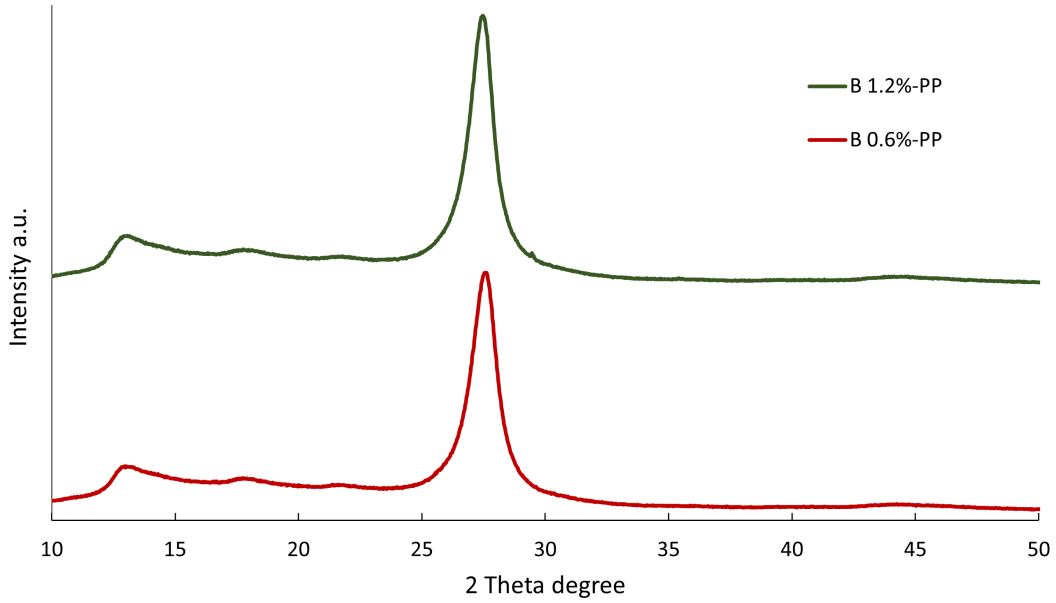

(a) $BF_3 \cdot OEt_2$ doping

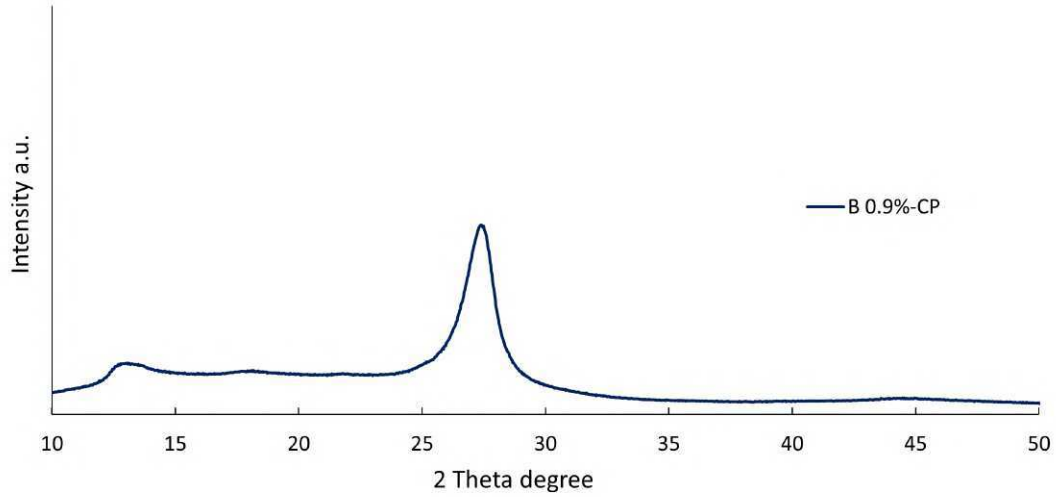

(b) Boric acid doping

Figure 5.46: XRD graph of boron-doped g-C_3N_4

5.4 Test results - RhB degradation

In this section, the results on photocatalytic performance of pristine g-C_3N_4 and the heteroatom-doped derivatives using Rhodamine B (RhB) as a model organic dye are reported. RhB possesses a well-defined spectral response and it is easy to monitor its concentration changes by UV–vis absorption spectroscopy. The degradation experiments were carried out under visible-light irradiation, and the decrease in RhB concentration was followed at regular time intervals to determine the photocatalytic activity of each material, as described in section 5.2.5. The comparison between the different samples provides insights into how the doping with bromine, phosphorus, or boron influences the optical absorption, charge carrier dynamics, and generation of reactive species. Materials exhibiting band-gap narrowing and red-shifted absorption edges are expected to utilize visible light more efficiently, thus enhancing the photocatalytic performance. Control experiments performed in the absence of catalyst or in dark conditions confirmed that the observed RhB degradation arises from the photocatalytic process and not from self-photolysis or simple adsorption. The following results are presented as of degradation curves, allowing a direct comparison between pristine and doped g-C_3N_4 samples.

5.4.1 Adsorption capacity

As a control experiment to determine the adsorption behavior of RhB a solution of the same concentration used in the pohtocatalytic experiments ($8.35\,\mu\mathrm{mol/L}$) was put in contact with the prsitine g-C_3N_4 under dark conditions (Figure 5.47).

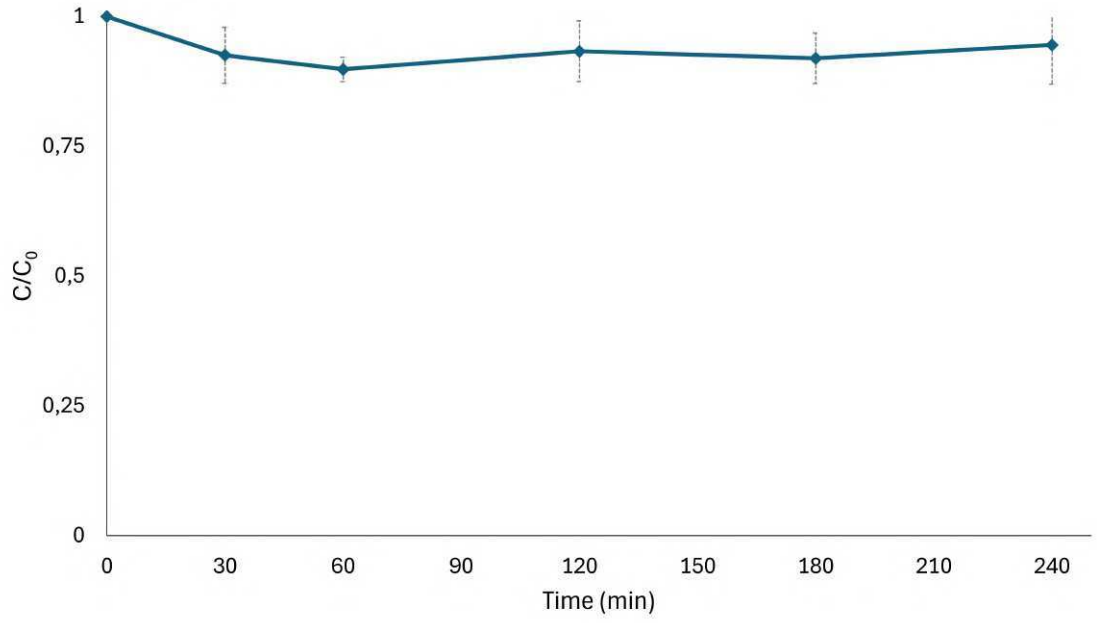

Figure 5.47: Adsorption kinetic of Rhodamine B using pristine g-C_3N_4 in dark conditions

The concentration profile, expressed as C/C_0, remains essentially constant over a period of 240

min, with only minor fluctuations within the error bars, after an initial limited decrease ($\sim$ 5–10% of RhB concentration decrease - adsorption capacity of 0.64 mg/g). This trend clearly indicates that g-C_3N_4 does not exhibit significant adsorption capacity for RhB molecules, and therefore its interaction with the dye is not governed by surface adsorption processes. The negligible removal of RhB observed here is consistent across the entire series of tested photocatalysts, including those doped with bromine, phosphorus, or boron. In all cases, the recorded curves showed nearly identical behaviors, confirming that heteroatom doping does not enhance the intrinsic adsorption properties of the material. This observation is particularly important for the interpretation of the subsequent photocatalytic tests, as it demonstrates that the decrease in dye concentration under irradiation cannot be attributed to adsorption phenomena, but solely to the photocatalytic degradation activity of the tested materials.

5.4.2 Photocatalytic results for pristine g-C_3N_4

The photodegradation efficiency of Rhodamine B (RhB) in aqueous solution, catalyzed by pristine g-C_3N_4, under two different light sources, namely visible light and UV light is presented in Figure 5.48.

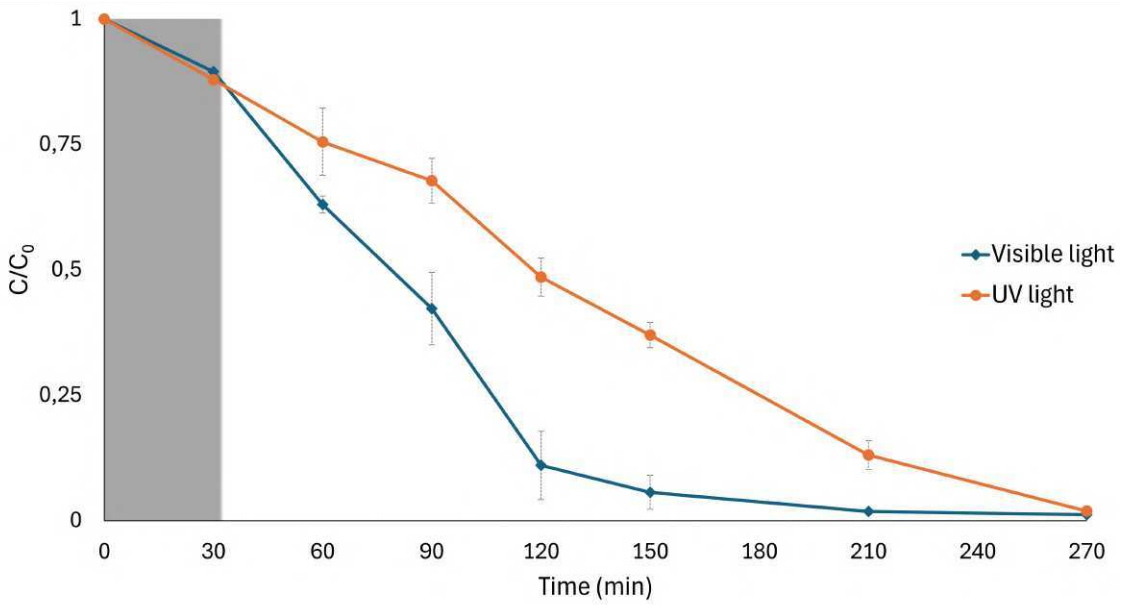

Figure 5.48: Photodegradation kinetics of Rhodamine B using pristine g-C_3N_4 with two different light sources

The y-axis reports the normalized concentration of RhB (C/C_0), where C_0 is the initial dye concentration, and C is the concentration measured at specific irradiation times (on the x-axis). In both cases, the initial 30 min of the experiment were carried out in the dark to assess the possible adsorption of RhB onto the photocatalyst surface. However, as confirmed by the control tests, g-C_3N_4 does not exhibit any significant adsorption capacity, and the concentration decrease observed during this stage is limited ($\sim$ 10%. Once the illumination stage started, a clear divergence

between the two irradiation conditions became evident. Under visible light, the catalyst rapidly degraded RhB, with the C/C_0 ratio dropping significantly within the first 90 min (by 90%) and approaching complete removal after 180 min of irradiation. By contrast, the performance under UV light irradiation was notably slower, with the concentration decreasing gradually and reaching complete degradation only after approximately 240 min. The faster kinetics under visible light highlight the ability of g-C_3N_4 to absorb in the visible region and efficiently generate electron–hole pairs that participate in the photocatalytic process. In this case, the strong activity can be ascribed to an enhanced separation and transfer of photogenerated carriers, which facilitate the generation of reactive oxygen species responsible for dye oxidation and breakdown. The error bars reported in the plot confirm the reproducibility of the experimental data and indicate only minor deviations among replicate measurements. Overall, these results demonstrate that pristine g-C_3N_4 exhibits good photocatalytic efficiency under visible light compared to UV irradiation, making it a promising material for applications in environmental remediation. Nonetheless the degradation time could be an issue in view of a scale-up application, thus the development of more efficient derivatives is necessary.

5.4.3 Photocatalytic results for bromine-doped samples

The photocatalytic performance of bromine-doped g-C_3N_4 samples towards RhB degradation under visible-light irradiation is summarized in Figure 5.49. The photocatalytic degradation of pristine g-C_3N_4 is included as a reference for comparison (orange curve). As in the previous experiments, the first 30 minutes were performed in the dark to take into account the adsorption contributions; adsorption remains limited (max 20%) for all samples, so the observed concentration decline after illumination reflects mainly photocatalytic activity.

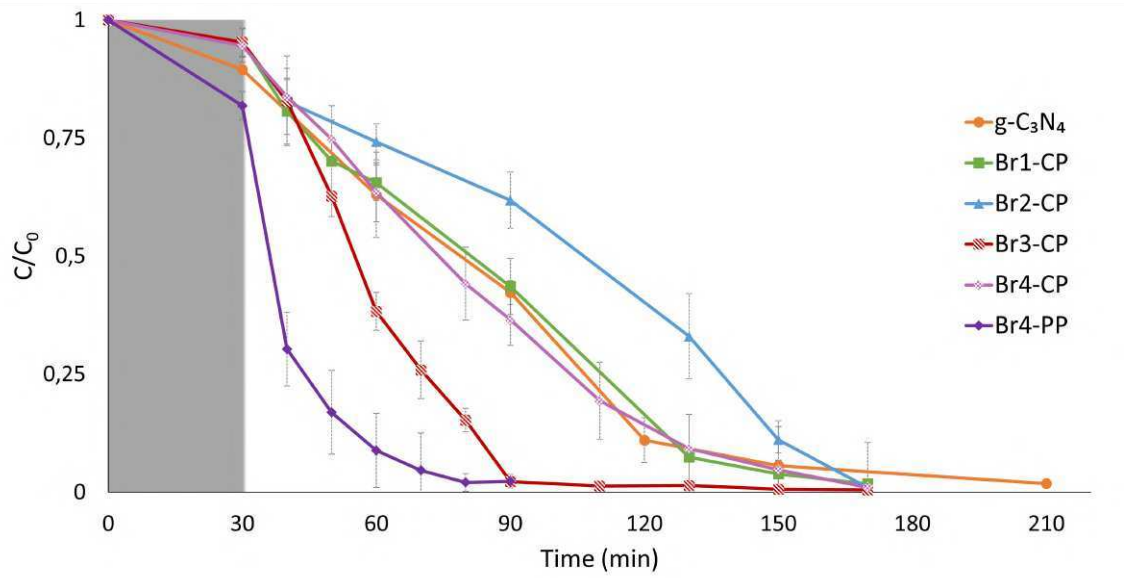

Figure 5.49: Adsorption kinetic of Rhodamine B using bromine doped g-C_3N_4 samples

Among the Br-doped samples, Br1-CP required about 120 minutes of visible-light irradiation

to reach 90% degradation, showing moderately faster kinetics than the pristine material, which also reached 90% degradation after roughly 120 minutes of irradiation and complete removal after approximately 180 minutes. Br2-CP was the least active sample, taking almost 140 minutes of irradiation to achieve 90% degradation, with a significant fraction of RhB still remaining after 120 minutes. Br3-CP reached 90% degradation in approximately 60 minutes of irradiation, with complete removal observed at about the same time, while Br4-CP displayed intermediate behaviour, attaining 90% degradation in around 120 minutes of irradiation (slightly faster than the pristine sample). Finally, Br4-PP was the most active photocatalyst, reaching 90% degradation in roughly 40 minutes of irradiation and nearly complete RhB removal within 50 minutes. These results indicate that the post-pyrolysis sample Br4-PP exhibits the fastest kinetics, followed by Br3-CP, while Br1-CP and Br4-CP show intermediate behaviour, and Br2-CP is the least active. These data suggest that both the chemical nature of the bromine precursor and the doping procedure co-pyrolysis (CP) versus post-pyrolysis (PP) strongly influence the type, location, and effectiveness of bromine-related defects. Post-pyrolysis bromination likely enriches the surface with brominated species and accessible active sites, enhancing interfacial charge transfer and rapid generation of reactive oxygen species. In contrast, co-pyrolysis can incorporate bromine into the bulk lattice, which may be beneficial at moderate levels but can also produce deep recombination centers. The particularly high activity of Br3-CP may be attributed to the dimethylamino substituent in the 4-bromo-N,N-dimethylaniline precursor, which can promote electron-donating interactions or favourable defect states that assist charge separation, whereas nitrile-bearing precursors (Br2-CP) doesn't seem to introduce beneficial modification in the graphitic structure or surface.

5.4.4 Photocatalytic results for phosphorous-doped samples

The photocatalytic degradation curves of RhB under visible-light irradiation for pristine and P-doped g-C_3N_4 samples are plotted in Figure 5.50.

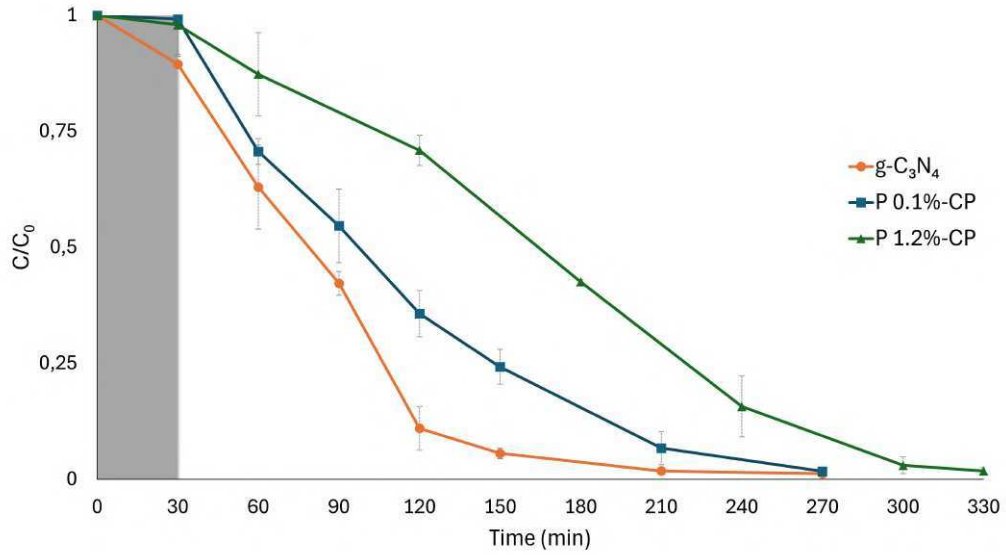

Figure 5.50: Adsorption kinetic of Rhodamine B using phosphorous doped g-C_3N_4 samples

As for the other experiments, the first 30 minutes were carried out in the dark, and adsorption was confirmed to be practically negligible. If the pristine g-C_3N_4 reached 90% degradation in about 120 minutes of irradiation, the phosphorus-doped ones exhibited slower degradation kinetics: the P 0.1%-CP required around 180 minutes of irradiation to reach the same level of degradation, while P 1.2%-CP was the least active, taking roughly 270 minutes to achieve it, with a significant fraction still remaining at 180 minutes (28%). This behaviour indicates that phosphorus incorporation under co-pyrolysis conditions does not necessarily enhance photocatalytic performance and can even be detrimental at higher nominal loadings. In fact, elevated P concentrations or incomplete decomposition of triphenylphosphine may generate deep trap states or carbonaceous residues that act as non-radiative recombination centres. The thermal history (550 °C for 2 h) and the presence of the bulky triphenyl fragment during condensation can also influence the polymerization pathways, affecting the condensation degree, layer stacking, and porosity, which in turn impact carrier transport and surface accessibility. Consequently, the poorer performance of P 1.2%-CP could reflect increased bulk incorporation of phosphorus, reducing surface-active sites, or the formation of defect centres that shorten carrier lifetimes. From a practical perspective, these results suggest that an optimal doping window exists below the 1.2% nominal level. Alternative strategies, such as using lower amounts of triphenylphosphine, post-pyrolysis doping, or co-doping with a complementary heteroatom, may achieve a more beneficial electronic modulation without creating recombination centres.

5.4.5 Photocatalytic degradation with boron-doped samples

Tests performed with trifluoride diethyl etherate doping

The photocatalytic degradation curves of RhB under visible light irradiation using $BF_3 \cdot OEt_2$-doped samples and pristine g-C_3N_4 (as comparison) are reported in Figure 5.51.

As in all photocatalytic tests, the first 30 minutes were carried out in the dark to evaluate the contribution of adsorption processes. During this stage, only a slight decrease in RhB concentration was observed for all samples, confirming that boron doping does not drastically alter the surface affinity of g-C_3N_4 towards the dye. After the irradiation began, clear differences in photocatalytic performance were detected between the samples, depending on the boron loading. The sample doped with 0.6% boron (B 0.6%-PP) showed moderately faster kinetics than the pristine material, achieving 90% degradation in about 90 minutes and almost complete RhB removal within 150 minutes. This improvement can be attributed to the introduction of boron atoms into the carbon nitride framework, as seen in section 5.3.4, which likely act as electron acceptors, suppressing the recombination of photogenerated electron–hole pairs and enhancing charge carrier separation. The sample with intermediate boron loading (B 1.2%-PP) displayed the best overall performance, reaching 90% degradation in roughly 90 minutes and achieving almost complete dye removal within two hours. The degradation profile indicates a rapid decrease in concentration during the first 90 minutes of irradiation, suggesting that a moderate level of boron incorporation improves light harvesting and reactivity. In contrast, the highest loaded sample (B 5.8%-PP) showed slower kinetics, taking approximately 150 minutes to reach 90% degradation, with the slowest overall performance among the series. Overall, the data indicate a non-linear dependence of photocatalytic activity on boron loading. In fact, although boron can create defect sites that improve activity at low

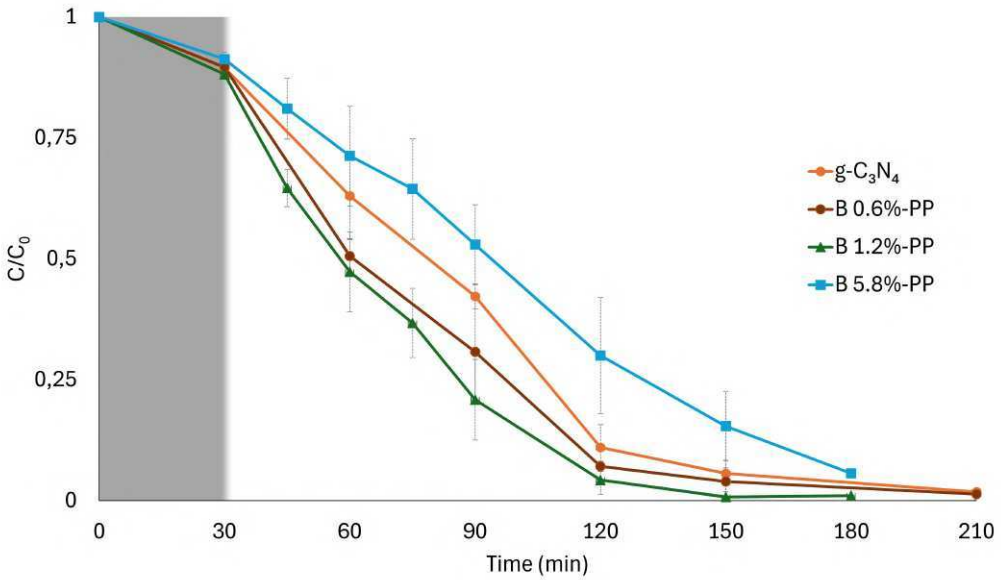

Figure 5.51: Adsorption kinetic of Rhodamine B using boron doped g-C_3N_4 samples

or moderate levels, exceeding these levels may distort the g-C_3N_4 lattice, generate recombination centres, or reduce the degree of conjugation within the polymeric network, ultimately decreasing the photocatalytic efficiency. These results emphasize the importance of carefully tuning the dopant concentration to maximize photocatalytic efficiency.

Tests performed with boric acid doping

The results pf the photocatalytic degradation of RhB under visible light irradiation using the boric acid-doped samples are reported in Figure 5.52.

As in all experiments, the first 30 minutes were carried out in the dark to evaluate the contribution of adsorption, which proved almost negligible for all samples. In contrast with the $BF_3 \cdot OEt_2$ derivatives, the boron-doped samples prepared using boric acid showed markedly suppressed activity. Both B 0.9%-CP and B 0.9%-PP exhibited very slow degradation kinetics, with more than 70% of RhB remaining even after extended irradiation, indicating that the introduction of boron significantly reduced the photocatalytic performance. Only minor differences were observed between the co-pyrolyzed and post-pyrolysis treated samples, suggesting that the synthetic route does not substantially influence the final activity. The decreased performance can be attributed to the formation of structural defects or mid-gap states induced by boron incorporation, which likely act as recombination centers for photogenerated charge carriers, thereby drastically reducing their lifetimes and limiting their participation in the redox reactions necessary for RhB degradation. Furthermore, boron doping may distort the local lattice of g-C_3N_4, affecting its band structure and reducing its capacity to generate reactive species under visible light. These results demonstrate that, at the tested concentration, boric acid does not enhance photocatalytic efficiency; rather, it has a detrimental effect, effectively suppressing the activity of g-C_3N_4. This outcome underscores the importance of carefully selecting both the dopant type and loading when designing g-C_3N_4-based

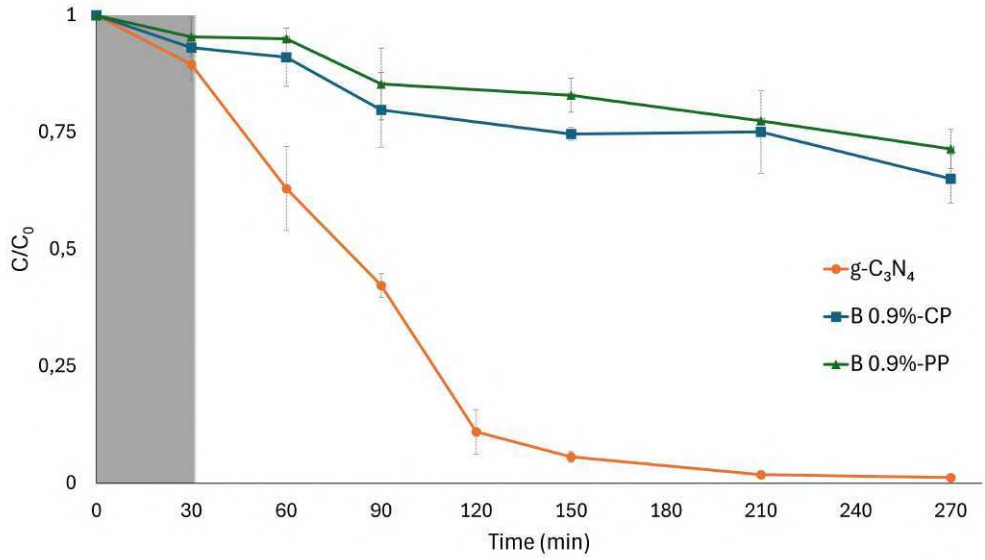

Figure 5.52: Adsorption kinetic of Rhodamine B using boron doped g-C_3N_4 samples

photocatalysts, as certain modifications can be counterproductive.

The comparison between the two sets of boron-doped g-C_3N_4 photocatalysts provides important insights into the role of dopant concentration and synthetic strategy. In the first case (B 0.6%-PP, B 1.2%-PP, B 5.8%-PP), a clear dependence on the boron loading was observed. At low to moderate doping levels (0.6% and 1.2%), the photocatalytic degradation of RhB under visible light proceeded at a slightly faster rate than pristine g-C_3N_4, with the 1.2% loaded sample achieving the highest efficiency. This indicates that small amounts of boron may introduce shallow defect states that facilitate charge separation and enhance the production of reactive oxygen species. However, when the boron loading was increased further to 5.8%, the degradation efficiency drastically decreased, with the sample showing significantly lower activity compared to pristine g-C_3N_4. This suggests that excessive boron loading hinders the photocatalytic process. In contrast, the second set of samples (B 0.9%-CP and B 0.9%-PP) showed a completely different behavior. Both materials exhibited almost no photocatalytic activity, with less than 30% RhB removal after 270 minutes, while pristine g-C_3N_4 reached complete degradation within 210 minutes. The near-identical performance of the two samples indicates that the synthetic method has little effect on the final photocatalytic outcome at this concentration. Instead, the data suggest that at a boron loading close to 1%, the structural perturbations introduced by doping are already sufficient to suppress activity, regardless of the preparation route. Taken together, these results highlight a dual trend. On the one hand, low boron doping (around 1% via post-pyrolysis) can be beneficial. On the other hand, either higher boron loadings (above 5%) or the use of co-polymerization even at moderate levels (0.9%) have a detrimental effect, essentially quenching the photocatalytic response. This points to a narrow optimal window for boron incorporation, outside of which recombination effects dominate. Importantly, the comparison underscores how delicate the balance is between beneficial and detrimental defect formation.

5.5 Test result - SMX degradation

The photocatalytic degradation of sulfamethoxazole (SMX) under visible-light irradiation by Br-doped g-C_3N_4 samples is shown in Figure 5.53. The photodegradation tests were performed as described in Section 5.2.6. As in the case of RhB, the first 30 minutes were conducted in the dark to assess adsorption effects, which remain limited for almost all tested materials (except for Br4-PP), confirming that the subsequent decline is attributable mainly to their photocatalytic activity.

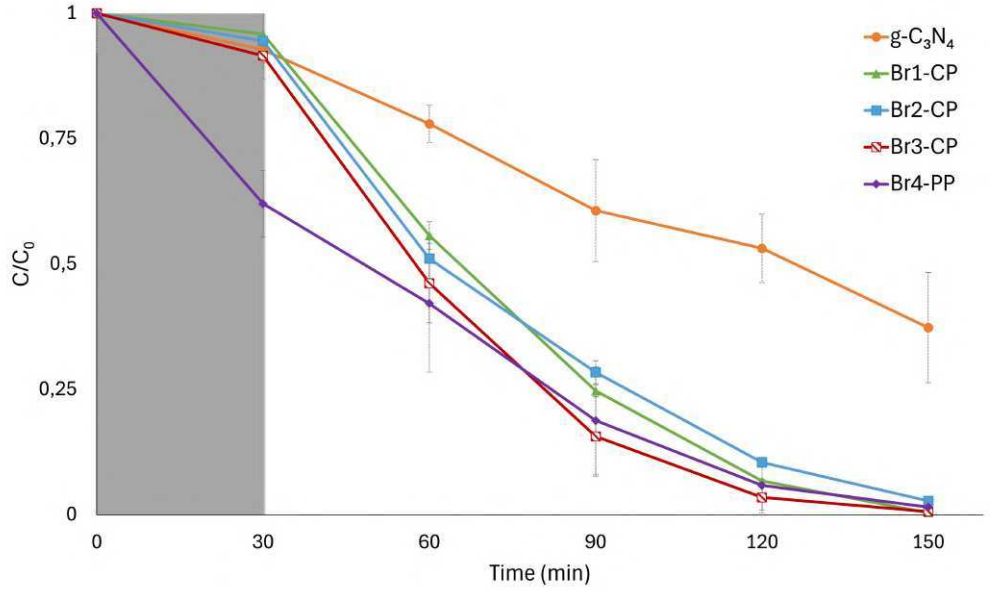

Figure 5.53: Photodegradation kinetics of SMX using bromine doped g-C_3N_4

The pristine g-C_3N_4 used as reference showed only limited activity, with a relatively slow and incomplete degradation of SMX even after 120 minutes of visible-light irradiation, making it the least active sample in the series. In contrast, all brominated samples exhibited markedly superior performance, highlighting the beneficial role of bromine doping. Among the co-pyrolyzed samples, Br3-CP (derived from 4-bromo-N,N-dimethylaniline) shows the fastest degradation kinetics, achieving 90% removal of SMX within 90 minutes, closely followed by Br1-CP (hydrobromic acid precursor), which also reaches significant degradation in about 90 minutes but slightly slower than Br3-CP. Br2-CP (obtained from 2-bromobenzonitrile precursor) is somewhat slower than the other doped materials, requiring approximately 120 minutes to achieve 90% degradation. The post-pyrolysis Br4-PP sample demonstrates strong photocatalytic activity as well, reaching 90% degradation in roughly 90 minutes, slightly below the performance of Br3-CP. This ranking differs somewhat from the trends observed in RhB degradation, suggesting that the chemical nature of the pollutant and its interaction with active sites play a decisive role. In particular, the electron-rich substituents of Br3-CP's precursor may generate favourable defect states that facilitate the degradation of more recalcitrant molecules such as SMX, while the post-pyrolysis Br4-PP provides abundant surface bromine species that enhance radical generation but perhaps without the same degree of selectivity. Br1-CP and Br2-CP, while less active than Br3-CP, still demonstrate improved

degradation compared to pristine g-C_3N_4, supporting the conclusion that bromine incorporation enhances charge separation and visible-light harvesting regardless of precursor. Overall, bromine doping proves to be an effective strategy to enhance photocatalytic degradation of both dyes and pharmaceutical pollutants, with the highest efficiency depending on a balance between the doping method and pollutant-specific interactions.

Making a specific note on Figure 5.53, it can be observed that Br4-PP behaves differently from the other bromine-doped samples in the adsorption phase. In fact, this material is the only one exhibiting a consistent adsorption of SMX in dark conditions. However, as shown in Figure 5.54, the adsorption process mainly occurs within the first 30 minutes, after which the removal stabilizes at about 40%, indicating that equilibrium is rapidly reached with that time and no further uptake takes place.

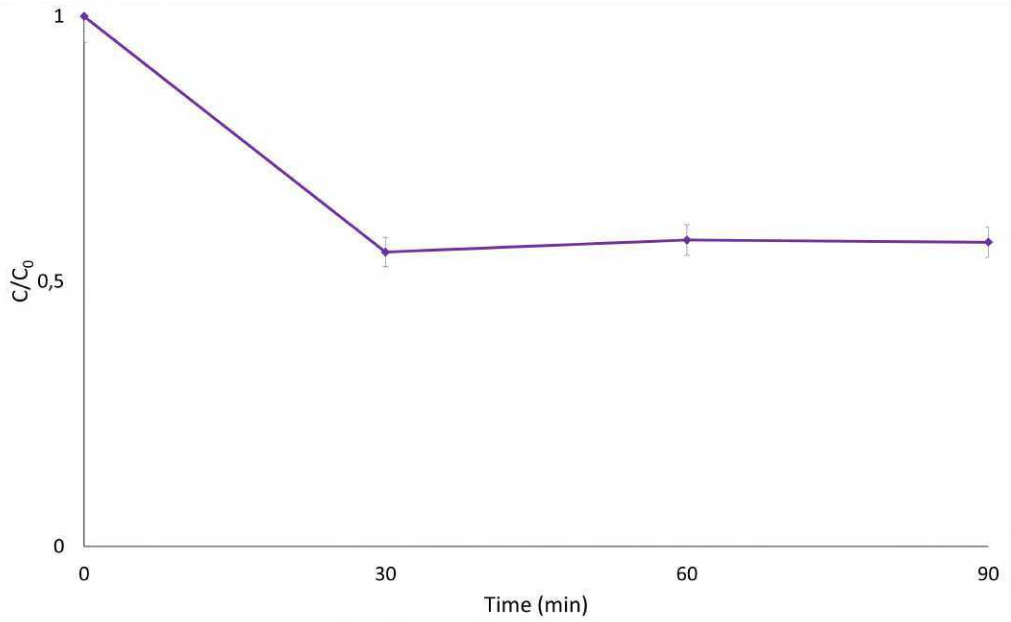

Figure 5.54: Adsorption kinetic of SMX using Br4-PP in dark conditions

5.6 Test result - AT degradation

The photocatalytic degradation of atenolol (AT) under visible-light irradiation using Br-doped g-C_3N_4 samples is presented in Figure 5.55. Photodegradation tests were performed as described in Section 5.2.6. As with RhB and SMX, the first 30 minutes were conducted in the dark to assess adsorption phenomena, which remain negligible for all materials, confirming that the subsequent concentration decrease is driven by the photocatalytic activity.

The pristine g-C_3N_4 exhibits limited photocatalytic efficiency, showing slow and incomplete degradation of AT even after 180 minutes of visible-light irradiation. Bromine-doped samples, in contrast, display significantly enhanced activity, although with notable differences depending on the doping route. Br3-CP, synthesized via co-pyrolysis with 4-bromo-N,N-dimethylaniline,

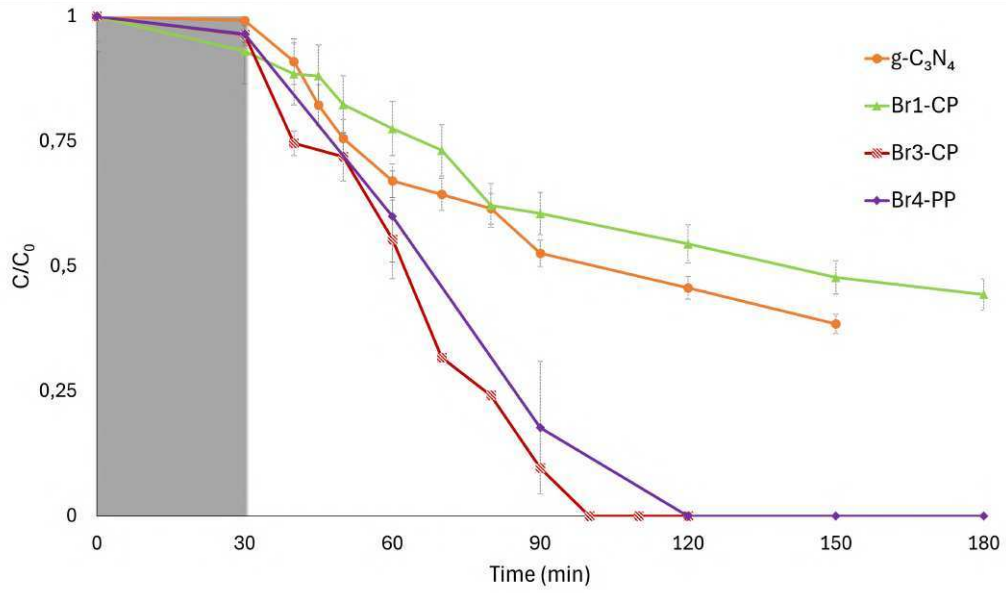

Figure 5.55: Photodegradation kinetics of AT using bromine doped g-C_3N_4

demonstrates the fastest photocatalytic performance, achieving 90% degradation in approximately 60 minutes and complete removal within the same time frame. The post-pyrolysis Br4-PP sample also exhibits strong activity, reaching near-complete degradation in about 80 minutes, slightly lower than the efficiency of Br3-CP. Conversely, Br1-CP, derived from melamine bis-hydrobromide, shows unexpectedly poor performance, taking over 150 minutes to approach 90% degradation and performing even worse than the pristine reference, which itself does not reach full removal within 180 minutes. These results indicate that, unlike in the case of RhB and SMX, the photocatalytic activity towards AT is highly sensitive to the chemical nature of the bromine precursor. Br3-CP likely allows for specific interactions with the pollutants or generates favorable defect states that promote a more rapid degradation. Overall, these observations confirm that bromine incorporation enhances photocatalytic reactivity, but the precursor chemistry and doping method critically determine the pollutant-specific degradation efficiency.

5.6.1 Scavenger tests

To clarify the role of the different reactive oxygen species (ROS) in the photocatalytic mechanism, scavenger tests were performed using the Br3-CP photocatalyst, which had previously shown the highest activity in atenolol (AT) degradation. Two scavengers were employed: isopropanol (IPA, 20 mmol L^{-1}), a well-known hydroxyl radical (·OH) scavenger, and p-benzoquinone (BQ, 0.05 mmol L^{-1}), a superoxide radical ($O_2^{\cdot-}$) quencher. In all cases, 62.5 mg of catalyst was suspended in 200 mL of AT solution (1 mg L^{-1}), corresponding to 0.200 mg of pollutant, i.e., 7.9×10^{-7} mol. Tests were performed as described in Section 5.2.7. The addition of IPA provided 4.0×10^{-3} mol of scavenger, corresponding to a $\sim 5 \times 10^3$-fold molar excess over AT, while BQ was added at 1.0×10^{-5} mol, i.e., approximately 13 times in excess relative to the pollutant. These conditions

ensured that the selected ROS would be efficiently intercepted during the photocatalytic process.

The kinetic curve obtained in the presence of IPA is shown in Figure 5.56.

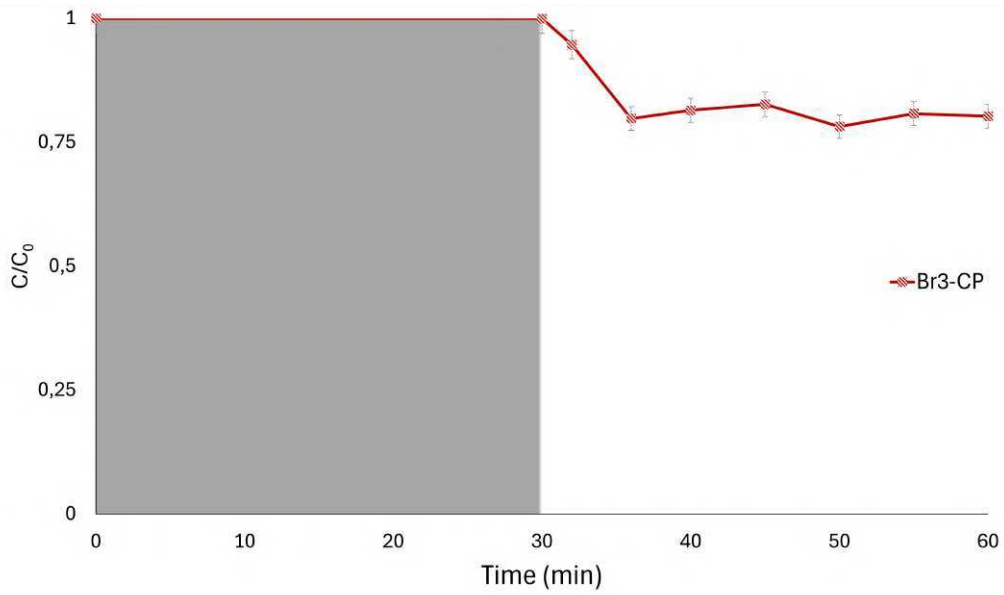

Figure 5.56: Effect of IPA (20 mmol L^{-1}) on AT photodegradation over Br3-CP

After the 30 min dark adsorption stage, the concentration of AT remained essentially constant until illumination was started. Once the lamp was switched on, only a very limited decrease in concentration was observed, with C/C_0 stabilizing around 0.8 after one hour, corresponding to a removal of about 20%. This result indicates that hydroxyl radicals contribute significantly to the degradation, but their suppression does not fully inhibit the process, as superoxide-related pathways can still oxidize the pollutant. In fact, with IPA, hydroxyl radicals are selectively removed:

$$(CH_3)_2CHOH + \cdot OH \rightarrow (CH_3)_2C \cdot OH + H_2O$$

but the superoxide pathway remains active, leading to the partial degradation observed in Figure 5.56.

In contrast, the test with BQ led to a complete suppression of the photocatalytic activity, with AT concentration remaining constant throughout irradiation. This clearly identifies $O_2^{\cdot -}$ as a key oxidant in the degradation mechanism, while ·OH plays a secondary yet relevant role. In fact, as shown in Figure 5.57, the HPLC chromatograms provide clear evidence of the role of p-benzoquinone (BQ) in the photocatalytic process. The peak corresponding to AT remains essentially unchanged during irradiation, demonstrating that in the presence of BQ the degradation of the pollutant is strongly inhibited. At the same time, a progressive decrease of the BQ peak is observed, accompanied by the appearance and growth of a new signal at longer retention time, assigned to hydroquinone (HQ). This transformation is attributed to the reduction of BQ into HQ by reaction with superoxide radicals ($O_2^{\cdot -}$). The efficient conversion of BQ into HQ confirms the quenching of $O_2^{\cdot -}$ and highlights the crucial involvement of this reactive oxygen species in the photocatalytic degradation pathway of AT. In other words, when $O_2^{\cdot -}$ is selectively scavenged by

BQ, AT cannot undergo efficient degradation, indicating that superoxide radicals play a key role as the main oxidizing species in the process.

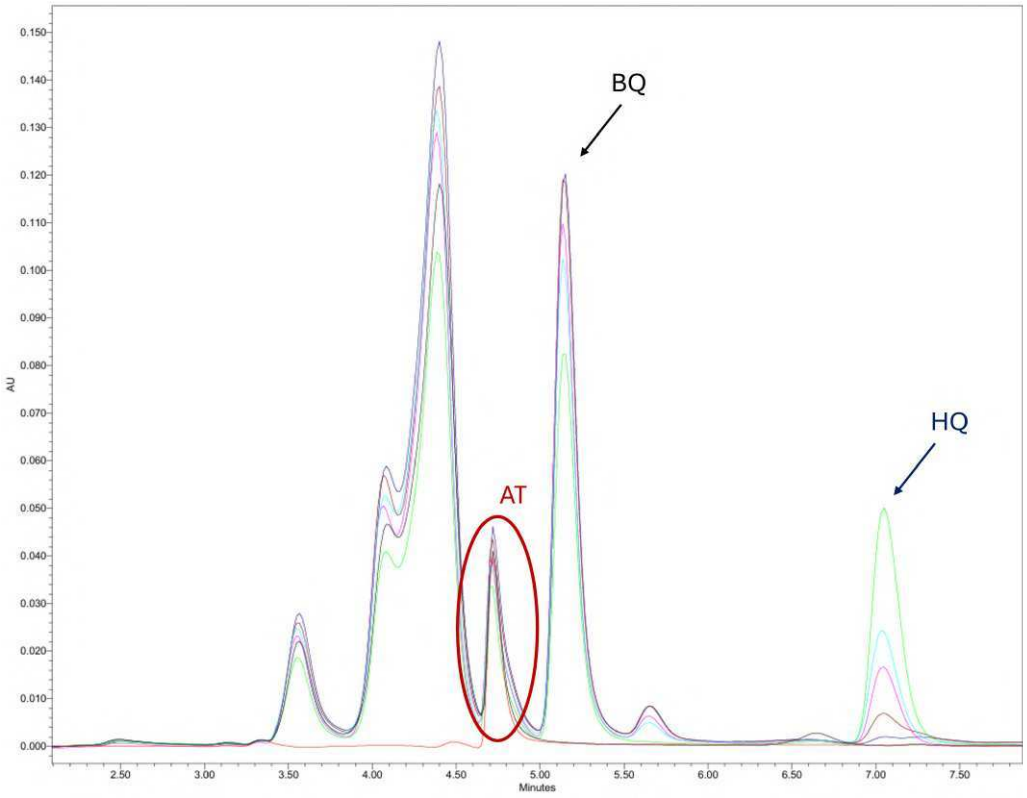

Figure 5.57: HPLC chromatograms of the scavenger test with BQ

The observed effect can be rationalized by the main photocatalytic reactions. Upon light irradiation, the photocatalyst generates conduction band electrons and valence band holes:

$$\mathrm{h}\nu + \text{Photocatalyst} \rightarrow e^-_{CB} + h^+_{VB}$$

Electrons reduce dissolved oxygen to superoxide:

$$e^-_{CB} + \mathrm{O_2} \rightarrow \mathrm{O_2^{\cdot -}}$$

which may undergo further reactions to form H_2O_2 and, eventually, hydroxyl radicals. Holes can also directly generate ·OH from water or hydroxide ions. These reactive species then oxidize AT to intermediates and finally to CO_2 and H_2O. In the presence of BQ, superoxide is efficiently quenched according to:

$$\mathrm{BQ} + e^-_{CB} \text{ or } \mathrm{O_2^{\cdot -}} \rightarrow \text{inactive reduced species}$$

which prevents the initiation of the oxidative cascade and explains the complete inhibition observed.

Overall, the scavenger tests confirm that both ·OH and $\mathrm{O_2^{\cdot -}}$ participate in AT degradation over Br3-CP, but the reaction is predominantly driven by superoxide species. Hydroxyl radicals are

mainly formed by $O_2^{\cdot-}$ conversion and accelerate the process, contributing to the high activity in the absence of scavengers, yet they are not indispensable. This mechanistic insight underlines the importance of bromine doping in promoting efficient charge separation and oxygen reduction, which ensures the continuous formation of superoxide and maintains the photocatalytic activity.

5.7 Conclusions

In this chapter, a series of heteroatom-doped derivatives of graphitic carbon nitride (g-C_3N_4) were successfully synthesized and characterized. The pristine g-C_3N_4 material was obtained via melamine polymerization, while bromine, phosphorus, and boron doping was performed either through co-pyrolysis or post-synthesis functionalization.

Five different bromine-doped g-C_3N_4 samples were prepared using distinct bromine precursors: melamine bis-hydrobromide, 2-bromobenzonitrile, 4-bromo-N,N-dimethylaniline, and elemental bromine (Br_2). The samples obtained via co-pyrolysis were named Br1-CP, Br2-CP, Br3-CP, and Br4-CP respectively, whereas a post-pyrolysis functionalization with elemental bromine produced Br4-PP.

The phosphorus-doped g-C_3N_4 derivatives were obtained using triphenylphosphine as a precursor. Two different nominal loadings were investigated: P 0.1%-CP (low loading) and P 1.2%-CP (higher loading), both synthesized via co-pyrolysis.

The boron-doped derivatives were synthesized using two distinct precursors: boron trifluoride diethyl etherate ($BF_3{\cdot}OEt_2$) and boric acid (H_3BO_3). For $BF_3{\cdot}OEt_2$, post-pyrolysis functionalization was employed to obtain B 0.6%-PP, B 1.2%-PP, and B 5.8%-PP, differing in the precursor amount to tune boron incorporation. Boric acid was used both in co-pyrolysis (B 0.9%-CP) and post-pyrolysis (B 0.9%-PP) approaches, serving as a benchmark to compare the influence of precursor reactivity on the properties of g-C_3N_4.

Overall, this systematic set of doped g-C_3N_4 samples provides a comprehensive basis to investigate how the heteroatom type, dopant precursor, dopant loading, and functionalization strategy affect the structural, optical, and photocatalytic properties of graphitic carbon nitride.

Morphological analyses using TEM and ESEM confirmed that all samples preserved the characteristic layered structure of g-C_3N_4, with doped materials exhibiting minor modifications depending on the dopant and synthesis method. FTIR spectra consistently showed the broad N–H stretching band in the 3000–3300 cm^{-1} region, C–N and C=N stretching in the 1200–1650 cm^{-1} range, and the sharp triazine breathing mode around 810 cm^{-1}, confirming the presence of the g-C_3N_4 framework across all samples. XRD analysis highlighted the influence of heteroatom doping on crystallinity. Bromine doping via in situ co-pyrolysis (Br3-CP) preserved and even enhanced the lamellar ordering, while post-pyrolysis bromination (Br4-PP) slightly reduced interlayer stacking, likely due to oxidative etching. Boron-doped samples derived from $BF_3{\cdot}OEt_2$ showed a sharp (002) peak with increasing intensity and narrowing at higher doping levels, indicating improved crystallinity, whereas boric acid-derived samples displayed broader peaks, suggesting lower structural order. Phosphorus incorporation did not significantly disrupt the g-C_3N_4 network, although at higher doping (1.2 %), caused some peak broadening and reduced (002) intensity, indicative of structural disorder. DRS analysis revealed that heteroatom doping affected the electronic properties and band gap energies. Pristine g-C_3N_4 exhibited a band gap of 2.68 eV,

with the bromine-doped samples showed a consistent band gap reduction, with values ranging from 2.60 eV to 2.45 eV, enhancing visible-light absorption. The lower band gap was achieved with the samples obtained by the co-pyrolysis of melmaine and 4-bromo-N,N-dimethylaniline (Br3-CP). Phosphorus-doped samples displayed minimal changes (2.64–2.66 eV), indicating that phosphorus incorporation primarily influenced surface and structural features rather the bulk electronic transitions. The boron-doped materials, despite low loading, also suggested minor modifications of the electronic structure.

Photocatalytic tests demonstrated that bromine doping consistently enhanced activity compared to pristine g-C_3N_4, with post-pyrolysis samples generally outperforming co-pyrolyzed ones. Br3-CP and Br4-PP exhibited the fastest degradation kinetics for RhB, SMX, and AT, confirming the critical role of dopant precursor chemistry and synthetic pathway in promoting efficient charge separation and reactive oxygen species generation. The phosphorus-doped samples, particularly at higher loadings, displayed slower photocatalytic kinetics, suggesting the formation of trap states that hinder charge carrier mobility. Boron doping showed that moderate $BF_3{\cdot}OEt_2$ loading optimized photocatalytic performance, while excessive loading or the use of boric acid suppressed activity, likely due to lattice distortions and recombination centers.

Overall, the systematic comparison of pristine and doped g-C_3N_4 demonstrates that heteroatom doping can affect the optical, structural, and electronic properties of carbon nitride. Bromine doping, especially via post-pyrolysis, emerges as an effective strategy for enhancing visible-light-driven photocatalysis, whereas phosphorus and boron incorporation must be carefully controlled to avoid detrimental effects. These findings highlight the potential of tailored g-C_3N_4 derivatives for environmental remediation applications, particularly in the degradation of dyes and emerging pharmaceutical pollutants in aqueous media.

6 FINAL REMARKS

Water pollution, particularly from organic dyes, pharmaceuticals, and emerging contaminants, remains a critical challenge for sustainable development. The United Nations Sustainable Development Goals (SDGs) provide a global framework to address these issues, with six goals directly related to water and sanitation: ensuring availability and sustainable management of water and sanitation for all (SDG 6), promoting sustainable consumption and production (SDG 12), and supporting health and well-being (SDG 3), among others. Achieving these goals requires the development of efficient, scalable, and environmentally friendly water treatment technologies.

Current depuration methods include conventional approaches such as adsorption, coagulation, and biological treatments, as well as advanced oxidation processes (AOPs), membrane technologies, and photocatalysis. While these methods have demonstrated varying degrees of effectiveness, limitations remain in terms of selectivity, energy efficiency, cost, and the ability to remove emerging contaminants such as pharmaceuticals and personal care products. There is therefore a pressing need for innovative materials that can improve treatment efficiency, expand the range of removable pollutants, and operate under mild and sustainable conditions.

Within this context, the development of functionalized adsorbents based on a biopolymer such as alginate for the removal of heavy metal ions and heteroatom-doped graphitic carbon nitride (g-C_3N_4) for the photocatalytic degradation of organic pollutants with solar light represents a promising strategy. Alginate matrices offer a biodegradable and tunable platform that can be shaped into versatile forms such as beads or packed columns, facilitating continuous-flow applications and scalable water treatment systems. The integration of these materials into real-world systems holds considerable industrial relevance. Alginate-based adsorbents could be implemented in modular filtration units for decentralized wastewater treatment or as polishing stages in industrial effluents where biocompatibility and regeneration are critical. On the other hand, heteroatom-doped g-C_3N_4 materials can harvest visible light, including solar irradiation, to drive photocatalytic degradation of pollutants, providing an energy-efficient and environmentally friendly ("green") approach. Doped g-C_3N_4 photocatalysts offer a cost-effective alternative to noble-metal-based catalysts and could be incorporated into photoreactors powered by solar energy, significantly reducing operational costs and energy demands. Their adaptability to both batch and continuous-flow systems further enhances their potential for upscaling and integration into existing infrastructures.

Despite the promising outcomes, several challenges remain. The long-term stability and mechanical robustness of biopolymer-based adsorbents under continuous operation is limited and must be improved, as swelling, fouling, or partial degradation may affect performance. For the photocatalytic systems, issues such as charge recombination, limited surface area, sedimentation, and the difficulty of recovering the powdered catalysts from treated water still constrain practical applications. From a methodological perspective, ensuring reproducibility and scalability of synthesis routes—particularly for doped g-C_3N_4—requires more precise control over the dopant distribution, and batch-to-batch consistency. Addressing these limitations will be crucial for bridging the gap between laboratory-scale proof-of-concept studies and industrial-scale deployment. Future research should focus on several complementary directions. In the short term, optimiza-

tion of dopant concentration could further enhance photocatalytic efficiency. For alginate-based adsorbents, tailoring crosslinking density and incorporating functional fillers may improve both mechanical resistance and sorption properties. Moreover, scalability studies should include pilot-scale experiments, techno-economic assessments, and life-cycle analyses to evaluate environmental impact and industrial feasibility. Ultimately, the integration of sustainable materials into real-world depuration systems can play a pivotal role in achieving clean water access, reducing industrial pollution, and advancing the global sustainability agenda outlined in the United Nations SDGs.

LIST OF FIGURES

LIST OF TABLES

BIBLIOGRAPHY

[1] M. Tariq, Z. Hussain, L. Gao, M. Asif, S. Hanif, Z. Qin, M. Q. Abbas, and A. Zhou, "Recent advances in graphene oxide and metal oxides composites synthesis and their applications in wastewater treatment: Removal of dyes, heavy metals, and pharmaceutical contaminants," 12 2025.

[2] B. Wang, Y. Wan, Y. Zheng, X. Lee, T. Liu, Z. Yu, J. Huang, Y. S. Ok, J. Chen, and B. Gao, "Alginate-based composites for environmental applications: a critical review," *Critical Reviews in Environmental Science and Technology*, vol. 49, pp. 318–356, 2 2019.

[3] H. Guven, M. E. Ersahin, H. Ozgun, I. Ozturk, and I. Koyuncu, "Energy and material refineries of future: Wastewater treatment plants," 3 2023.

[4] K. E. Lee, N. Morad, T. T. Teng, and B. T. Poh, "Development, characterization and the application of hybrid materials in coagulation/flocculation of wastewater: A review," 9 2012.

[5] I. Ali, A. A. Basheer, X. Y. Mbianda, A. Burakov, E. Galunin, I. Burakova, E. Mkrtchyan, A. Tkachev, and V. Grachev, "Graphene based adsorbents for remediation of noxious pollutants from wastewater," 6 2019.

[6] Y. G. Wibowo, D. Anwar, H. Safitri, A. Setiawan, S. Sudibyo, A. T. Yuliansyah, and H. T. B. M. Petrus, "Comprehensive review of hybrid absorption-adsorption techniques for chromium removal from wastewater using magnetite-zeolite suspended in glycol slurry," *Colloids and Surfaces C: Environmental Aspects*, vol. 3, p. 100066, 11 2025.

[7] S. Ullah, S. S. A. Shah, M. Altaf, I. Hossain, M. E. E. Sayed, M. Kallel, Z. M. El-Bahy, A. ur Rehman, T. Najam, and M. A. Nazir, "Activated carbon derived from biomass for wastewater treatment: Synthesis, application and future challenges," *Journal of Analytical and Applied Pyrolysis*, vol. 179, 5 2024.

[8] S. Jadoun, J. P. Fuentes, B. F. Urbano, and J. Yáñez, "A review on adsorption of heavy metals from wastewater using conducting polymer-based materials," *Journal of Environmental Chemical Engineering*, vol. 11, 2 2023.

[9] H. Wu, G. Lin, C. Liu, S. Chu, C. Mo, and X. Liu, "Progress and challenges in molecularly imprinted polymers for adsorption of heavy metal ions from wastewater," *Trends in Environmental Analytical Chemistry*, vol. 36, 12 2022.

[10] H. Soni, P. Kanjariya, S. Ballal, R. Panigrahi, I. A. Ariffin, D. Tantawi, M. K. Abosaoda, D. Nathiya, K. Jayabalan, and A. S. Chauhan, "Recent advances in the synthesis of magnetic nanocomposites for the adsorption of heavy metal ions from wastewater," *Journal of Molecular Structure*, vol. 1345, 11 2025.

[11] Rajni, Taruna, A. Udayasri, N. Raghav, A. Bendi, and R. Tomar, "Revolutionizing wastewater treatment: Polymeric metal oxide nanocomposites for effective dye and heavy metal removal," *Chemical Engineering Journal*, vol. 511, 5 2025.

[12] L. Burratti, E. Sgreccia, F. Bertelà, and F. Galiano, "Metal nanostructures in polymeric matrices for optical detection and removal of heavy metal ions, pesticides and dyes from water," *Chemosphere*, vol. 362, 8 2024.

[13] N. Loura, K. Rathee, R. Dhull, M. Singh, and V. Dhull, "Carbon nanotubes for dye removal: A comprehensive study of batch and fixed-bed adsorption, toxicity, and functionalization approaches," *Journal of Water Process Engineering*, vol. 67, 11 2024.

[14] B. Mohan, M. B. Asif, R. K. Gupta, A. J. Pombeiro, C. T. Yavuz, and P. Ren, "Engineered covalent organic frameworks (cofs) for adsorption-based metal separation technologies: A critical review," *Advances in Colloid and Interface Science*, vol. 342, 8 2025.

[15] K. H. H. Aziz, F. S. Mustafa, R. F. Hamarawf, and K. M. Omer, "Adsorptive removal of toxic heavy metals from aquatic environment by metal organic framework (mof): A review," *Journal of Water Process Engineering*, vol. 70, 2 2025.

[16] S. C. Tang and I. M. Lo, "Magnetic nanoparticles: Essential factors for sustainable environmental applications," 5 2013.

[17] M. Granger and D. Montalvo, "Industrial waste water treatment - pressure on europe's environment," tech. rep., European Environment Agency, 2018.

[18] E. Commission, "Directive 2000/60/ec of the european parliament and of the council establishing a framework for community action in the field of water policy," tech. rep., Official Journal of the European Communities, 10 2000.

[19] E. Parlament and C. of the European Union, "Direttiva del consiglio del 21 maggio 1991 concernente il trattamento delle acque reflue urbane (91 /271 /cee)," tech. rep., Official Journal of the European Union, 5 1991.

[20] E. Commission, "Directive 2006/118/ec of the european parliament and of the council of 12 december 2006 on the protection of groundwater against pollution and deterioration," *Official Journal of the European Union*, 12 2006.

[21] E. Parlament and C. of the European Union, "Directive 2008/105/ec of the european parliament and of the council of 16 december 2008 on environmental quality standards in the field of water policy," tech. rep., Official Journal of the European Union, 12 2008.

[22] E. Parlament and C. of the European Union, "Direttiva 2010/75/ue del parlamento europeo e del consiglio del 24 novembre 2010 relativa alle emissioni industriali (prevenzione e riduzione integrate dell'inquinamento)," tech. rep., 11 2010.

[23] E. Parliament and Council, "Direttiva (ue) 2024/3019 del parlamento europeo e del consiglio, del 27 novembre 2024, concernente il trattamento delle acque reflue urbane, (rifusione) (testo rilevante ai fini del see)," tech. rep., Official Journal of the European Union, 11 2024.

[24] C. of the European Union, "Directive of the european parliament and of the council amending directive 2000/60/ec establishing a framework for community action in the field of water

policy, directive 2006/118/ec and and directive 2008/105/ec," tech. rep., Official Journal of the European Union, 6 2024.

[25] P. Sahu, A. R. Patel, A. Pandey, M. Hait, and G. K. Patra, "Assessment of heavy metal ion toxicity in wastewater: A comprehensive review," *Inorganica Chimica Acta*, vol. 585, 9 2025.

[26] S. S. Raychaudhuri, P. Pramanick, P. Talukder, and A. Basak, *Polyamines, metallothioneins, and phytochelatins—Natural defense of plants to mitigate heavy metals*, vol. 69, pp. 227–261. Elsevier B.V., 1 2021.

[27] E. Parlament and C. of the European Union, "Direttiva 2013/39/ue del parlamento europeo e del consiglio, del 12 agosto 2013, che modifica le direttive 2000/60/ce e 2008/105/ce per quanto riguarda le sostanze prioritarie nel settore della politica delle acque," tech. rep., Official Journal of the European Union, 8 2013.

[28] C. of the European Union, "Council directive 98/83/ec of 3 november 1998 on the quality of water intended for human consumption," *Official Journal of the European Communities*, 11 1998.

[29] E. Parlament and C. of the European Union, "Direttiva (ue) 2020/2184 del parlamento europeo e del consiglio del 16 dicembre 2020 concernente la qualità delle acque destinate al consumo umano," tech. rep., Official Journal of the European Union, 12 2020.

[30] E. Commission, "Proposal for a directive of the european parliament and of the council amending directive 2000/60/ec establishing a framework for community action in the field of water policy, directive 2006/118/ec on the protection of groundwater against pollution and deterioration, and directive 2008/105/ec on environmental quality standards in the field of water policy," tech. rep., Official Journal of the European Union, 10 2022.

[31] E. Commission, "Annex - proposal for a directive of the european parliament and of the council amending directive 2000/60/ec establishing a framework for community action in the field of water policy, directive 2006/118/ec on the protection of groundwater against pollution and deterioration, and directive 2008/105/ec on environmental quality standards in the field of water policy," tech. rep., Official Journal of the European Union, 10 2022.

[32] E. Commision, "Decisione di esecuzione (ue) 2025439 della commissione che istituisce un elenco di controllo delle sostanze da sottoporre a monitoraggio a livello dell'unione nel settore della politica delle acque in attuazione della direttiva 2008/105/ce del parlamento europeo e del consiglio," tech. rep., Official Journal of the European Union, 2 2025.

[33] E. D. H. Kong, C. W. Lai, J. C. Juan, Y. L. Pang, C. S. Khe, I. A. Badruddin, F. Gapsari, and K. Anam, "Recent advances in titanium dioxide bio-derived carbon photocatalysts for organic pollutant degradation in wastewater," 5 2025.

[34] W. Xiao, X. Jiang, X. Liu, W. Zhou, Z. N. Garba, I. Lawan, L. Wang, and Z. Yuan, "Adsorption of organic dyes from wastewater by metal-doped porous carbon materials," 2 2021.

[35] Y. H. Chiu, T. F. M. Chang, C. Y. Chen, M. Sone, and Y. J. Hsu, "Mechanistic insights into photodegradation of organic dyes using heterostructure photocatalysts," *Catalysts*, vol. 9, 5 2019.

[36] M. Shabir, M. Yasin, M. Hussain, I. Shafiq, P. Akhter, A. S. Nizami, B. H. Jeon, and Y. K. Park, "A review on recent advances in the treatment of dye-polluted wastewater," 8 2022.

[37] S. K. Yadav, S. R. Dhakate, and B. P. Singh, "Carbon nanotube incorporated eucalyptus derived activated carbon-based novel adsorbent for efficient removal of methylene blue and eosin yellow dyes," *Bioresource Technology*, vol. 344, 1 2022.

[38] B. Lellis, C. Z. Fávaro-Polonio, J. A. Pamphile, and J. C. Polonio, "Effects of textile dyes on health and the environment and bioremediation potential of living organisms," *Biotechnology Research and Innovation*, vol. 3, pp. 275–290, 7 2019.

[39] B. S. Rathi, P. S. Kumar, and D. V. N. Vo, "Critical review on hazardous pollutants in water environment: Occurrence, monitoring, fate, removal technologies and risk assessment," *Science of the Total Environment*, vol. 797, 11 2021.

[40] A. J. Ebele, M. A.-E. Abdallah, and S. Harrad, "Pharmaceuticals and personal care products (ppcps) in the freshwater aquatic environment," 3 2017.

[41] L. M. Bexfield, P. L. Toccalino, K. Belitz, W. T. Foreman, and E. T. Furlong, "Hormones and pharmaceuticals in groundwater used as a source of drinking water across the united states," *Environmental Science and Technology*, vol. 53, pp. 2950–2960, 3 2019.

[42] R. K. Mishra, S. S. Mentha, Y. Misra, and N. Dwivedi, "Emerging pollutants of severe environmental concern in water and wastewater: A comprehensive review on current developments and future research," *Water-Energy Nexus*, vol. 6, pp. 74–95, 12 2023.

[43] R. B. González-González, A. Sharma, R. Parra-Saldívar, R. A. Ramirez-Mendoza, M. Bilal, and H. M. Iqbal, "Decontamination of emerging pharmaceutical pollutants using carbon-dots as robust materials," *Journal of Hazardous Materials*, vol. 423, 2 2022.

[44] E. Commission, "European union strategic approach to pharmaceuticals in the environment," tech. rep., Official Journal of the European Union, 3 2019.

[45] X. Gao, C. Guo, J. Hao, Z. Zhao, H. Long, and M. Li, "Adsorption of heavy metal ions by sodium alginate based adsorbent-a review and new perspectives," *International Journal of Biological Macromolecules*, vol. 164, pp. 4423–4434, 12 2020.

[46] A. K. Thakur, R. Singh, R. T. Pullela, and V. Pundir, "Green adsorbents for the removal of heavy metals from wastewater: A review," *Materials Today: Proceedings*, vol. 57, pp. 1468–1472, 2022.

[47] H. K. Agbovi and L. D. Wilson, *Adsorption processes in biopolymer systems: fundamentals to practical applications*, pp. 1–51. Elsevier, 2021.

[48] S. Dong, Y. Li, K. Zhu, C. Wang, and S. Zhai, "Advances in structure designing and function tailoring strategy toward alginate-based hydrogels for efficient water remediation: A review," 4 2025.

[49] M. Bilal, I. Ihsanullah, M. Younas, and M. U. H. Shah, "Recent advances in applications of low-cost adsorbents for the removal of heavy metals from water: A critical review," 1 2022.

[50] T. S. Anirudhan and S. S. Sreekumari, "Adsorptive removal of heavy metal ions from industrial effluents using activated carbon derived from waste coconut buttons," *Journal of Environmental Sciences*, vol. 23, pp. 1989–1998, 12 2011.

[51] F. Sardella, M. Gimenez, C. Navas, C. Morandi, C. Deiana, and K. Sapag, "Conversion of viticultural industry wastes into activated carbons for removal of lead and cadmium," *Journal of Environmental Chemical Engineering*, vol. 3, pp. 253–260, 2015.

[52] R. Shahrokhi-Shahraki, C. Benally, M. G. El-Din, and J. Park, "High efficiency removal of heavy metals using tire-derived activated carbon vs commercial activated carbon: Insights into the adsorption mechanisms," *Chemosphere*, vol. 264, 2 2021.

[53] S. S. Fiyadh, M. A. AlSaadi, W. Z. Jaafar, M. K. AlOmar, S. S. Fayaed, N. S. Mohd, L. S. Hin, and A. El-Shafie, "Review on heavy metal adsorption processes by carbon nanotubes," *Journal of Cleaner Production*, vol. 230, pp. 783–793, 9 2019.

[54] E. D. Duarte, M. G. Oliveira, M. P. Spaolonzi, H. P. Costa, T. L. Silva, M. G. Silva, and M. G. Vieira, "Adsorption of pharmaceutical products from aqueous solutions on functionalized carbon nanotubes by conventional and green methods: A critical review," *Journal of Cleaner Production*, vol. 372, 10 2022.

[55] R. H. Krishna, M. N. Chandraprabha, K. Samrat, T. P. K. Murthy, C. Manjunatha, and S. G. Kumar, "Carbon nanotubes and graphene-based materials for adsorptive removal of metal ions – a review on surface functionalization and related adsorption mechanism," *Applied Surface Science Advances*, vol. 16, 8 2023.

[56] N. Mahesh, S. Balakumar, S. Shyamalagowri, J. Manjunathan, M. Pavithra, P. S. Babu, M. Kamaraj, and M. Govarthanan, "Carbon-based adsorbents as proficient tools for the removal of heavy metals from aqueous solution: A state of art-review emphasizing recent progress and prospects," *Environmental Research*, p. 113723, 10 2022.

[57] M. Vesali-Naseh, M. R. V. Naseh, and P. Ameri, "Adsorption of pb (ii) ions from aqueous solutions using carbon nanotubes: A systematic review," *Journal of Cleaner Production*, vol. 291, 4 2021.

[58] S. K. Das, G. K. Ghosh, and R. Avasthe, "Conversion of crop, weed and tree biomass into biochar for heavy metal removal and wastewater treatment," *Biomass Conversion and Biorefinery*, 2021.

[59] S. H. Ho, Y. di Chen, Z. kai Yang, D. Nagarajan, J. S. Chang, and N. qi Ren, "High-efficiency removal of lead from wastewater by biochar derived from anaerobic digestion sludge," *Bioresource Technology*, vol. 246, pp. 142–149, 12 2017.

[60] F. Khamis, H. M. Hegab, F. Banat, H. A. Arafat, and S. W. Hasan, "Comprehensive review on ph and temperature-responsive polymeric adsorbents: Mechanisms, equilibrium, kinetics, and thermodynamics of adsorption processes for heavy metals and organic dyes," *Chemosphere*, vol. 349, 2 2024.

[61] S. Lakard and B. Lakard, "Environmental applications of conducting polymers and their composites: adsorption and detection of heavy metal ions," *Journal of Environmental Chemical Engineering*, vol. 13, 6 2025.

[62] M. Sajid, M. K. Nazal, Ihsanullah, N. Baig, and A. M. Osman, "Removal of heavy metals and organic pollutants from water using dendritic polymers based adsorbents: A critical review," *Separation and Purification Technology*, vol. 191, pp. 400–423, 2018.

[63] T. Wu, H. Karimi-Maleh, Y. Li, D. Zhang, Z. Zhang, N. Zhong, Y. Wen, and T. M. Aminabhavi, "3d printed porous chitosan/metal–organic framework composites as effective adsorbents to remove heavy metals from wastewater," *Chemical Engineering Journal*, vol. 493, 8 2024.

[64] Baldev, G. Kumar, V. Sharma, and M. Nemiwal, "Biomass-derived zirconium composite: An adsorbent for preferential removal of heavy metals and contaminants in wastewater," *Journal of Water Process Engineering*, vol. 69, 1 2025.

[65] Y. He, D. Lin, G. Jiang, L. Jiang, J. Xiao, H. Li, L. Zhou, and S. Gou, "Carboxyl-functionalized montmorillonite composite hydrogel containing alginate as a highly efficient adsorbent for simultaneous removal of cationic dyes and heavy metal ions," *Journal of Water Process Engineering*, vol. 69, 1 2025.

[66] E. Fernandes, S. Contreras, F. Medina, R. C. Martins, and J. Gomes, "N-doped titanium dioxide for mixture of parabens degradation based on ozone action and toxicity evaluation: Precursor of nitrogen and titanium effect," *Process Safety and Environmental Protection*, vol. 138, pp. 80–89, 6 2020.

[67] F. Nunzi and F. D. Angelis, "Modeling titanium dioxide nanostructures for photocatalysis and photovoltaics," *Chemical Science*, vol. 13, pp. 9485–9497, 7 2022.

[68] K. Nagaraj, S. Radha, C. G. Deepa, K. Raja, V. Umapathy, N. P. Badgujar, N. M. Parekh, T. Manimegalai, L. A. Devi, and C. Uthra, "Photocatalytic advancements and applications of titanium dioxide (tio2): Progress in biomedical, environmental, and energy sustainability," *Next Research*, vol. 2, p. 100180, 3 2025.

[69] K. P. Gopinath, N. V. Madhav, A. Krishnan, R. Malolan, and G. Rangarajan, "Present applications of titanium dioxide for the photocatalytic removal of pollutants from water: A review," *Journal of Environmental Management*, vol. 270, 9 2020.

[70] Y. Le and H. Wang, "Remediation of wastewater by using cds-based biohybrids: Challenges and enhancement strategies," 6 2025.

[71] M. Choudhary, P. Saini, N. Chakinala, P. K. Surolia, and A. G. Chakinala, "Carbon dots decorated cadmium sulfide nanomaterials for boosting photocatalytic activity for ciprofloxacin

degradation," *Spectrochimica Acta - Part A: Molecular and Biomolecular Spectroscopy*, vol. 319, 10 2024.

[72] P. Li, J. Yang, Z. Liu, and Z. Jiang, "Preparation of z-type heterojunction ammonium phosphotungstate/cds composite photocatalyst and photocatalytic degradation of tetracycline," *Results in Chemistry*, vol. 16, 7 2025.

[73] A. Hojjati-Najafabadi, E. Farahbakhsh, G. Gholamalian, P. Feng, F. Davar, T. M. Aminabhavi, Y. Vasseghian, H. Kamyab, and H. Rahimi, "Controllable synthesis of nanostructured flower-like cadmium sulfides for photocatalytic degradation of methyl orange under different light sources," *Journal of Water Process Engineering*, vol. 59, 3 2024.

[74] C. N. Hitam and A. A. Jalil, "A review on exploration of fe2o3 photocatalyst towards degradation of dyes and organic contaminants," 3 2020.

[75] Y. Ruan, L. Kong, Y. Zhong, Z. Diao, K. Shih, L. Hou, S. Wang, and D. Chen, "Review on the synthesis and activity of iron-based catalyst in catalytic oxidation of refractory organic pollutants in wastewater," *Journal of Cleaner Production*, vol. 321, 10 2021.

[76] G. Halligudra, C. Sabbanahalli, S. Singh, P. Choudhary, M. R, G. Tigari, Shantharaja, and S. L. Lo, "Catalytic behaviour of iron-based nanomaterials for the remediation of hazardous chemicals from wastewater: A review," *Journal of Physics and Chemistry of Solids*, vol. 203, 8 2025.

[77] Q. Sun, Y. Sun, M. Zhou, H. Cheng, H. Chen, B. Dorus, M. Lu, and T. Le, "A 2d/3d g-c3n4/zno heterojunction enhanced visible-light driven photocatalytic activity for sulfonamides degradation," *Ceramics International*, vol. 48, pp. 7283–7290, 3 2022.

[78] R. T. Hussain, M. S. Hossain, and J. H. Shariffuddin, "Green synthesis and photocatalytic insights: A review of zinc oxide nanoparticles in wastewater treatment," *Materials Today Sustainability*, vol. 26, 6 2024.

[79] A. Aslam, N. Nadeem, B. Balgabayeva, S. U. Khan, Q. Abbas, S. Noreen, M. Zahid, and Z. Supiyeva, "Synergy in metal oxide/metal sulfide binary composites for photocatalysis: mechanisms, applications, and emerging trends," *Inorganic Chemistry Communications*, vol. 181, 11 2025.

[80] S. Zhu and D. Wang, "Photocatalysis: Basic principles, diverse forms of implementations and emerging scientific opportunities," 12 2017.

[81] H. Zhang, Z. Yuan, X. Zhao, X. Zhu, H. Wang, Y. Luo, Z. Wang, and Z. Jiang, "Graphitic carbon nitride photocatalysts for sustainable energy and environmental remediation: performance optimization and future perspectives," *Journal of Environmental Sciences*, 9 2025.

[82] K. T. Amakiri, A. Angelis-Dimakis, and A. R. Canon, "Recent advances, influencing factors, and future research prospects using photocatalytic process for produced water treatment," *Water Science and Technology*, vol. 85, pp. 769–788, 2 2022.

[83] D. Zhu and Q. Zhou, "Action and mechanism of semiconductor photocatalysis on degradation of organic pollutants in water treatment: A review," 12 2019.

[84] J. Han, Q. Liu, H. Xu, Y. Wu, S. Le, and C. Zhu, "Cerium valence state conversion: Fabrication and environmental remediation of modified ceo2 materials," *Journal of Rare Earths*, vol. 43, pp. 430–440, 3 2025.

[85] D. P. Tran, M. T. Pham, X. T. Bui, Y. F. Wang, and S. J. You, "Ceo2 as a photocatalytic material for co2 conversion: A review," 7 2022.

[86] A. K. Sibhatu, G. K. Weldegebrieal, S. Sagadevan, N. N. Tran, and V. Hessel, "Photocatalytic activity of cuo nanoparticles for organic and inorganic pollutants removal in wastewater remediation," *Chemosphere*, vol. 300, 8 2022.

[87] P. Chen, P. Zhang, Y. Cui, X. Fu, and Y. Wang, "Recent progress in copper-based inorganic nanostructure photocatalysts: properties, synthesis and photocatalysis applications," 3 2023.

[88] S. K. Lahiri, C. Zhang, M. Sillanpää, and L. Liu, "Nanoporous nio@sio2 photo-catalyst prepared by ion-exchange method for fast elimination of reactive dyes from wastewater," *Materials Today Chemistry*, vol. 23, 3 2022.

[89] K. P. Makhado, M. M. Mphahlele-Makgwane, N. Kumar, P. G. Baker, and P. R. Makgwane, "Current updates on p-type nickel oxide (nio) based photocatalysts towards decontamination of organic pollutants from wastewater," 3 2024.

[90] C. Sun, J. Yang, M. Xu, Y. Cui, W. Ren, J. Zhang, H. Zhao, and B. Liang, "Recent intensification strategies of sno2-based photocatalysts: A review," 1 2022.

[91] W. Ren, J. Yang, J. Zhang, W. Li, C. Sun, H. Zhao, Y. Wen, O. Sha, and B. Liang, "Recent progress in sno2/g-c3n4 heterojunction photocatalysts: Synthesis, modification, and application," 6 2022.

[92] N. K. Sompalli, A. Mohanty, A. M. Mohan, and P. Deivasigamani, "Heterojunction cr2o3-ag2o nanocomposite decorated porous polymer monoliths a new class of visible light fast responsive heterogeneous photocatalysts for pollutant clean-up," *Journal of Environmental Chemical Engineering*, vol. 9, 2 2021.

[93] S. Sakhaie and F. Taghipour, "Highly durable zirconium/titanium dioxide–silicon carbide photocatalytic membrane for water and wastewater treatment," *Journal of Environmental Chemical Engineering*, vol. 11, 6 2023.

[94] Y. Zhong, Y. Lin, Q. Chen, Y. Sun, and F. F. Fu, "Rapid photo-degradation of various organic dyes with thin-layer boron-doped graphitic carbon nitride nano-sheets under visible light irradiation," *Journal of Environmental Chemical Engineering*, vol. 8, 4 2020.

[95] M. Antonopoulou, C. Kosma, T. Albanis, and I. Konstantinou, "An overview of homogeneous and heterogeneous photocatalysis applications for the removal of pharmaceutical compounds from real or synthetic hospital wastewaters under lab or pilot scale," *Science of the Total Environment*, vol. 765, 4 2021.

[96] Z. Wei, J. Liu, and W. Shangguan, "A review on photocatalysis in antibiotic wastewater: Pollutant degradation and hydrogen production," *Chinese Journal of Catalysis*, vol. 41, pp. 1440–1450, 2020.

[97] M. S. Javed, M. A. Nazir, Z. Shafiq, S. Ullah, T. Najam, R. Iqbal, M. A. Ismail, T. L. Tamang, and S. S. A. Shah, "Advanced materials for photocatalytic removal of antibiotics from wastewater," *Journal of Alloys and Compounds*, vol. 1010, 1 2025.

[98] A. Setiawan, Sulissetiawati, E. K. Sari, L. J. Mahardhika, Zurnansyah, P. D. Jayanti, N. P. Rini, N. I. Istiqomah, H. Aliah, N. S. Asri, J. Angel, and E. Suharyadi, "Magnetically separable and reusable fe3o4/rgo photocatalyst synthesized through green approach for heavy metal ion reduction application," *Diamond and Related Materials*, vol. 151, 1 2025.

[99] J. Avinash, G. Madhumitha, and S. M. Roopan, "Znin2s4-based heterojunction photocatalysts for enhanced cr(vi) reduction: A review," *Journal of Environmental Chemical Engineering*, p. 118368, 10 2025.

[100] C. Shen, K. Sun, Y. Yang, C. Liu, Y. Liu, and X. Wang, "Photoreductive elimination of heavy metal ions and radionuclides by g-c3n4-based materials: A review," *Separation and Purification Technology*, vol. 363, 8 2025.

[101] V. U. Siddiqui, R. A. Ilyas, S. M. Sapuan, N. H. A. Hamid, P. S. Khoo, A. Chowdhury, M. S. Atikah, M. S. Rani, and M. R. Asyraf, "Alginate-based materials as adsorbent for sustainable water treatment," 4 2025.

[102] C. Bertagnolli, M. G. C. da Silva, and E. Guibal, "Chromium biosorption using the residue of alginate extraction from sargassum filipendula," *Chemical Engineering Journal*, vol. 237, pp. 362–371, 2 2014.

[103] M. R. Alam, M. A. Shahid, S. Alimuzzaman, and A. N. Khan, "Sources, extractions and applications of bio-maker collagen–a review," *Biomedical Engineering Advances*, vol. 4, p. 100064, 12 2022.

[104] H. Bojorges, A. López-Rubio, A. Martínez-Abad, and M. J. Fabra, "Overview of alginate extraction processes: Impact on alginate molecular structure and techno-functional properties," *Trends in Food Science and Technology*, vol. 140, 10 2023.

[105] A. Dobrinčić, S. Balbino, Z. Zorić, S. Pedisić, D. B. Kovačević, I. E. Garofulić, and V. Dragović-Uzelac, "Advanced technologies for the extraction of marine brown algal polysaccharides," 2020.

[106] J. Wang, S. Liu, J. Huang, K. Ren, Y. Zhu, and S. Yang, "Alginate: Microbial production, functionalization, and biomedical applications," *International Journal of Biological Macromolecules*, vol. 242, 7 2023.

[107] M. M. Rahman, M. A. Shahid, M. T. Hossain, M. S. Sheikh, M. S. Rahman, N. Uddin, A. Rahim, R. A. Khan, and I. Hossain, "Sources, extractions, and applications of alginate: a review," *Discover Applied Sciences*, vol. 6, 8 2024.

[108] S. Selvaraj, A. Bains, M. Sharma, P. Chawla, and K. Sridhar, "Freshwater edible algae polysaccharides: A recent overview of novel extraction technologies, characterization, and future food applications," *Journal of Polymers and the Environment*, 2023.

[109] N. Hans, F. Pattnaik, A. Malik, and S. Naik, "Comparison of different green extraction techniques and their influence on chemical characteristics of sulfated polysaccharide (fucoidan) from padina tetrastromatica and turbinaria conoides," *Algal Research*, vol. 74, 7 2023.

[110] S. Thakur and O. Arotiba, "Synthesis, characterization and adsorption studies of an acrylic acid-grafted sodium alginate-based tio2 hydrogel nanocomposite," *Adsorption Science and Technology*, vol. 36, pp. 458–477, 2 2018.

[111] T. H. Duc, T. K. Vu, C. T. Dang, V. H. Nguyen, D. D. La, G. M. Kim, S. W. Chang, X. T. Bui, T. D. Dang, and D. D. Nguyen, "Synthesis and application of hydrogel calcium alginate microparticles as a biomaterial to remove heavy metals from aqueous media," *Environmental Technology and Innovation*, vol. 22, 5 2021.

[112] H. Paudyal, B. Pangeni, K. Inoue, H. Kawakita, K. Ohto, K. N. Ghimire, and S. Alam, "Preparation of novel alginate based anion exchanger from ulva japonica and its application for the removal of trace concentrations of fluoride from water," *Bioresource Technology*, vol. 148, pp. 221–227, 2013.

[113] R. Russo, M. Malinconico, and G. Santagata, "Effect of cross-linking with calcium ions on the physical properties of alginate films," *Biomacromolecules*, vol. 8, pp. 3193–3197, 10 2007.

[114] M. Nasrollahzadeh, M. Sajjadi, S. Iravani, and R. S. Varma, "Starch, cellulose, pectin, gum, alginate, chitin and chitosan derived (nano)materials for sustainable water treatment: A review," 1 2021.

[115] H. Sable, V. Kumar, V. Singh, S. Rustagi, S. Chahal, and V. Chaudhary, "Strategically engineering advanced nanomaterials for heavy-metal remediation from wastewater," *Coordination Chemistry Reviews*, vol. 518, 11 2024.

[116] M. Margaritis, E. Gkazeli, and M. Atzemi, "Removal of heavy metals from industrial wastewater using natural and organically modified minerals," *Sustainable Futures*, vol. 9, 6 2025.

[117] S. Teotia, D. Verma, Toshani, K. P. Ting, V. Kumari, M. U. Ahmed, and M. D. Mukherjee, "Engineered 2d smart nanomaterials and nanocomposites: Advanced frontiers in heavy metal ion detection for water purification," *Journal of Environmental Chemical Engineering*, p. 119367, 9 2025.

[118] A. Y. Jassim, B. S. Al-Ali, W. R. Kadhum, and E. kianfar, "Heavy metal removal from wastewater using functionalized nano-structures and graphene oxide," *Hybrid Advances*, p. 100552, 9 2025.

[119] A. F. Senaut, N. M. Mubarak, K. N. Ruslan, Y. H. Tan, R. R. Karri, and D. M. R. Prasad, "Mechanistic insights into carbon-nano based adsorbents for heavy metal removal: A comprehensive review," 8 2025.

[120] X. Yang, Y. Wan, Y. Zheng, F. He, Z. Yu, J. Huang, H. Wang, Y. S. Ok, Y. Jiang, and B. Gao, "Surface functional groups of carbon-based adsorbents and their roles in the removal of heavy metals from aqueous solutions: A critical review," *Chemical Engineering Journal*, vol. 366, pp. 608–621, 6 2019.

[121] C. Manfredi, R. Mozzillo, S. Volino, M. Trifuoggi, A. Giarra, V. Gargiulo, and M. Alfé, "On the modeling of heavy metals and rare earth elements adsorption on colloidal carbon-based nanoparticles," *Applied Surface Science*, vol. 505, 3 2020.

[122] D. Das, B. K. Das, R. Sarkar, S. Mukherjee, and K. K. Chattopadhyay, "Highly exfoliated graphitic carbon nitride for efficient removal of wastewater pollutants: Insights from dft and statistical modelling," *Environmental Research*, vol. 221, 3 2023.

[123] Z. Luo, J. Zhu, L. Yu, and K. Yin, "Heavy metal remediation by nano zero-valent iron in the presence of microplastics in groundwater: Inhibition and induced promotion on aging effects," *Environmental Pollution*, vol. 287, 10 2021.

[124] G. Vilardi, T. Mpouras, D. Dermatas, N. Verdone, A. Polydera, and L. D. Palma, "Nanomaterials application for heavy metals recovery from polluted water: The combination of nano zero-valent iron and carbon nanotubes. competitive adsorption non-linear modeling," *Chemosphere*, vol. 201, pp. 716–729, 6 2018.

[125] P. Deivasigamani, V. Gajendiran, B. Chitra, P. S. Kumar, N. Balasubramanian, S. Sundararaman, V. Dhananjeyan, L. Subramani, A. K. Jagadeesan, S. Sivamani, R. Chellappa, and G. Rangasamy, "Magnetic nanoparticles: Synthesis, characterization and application based on environmental perspective," *Results in Chemistry*, vol. 14, 3 2025.

[126] S. Abuhatab, A. El-Qanni, H. Al-Qalaq, M. Hmoudah, and W. Al-Zerei, "Effective adsorptive removal of zn2+, cu2+, and cr3+ heavy metals from aqueous solutions using silica-based embedded with nio and mgo nanoparticles," *Journal of Environmental Management*, vol. 268, 8 2020.

[127] F. D. Natale, V. Gargiulo, and M. Alfè, "Adsorption of heavy metals on silica-supported hydrophilic carbonaceous nanoparticles (shnps)," *Journal of Hazardous Materials*, vol. 393, 7 2020.

[128] P. Shao, D. Liang, L. Yang, H. Shi, Z. Xiong, L. Ding, X. Yin, K. Zhang, and X. Luo, "Evaluating the adsorptivity of organo-functionalized silica nanoparticles towards heavy metals: Quantitative comparison and mechanistic insight," *Journal of Hazardous Materials*, vol. 387, 4 2020.

[129] M. E. Mahmoud, N. A. Fekry, and M. M. El-Latif, "Nanocomposites of nanosilica-immobilized-nanopolyaniline and crosslinked nanopolyaniline for removal of heavy metals," *Chemical Engineering Journal*, vol. 304, pp. 679–691, 11 2016.

[130] V. B. Yadav, R. Gadi, and S. Kalra, "Clay based nanocomposites for removal of heavy metals from water: A review," *Journal of Environmental Management*, vol. 232, pp. 803–817, 2 2019.

[131] J. Feng, M. Gao, Z. Zhang, M. Gu, J. Wang, W. Zeng, and Y. Ren, "Comparing the photocatalytic properties of g-c3n4 treated by thermal decomposition, solvothermal and protonation," *Results in Physics*, vol. 11, pp. 331–334, 12 2018.

[132] M. F. Iannone, M. D. Groppa, M. S. Zawoznik, D. F. Coral, M. B. F. van Raap, and M. P. Benavides, "Magnetite nanoparticles coated with citric acid are not phytotoxic and stimulate soybean and alfalfa growth," *Ecotoxicology and Environmental Safety*, vol. 211, 3 2021.

[133] J. Song, H. Kong, and J. Jang, "Adsorption of heavy metal ions from aqueous solution by polyrhodanine-encapsulated magnetic nanoparticles," *Journal of Colloid and Interface Science*, vol. 359, pp. 505–511, 2011.

[134] S. K. Hubadillah, M. H. D. Othman, Z. Harun, A. F. Ismail, M. A. Rahman, and J. Jaafar, "A novel green ceramic hollow fiber membrane (chfm) derived from rice husk ash as combined adsorbent-separator for efficient heavy metals removal," *Ceramics International*, vol. 43, pp. 4716–4720, 4 2017.

[135] A. Pérez-Vidal, J. A. Silva-Leal, J. Diaz-Gómez, C. J. Meneses-Torres, J. E. Arias-Vallejo, G. A. Giraldo-Tenorio, and M. C. Bacca-Jordán, "Performance evaluation of ceramic pot filters combined with adsorption processes for the removal of heavy metals and phenolic compounds," *Journal of Water and Health*, vol. 19, pp. 750–761, 10 2021.

[136] M. D. Nguyen, H. V. Tran, S. Xu, and T. R. Lee, "Fe3o4 nanoparticles: Structures, synthesis, magnetic properties, surface functionalization, and emerging applications," 12 2021.

[137] C. Comanescu, "Recent advances in surface functionalization of magnetic nanoparticles," 10 2023.

[138] S. Sharma, H. Sharma, and R. Sharma, "A review on functionalization and potential application spectrum of magnetic nanoparticles (mnps) based systems," *Chemistry of Inorganic Materials*, vol. 2, p. 100035, 4 2024.

[139] A. Peigneux, J. D. Puentes-Pardo, A. B. Rodríguez-Navarro, M. T. Hincke, and C. Jimenez-Lopez, "Development and characterization of magnetic eggshell membranes for lead removal from wastewater," *Ecotoxicology and Environmental Safety*, vol. 192, 4 2020.

[140] S. Bhogal and R. Sharma, "Harnessing magnetic nanoparticles for cleaner water: A green technology perspective," 9 2025.

[141] W. Fu, H. Yang, Hari-Bala, S. Liu, M. Li, and G. Zou, "Preparation and magnetic characterization of core-shell structure stainless steel/silica nanoparticles," *Materials Letters*, vol. 60, pp. 1728–1732, 6 2006.

[142] D. Chen, T. Awut, B. Liu, Y. Ma, T. Wang, and I. Nurulla, "Functionalized magnetic fe3o4 nanoparticles for removal of heavy metal ions from aqueous solutions," *E-Polymers*, vol. 16, pp. 313–322, 7 2016.

[143] D. P. Kumar, L. M. Nollen, A. P. Rangappa, and T. K. Kim, "Effective dye degradation by an environment-friendly porous few-layered carbon nitride photocatalyst developed using sequential molecule self-assembly," *Environmental Research*, vol. 204, 3 2022.

[144] M. S. Bhuyan, M. A. Bakar, M. Rashed-Un-Nabi, V. Senapathi, S. Y. Chung, and M. S. Islam, "Monitoring and assessment of heavy metal contamination in surface water and sediment of the old brahmaputra river, bangladesh," *Applied Water Science*, vol. 9, 7 2019.

[145] Y. Venkatraman and A. K. Priya, "Removal of heavy metal ion concentrations from the wastewater using tobacco leaves coated with iron oxide nanoparticles," *International Journal of Environmental Science and Technology*, vol. 19, pp. 2721–2736, 4 2022.

[146] S. Singh, S. Perween, and A. Ranjan, "Dramatic enhancement in adsorption of congo red dye in polymer-nanoparticle composite of polyaniline-zinc titanate," *Journal of Environmental Chemical Engineering*, vol. 9, 6 2021.

[147] C. Tamez, R. Hernandez, and J. G. Parsons, "Removal of cu (ii) and pb (ii) from aqueous solution using engineered iron oxide nanoparticles," *Microchemical Journal*, vol. 125, pp. 97–104, 3 2016.

[148] R. S. Hamida, M. A. Ali, N. E. Abdelmeguid, M. I. Al-Zaban, L. Baz, and M. M. Bin-Meferij, "Lichens—a potential source for nanoparticles fabrication: A review on nanoparticles biosynthesis and their prospective applications," *Journal of Fungi*, vol. 7, 4 2021.

[149] J. Jeevanandam, A. Barhoum, Y. S. Chan, A. Dufresne, and M. K. Danquah, "Review on nanoparticles and nanostructured materials: History, sources, toxicity and regulations," *Beilstein Journal of Nanotechnology*, vol. 9, pp. 1050–1074, 4 2018.

[150] A. Alkhouzaam, H. Qiblawey, M. Khraisheh, M. Atieh, and M. Al-Ghouti, "Synthesis of graphene oxides particle of high oxidation degree using a modified hummers method," *Ceramics International*, vol. 46, pp. 23997–24007, 10 2020.

[151] S. Park, H. Seok, D. Oh, H. cheol Oh, S. Kim, and J. Ahn, "Machine learning-based prediction of adsorption capacity of metal-doped and undoped activated carbon: Assessing the role of metal doping," *Chemosphere*, vol. 366, 10 2024.

[152] M. Achache, D. Bouchta, K. Draoui, and M. Choukairi, "Synthesis, physicochemical and electrochemical characterization of graphene oxide nanosheets obtained through improved and modified hummers methods," *Inorganic Chemistry Communications*, vol. 174, 4 2025.

[153] A. Nqombolo and P. N. Nomngongo, *Graphene and graphene oxide-based nanoadsorbents in wastewater treatment*, pp. 143–161. Elsevier, 1 2023.

[154] M. A. Darweesh, M. Y. Elgendy, M. I. Ayad, A. M. M. Ahmed, N. M. Elsayed, and W. A. Hammad, "Adsorption isotherm, kinetic, and optimization studies for copper (ii) removal from aqueous solutions by banana leaves and derived activated carbon," *South African Journal of Chemical Engineering*, vol. 40, pp. 10–20, 4 2022.

[155] L. Qian, C. Mei, T. Li, W. Luo, W. Liu, M. Chen, X. Yang, X. Li, B. Cheng, and H. Ma, "A versatile biochar fertilizer used for adsorption of heavy metals and enhancement of plant growth in metal contaminated soil," *Environmental Technology and Innovation*, vol. 36, 11 2024.

[156] X. Zhu, K. Wang, X. Ma, Z. Zhang, J. Wang, X. Zhang, B. Shen, and S. Si, "Loading organic phosphorus-degrading bacteria enhanced biochar performance for heavy metals adsorption," *Environmental Technology and Innovation*, vol. 34, 5 2024.

[157] X. Zheng, S. Chen, J. Li, H. Wu, C. Zhang, D. Zhang, X. Chen, Y. Gao, F. He, L. Hui, H. Liu, T. Jiu, N. Wang, G. Li, J. Xu, Y. Xue, C. Huang, C. Chen, Y. Guo, T. B. Lu, D. Wang, L. Mao, J. Zhang, Y. Zhang, L. Chi, W. Guo, X. H. Bu, H. Zhang, L. Dai, Y. Zhao, and Y. Li, "Two-dimensional carbon graphdiyne: Advances in fundamental and application research," *ACS Nano*, vol. 17, pp. 14309–14346, 8 2023.

[158] B. Kuppusamy, S. Gopalakrishnan, S. Natesan, N. Rajamohan, M. Rajasimman, M. Yusuf, and H. Kamyab, "Valorization of sugarcane bagasse cellulose to synthesize novel graphene oxide-based composite for remediation of atrazine – optimization studies," *Journal of Environmental Chemical Engineering*, vol. 12, 6 2024.

[159] R. Hasanzadeh, P. N. Moghadam, N. Bahri-Laleh, and M. Sillanpää, "Effective removal of toxic metal ions from aqueous solutions: 2-bifunctional magnetic nanocomposite base on novel reactive pgma-man copolymer@fe3o4 nanoparticles," *Journal of Colloid and Interface Science*, vol. 490, pp. 727–746, 3 2017.

[160] V. Javanbakht, S. M. Ghoreishi, N. Habibi, and M. Javanbakht, "A novel magnetic chitosan/clinoptilolite/magnetite nanocomposite for highly efficient removal of pb(ii) ions from aqueous solution," *Powder Technology*, vol. 302, pp. 372–383, 11 2016.

[161] A. Vahdat, B. Ghasemi, and M. Yousefpour, "Synthesis of hydroxyapatite and hydroxyapatite/fe3o4 nanocomposite for removal of heavy metals," *Environmental Nanotechnology, Monitoring and Management*, vol. 12, 12 2019.

[162] A. A. Alqadami, M. Naushad, M. A. Abdalla, T. Ahamad, Z. A. ALOthman, S. M. Alshehri, and A. A. Ghfar, "Efficient removal of toxic metal ions from wastewater using a recyclable nanocomposite: A study of adsorption parameters and interaction mechanism," *Journal of Cleaner Production*, vol. 156, pp. 426–436, 7 2017.

[163] B. Ramalingam, T. Parandhaman, P. Choudhary, and S. K. Das, "Biomaterial functionalized graphene-magnetite nanocomposite: A novel approach for simultaneous removal of anionic dyes and heavy-metal ions," *ACS Sustainable Chemistry and Engineering*, vol. 6, pp. 6328–6341, 5 2018.

[164] A. Mittal, R. Ahmad, and I. Hasan, "Poly (methyl methacrylate)-grafted alginate/fe3o4 nanocomposite: synthesis and its application for the removal of heavy metal ions," *Desalination and Water Treatment*, vol. 57, pp. 19820–19833, 9 2016.

[165] M. J. Sharifi, A. Nouralishahi, and A. Hallajisani, "Fe3o4-chitosan nanocomposite as a magnetic biosorbent for removal of nickel and cobalt heavy metals from polluted water," *International Journal of Biological Macromolecules*, vol. 248, 9 2023.

[166] P. Maneechakr and S. Mongkollertlop, "Investigation on adsorption behaviors of heavy metal ions (cd2+, cr3+, hg2+and pb2+) through low-cost/active manganese dioxide-modified magnetic biochar derived from palm kernel cake residue," *Journal of Environmental Chemical Engineering*, vol. 8, 12 2020.

[167] S. S. Hosseini, A. Hamadi, R. Foroutan, S. J. Peighambardoust, and B. Ramavandi, "Decontamination of cd2+ and pb2+ from aqueous solution using a magnetic nanocomposite of eggshell/starch/fe3o4," *Journal of Water Process Engineering*, vol. 48, 8 2022.

[168] X. Liu, J. Guan, G. Lai, Q. Xu, X. Bai, Z. Wang, and S. Cui, "Stimuli-responsive adsorption behavior toward heavy metal ions based on comb polymer functionalized magnetic nanoparticles," *Journal of Cleaner Production*, vol. 253, 4 2020.

[169] A. Sharma, D. Mangla, Shehnaz, and S. A. Chaudhry, "Recent advances in magnetic composites as adsorbents for wastewater remediation," *Journal of Environmental Management*, vol. 306, 3 2022.

[170] A. Sharma, A. Choudhry, G. Rathi, N. Tara, N. K. Abdulla, M. Sajid, and S. A. Chaudhry, *Ferrite based magnetic nanocomposites for wastewater treatment through adsorption*, pp. 449–460. Elsevier, 1 2021.

[171] F. Ge, M. M. Li, H. Ye, and B. X. Zhao, "Effective removal of heavy metal ions cd 2+, zn 2+, pb 2+, cu 2+ from aqueous solution by polymer-modified magnetic nanoparticles," *Journal of Hazardous Materials*, vol. 211-212, pp. 366–372, 4 2012.

[172] S. S. Gupta and K. G. Bhattacharyya, "Kinetics of adsorption of metal ions on inorganic materials: A review," *Advances in Colloid and Interface Science*, vol. 162, pp. 39–58, 2 2011.

[173] M. Chen, A. Long, W. Zhang, Z. Wang, X. Xiao, Y. Gao, L. Zhou, Y. Li, J. Wang, S. Sun, M. Tang, Y. Peng, and H. Wang, "Recent advances in alginate-based hydrogels for the adsorption–desorption of heavy metal ions from water: A review," *Separation and Purification Technology*, vol. 353, 1 2025.

[174] W. Wang, L. Zong, and A. Wang, "A nanoporous hydrogel based on vinyl-functionalized alginate for efficient absorption and removal of pb2+ ions," *International Journal of Biological Macromolecules*, vol. 62, pp. 225–231, 2013.

[175] L. Song, F. Liu, C. Zhu, and A. Li, "Facile one-step fabrication of carboxymethyl cellulose based hydrogel for highly efficient removal of cr(vi) under mild acidic condition," *Chemical Engineering Journal*, vol. 369, pp. 641–651, 8 2019.

[176] J. Nastaj, A. Przewłocka, and M. Rajkowska-Myśliwiec, "Biosorption of ni(ii), pb(ii) and zn(ii) on calcium alginate beads: Equilibrium, kinetic and mechanism studies," *Polish Journal of Chemical Technology*, vol. 18, pp. 81–87, 9 2016.

[177] F. Wang, X. Lu, and X. Y. Li, "Selective removals of heavy metals (pb2+, cu2+, and cd2+) from wastewater by gelation with alginate for effective metal recovery," *Journal of Hazardous Materials*, vol. 308, pp. 75–83, 5 2016.

[178] H. J. Hong, J. Ryu, I. S. Park, T. Ryu, K. S. Chung, and B. G. Kim, "Investigation of the strontium (sr(ii)) adsorption of an alginate microsphere as a low-cost adsorbent for removal and recovery from seawater," *Journal of Environmental Management*, vol. 165, pp. 263–270, 1 2016.

[179] D. Tahtat, M. N. Bouaicha, S. Benamer, A. Nacer-Khodja, and M. Mahlous, "Development of alginate gel beads with a potential use in the treatment against acute lead poisoning," *International Journal of Biological Macromolecules*, vol. 105, pp. 1010–1016, 12 2017.

[180] M. T. ALSamman and J. Sánchez, "Recent advances on hydrogels based on chitosan and alginate for the adsorption of dyes and metal ions from water," *Arabian Journal of Chemistry*, vol. 14, 12 2021.

[181] Z. A. Sutirman, M. M. Sanagi, and W. I. W. Aini, "Alginate-based adsorbents for removal of metal ions and radionuclides from aqueous solutions: A review," *International Journal of Biological Macromolecules*, vol. 174, pp. 216–228, 3 2021.

[182] B. Wang, Y. Wan, Y. Zheng, X. Lee, T. Liu, Z. Yu, J. Huang, Y. S. Ok, J. Chen, and B. Gao, "Alginate-based composites for environmental applications: a critical review," *Critical Reviews in Environmental Science and Technology*, vol. 49, pp. 318–356, 2 2019.

[183] N. Mohammadi, H. Khani, V. K. Gupta, E. Amereh, and S. Agarwal, "Adsorption process of methyl orange dye onto mesoporous carbon material-kinetic and thermodynamic studies," *Journal of Colloid and Interface Science*, vol. 362, pp. 457–462, 10 2011.

[184] V. K. Gupta, A. Nayak, S. Agarwal, and I. Tyagi, "Potential of activated carbon from waste rubber tire for the adsorption of phenolics: Effect of pre-treatment conditions," *Journal of Colloid and Interface Science*, vol. 417, pp. 420–430, 3 2014.

[185] B. Wang, B. Gao, and Y. Wan, "Entrapment of ball-milled biochar in ca-alginate beads for the removal of aqueous cd(ii)," *Journal of Industrial and Engineering Chemistry*, vol. 61, pp. 161–168, 5 2018.

[186] Z. Ding, X. Hu, V. L. Morales, and B. Gao, "Filtration and transport of heavy metals in graphene oxide enabled sand columns," *Chemical Engineering Journal*, vol. 257, pp. 248–252, 12 2014.

[187] M. Inyang, B. Gao, A. Zimmerman, M. Zhang, and H. Chen, "Synthesis, characterization, and dye sorption ability of carbon nanotube-biochar nanocomposites," *Chemical Engineering Journal*, vol. 236, pp. 39–46, 1 2014.

[188] X. Qu, P. J. Alvarez, and Q. Li, "Applications of nanotechnology in water and wastewater treatment," *Water Research*, vol. 47, pp. 3931–3946, 8 2013.

[189] J. Theron, J. A. Walker, and T. E. Cloete, "Nanotechnology and water treatment: Applications and emerging opportunities," 2 2008.

[190] A. Idris, N. S. M. Ismail, N. Hassan, E. Misran, and A. F. Ngomsik, "Synthesis of magnetic alginate beads based on maghemite nanoparticles for pb(ii) removal in aqueous solution," *Journal of Industrial and Engineering Chemistry*, vol. 18, pp. 1582–1589, 9 2012.

[191] C. udia Silveira Martins Suzana, M. Claudia, M. a, M. C. o Larissa Guedes Fiuacute za, and T. dde Santaella ra, "Immobilization of microbial cells: A promising tool for treatment of toxic pollutants in industrial wastewater," *African Journal of Biotechnology*, vol. 12, pp. 4412–4418, 7 2013.

[192] H. Liu, L. Guo, S. Liao, and G. Wang, "Reutilization of immobilized fungus rhizopus sp. lg04 to reduce toxic chromate," *Journal of Applied Microbiology*, vol. 112, pp. 651–659, 2012.

[193] J. Wang, M. Guo, Y. Luo, D. Shao, S. Ge, L. Cai, C. Xia, and S. S. Lam, "Production of magnetic sodium alginate polyelectrolyte nanospheres for lead ions removal from wastewater," *Journal of Environmental Management*, vol. 289, 7 2021.

[194] J. Wang, M. Guo, Y. Luo, D. Shao, S. Ge, L. Cai, C. Xia, and S. S. Lam, "Preparation of a novel bio-adsorbent of sodium alginate grafted polyacrylamide/graphene oxide hydrogel for the adsorption of heavy metal ion," *Science of the Total Environment*, vol. 744, p. 140653, 2020.

[195] A. Bée, D. Talbot, S. Abramson, and V. Dupuis, "Magnetic alginate beads for pb(ii) ions removal from wastewater," *Journal of Colloid and Interface Science*, vol. 362, pp. 486–492, 10 2011.

[196] Z. H. Hu, A. M. Omer, X. K. Ouyang, and D. Yu, "Fabrication of carboxylated cellulose nanocrystal/sodium alginate hydrogel beads for adsorption of pb(ii) from aqueous solution," *International Journal of Biological Macromolecules*, vol. 108, pp. 149–157, 3 2018.

[197] R. D. C. Soltani, G. S. Khorramabadi, A. R. Khataee, and S. Jorfi, "Silica nanopowders/alginate composite for adsorption of lead (ii) ions in aqueous solutions," *Journal of the Taiwan Institute of Chemical Engineers*, vol. 45, pp. 973–980, 2014.

[198] S. Cataldo, A. Gianguzza, D. Milea, N. Muratore, and A. Pettignano, "Pb(ii) adsorption by a novel activated carbon – alginate composite material. a kinetic and equilibrium study," *International Journal of Biological Macromolecules*, vol. 92, pp. 769–778, 11 2016.

[199] Y. yan WANG, W. bin YAO, Q. wei WANG, Z. hui YANG, L. fen LIANG, and L. yuan CHAI, "Synthesis of phosphate-embedded calcium alginate beads for pb(ii) and cd(ii) sorption and immobilization in aqueous solutions," *Transactions of Nonferrous Metals Society of China (English Edition)*, vol. 26, pp. 2230–2237, 2016.

[200] A. M. Omer, R. E. Khalifa, Z. Hu, H. Zhang, C. Liu, and X. kun Ouyang, "Fabrication of tetraethylenepentamine functionalized alginate beads for adsorptive removal of cr (vi) from aqueous solutions," *International Journal of Biological Macromolecules*, vol. 125, pp. 1221–1231, 3 2019.

[201] N. E. Mousa, C. M. Simonescu, R. E. Pătescu, C. Onose, C. Tardei, D. C. Culiţă, O. Oprea, D. Patroi, and V. Lavric, "Pb2 + removal from aqueous synthetic solutions by calcium alginate

and chitosan coated calcium alginate," *Reactive and Functional Polymers*, vol. 109, pp. 137–150, 12 2016.

[202] R. Verma, A. Asthana, A. K. Singh, S. Prasad, and M. A. B. H. Susan, "Novel glycine-functionalized magnetic nanoparticles entrapped calcium alginate beads for effective removal of lead," *Microchemical Journal*, vol. 130, pp. 168–178, 1 2017.

[203] S. Zhang, F. Xu, Y. Wang, W. Zhang, X. Peng, and F. Pepe, "Silica modified calcium alginate-xanthan gum hybrid bead composites for the removal and recovery of pb(ii) from aqueous solution," *Chemical Engineering Journal*, vol. 234, pp. 33–42, 9 2013.

[204] Z. Mahmood, A. Amin, U. Zafar, M. A. Raza, I. Hafeez, and A. Akram, "Adsorption studies of cadmium ions on alginate–calcium carbonate composite beads," *Applied Water Science*, vol. 7, pp. 915–921, 5 2017.

[205] C. S. C. Chiew, H. K. Yeoh, P. Pasbakhsh, K. Krishnaiah, P. E. Poh, B. T. Tey, and E. S. Chan, "Halloysite/alginate nanocomposite beads: Kinetics, equilibrium and mechanism for lead adsorption," *Applied Clay Science*, vol. 119, pp. 301–310, 1 2016.

[206] H. Ren, Z. Gao, D. Wu, J. Jiang, Y. Sun, and C. Luo, "Efficient pb(ii) removal using sodium alginate-carboxymethyl cellulose gel beads: Preparation, characterization, and adsorption mechanism," *Carbohydrate Polymers*, vol. 137, pp. 402–409, 2 2016.

[207] K. Sangeetha, G. Vidhya, G. Vasugi, and G. V. E. Girija, "Lead and cadmium removal from single and binary metal ion solution by novel hydroxyapatite/alginate/gelatin nanocomposites," *Journal of Environmental Chemical Engineering*, vol. 6, pp. 1118–1126, 2 2018.

[208] A. Salisu, M. M. Sanagi, A. A. Naim, K. J. A. Karim, W. A. W. Ibrahim, and U. Abdulganiyu, "Alginate graft polyacrylonitrile beads for the removal of lead from aqueous solutions," *Polymer Bulletin*, vol. 73, pp. 519–537, 2 2016.

[209] W. M. Algothmi, N. M. Bandaru, Y. Yu, J. G. Shapter, and A. V. Ellis, "Alginate-graphene oxide hybrid gel beads: An efficient copper adsorbent material," *Journal of Colloid and Interface Science*, vol. 397, pp. 32–38, 5 2013.

[210] Y. Wang, Y. Feng, X. F. Zhang, X. Zhang, J. Jiang, and J. Yao, "Alginate-based attapulgite foams as efficient and recyclable adsorbents for the removal of heavy metals," *Journal of Colloid and Interface Science*, vol. 514, pp. 190–198, 3 2018.

[211] J. Guo, Y. Han, Y. Mao, and M. N. Wickramaratne, "Influence of alginate fixation on the adsorption capacity of hydroxyapatite nanocrystals to cu2+ ions," *Colloids and Surfaces A: Physicochemical and Engineering Aspects*, vol. 529, pp. 801–807, 9 2017.

[212] A. Asthana, R. Verma, A. K. Singh, and M. A. B. H. Susan, "Glycine functionalized magnetic nanoparticle entrapped calcium alginate beads: A promising adsorbent for removal of cu(ii) ions," *Journal of Environmental Chemical Engineering*, vol. 4, pp. 1985–1995, 6 2016.

[213] B. Wang, B. Gao, and Y. Wan, "Entrapment of ball-milled biochar in ca-alginate beads for the removal of aqueous cd(ii)," *Journal of Industrial and Engineering Chemistry*, vol. 61, pp. 161–168, 5 2018.

[214] R. Dubey, J. Bajpai, and A. K. Bajpai, "Chitosan-alginate nanoparticles (canps) as potential nanosorbent for removal of hg (ii) ions," *Environmental Nanotechnology, Monitoring and Management*, vol. 6, pp. 32–44, 12 2016.

[215] V. Gopalakannan, S. Periyasamy, and N. Viswanathan, "Synthesis of assorted metal ions anchored alginate bentonite biocomposites for cr(vi) sorption," *Carbohydrate Polymers*, vol. 151, pp. 1100–1109, 10 2016.

[216] W. Jung, B. H. Jeon, D. W. Cho, H. S. Roh, Y. Cho, S. J. Kim, and D. S. Lee, "Sorptive removal of heavy metals with nano-sized carbon immobilized alginate beads," *Journal of Industrial and Engineering Chemistry*, vol. 26, pp. 364–369, 6 2015.

[217] F. Karkeh-abadi, S. Saber-Samandari, and S. Saber-Samandari, "The impact of functionalized cnt in the network of sodium alginate-based nanocomposite beads on the removal of co(ii) ions from aqueous solutions," *Journal of Hazardous Materials*, vol. 312, pp. 224–233, 7 2016.

[218] J. V. Milojković, Z. R. Lopičić, I. P. Anastopoulos, J. T. Petrović, S. Z. Milićević, M. S. Petrović, and M. D. Stojanović, "Performance of aquatic weed - waste myriophyllum spicatum immobilized in alginate beads for the removal of pb(ii)," *Journal of Environmental Management*, vol. 232, pp. 97–109, 2 2019.

[219] Y. Huang and Z. Wang, "Preparation of composite aerogels based on sodium alginate, and its application in removal of pb2+and cu2+from water," *International Journal of Biological Macromolecules*, vol. 107, pp. 741–747, 2 2018.

[220] T. M. Joseph, A. Sathian, K. S. Joshy, D. K. Mahapatra, J. T. Haponiuk, and S. Thomas, *Chemical modifications of alginate-based biopolymers*, pp. 97–122. Elsevier, 1 2024.

[221] D. Shi, J. Shen, Z. Zhang, C. Shi, M. Chen, Y. Gu, and Y. Liu, "Preparation and properties of dopamine-modified alginate/chitosan–hydroxyapatite scaffolds with gradient structure for bone tissue engineering," *Journal of Biomedical Materials Research - Part A*, vol. 107, pp. 1615–1627, 8 2019.

[222] J. Ma, S. Fang, P. Shi, and M. Duan, "Hydrazine-functionalized guar-gum material capable of capturing heavy metal ions," *Carbohydrate Polymers*, vol. 223, 11 2019.

[223] M. Duan, J. Ma, and S. Fang, "Synthesis of hydrazine-grafted guar gum material for the highly effective removal of organic dyes," *Carbohydrate Polymers*, vol. 211, pp. 308–314, 5 2019.

[224] Y. Wen, Z. Xie, S. Xue, W. Li, H. Ye, W. Shi, and Y. Liu, "Functionalized polymethyl methacrylate-modified dialdehyde guar gum containing hydrazide groups for effective removal and enrichment of dyes, ion, and oil/water separation," *Journal of Hazardous Materials*, vol. 426, 3 2022.

[225] C. Zhou, Q. Wu, T. Lei, and I. I. Negulescu, "Adsorption kinetic and equilibrium studies for methylene blue dye by partially hydrolyzed polyacrylamide/cellulose nanocrystal nanocomposite hydrogels," *Chemical Engineering Journal*, vol. 251, pp. 17–24, 9 2014.

[226] K. Gul, S. Sohni, M. Waqar, F. Ahmad, N. A. Norulaini, and M. O. A. K., "Functionalization of magnetic chitosan with graphene oxide for removal of cationic and anionic dyes from aqueous solution," *Carbohydrate Polymers*, vol. 152, pp. 520–531, 11 2016.

[227] T. Shi, Z. Xie, Z. Zhu, W. Shi, Y. Liu, and M. Liu, "Highly efficient and selective adsorption of heavy metal ions by hydrazide-modified sodium alginate," *Carbohydrate Polymers*, vol. 276, 1 2022.

[228] T. Shi, Z. Xie, X. Mo, W. Shi, H. Qiu, G. Lan, and Y. Liu, "Adsorption behaviors of heavy metal ions by different hydrazone-modified sodium alginate in aqueous medium: Experimental and dft studies," *Colloids and Surfaces A: Physicochemical and Engineering Aspects*, vol. 659, 2 2023.

[229] B. M. Córdova, C. R. Jacinto, H. Alarcón, I. M. Mejía, R. C. López, D. de Oliveira Silva, E. Cavalheiro, T. Venâncio, J. Z. Dávalos, and A. C. Valderrama, "Chemical modification of sodium alginate with thiosemicarbazide for the removal of pb(ii) and cd(ii) from aqueous solutions," *International Journal of Biological Macromolecules*, vol. 120, pp. 2259–2270, 12 2018.

[230] M. Modestino, A. Galluzzi, M. Barozzi, S. Copelli, F. Daniele, E. Russo, E. Sieni, P. Sgarbossa, P. Lamberti, and M. Polichetti, "The effect of copper adsorption on iron oxide magnetic nanoparticles embedded in a sodium alginate bead," *Nanomaterials*, vol. 15, 8 2025.

[231] M. Barozzi, M. S. Scotton, E. Sieni, P. Sgarbossa, A. Sandon, and S. Copelli, "Magnetically separable nanoparticles for wastewater treatment," *Chemical Engineering Transactions*, vol. 86, pp. 1033–1038, 2021.

[232] F. Pendolino, N. Armata, T. Masullo, and A. Cuttitta, "Temperature influence on the synthesis of pristine graphene oxide and graphite oxide," *Materials Chemistry and Physics*, vol. 164, pp. 71–77, 8 2015.

[233] E. Ghasemi, A. Mirhabibi, and M. Edrissi, "Synthesis and rheological properties of an iron oxide ferrofluid," *Journal of Magnetism and Magnetic Materials*, vol. 320, pp. 2635–2639, 2008.

[234] J. Liu, Y. Chen, S. Jiang, J. Huang, Y. Lv, Y. Liu, and M. Liu, "Rapid removal of cr(iii) from high-salinity wastewater by cellulose-g-poly-(acrylamide-co-sulfonic acid) polymeric bioadsorbent," *Carbohydrate Polymers*, vol. 270, 10 2021.

[235] K. Kayalvizhi, N. M. Alhaji, D. Saravanakkumar, S. B. Mohamed, K. Kaviyarasu, A. Ayeshamariam, A. M. Al-Mohaimeed, M. R. AbdelGawwad, and M. S. Elshikh, "Adsorption of copper and nickel by using sawdust chitosan nanocomposite beads – a kinetic and thermodynamic study," *Environmental Research*, vol. 203, 1 2022.

[236] M. Azam, S. M. Wabaidur, M. R. Khan, M. S. Islam, and S. I. Al-Resayes, "Removal of chromium(iii) and cadmium(ii) heavy metal ions from aqueous solutions using treated date seeds: An eco-friendly method," *Molecules*, vol. 26, 6 2021.

[237] M. Barozzi, S. Copelli, E. Russo, P. Sgarbossa, M. C. Lavagnolo, A. Sandon, C. Morosini, and E. Sieni, "Implementation of magnetic nanostructured adsorbents for heavy metals separation from textile wastewater," *Sustainability (Switzerland)*, vol. 14, 9 2022.

[238] K. Deb, A. Pratap, S. Agarwal, and T. Meyarivan, "A fast and elitist multiobjective genetic algorithm: Nsga-ii," tech. rep., IEEE Transactions on Evolutionary Computation, 2002.

[239] S. A. Haris, S. Dabagh, H. Mollasalehi, and Y. N. Ertas, "Alginate coated superparamagnetic iron oxide nanoparticles as nanocomposite adsorbents for arsenic removal from aqueous solutions," *Separation and Purification Technology*, vol. 310, 4 2023.

[240] A. M. Donald, "The use of environmental scanning electron microscopy for imaging wet and insulating materials," *Nature Materials*, vol. 2, 8 2003.

[241] S. Horváth, D. Lukács, E. Farsang, and K. Horváth, "Unbiased determination of adsorption isotherms by inverse method in liquid chromatography," *Molecules*, vol. 28, 2 2023.

[242] G. Germanos, S. Youssef, M. Abboud, W. Farah, B. Lescop, and S. Rioual, "Diffusion and agglomeration of iron oxide nanoparticles in magnetic calcium alginate beads initiated by copper sorption," *Journal of Environmental Chemical Engineering*, vol. 5, pp. 3727–3733, 8 2017.

[243] L. Maldonado-Camargo, M. Unni, and C. Rinaldi, *Magnetic characterization of iron oxide nanoparticles for biomedical applications*, vol. 1570, pp. 47–71. Humana Press Inc., 2017.

[244] L. de Castro Alves, S. Yáñez-Vilar, Y. Piñeiro-Redondo, and J. Rivas, "Efficient separation of heavy metals by magnetic nanostructured beads," *Inorganics*, vol. 8, 9 2020.

[245] Z. X. Li, D. Luo, M. M. Li, X. F. Xing, Z. Z. Ma, and H. Xu, "Recyclable fe3o4 nanoparticles catalysts for aza-michael addition of acryl amides by magnetic field," *Catalysts*, vol. 7, 7 2017.

[246] S. Yuan, L. Dai, M. Xie, J. Liu, and H. Peng, "Modification optimization and application of graphitic carbon nitride in photocatalysis: Current progress and future prospects," *Chemical Engineering Science*, vol. 296, 8 2024.

[247] F. Basumatary, A. Sarkar, N. Mushahary, B. Das, P. Saikia, M. Selvaraj, and S. Basumatary, "Graphitic carbon nitride composites as advanced versatile materials for adsorption and photocatalytic degradation of emerging pollutants from wastewater," *Process Safety and Environmental Protection*, vol. 191, pp. 2416–2468, 11 2024.

[248] D. M. Teter and R. J. Hemley, "Low-compressibility carbon nitrides," *Science*, vol. 271, pp. 53–55, 1 1996.

[249] N. Liu, T. Li, Z. Zhao, J. Liu, X. Luo, X. Yuan, K. Luo, J. He, D. Yu, and Y. Zhao, "From triazine to heptazine: Origin of graphitic carbon nitride as a photocatalyst," *ACS Omega*, vol. 5, pp. 12557–12567, 6 2020.

[250] V. Saraswat, S. Kohli, N. K. Sinha, G. Purohit, N. Sandhu, S. Swami, G. Rathee, M. Rawat, and N. Kumari, "Metal-free graphitic carbon nitride as a promising nano-adsorbent for the efficient photocatalytic degradation of toxic dyes: Recent trends and future perspectives," 9 2025.

[251] J. Barrio and M. Shalom, "Ultralong nanostructured carbon nitride wires and self-standing c-rich filters from supramolecular microspheres," *ACS Applied Materials and Interfaces*, vol. 10, pp. 39688–39694, 11 2018.

[252] H. Yan, "Soft-templating synthesis of mesoporous graphitic carbon nitride with enhanced photocatalytic h2 evolution under visible light," *Chemical Communications*, vol. 48, pp. 3430–3432, 3 2012.

[253] P. Zhang, H. Li, and Y. Wang, "Post-functionalization of graphitic carbon nitrides by grafting organic molecules: Toward c-h bond oxidation using atmospheric oxygen," *Chemical Communications*, vol. 50, pp. 6312–6315, 5 2014.

[254] Y. Zhang, T. Mori, L. Niu, and J. Ye, "Non-covalent doping of graphitic carbon nitride polymer with graphene: Controlled electronic structure and enhanced optoelectronic conversion," *Energy and Environmental Science*, vol. 4, pp. 4517–4521, 11 2011.

[255] J. Zhang, X. Chen, K. Takanabe, K. Maeda, K. Domen, J. D. Epping, X. Fu, M. Antonieta, and X. Wang, "Synthesis of a carbon nitride structure for visible-light catalysis by copolymerization," *Angewandte Chemie - International Edition*, vol. 49, pp. 441–444, 1 2010.

[256] X. Wang, K. Maeda, A. Thomas, K. Takanabe, G. Xin, J. M. Carlsson, K. Domen, and M. Antonietti, "A metal-free polymeric photocatalyst for hydrogen production from water under visible light," *Nature Materials*, vol. 8, pp. 76–80, 2009.

[257] S. C. Yan, Z. S. Li, and Z. G. Zou, "Photodegradation performance of g-c3n4 fabricated by directly heating melamine," *Langmuir*, vol. 25, pp. 10397–10401, 9 2009.

[258] J. Liu, T. Zhang, Z. Wang, G. Dawson, and W. Chen, "Simple pyrolysis of urea into graphitic carbon nitride with recyclable adsorption and photocatalytic activity," *Journal of Materials Chemistry*, vol. 21, pp. 14398–14401, 9 2011.

[259] B. Li, T. Tian, Y. Zheng, D. Jiang, G. Xu, Y. Sun, Z. Li, and Y. Yuan, "Exploring n-pi greco electronic transitions in graphitic carbon nitride: Fundamentals, strategies, and photocatalytic advances," *Chemistry - A European Journal*, vol. 31, 4 2025.

[260] Y. Chen, B. Wang, S. Lin, Y. Zhang, and X. Wang, "Activation of n- transitions in two-dimensional conjugated polymers for visible light photocatalysis," *Journal of Physical Chemistry C*, vol. 118, pp. 29981–29989, 12 2014.

[261] A. B. Jorge, D. J. Martin, M. T. Dhanoa, A. S. Rahman, N. Makwana, J. Tang, A. Sella, F. Corà, S. Firth, J. A. Darr, and P. F. McMillan, "H2 and o2 evolution from water half-splitting reactions by graphitic carbon nitride materials," *Journal of Physical Chemistry C*, vol. 117, pp. 7178–7185, 4 2013.

[262] V. W. hei Lau and B. V. Lotsch, "A tour-guide through carbon nitride-land: Structure- and dimensionality-dependent properties for photo(electro)chemical energy conversion and storage," *Advanced Energy Materials*, vol. 12, 1 2022.

[263] P. Sha, Y. You, D. Wen, Z. Wu, Q. Wang, D. Bu, and S. Huang, "Two-dimensional ultrathin graphic carbon nitrides with extended pi greco-conjugation as extraordinary efficient hydrogen evolution photocatalyst," *Small*, vol. 19, 2 2023.

[264] S. Chandrappa, S. J. Galbao, A. Furube, and D. H. Murthy, "Extending the optical absorption limit of graphitic carbon nitride photocatalysts: A review," *ACS Applied Nano Materials*, vol. 6, pp. 19551–19572, 11 2023.

[265] T. Bao, X. Li, S. Li, H. Rao, X. Men, P. She, and J. sheng Qin, "Recent advances of graphitic carbon nitride (g-c3n4) based materials for photocatalytic applications: A review," 2024.

[266] A. Javaid, M. Imran, M. P. Rayaroth, X. Sun, C. Wang, G. Boczkaj, and M. Momotko, "Graphitic carbon nitride/bismuth-based z-scheme heterojunctions for the photocatalytic removal of pharmaceuticals and personal care products — a review," 12 2024.

[267] Y. Ji, G. Luan, J. Wei, L. Bao, M. Cui, Z. Tian, and C. Li, "Zinc indium sulfide coupling with graphitic carbon nitride containing non-intrinsic oxygen vacancies to form z-scheme heterojunction for boosting photodegradation of tetracycline," *Journal of Environmental Chemical Engineering*, vol. 12, 10 2024.

[268] A. A., A. P. Chowdhury, K. S. Anantharaju, and Y. S. Vidya, "Neodymium doped bismuth oxybromide anchored graphitic carbon nitride z-scheme heterojunction photocatalyst for photodegradation of acid red 27 and orange g dyes and its mechanism insights," *Materials Science and Engineering: B*, vol. 323, 1 2026.

[269] M. M. Xavier, S. Mohanapriya, K. S. Divya, N. N. Adarsh, P. R. Nair, and S. Mathew, "Exploring the effect of precursors of polymeric carbon nitride nanosheets on their photo and electrocatalytic applications," *ChemistrySelect*, vol. 5, pp. 12679–12689, 11 2020.

[270] S. Ganesan, T. Kokulnathan, S. Sumathi, and A. Palaniappan, "Efficient photocatalytic degradation of textile dye pollutants using thermally exfoliated graphitic carbon nitride (te–g–c3n4)," *Scientific Reports*, vol. 14, 12 2024.

[271] Z. K. Bolaghi, C. Rodriguez-Seco, A. Yurtsever, and D. Ma, "Exploring the remarkably high photocatalytic efficiency of ultra-thin porous graphitic carbon nitride nanosheets," *Nanomaterials*, vol. 14, 1 2024.

[272] P. Sarmah, K. Patir, and S. K. Gogoi, "Graphitic carbon nitride nanospheres as an adsorbent for effective wastewater treatment: Methylene blue removal from aqueous medium," *Journal of Water and Environmental Nanotechnology*, vol. 8, pp. 369–383, 11 2023.

[273] Z. Chen, S. Zhang, Y. Liu, N. S. Alharbi, S. O. Rabah, S. Wang, and X. Wang, "Synthesis and fabrication of g-c3n4-based materials and their application in elimination of pollutants," *Science of the Total Environment*, vol. 731, 8 2020.

[274] Y. Xing, X. Wang, S. Hao, X. Zhang, X. Wang, W. Ma, G. Zhao, and X. Xu, "Recent advances in the improvement of g-c3n4 based photocatalytic materials," *Chinese Chemical Letters*, vol. 32, pp. 13–20, 1 2021.

[275] S. Patnaik, S. Martha, and K. M. Parida, "An overview of the structural, textural and morphological modulations of g-c3n4 towards photocatalytic hydrogen production," *RSC Advances*, vol. 6, pp. 46929–46951, 2016.

[276] S. Liu, X. Jiang, G. I. Waterhouse, Z. M. Zhang, and L. min Yu, "Protonated graphitic carbon nitride/polypyrrole/reduced graphene oxide composites as efficient visible light driven photocatalysts for dye degradation and e. coli disinfection," *Journal of Alloys and Compounds*, vol. 873, 8 2021.

[277] M. Chegeni and N. Dehghan, "Preparation of phosphorus doped graphitic carbon nitride using a simple method and its application for removing methylene blue," *Physical Chemistry Research*, vol. 8, pp. 31–44, 12 2020.

[278] Z. Li, Q. Chen, Q. Lin, Y. Chen, X. Liao, H. Yu, and C. Yu, "Three-dimensional p-doped porous g-c3n4 nanosheets as an efficient metal-free photocatalyst for visible-light photocatalytic degradation of rhodamine b model pollutant," *Journal of the Taiwan Institute of Chemical Engineers*, vol. 114, pp. 249–262, 9 2020.

[279] M. I. Nabeel, D. Hussain, N. Ahmad, H. M. Xiao, and S. G. Musharraf, "Improved visible light-driven photocatalytic degradation of an industrial dye acid orange 7 using metal-free sulfur-doped graphitic carbon nitride," *Environmental Science: Nano*, vol. 10, pp. 2810–2830, 8 2023.

[280] X. Luo, B. Li, T. Su, X. Xie, Z. Qin, and H. Ji, "B/g-c3n4 for selectively regulating oxygen-guided photocatalytic oxidation of cinnamaldehyde to benzaldehyde: Effects of boron sources," *ACS Catalysis*, vol. 15, pp. 1097–1111, 1 2025.

[281] Z. Liu, C. Li, Y. Xu, Y. Jiao, Y. Liu, and L. Wang, "One-pot synthesis of porous graphitic carbon nitride with rich nitrogen vacancies and oxygen heteroatoms for boosting photocatalytic performance," *Optical Materials*, vol. 139, 5 2023.

[282] A. Hussain, N. Ali, S. S. Ali, J. Hou, I. Aslam, H. Naeem, M. Boota, M. Ul-Hussan, J. Yin, and X. Wang, "Diverse morphological study for nonmetal-doped g-c3n4 composites with narrow bandgap for improved photocatalytic activity," *Research on Chemical Intermediates*, vol. 48, pp. 2857–2870, 7 2022.

[283] B. M. Bresolin, P. Sgarbossa, D. W. Bahnemann, and M. Sillanpää, "Cs3bi2i9/g-c3n4 as a new binary photocatalyst for efficient visible-light photocatalytic processes," *Separation and Purification Technology*, vol. 251, 11 2020.

[284] B. M. Bresolin, P. Sgarbossa, and D. W. Bahnemann, "Synthesis of metal-free functionalized g-c3n4 nanosheets for enhanced photocatalytic activity," *Journal of Environmental Chemical Engineering*, vol. 9, 12 2021.

[285] T. Ma, Q. Shen, B. Z. J. Xue, R. Guan, X. Liu, H. Jia, and B. Xu, "Facile synthesis of fe-doped g-c3n4 for enhanced visible-light photocatalytic activity," *Inorganic Chemistry Communications*, vol. 107, 9 2019.

[286] M. Imran, A. Z. Abdullah, M. E. Khan, and A. Mohammad, "A focused review on photocatalytic potential of graphitic carbon nitride (g-c3n4) based metal oxide-nanostructures for effective remediation of most overused antibiotics," *Journal of Environmental Management*, vol. 373, 1 2025.

[287] S. J. Singh, S. Sellaiyan, and P. Chinnamuthu, "Synthesis and characterization of cuo/gc3n4 nanocomposite for efficient photocatalytic activities under natural sunlight," *Physica B: Condensed Matter*, vol. 650, 2 2023.

[288] Y. M. Hunge, A. A. Yadav, S. W. Kang, and H. Kim, "Photocatalytic degradation of tetracycline antibiotics using hydrothermally synthesized two-dimensional molybdenum disulfide/titanium dioxide composites," *Journal of Colloid and Interface Science*, vol. 606, pp. 454–463, 1 2022.

[289] S. Ni, Z. Fu, L. Li, M. Ma, and Y. Liu, "Step-scheme heterojunction g-c3n4/tio2 for efficient photocatalytic degradation of tetracycline hydrochloride under uv light," *Colloids and Surfaces A: Physicochemical and Engineering Aspects*, vol. 649, 9 2022.

[290] R. Msalmi, S. Elleuch, B. Hamdi, E. Radicchi, A. Tozri, H. Naïli, and M. R. Berber, "Tunable broad-band white-light emission in two-dimensional (110)-oriented lead bromide perovskite (c3h8n6)[pbbr4]: Optical, electronic and luminescence properties," *New Journal of Chemistry*, vol. 45, pp. 20850–20859, 11 2021.

[291] A. Ghorbani-Choghamarani, M. A. Zolfigol, M. Hajjami, and S. Jafari, "Trimethylsilylation of hydroxyl group with 1,1,1,3,3,3-hexamethyldisilazane (hmds) catalyzed by tribromomelamine (tbm)," *Journal of the Chinese Chemical Society*, vol. 55, pp. 1208–1213, 2008.

[292] B. R. Groves, S. M. Crawford, T. Lundrigan, C. F. Matta, S. Sowlati-Hashjin, and A. Thompson, "Synthesis and characterisation of the unsubstituted dipyrrin and 4,4-dichloro-4-bora-3a,4a-diaza-s-indacene: Improved synthesis and functionalization of the simplest bodipy framework," *The Royal Society of Chemistry*, 2013.

[293] P. Sharma, A. Kumar, P. Dhiman, G. Sharma, T. Wang, A. García-Penas, and C. W. Lai, "Recent advances and perspective in boron carbon nitride and boron nitride based materials for photocatalytic energy and environmental applications," *Journal of Water Process Engineering*, vol. 70, 2 2025.

[294] A. K. Singh, R. Yadav, A. Pal, and Rosy, "Boron doped graphitic carbon nitride modified interface for electroanalysis of hazardous p-benzoquinone in water," *Electrochimica Acta*, vol. 523, 5 2025.

[295] Q. P. Zhang, D. M. Liang, W. F. Zhu, J. H. Liu, Y. Wu, D. G. Xu, X. Y. Bai, M. Wei, and Y. L. Zhou, "Fabrication of h-bn@pbwo4 with a facile sol-gel method towards enhanced photocatalytic and radiation shielding properties," *Journal of Solid State Chemistry*, vol. 269, pp. 594–599, 1 2019.

[296] L. Liang, L. Cheng, Y. Zhang, Q. Wang, Q. Wu, Y. Xue, and X. Meng, "Efficiency and mechanisms of rhodamine b degradation in fenton-like systems based on zero-valent iron," *RSC Advances*, vol. 10, pp. 28509–28515, 8 2020.

[297] H. Kaur and R. Kaur, "Removal of rhodamine-b dye from aqueous solution onto pigeon dropping: Adsorption, kinetic, equilibrium and thermodynamic studies," *J. Mater. Environ. Sci*, vol. 5, pp. 1830–1838, 2014.

[298] M. I. Khan and A. Shanableh, "Adsorption of rhodamine b from an aqueous solution onto naoh-treated rice husk," *Desalination and Water Treatment*, vol. 254, pp. 104–115, 4 2022.

[299] K. Fent, A. A. Weston, and D. Caminada, "Ecotoxicology of human pharmaceuticals," *Aquatic Toxicology*, vol. 76, pp. 122–159, 2 2006.